



**HAL**  
open science

# Development of laser ultrasonic methods for the nondestructive evaluation of bonded aeronautical assemblies

Romain Hodé

► **To cite this version:**

Romain Hodé. Development of laser ultrasonic methods for the nondestructive evaluation of bonded aeronautical assemblies. Acoustics [physics.class-ph]. Le Mans Université, 2020. English. NNT : 2020LEMA1030 . tel-03151744

**HAL Id: tel-03151744**

**<https://theses.hal.science/tel-03151744>**

Submitted on 25 Feb 2021

**HAL** is a multi-disciplinary open access archive for the deposit and dissemination of scientific research documents, whether they are published or not. The documents may come from teaching and research institutions in France or abroad, or from public or private research centers.

L'archive ouverte pluridisciplinaire **HAL**, est destinée au dépôt et à la diffusion de documents scientifiques de niveau recherche, publiés ou non, émanant des établissements d'enseignement et de recherche français ou étrangers, des laboratoires publics ou privés.

# THESE DE DOCTORAT DE

LE MANS UNIVERSITE

ECOLE DOCTORALE N° 602  
*Sciences pour l'Ingénieur*  
Spécialité : Acoustique

Par

**Romain HODÉ**

## **Development of laser ultrasonic methods for the nondestructive evaluation of bonded aeronautical assemblies**

Thèse présentée et soutenue à Le Mans, le 24 novembre 2020

Unité de recherche : Laboratoire d'Acoustique de l'Université du Mans – UMR-CNRS 6613

Thèse N° : 2020LEMA1030

### **Rapporteurs avant soutenance :**

Christ Glorieux      Professeur, KU Leuven  
Jean-Louis Thomas      Directeur de recherche CNRS, Institut des NanoSciences de Paris

### **Composition du Jury :**

Président :	Michel Castaings	Professeur, Bordeaux INP
Examinatrice :	Bénédicte Levasseur	Manager d'affaires matériaux structuraux et dynamique des structures, DGA
Rapporteurs :	Christ Glorieux	Professeur, KU Leuven
	Jean-Louis Thomas	Directeur de recherche CNRS, Institut des NanoSciences de Paris
Dir. de thèse :	Vincent Tournat	Directeur de recherche CNRS, LAUM – Le Mans Université
Co-encadrant :	Samuel Raetz	Maître de conférences, LAUM – Le Mans Université
Co-encadrant :	Mathieu Ducouso	Ing. Chercheur, HDR, Safran Group
Co-encadrant :	Vitalyi Gusev	Professeur, LAUM – Le Mans Université



# Remerciements

Pour débiter ce manuscrit, je souhaite remercier les personnes m'ayant permis de réaliser cette thèse dans les meilleures conditions et qui m'ont accompagné et soutenu durant ces trois années.

Tout d'abord, je souhaite remercier Pierrick Lotton, directeur du Laboratoire d'Acoustique de l'Université du Mans (LAUM), Nicolas Cuvillier, pilote de la plateforme collage à Safran Composites, et Daniel Duclos, responsable du pôle TSI à Safran Tech, de m'avoir accueilli dans leurs équipes respectives.

Je tiens à remercier Christ Glorieux, professeur à l'université KU Leuven, ainsi que Jean-Louis Thomas, directeur de recherche au CNRS, d'avoir accepté de rapporter ce manuscrit de thèse.

Mes remerciements vont également à Michel Castaings, professeur à Bordeaux INP, et Bénédicte Levasseur, manager d'affaires matériaux structuraux et dynamiques des structures à la DGA, d'avoir accepté d'être membres du jury. Merci à Nicolas Leymarie, ingénieur chercheur au CEA, d'avoir accepté l'invitation à ma soutenance de thèse. Je tiens aussi à remercier les membres de mon « comité de suivi individuel » de thèse : Frédéric Jenson, responsable des programmes CND à Safran Tech, et Aroune Duclos, maître de conférences à Le Mans Université.

Je souhaite remercier chaleureusement les personnes qui ont dirigé et encadré ces travaux de recherche. J'ai énormément appris à leur côté. Merci à Vincent Tournat, directeur de recherche au CNRS et directeur de l'Institut d'Acoustique-Graduate School (IA-GS), d'avoir dirigé cette thèse. Merci pour la confiance que tu m'as accordée et tes conseils toujours avisés. Merci à Vitalyi Gusev, professeur à le Mans Université, pour sa rigueur scientifique et la bienveillance dont il a toujours fait preuve à mon égard. Merci à Mathieu Ducouso, ingénieur chercheur à Safran Tech, de m'avoir encadré pendant ces trois années. Merci pour tout ce que tu m'as apporté, pour ton enthousiasme et pour ton soutien sans faille. Si j'en suis arrivé jusqu'ici c'est aussi grâce à toi, merci Mathieu! Enfin, je remercie Samuel Raetz, maître de conférences à Le Mans Université, de m'avoir encadré au quotidien, du stage jusqu'à la thèse. Cela a été une chance et un réel plaisir de travailler avec toi. Merci pour ta présence, pour l'attention que tu as toujours portée à mon travail et pour tes qualités humaines remarquables.

Je souhaite aussi remercier toutes les personnes m'ayant aidé dans l'élaboration de cette thèse, que ce soit à Safran ou au LAUM. Merci notamment à William Albouy, ingénieur à Safran Composites, de m'avoir appris à utiliser le cluster « rosetta » pour les simulations Abaqus. Un merci particulier à Nikolay Chigarev, ingénieur de recherche à le Mans Université, et James Blondeau, assistant ingénieur au CNRS, pour l'aide apportée sur les expériences ultrasons-laser. Plus généralement, merci aux stagiaires, doctorants et post-doctorants de l'équipe US-laser que j'ai eu le plaisir de rencontrer : Guqi, Artem, Théo, Haiyang, Elton, Changxiu, Sandeep, Juliette, Elise et Nicolas.

Merci à tous ceux qui ont rendu cette vie de doctorant agréable. Un grand merci à mes co-bureaux : Thomas, Massimo, Jean-Michel et Alann pour les bons moments passés ensemble (même si la fin a été quelque peu chamboulée !) et pour les découvertes musicales. Merci à tous les doctorants du labo et notamment à ceux pour qui nos thèses ont débuté à la même période : Matthieu, Robin, Théo, Thibault, Sobin, Romain, Charlotte et Jean. Merci aussi à Cécile et Eduardo, bon courage à vous pour la suite.

Pour terminer, je tiens à remercier mes amis et ma famille pour leur soutien et les moments de détente passés auprès d'eux. Merci en particulier à mes amis de « La Pièce » et à ceux de Chevrollier ! Merci aussi aux familles Vion, Sarrazin et Favreau pour les moments conviviaux passés ensemble ; merci notamment à Sylvie et Patrice. Merci aussi à tous les membres de la famille Fauchoux et de la famille Hodé. Je ne vais pas avoir assez de place pour tous vous citer, mais je pense fort à vous. Je remercie affectueusement mes grands-parents, Madeleine et Charles, pour tout ce que vous m'apportez. J'ai une pensée émue pour toi mamie Hodé. Un grand merci à ma sœur Léa et à son copain Bastien, ainsi qu'à mes deux petits frères Thomas et Lucas, pour les moments heureux passés en famille. Enfin, un immense merci à mes parents, Annie et André, pour votre écoute et pour la confiance que vous m'avez toujours témoignée. Merci pour votre soutien inconditionnel !

Et puis rien de cela n'aurait été possible sans toi Cyrielle. Merci pour l'amour que tu m'as apporté et pour ces bouffées d'oxygène qui m'ont permis de surmonter toutes les difficultés. Merci d'être à mes côtés ! Merci pour tout.

# Contents

<b>List of Figures</b>	<b>ix</b>
<b>List of Tables</b>	<b>xvii</b>
<b>General Introduction</b>	<b>1</b>
<b>1 State-of-the-art on the nondestructive evaluation of adhesive bonding</b>	<b>5</b>
1.1 Introduction . . . . .	7
1.2 Adhesive bonding: definition, terminology, defects and evaluation methods	7
1.2.1 Definition, terminology and bonding defects . . . . .	7
1.2.2 Overview of destructive and nondestructive evaluation methods of adhesive bonding . . . . .	11
1.3 Ultrasonic nondestructive evaluation methods for bonded structures . . . .	19
1.3.1 Linear ultrasonic nondestructive evaluation methods using bulk waves	20
1.3.2 Linear ultrasonic nondestructive evaluation methods using guided waves . . . . .	23
1.3.3 Non-linear ultrasonic nondestructive evaluation methods . . . . .	29
1.4 Conclusion . . . . .	39
<b>2 Semi-analytic simulations of laser-generated ultrasounds in a multilayer   structure</b>	<b>41</b>
2.1 Introduction . . . . .	43
2.2 Geometry and assumptions . . . . .	44
2.3 Electromagnetic problem . . . . .	46
2.3.1 Formulation of the electromagnetic problem . . . . .	46
2.3.2 Propagation of the electromagnetic waves in the multilayer structure	47
2.3.3 Determination of the power density $Q$ . . . . .	49
2.4 Heat diffusion problem . . . . .	50
2.4.1 Homogeneous solutions of the heat equation . . . . .	52
2.4.2 Particular solutions of the heat equation . . . . .	53

2.4.3	Application of the boundary conditions . . . . .	54
2.5	Elastodynamic problem . . . . .	56
2.5.1	Homogeneous solutions of the elastodynamic equations . . . . .	57
2.5.2	Particular solutions of the elastodynamic equations . . . . .	59
2.5.3	Application of the boundary conditions . . . . .	59
2.6	Numerical simulation results . . . . .	61
2.6.1	Analysis of the guided elastic waves in an aluminum alloy plate . .	62
2.6.2	Bilayer/trilayer with interfacial stiffnesses . . . . .	63
2.6.3	Bilayer with the heat source at the interface . . . . .	65
2.7	Conclusion . . . . .	65
<b>3</b>	<b>Plane wave synthesis and inverse problem for nondestructive evaluation of adhesive bondings</b>	<b>67</b>
3.1	Introduction . . . . .	69
3.2	Plane wave synthesis for the nondestructive evaluation of adhesive bondings	70
3.2.1	Description of the plane wave synthesis . . . . .	71
3.2.2	Application for the nondestructive evaluation of adhesive bondings	73
3.3	Solving the direct problem . . . . .	74
3.3.1	Analytic formulation . . . . .	74
3.3.2	Semi-analytic model . . . . .	75
3.3.3	Results of semi-analytic simulations . . . . .	78
3.4	Resolution of inverse problems with simulated data . . . . .	78
3.5	Resolution of inverse problems with experimental data . . . . .	85
3.5.1	Sample preparation . . . . .	85
3.5.2	Experimental set-up . . . . .	86
3.5.3	Simple case of the free-standing plate . . . . .	87
3.5.4	Quantification and differentiation of two adhesive bonding condi- tions: nominal and degraded . . . . .	91
3.6	Conclusion . . . . .	92
<b>4</b>	<b>Nondestructive evaluation of structural adhesive bonding using the at- tenuation of zero-group-velocity Lamb modes</b>	<b>95</b>
4.1	Introduction . . . . .	97
4.2	Dispersion curves in a bilayer structure . . . . .	98
4.3	Presentation of the samples, the laser-ultrasonic set-up and experimental measurements . . . . .	100

4.3.1	Presentation of the samples . . . . .	100
4.3.2	Description of the laser-ultrasonic set-up . . . . .	101
4.3.3	Experimental measurements . . . . .	101
4.4	Damping of local resonances . . . . .	103
4.5	2D maps of a trilayer assembly with inhomogeneously distributed defects .	107
4.6	Conclusion . . . . .	109
<b>General conclusion</b>		<b>111</b>
<b>Perspectives</b>		<b>117</b>
<b>Résumé de la thèse</b>		<b>123</b>
<b>Appendices</b>		<b>133</b>
<b>A Semi-analytic model: additional calculations</b>		<b>135</b>
A.1	Electromagnetic problem . . . . .	135
A.1.1	Obtaining the Helmholtz equation . . . . .	135
A.1.2	Coefficients $A_{ij}^E$ . . . . .	138
A.1.3	Obtaining the power density $Q$ with Poynting's theorem . . . . .	139
A.1.4	Detailed calculation of the transfer matrix $[L_i^{EM}]_{2 \times 2}$ . . . . .	140
A.2	Heat diffusion problem . . . . .	142
A.2.1	Laser pulse distributions in time and space . . . . .	142
A.2.2	Coefficients $A_{ij}^T$ and $B_i^T$ . . . . .	144
A.3	Elastodynamic problem . . . . .	146
A.3.1	Homogeneous solutions of the elastodynamic equations . . . . .	146
A.3.2	Particular solutions of the elastodynamic equations . . . . .	148
A.3.3	Application of the boundary conditions . . . . .	149
A.3.4	Coupling matrix $[L_i^M]_{4 \times 4}$ . . . . .	161
<b>B Coupling matrix <math>[L_i^M]</math> expressed with the angles</b>		<b>165</b>
<b>C Reflection/transmission coefficients</b>		<b>173</b>
C.1	Incident plane wave: longitudinal polarization . . . . .	174
C.1.1	Displacement/stress vectors in medium I . . . . .	174
C.1.2	Displacement/stress vectors in medium II . . . . .	176
C.1.3	Application of the boundary conditions . . . . .	178

C.2	Incident plane wave: transverse polarization . . . . .	179
C.2.1	Displacement/stress vectors in medium I . . . . .	179
C.2.2	Displacement/stress vectors in medium II . . . . .	181
C.2.3	Application of the boundary conditions . . . . .	183

<b>Bibliography</b>		<b>185</b>
---------------------	--	------------

# List of Figures

1.1	Types of defects encountered in a bonded assembly. <sup>14</sup> . . . . .	10
1.2	Illustration of the three failure modes: (a) cohesive failure, (b) adhesive failure and (c) mixed failure (translated from French to English). <sup>10</sup> . . . . .	11
1.3	Peel tests: presentation of the different geometries. <sup>7</sup> . . . . .	13
1.4	Cleavage tests: (a) the Double Cantilever Beam (DCB) test consisting in imposing a mechanical loading (applied forces symbolized by arrows) and (b) the wedge cleavage test consisting in imposing a displacement to generate the rupture of the bonded assembly (translated from French to English). <sup>29</sup> . . . . .	14
1.5	Standardized tests of type: (a) single lap shear and (b) double lap shear (translated from French to English). <sup>3</sup> . . . . .	14
1.6	Representation of the Arcan mounting for different angular positions to induce tensile, shear and compressive stresses in the adhesive bonding. <sup>35</sup> . . . . .	15
1.7	Generation of a laser shock in: (a) direct irradiation and (b) confined regime. <sup>68</sup> . . . . .	19
1.8	Experimental transmission set-up used by Siryabe <sup>10</sup> on an Al/epoxy/Al bonded assembly. <sup>81</sup> . . . . .	22
1.9	Experimental set-up used by Singher <sup>96</sup> with (contact) generation and (non-contact) detection of Rayleigh waves on aluminum substrates. R (Rayleigh wave), B (bulk wave), G (guided wave), B.S. (beam splitter). . . . .	24
1.10	(a) Schematic diagram of the aluminum/epoxy/composite trilayer studied by Le Crom and Castaings using one-dimensional semi-analytical finite element code (SAFE). (b) Picture of the experimental set-up used to generate and detect SH guided waves and to measure the phase velocities of the different modes. <sup>98</sup> . . . . .	26
1.11	Figure and table taken from the article of Mezil <i>et al.</i> : <sup>112</sup> (a) geometry of the trilayer model used to compute the dispersion curves following the approach proposed by Vlasie and Rousseau, <sup>114</sup> (b) comparison between experimental and theoretical ZGV resonance frequencies. . . . .	29

1.12	Schematic of the experimental set-up used by Yan <i>et al.</i> <sup>119</sup> for the generation of high-amplitude ultrasonic waves. . . . .	31
1.13	Diagram of the experimental set-up used by Shui <i>et al.</i> <sup>121</sup> for the generation of harmonics on bonded specimens subjected to fatigue. . . . .	32
1.14	Figures extracted from Potter <i>et al.</i> : <sup>125</sup> (a) schematic of the experimental set-up consisting of the multi-element transducer in contact with the surface of the aluminum alloy part having a closed through crack, (b) visualization of the crack with the non-linear imaging method presented in the paper. . . . .	33
1.15	Figures from Zabbal <i>et al.</i> : <sup>126</sup> (a) representation of the chaotic cavity transducer used to generate high amplitude plane waves, (b) Fourier transforms of the signals measured on bonded assemblies [aluminum(5 mm)/epoxy (0.1 mm)/aluminum(5 mm)] with and without defect (denoted “Defect” and “Reference”, respectively). . . . .	34
1.16	Schematic from Zhang <i>et al.</i> <sup>127</sup> on the non-collinear wave mixing at an imperfect interface. . . . .	36
1.17	Diagram of the principle of the heat flux modulation taken from the PhD thesis of Mezil. <sup>133</sup> . . . . .	37
1.18	Diagram of the principle used by Goursole <sup>136</sup> to measure the coefficient of non-linearity of bonded samples using phase modulation (translated from French to English). . . . .	38
1.19	Extract from Rokhlin <i>et al.</i> : <sup>137</sup> picture of the experimental set-up (left) and results obtained (right) for different degradations of the bonded samples. . . . .	39
2.1	The geometry of the multilayer structure is represented with the two semi-infinite media (0 and III) and the media I and II of thicknesses $h_1$ and $h_2$ , respectively. The uppercase letter “EM” symbolizes the sublayers, with a total thickness of $\Delta h$ , that can be inserted between media I and II. The black arrows represent the $\mathbf{k}$ -wave vectors and the red (blue) arrows indicate the electric vectors $\mathbf{E}$ (magnetic vectors $\mathbf{H}$ ). . . . .	45
2.2	Illustration of the multilayer structure used to solve the thermal diffusion problem. The uppercase letter “T” denotes the sublayers that can be inserted between media I and II. The black arrows represent the wave vectors of the thermal waves propagating in the $\pm x_1$ -direction. The two dotted arrows indicate the thermal convection at the upper surface of medium I and the lower surface of medium II. . . . .	52

2.3	Representation of the multilayer structure used to solve the elastodynamic problem. The uppercase letter “M” denotes the sublayers that can be inserted between media I and II to mechanically couple these two media. The black (red) arrows represent the wave vectors of the longitudinal (transverse) polarized waves propagating in the $\pm x_1$ -direction. . . . .	56
2.4	Zoom views of $f$ - $k$ diagrams (in dB), for a 1.23 mm-thick aluminum alloy plate at $x_1 = 1.23$ mm, for two different laser sources. (a) Gaussian laser pulse ( $\tau_p = 8$ ns, $a_s = 0.2$ mm). (b) Modulated laser source in time (tone burst of 2.5 MHz central frequency) and space (phase mask of $1.5$ rad $\text{mm}^{-1}$ central wavenumber). A good agreement is obtained with the dispersion curves simulated with the commercial software “CIVA 2020” in dashed (dash-dotted) lines for symmetric (antisymmetric) modes. . . . .	62
2.5	Normal displacements $u_1(x_1, x_2, t)$ simulated at $t = 1$ $\mu\text{s}$ in: (a) a bilayer Al (1.5 mm)/Al (3.1 mm) and (b) a trilayer Al (1.5 mm)/Epoxy (0.1 mm)/Al (3.0 mm). . . . .	63
2.6	Normal displacements $u_1(x_1, x_2, t)$ simulated at $t = 0.35$ $\mu\text{s}$ in a bilayer glass (2 mm)/Ti (2 mm) with interfacial stiffnesses equal to: (a) $K_N = K_T = 10^5$ kN $\text{mm}^{-3}$ and (b) $K_N = K_T = \infty$ kN $\text{mm}^{-3}$ . . . . .	65
3.1	(a) Representation of the elastic plane waves that are synthesized in the medium I. First, a laser line source, of infinite length in the $\mathbf{x}_3$ -direction, is moved over the sample surface in $2N + 1$ positions with a constant $\delta x$ -step. Secondly, a time delay $\delta t$ is applied between the laser pulses, in post-processing, to synthesized longitudinal (L) and transverse (T) plane waves. (b) The application of delays between the $2N + 1$ sources leads to constructive and destructive interferences between the divergent elastic waves, resulting in the generation of a plane wave. (c) Slowness diagram of the longitudinal and transverse plane waves that are synthesized by imposing the wave vector $k_s = \omega \delta t / \delta x$ with $\omega$ the angular frequency. . .	72

3.2	Results of semi-analytic simulations in three different cases. Snapshots at $t = 1.25 \mu\text{s}$ of the normalized normal displacement $u_1$ in a bilayer structure with normal and transverse interfacial stiffnesses [illustrated in Fig. 3.1(a)] equal to (a) $K_N = K_T = 10^{-3} \text{ kN mm}^{-3}$ for the decoupling case, (b) $K_N = 10^3 \text{ kN mm}^{-3}$ and $K_T = 10^1 \text{ kN mm}^{-3}$ for the intermediate coupling, (c) $K_N = K_T = 10^5 \text{ kN mm}^{-3}$ for the high mechanical coupling between media I and II. . . . .	77
3.3	Diagram of the method to solve the inverse problem. The input data is a B-scan where the plane wave synthesis (PWS) is applied. It is then compared to a database of semi-analytic simulations for different values of interfacial stiffnesses. The minimum of the cost function is finally searched to identify the values of $K_N$ and $K_T$ which gives the lowest mean squared error (MSE) between the input and the database. . . . .	79
3.4	Cost functions (in dB) obtained when the plane wave synthesis is applied on simulated B-scans, with the addition of noise, for interfacial stiffnesses equal to: (a) $K_N = K_T = 10^{-3} \text{ kN mm}^{-3}$ , (b) $K_N = 10^3 \text{ kN mm}^{-3}$ and $K_T = 10^1 \text{ kN mm}^{-3}$ , (c) $K_N = K_T = 10^5 \text{ kN mm}^{-3}$ . The red rectangles indicate the location of the minimum of each cost function with an uncertainty margin of $\pm 0.1 \text{ dB}$ . . . . .	81
3.5	Results of the plane wave synthesis applied on simulated data, with the addition of Gaussian noise, for different values of $K_N$ and $K_T$ (8 different cases). The times of flight of the reflected synthesized plane waves are identified as: dash-dotted line for the 2L longitudinal plane wave, dashed line for the 2T transverse plane wave and dotted line for the sum of the LT and TL plane waves. . . . .	83
3.6	Water droplet on an aluminum surface (a) without and (b) with one layer of Frekote. . . . .	86
3.7	Laser ultrasonic set-up for the acquisition of experimental B-scan. . . . .	87
3.8	Comparisons between simulation and experiment for the 1.23 mm-thick aluminum alloy plate. (a) Simulated B-scan obtained with the semi-analytic model described in Chap. 2. The normalized normal displacements at the top surface of the aluminum alloy plate are simulated as a function of time and position $x_2$ . (b) Experimental B-scan measured with the set-up presented in Fig. 3.7. The longitudinal wave (L) and the Rayleigh wave (R) are identified with solid lines. . . . .	88

3.9	Comparisons between simulation and experiment for the 1.23 mm-thick aluminum alloy plate. (a-b) Results of the plane wave synthesis applied on the simulated [Fig. 3.8(a)] and experimental [Fig. 3.8(b)] B-scans, respectively. The times of flight of the reflected synthesized plane waves are identified as: dash-dotted line for the 2L longitudinal plane wave, dashed line for the 2T transverse plane wave and dotted line for the sum of the LT and TL plane waves [previously illustrated in Fig. 3.1(a)]. . . . .	89
3.10	Cost functions obtained when experimental B-scans of (a) an aluminum alloy plate, bonded assemblies Al/Ep/Al (b) with and (c) without release agent, are used as input data for the algorithm shown in Fig. 3.3. The red rectangles indicate the minimum of each cost function with an uncertainty margin of $\pm 0.1$ dB. . . . .	91
4.1	(a) Schematic diagram of the generation and detection laser paths and of the bilayer model used to simulate the dispersion curves. d.m.: dichroic mirror. $K_N$ , $K_T$ : the normal and transverse interfacial stiffnesses per unit area. (b) The dispersion curves of the top aluminum alloy plate alone ( $Al_1$ ) are represented as dashed and dashed dotted lines for symmetrical and anti-symmetrical Lamb modes, respectively. The dispersion curves obtained for mechanical coupling between $Al_1$ and $Al_2$ , with $K_N = K_T = 10 \text{ kN mm}^{-3}$ , are represented as solid lines. ZGV resonances are indicated by white and red triangles. . . . .	99
4.2	Conventional immersion ultrasonic measurements (C-scan) in reflection at 15 MHz for the bonded samples R.A. <sub>1</sub> , C. <sub>50%</sub> , R.A. <sub>2</sub> and Nom. (from left to right). . . . .	101
4.3	Experimental frequency spectra in the range 0–8 MHz and around 2 MHz (inset) measured in reflection with the set-up presented in Fig. 4.1(a). . . .	102
4.4	Experimental frequency spectra with a set-up in transmission, i.e., where the generation laser spot is focused on the top aluminum alloy plate $Al_1$ and the detection laser spot is focused on the bottom aluminum alloy plate $Al_2$ . . . . .	103

4.5	(a) Experimental attenuation as a function of time to a logarithmic scale. For each sample, the average attenuation for the 11 measurement points is plotted and the standard deviation is represented with shaded error bars. The fitting lines with Eq. (4.2) are represented with dotted lines. (b) Temporal signals acquired from the aluminum alloy plate and from the nominal bonded sample after filtering the data with a bandpass filter around the ZGV frequency at $\sim 2$ MHz. . . . .	105
4.6	2D maps of the metrics of the trilayer sample split into four zones: (a) $\omega_m$ , (b) $\tau_1$ , and (c) $\delta\omega$ . When the RMSE of a fit is higher than $0.4 \times 10^{-3}$ (maximum value of the previous results for the bonded samples; Table 4.1), the point is rejected and replaced by a white square. (d) Frequency spectra and (e) attenuation of the signals for the red and black boxes in the maps.	108
P.1	(a) Picture of the Outlet Guide Vane (OGV) sample. (b) CAD of the sectional view of the OGV sample composed of an aluminum alloy hood bonded to an aluminum alloy body. (c) Visualization of the first resonance mode of the aluminum alloy hood with excitation by a piezoelectric cell and measurement by scanning laser vibrometry. (d) Picture of the OGV sample with compressed air supply. . . . .	118
P.2	(a) Schematic diagram of the proposed method to focus ultrasounds with a ring-shaped laser source in an isotropic medium. (b) Directivity pattern of a laser source in the thermoelastic regime. Figure extracted from the PhD Thesis of S. Raetz <sup>151</sup> . Longitudinal (transverse) waves are represented by solid (dashed) lines. Longitudinal (transverse) waves are represented by solid (dashed) lines. (c)–(d) Images obtained with the SLM. (e) Ring-shaped laser source obtained with the SLM. . . . .	120
P.3	Experimental set-up with the Spatial Light Modulator (SLM). . . . .	121
R.1	Déplacement normal $u_1(x_1, x_2, t)$ simulé à $t = 1 \mu\text{s}$ pour : (a) un bicouche Al (1,5 mm)/Al (3,1 mm) et (b) un tricouche Al (1,5 mm)/Epoxy (0,1 mm)/Al (3,0 mm). . . . .	125

- R.2 (a) Représentation des ondes planes synthétisées dans le milieu I. Tout d’abord, une ligne source laser de longueur infinie dans la direction  $\mathbf{x}_3$  est déplacée à la surface de l’échantillon en  $2N + 1$  positions avec un pas constant  $\delta x$  selon la direction  $\mathbf{x}_2$ . Puis, des retards à l’émission  $\delta t$  sont appliqués entre les différentes impulsions laser, dans une étape de post-traitement, afin de synthétiser des ondes planes longitudinales (L) et transversales (T). (b) L’application de retards à l’émission entre les  $2N + 1$  sources conduit à des interférences constructives et destructives entre les ondes divergentes entraînant la génération d’une onde plane. (c) Diagramme des lenteurs des ondes planes longitudinales et transversales qui sont synthétisées en imposant le vecteur d’onde  $k_s = \omega \delta t / \delta x$  avec  $\omega$  la fréquence angulaire. . . . . 126
- R.3 Fonctions coût obtenues lorsque les B-scans expérimentaux mesurés sur (a) une plaque d’alliage d’aluminium et deux assemblages collés Al/Ep/Al [(b) avec et (c) sans agent de démoulage] sont utilisés comme données d’entrée de l’algorithme permettant de résoudre le problème inverse. Les rectangles rouges indiquent les minima de chaque fonction coût avec une marge d’incertitude de  $\pm 0,1$  dB. . . . . 127
- R.4 (a) Atténuations expérimentales en fonction du temps selon une échelle logarithmique. Pour chaque échantillon, l’atténuation moyenne pour les 11 points de mesure est tracée et l’écart type est représenté par des barres d’erreur en transparence. Les courbes obtenues suite à l’identification des paramètres d’atténuation sont représentées par des lignes pointillées. (b) Signaux temporels mesurés, pour la plaque en alliage d’aluminium (Al) et pour l’assemblage collé nominal (Nom), après filtrage des données avec un filtre passe-bande centré à  $\sim 2$  MHz autour de la fréquence de résonance ZGV. 128
- R.5 Cartographies 2D des paramètres identifiés [(a)  $\omega_m$ , (b)  $\tau_1$ , et (c)  $\delta\omega$ ] sur l’assemblage collé Al/Ep/Al divisé en quatre zones : deux zones nominales (Nom), une zone avec une couche d’agent de démoulage à l’interface supérieure (R.A.<sub>1</sub>) et une zone avec une couche d’agent de démoulage à l’interface inférieure (R.A.<sub>2</sub>). Lorsque le RMSE du fit est supérieur à  $0,4 \times 10^{-3}$  (valeur maximale obtenue pour les assemblages collés testés), le point est rejeté et remplacé par un carré blanc. (d) Spectres de fréquence et (e) atténuation des signaux temporels aux positions indiquées par les cases rouges et noires représentées sur les cartographies (a)–(c). . . . . 129

R.6	(a) Schéma de la méthode proposée pour focaliser les ultrasons générés par laser au niveau du collage en utilisant, par exemple dans le cas d'un matériau isotrope, une source laser en forme d'anneau. (b) Diagramme de directivité d'une source laser en régime thermoélastique. Figure extraite de la thèse de S. Raetz. <sup>151</sup> Les ondes longitudinales (transversales) sont représentées par des lignes continues (pointillées). (c)–(d) Images obtenues avec le Spatial Light Modulator (SLM). (e) Source laser en forme d'anneau obtenue avec le SLM. . . . .	131
A.1	Geometry of the $i$ -th sublayer of thickness $h_i$ . The black arrows represent the $\mathbf{k}_i$ -wave vectors and the red (blue) arrows indicate the electric vectors $\mathbf{E}_i$ (magnetic vectors $\mathbf{H}_i$ ). . . . .	141
A.2	Representation of the Cartesian coordinate system $(O', \mathbf{x}'_1, \mathbf{x}'_2)$ translated and rotated through an angle $\theta$ to the Cartesian coordinate system $(O, \mathbf{x}_1, \mathbf{x}_2)$ . . . . .	143
A.3	Representation of the $i$ -th sublayer of thickness $h_i$ . The wave vectors of the longitudinal (transverse) elastic waves are represented with black (red) arrows. . . . .	162
B.1	Illustration of the $i$ -th sublayer of thickness $h_i$ . The wave vectors of the longitudinal (transverse) elastic waves are represented with black (red) arrows. . . . .	167
C.1	Schematic diagram of a longitudinal plane wave incident on one or more sublayers of total thickness $\Delta h$ which are located between two semi-infinite media I and II. The wave vectors of the longitudinal (transverse) plane waves are represented with black (red) arrows. . . . .	174
C.2	Schematic diagram of a transverse plane wave incident on one or more sublayers of total thickness $\Delta h$ which are located between two semi-infinite media I and II. The wave vectors of the longitudinal (transverse) plane waves are represented with black (red) arrows. . . . .	180

# List of Tables

2.1	Optical, thermal and mechanical properties of the aluminum alloy (Al), SCHOTT N-BK7 <sup>®</sup> glass and titanium (Ti). . . . .	61
3.1	Results obtained by solving the inverse problem with noisy simulations as input data. Three different cases are processed for input values of $K_N$ and $K_T$ given in $\text{kN mm}^{-3}$ : low, intermediate and high mechanical coupling between media I and II. The interfacial stiffnesses identified using the minima of the cost functions are reported below. . . . .	82
3.2	The interfacial stiffnesses identified by solving the inverse problem with experimental B-scans as input data in the three different experimental cases: aluminum alloy plate, adhesive bonding Al/Ep./Al with release agent (R.A.) and without (called nominal bonding). . . . .	92
4.1	Properties of the samples and fitted values for the attenuation. The bars indicate averages for 11 measurement points. $\sigma$ is the standard deviation. .	106



# General Introduction

Currently, the weight lightening of aeronautical structures is a major industrial issue, especially in terms of environmental impact. In order to reduce greenhouse gas emissions, aeronautical structures must be lightened to lower engine fuel consumption. The use of bonding as an assembly technique makes it possible to meet this need for weight savings. Indeed, compared to more conventional methods such as welding or riveting, adhesive bonding has many advantages. First of all, it does not require the addition of rivets, which adds weight to the structure. Second, no drilling, synonymous of stress concentration, must be performed in the parts to be assembled. Adhesive bonding then ensures a better distribution of stresses between the assembled structures; this guarantees a more homogeneous transmission of mechanical loads. Furthermore, it is one of the most efficient techniques for assembling composite material structures that address the objective of a high strength-to-weight ratio.

Although bonding has many advantages over more conventional techniques (riveting, welding, etc.), to date there is a lack of nondestructive methods for quantifying and certifying the mechanical strength of adhesively bonded assemblies. This lack therefore presents real safety and certification issues with air agencies such as the *Federal Aviation Administration* (FAA) or the *European Aviation Safety Agency* (EASA). Hence, a significant interest must be focused on the development of nondestructive evaluation (NDE) methods of bonded aeronautical assemblies. This would make it possible to remove one of the last technological locks currently limiting the development of this assembly technique in the aeronautical industry.

Over the last fifty years, a significant number of nondestructive methods have been investigated and reported in the literature concerning the NDE of adhesive bonding. Among the wide range of developed techniques in this field, such as those based on infrared thermography or laser-generated shock waves, ultrasonic methods are of particular interest as elastic waves interact mechanically with the bonding without damaging it. These methods can be classified into two principal categories depending on whether they are based on bulk acoustic waves or guided waves. First, ultrasonic methods using bulk acoustic waves are of real interest because these elastic waves are propagating in the volume of the inspected structure. In conventional pulse-echo technique, the reflection of

bulk waves from a defect, such as void, allows its detection and localization because of the high impedance mismatch between the solid medium and the defect (air in the case of a void). However, there is not a clear impedance discontinuity between bonding defects and the propagation medium, which complicates the direct application of this conventional technique to bonded assemblies. Thus, more advanced methods are investigated to detect the signature of bonding defects in reflected or transmitted ultrasonic signals. Secondly, other ultrasonic methods based on guided waves are studied for the NDE of adhesive bonding. Shear horizontal modes or Lamb modes can be used to obtain an averaged evaluation of the bonding quality along the propagation path of the guided waves. For a better defect localization, zero-group-velocity (ZGV) Lamb modes, which are sharp local resonances at well-defined frequencies, are of real interest for the NDE of adhesive bonding. In addition, these modes can be generated and detected by laser, allowing non-contact measurements particularly well suited for industrial applications.

In this PhD thesis, laser ultrasonic methods are investigated for the NDE of bonded aeronautical assemblies. The aim of this work is to develop nondestructive methods to identify quantitative parameters that are related to the mechanical strength of bonded structures. For this purpose, the propagation of laser-generated and detected elastic waves in bonded assemblies are studied. To generate ultrasounds, a pulsed laser source is used in the thermoelastic regime in order not to locally degrade the surface of the inspected sample (contrary to the ablation regime). The detection of ultrasounds is then performed with an interferometric method to measure the normal displacement of a free surface. The main advantages of such laser generation and detection of ultrasounds are: (i) the broadband content of elastic waves that are generated and detected (frequencies between  $\sim 1$  MHz and 40 MHz), (ii) the possibility to design the shape of the laser source (point source, line source, ring source, etc.) to favor the generation of desired elastic waves in the medium and (iii) the contactless nature of the measurement which is a main advantage compared to conventional ultrasonic techniques, such as contact measurements with piezoelectric transducers. One of the drawbacks concerning thermoelastic laser sources is the relatively low value of signal-to-noise ratio (SNR). However, this can be easily improved by averaging the detected signals over several acquisitions due to the high reproducibility of laser-ultrasound measurements. Therefore, laser ultrasonic methods are great tools for the NDE of materials, and especially the NDE of bonded assemblies in an industrial context.

The outline of this PhD dissertation is given as follows. In Chap. 1, a literature review concerning the NDE of adhesive bonding is presented. First, bonding defects that degrade the quality of bonded assemblies are reported and a preliminary overview of destructive

and nondestructive evaluation methods, such as infrared thermography or laser-generated shock waves, is given. Secondly, linear ultrasonic methods, using bulk or guided waves, and non-linear approaches are presented and discussed.

In Chap. 2, a semi-analytic 2D model to simulate the propagation of laser-generated elastic waves in a multilayer structure, that can model a bonded assembly, is described. The electromagnetic, thermal and elastodynamic problems are successively solved to model the optoacoustic source in the thermoelastic regime and to simulate the propagation of elastic waves in the structure. The optical penetration of the incident tilted laser line source, as well as thermal conduction and convection phenomena, are considered. This semi-analytic model allows to obtain fast and accurate results to solve the direct problem, i.e., to obtain the displacement field in the structure where the electromagnetic, thermal and mechanical parameters are known. Then, this model is at the basis of the developed method presented in the next chapter where inverse problems are solved using the propagation of bulk acoustic waves in bonded assemblies.

In Chap. 3, a laser ultrasonic method is proposed and is based on the reflection of elastic plane waves from the bonding interface. Although laser-generated plane waves are experimentally feasible, these techniques are difficult to achieve in practice. Hence, a post-processing method which allows to synthesize the amplitudes of the reflected plane waves for several angles of incidence with respect to the bonding interface is used. Then, inverse problems are solved, using the semi-analytic model presented in Chap. 2, to identify the normal and transverse interfacial stiffnesses ( $K_N$ ,  $K_T$ ) that model the mechanical coupling between two bonded media. The developed method is first validated with semi-analytic simulated input data where Gaussian noise has been added. Next, the method is applied using signals acquired on an aluminum alloy plate (Al) and on two bonded assemblies Al/Epoxy/Al (with and without adhesion defects), made with an aeronautical structural epoxy adhesive film. The identified values of  $K_N$  and  $K_T$  enable to distinguish the three samples and to obtain quantitative values of these two key parameters characterizing the adhesive bonding.

In Chap. 4, another approach is proposed for the NDE of structural adhesive bonding. The developed method uses the attenuation of ZGV Lamb modes. Experimental investigations are carried out with five trilayer assemblies composed of two asymmetric aluminum alloy plates bonded with an epoxy adhesive. ZGV resonances are generated and detected in these bonded samples where cohesive and adhesive defects were introduced to degrade the practical adhesion. The attenuation of the temporal signal of ZGV resonances are found to provide sufficient information to discriminate between strong

and weak bonding. Two metrics characterizing the attenuation are identified and allow to evaluate quantitatively the differences between the manufactured samples. Finally, a 2D scan of a trilayer assembly with different bonding defects demonstrates the imaging capability of this all-optical NDE method.

Last but not least, a conclusive part is ending this PhD thesis with a general summary of the main obtained results promoting the ability of laser ultrasonic techniques to help evaluating/characterizing bonded assemblies in industrial contexts. The perspectives of the results presented in the PhD dissertation are eventually discussed together with the already achieved steps towards the successful realization of those ideas mixing laser ultrasonics, non-linear acoustics and optical shaping techniques.

# Chapter 1

## State-of-the-art on the nondestructive evaluation of adhesive bonding

### Contents

---

1.1	Introduction . . . . .	7
1.2	Adhesive bonding: definition, terminology, defects and evaluation methods	7
1.2.1	Definition, terminology and bonding defects . . . . .	7
1.2.2	Overview of destructive and nondestructive evaluation methods of adhesive bonding . . . . .	11
1.3	Ultrasonic nondestructive evaluation methods for bonded structures . . . .	19
1.3.1	Linear ultrasonic nondestructive evaluation methods using bulk waves	20
1.3.2	Linear ultrasonic nondestructive evaluation methods using guided waves . . . . .	23
1.3.3	Non-linear ultrasonic nondestructive evaluation methods . . . . .	29
1.4	Conclusion . . . . .	39

---

## **Abstract**

A literature review is presented concerning the nondestructive evaluation (NDE) of adhesive bonding. In the first section, definitions and terminologies related to adhesive bonding are reported. The terms: *structural bonding*, *adhesion*, *adherence*, (etc.) are notably introduced. Then, the bonding defects that degrade the quality of bonded assemblies are listed and classified. Next, destructive tests allowing to quantify the mechanical strength of bonded structures are provided and a preliminary overview of NDE methods, such as infrared thermography or laser shock techniques, is given. In the second section, NDE approaches based on ultrasonic methods are presented and discussed. Linear ultrasonic methods, using bulk and guided waves, and non-linear methods are described.

## 1.1 Introduction

In this chapter, a state-of-the-art is provided concerning the scientific work carried out on the nondestructive evaluation of bonded assemblies. This literature review is divided into two main sections. In the first one, definitions and terminologies related to adhesive bonding are given. Then, the defects likely to degrade the quality of bonded assemblies are presented. Next, destructive tests allowing to quantify the mechanical strength of bonded structures are introduced. Sec. 1.2 ends with an overview of nondestructive testing and evaluation (NDT&E) methods of bonded assemblies such as infrared thermography, laser shock techniques, etc. In the second section, NDE approaches based on ultrasonic methods are studied. First, linear methods using bulk waves and then guided waves are given. Finally, non-linear ultrasonic methods are exposed: harmonic generation, non-collinear waves mixing, phase modulation, etc.

## 1.2 Adhesive bonding: definition, terminology, defects and evaluation methods

Numerous methods can be used to join mechanical structures, such as riveting or welding. The assembly method studied in this bibliographical review is adhesive bonding. In part 1.2.1, the terminology used in this field is detailed to define the terms of adhesion, cohesion, etc. Then, defects encountered in bonded assemblies are introduced. In part 1.2.2, an overview of the destructive/nondestructive methods for evaluating adhesive bonding is reported.

### 1.2.1 Definition, terminology and bonding defects

#### Definition and terminology

Adhesive bonding is a technique for firmly joining materials (substrates) together using an adhesive. As defined by Cognard,<sup>1</sup> the term *structural bonding* is used when the mechanical strength of the bond is of the order of magnitude of the substrates being assembled. This kind of bonded assembly must be durable over time and must be able to withstand high mechanical loads. Chataigner<sup>2</sup> specified that a bond may be qualified as “structural” when it is used in parts of the structure that are critical to its mechanical functioning. In aeronautics, *structural bonding* is especially used for the assembly of parts

constituting the primary (“vital”) structure of the aircraft. *Structural bonding* therefore requires high performance adhesives in terms of mechanical strength, heat resistance, etc. For instance, epoxy resin-based adhesives are generally used in the aeronautical industry to manufacture such bonding.<sup>3</sup>

As previously mentioned, a bonded assembly is composed of substrates (metal, composites, etc.) and an adhesive (epoxy, polyurethane, cyanoacrylate, etc.). The aim of this part is not to present the various theories of adhesion to explain the physico-chemical phenomena involved in bonding (mechanical anchoring, diffusion theory, thermodynamic theory, etc.),<sup>4,5</sup> but rather to recall the terminology that is used subsequently to present the defects encountered in a bonded assembly, as well as the methods for testing and evaluating it.

First, it is necessary to define the terms *cohesion* and *adhesion*. Dufour<sup>3</sup> indicated that these are two properties which have a direct impact on the reliability and mechanical strength of a bonded assembly. *Cohesion* is the term used to designate the forces of attraction (ionic, covalent, metallic, hydrogen, Van der Waals)<sup>6</sup> which unite the constituent elements of a medium together, to enable it to resist external mechanical stresses. According to the definition given by Cognard,<sup>7</sup> *adhesion* is the set of interactions that occur during contact between two surfaces. In the case of a bonded assembly, the term *cohesion* is generally used to refer to the adhesive. The term *adhesion* is used to designate the physico-chemical interactions that occur between the substrate and the adhesive.

Secondly, it is also important to define the terms *interface* and *interphase*. As Coulaud<sup>8</sup> pointed out, a distinction must be made between these two terms. The *interface* is defined as the common surface of two materials in intimate contact; its thickness is equal to zero. This surface delimits the boundary that exists between these two media with different mechanical and/or physico-chemical properties. However, in the case of a bonded assembly, there is no abrupt rupture of properties between one of the substrates and the adhesive. In reality, the adhesion between two substrates does not occur along a surface (*interface*) but in a certain volume called *interphase*. This volume is a transition zone of non-zero thickness. The *interphase* can have a gradient of properties (physical, chemical and mechanical) and does not admit well-defined boundaries. In other words, the *interface* is equivalent to simplifying the *interphase* by considering that the transition zone between the two bonded media is of zero thickness.

Finally, a clear distinction must be made between the notions of *adhesion* and *adherence* (also called *practical adhesion*).<sup>9</sup> *Adhesion*, as already mentioned, refers to the set of

fundamental interactions that occur during contact between the substrate and the adhesive.<sup>7</sup> Thus, the term *adhesion* refers to the physico-chemical mechanisms that lead to the creation of an interphase.<sup>10</sup> On the other hand, the term *adherence* (or *practical adhesion*) characterizes the force or energy required to successfully separate two bonded substrates. Therefore, *adherence* relates to the mechanical strength of the bonded assembly. Hence, these two terms do not have the same meaning and it is the *adhesion* that leads to the *adherence*.

The definition of structural bonding and the terminology used in this field (cohesion, adhesion, adherence, interface, interphase) have been defined. The defects encountered in bonded assemblies and the types of failure caused by them are reported in the following.

### Presentation of bonding defects

A large number of articles deal with the presentation and classification of bonding defects.<sup>11–15</sup> These classifications may vary from one paper to another. A diagram illustrating the different types of defects, that can degrade the quality of a bonded assembly, is given in Fig. 1.1. The classification of the different bonding defects that is used in this part is the one given by Jiao and Rose.<sup>16</sup> According to these two authors, these defects can be divided into three main categories: debonding, cohesive weakness and interface weakness.

Firstly, *debonding* refers to voids and complete separations between one of the substrates and the adhesive. Secondly, *cohesive weakness* indicates voids, porosities, or cracks that can be found within the adhesive layer. Thirdly, the last kind of defect is the *interface weakness* between the substrate and the adhesive, which can be divided into two categories: *weak adhesive bond* and *kissing bond*. Concerning the *weak adhesive bond*, this defect causes a mechanical strength of the bonded structure that is below the one expected by the specifications. This defect of adhesion is to be distinguished from the *kissing bond*. Indeed, the definition of this other defect is presented in many scientific articles<sup>16–20</sup> and its definition can vary from one author to another. Nagy<sup>18</sup> and Wood *et al.*<sup>20</sup> define the *kissing bond* as two surfaces in close contact but not (or very weakly) bonded to each other. Mechanical strength is therefore practically non-existent for bonded assemblies with this kind of defect. Jiao and Rose<sup>16</sup> define the *kissing bond* as a perfect contact in the normal direction with respect to the interface between two solid media (continuity of the normal stress and displacement). However, no shear stress can be transmitted from one solid to another at the interface. According to the authors, the *kissing bond* can be

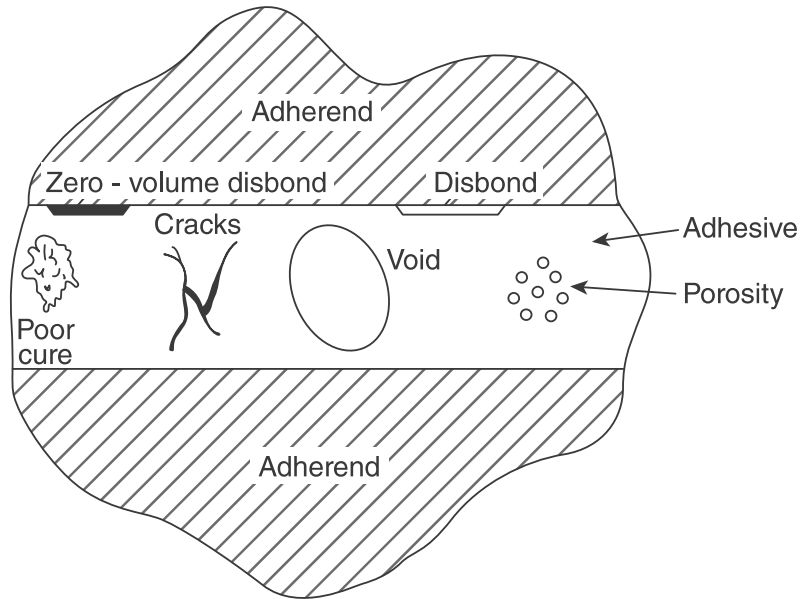


Figure 1.1 – Types of defects encountered in a bonded assembly. Fig. taken from Ref. 14.

represented by an ideal mathematical model but does not exist in real structures. Brotherhood *et al.*<sup>21</sup> define this defect as two surfaces linked to each other, regardless of the nature of the link (slip bonds, partial bonds, etc.). Thus, this term potentially encompasses all adhesion defects, including the *weak adhesive bond*. Marty *et al.*<sup>22</sup> indicate that the *kissing bond* may have various origins (surface contamination, moisture infiltration, etc.). In addition, the authors propose three criteria to qualify this defect. For instance, one of the criteria is that the mechanical shear strength of the bonded assembly must be less than 20% of its nominal value.

The three types of bonding defects, previously introduced,<sup>16</sup> result in several bonded assembly failure modes: *cohesive*, *adhesive* and *mixed failures* (as represented in Fig. 1.2). *Cohesive failure* occurs in the adhesive layer, as shown in Fig. 1.2(a), and can be induced by cohesive defects such as those presented above (voids, porosities, cracks, etc.). In this case, the practical adhesion between the substrate and the adhesive is higher than the cohesive strength of the adhesive, which means that the bonding has been performed correctly. The *adhesive failure* takes place at the interface between the adhesive and the substrate [Fig. 1.2(b)]. It means that the bonding has been poorly manufactured because the adhesion between one of the substrates and the adhesive is weaker than the cohesion of the adhesive. This failure can be caused either by debonding defects or by adhesion

defects. Finally, *mixed failure* is a combination of these two types of cohesive and adhesive failures [Fig. 1.2(c)]. In fact, a rupture can be initiated in the adhesive and then propagate to the adhesive/substrate interface (and vice versa).

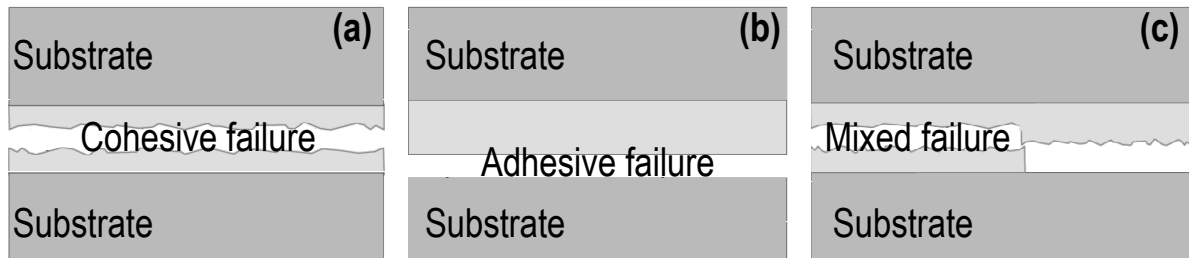


Figure 1.2 – Illustration of the three failure modes: (a) cohesive failure, (b) adhesive failure and (c) mixed failure. Fig. taken from Ref. 10 (translated from French to English).

The bonding defects and the failure modes have been introduced. To control/evaluate bonded structures, an overview of destructive and nondestructive methods is presented hereafter.

### 1.2.2 Overview of destructive and nondestructive evaluation methods of adhesive bonding

Defects encountered in bonded assembly can have dramatic consequences on the integrity of the structure. Indeed, different types of failure modes (adhesive, cohesive, mixed) are induced by bonding defects, as introduced previously. Hence, it is essential to be able to control, after the manufacturing process or during maintenance stages, the integrity of bonded assemblies. First of all, some destructive methods that allow to quantify the mechanical strength of bonded assemblies are presented. Then, a preliminary overview of nondestructive methods is given.

#### Destructive mechanical tests

In order to quantify the practical adhesion, i.e., the mechanical strength of the bonded assembly, numerous standardized destructive tests (ISO, <sup>a</sup> ASTM, <sup>b</sup> AFNOR, <sup>c</sup> etc.) have

---

a. International Organization for Standardization: [URL link](#) [Accessed on 09/18/2020].

b. American Society for Testing and Materials: [URL link](#) [Accessed on 09/18/2020].

c. French Standardization Association: [URL link](#) [Accessed on 09/18/2020].

been developed. The objective of this part is to present a general overview of these various destructive mechanical tests. Interesting introductions and studies concerning destructive tests are presented in the PhD theses of De Barros,<sup>23</sup> Joannes,<sup>24</sup> Mario,<sup>25</sup> Gay,<sup>26</sup> Chauffaille<sup>5</sup> and Dufour.<sup>3</sup> In addition, in-depth studies of the different mechanical tests applied to structural adhesive bonding are given by Gleich<sup>27</sup> and also by Mays and Hutchinson.<sup>28</sup> According to Petit *et al.*,<sup>29</sup> a real practical adhesion test is the one that causes a rupture of the substrate/adhesive interface and allows to quantify the force or energy of separation. The most commonly used destructive mechanical tests for the characterization of bonded assemblies are (non-exhaustive list):

- the peel tests;
- the cleavage tests;
- the standard shear, flexural, torsional and tensile tests;
- the tests with Arcan mountings<sup>30</sup> (single or mixed tensile solicitations, shear stress, compression-shear stress);
- the dynamic tests with Hopkinson bars.

First, the peel tests, described by Cognard,<sup>7</sup> Fortier *et al.*<sup>31</sup> and also Moore,<sup>32</sup> aim to obtain the peeling force necessary to separate two substrates by considering different imposed conditions of angle and speed, as shown in Fig. 1.3. Several types of peel tests can be used depending on the stiffness of the bonded substrates: 90° peel in “L” (soft substrate on rigid substrate), 90° peel in “T” (soft substrate on soft substrate), etc. The measured peeling force can then be related to the fracture energy (unit:  $\text{J m}^{-2}$  equivalent to  $\text{N m}^{-1}$ ). The fracture energy is “*the force that must be applied per unit width of adhesive to cause fracture*” (translation of the original quote<sup>d</sup> from Cognard<sup>7</sup>). For example, in the case of a peel test involving the bonding of a thin substrate to a rigid substrate, Kendall’s formula<sup>33</sup> relates the peeling force to the fracture energy.

The cleavage tests are used to quantify the mechanical strength of a bonded assembly when failure is localized at the substrate/adhesive interface. These tests, as precised by Petit *et al.*,<sup>29</sup> are studied according to an approach based on fracture mechanics. They can be classified in two categories: those with an imposed force [example: Double Cantilever Beam (DCB)] and those with an imposed displacement (example: wedge cleavage). Illustrations of these two examples of cleavage tests are provided in Fig. 1.4.

Many standardized shear, flexural, torsional and tensile tests of adhesive bonding can be performed and some of them are presented below. To measure the shear mechanical strength of a bonded assembly, single and double lap shear tests can be performed as

---

d. Ref 7, p. 62: « *la force qu’il faut appliquer par unité de largeur d’adhésif pour provoquer la rupture* ».

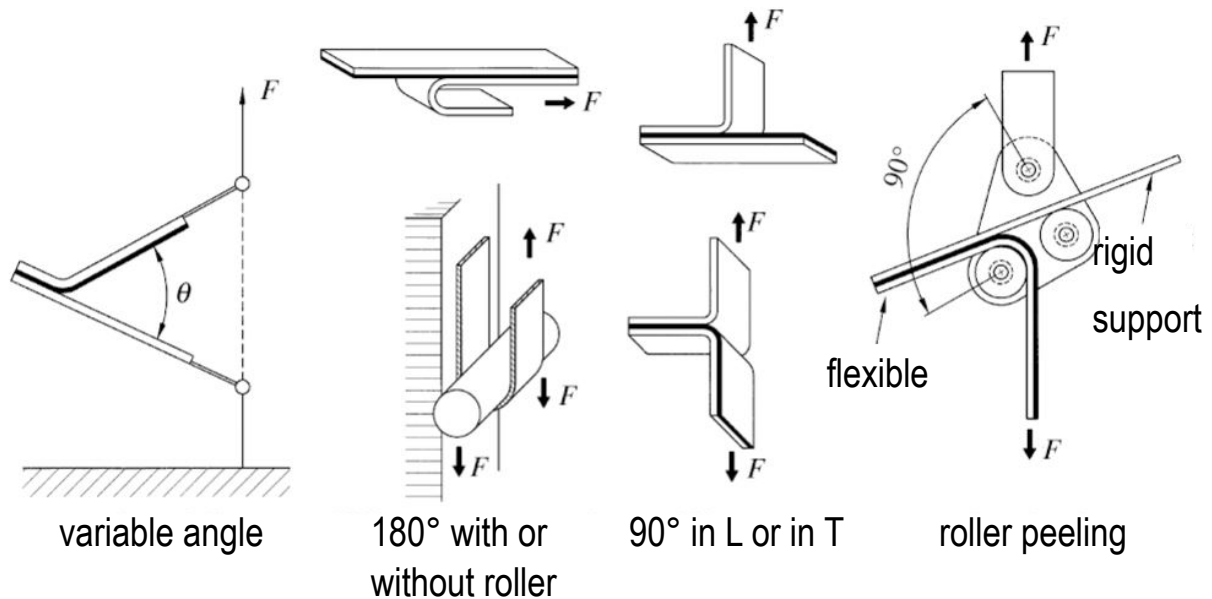


Figure 1.3 – Peel tests: presentation of the different geometries. Fig. taken from Ref. 7 (translated from French to English).

shown in Fig. 1.5(a) and Fig. 1.5(b), respectively. Indeed, the bonded substrates are mechanically loaded with a tensile machine to generate shear stresses along one or two overlapping areas. A double lap shear test, rather than a single one, is preferable to prevent substrates from bending during loading. Indeed, such a bending of the substrates creates tensile stresses at the ends of the overlap area, in addition to shear stresses, which complicate the mechanical loading of the bond. In addition, for destructive tests designed to apply tensile stress to adhesive bonding, there is the butt joint test consisting of mechanically loading two bonded substrates using a tensile machine.<sup>28</sup> In the literature, there is also the scarf joint test which combines tensile and shear stresses by imposing a certain angle between the bond interface and the direction of the mechanical loading.<sup>3,34</sup>

Tensile, shear and compression loads can be applied to the bond with a destructive test carried out on the Arcan mounting. This device was initially developed by Arcan<sup>30</sup> in 1978. It was then modified and improved, notably by Cognard.<sup>36</sup> The Arcan mounting was used by Alfonso,<sup>35</sup> especially to study metal/metal or metal/composite bonded assemblies. As represented in Fig. 1.6, the modification of the loading angle allows to generate different kind of stresses in the bonding. Moreover, according to Alfonso,<sup>35</sup> the mechanical tests carried out on this mounting make it possible to limit the edge effects compared to more traditional methods, such as those presented previously. To conclude this non-exhaustive list, dynamic tests on bonded assemblies have been conducted using Hopkinson bars.

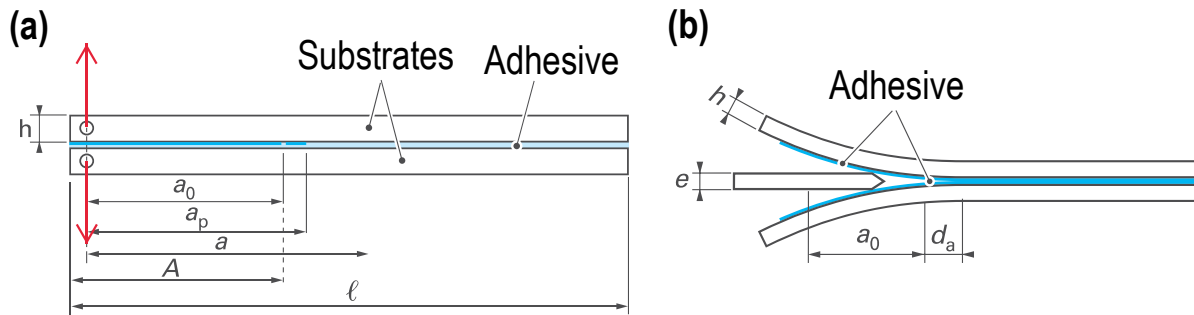


Figure 1.4 – Cleavage tests: (a) the Double Cantilever Beam (DCB) test consisting in imposing a mechanical loading (applied forces symbolized by arrows) and (b) the wedge cleavage test consisting in imposing a displacement to generate the rupture of the bonded assembly. Fig. taken from Ref. 29 (translated from French to English).

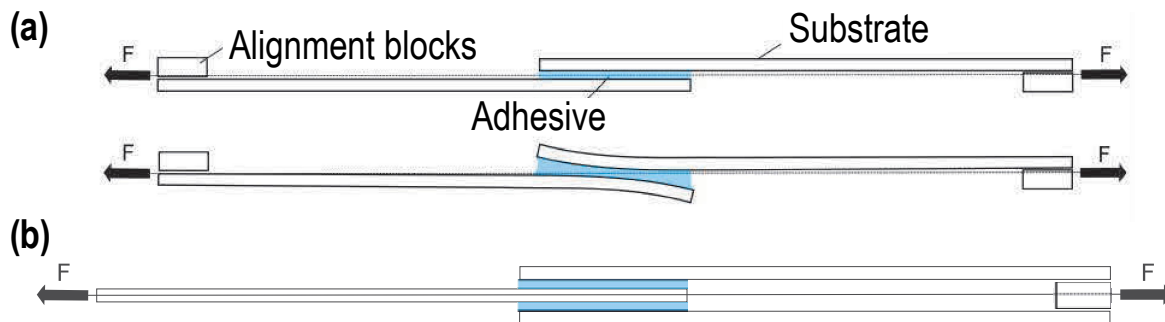


Figure 1.5 – Standardized tests of type: (a) single lap shear and (b) double lap shear. Fig. taken from Ref. 3 (translated from French to English).

Experimental and/or modeling work have been carried out notably by Sassi,<sup>37</sup> Bourel,<sup>38</sup> Challita<sup>39</sup> and Janin.<sup>40</sup>

The main destructive tests to measure the mechanical strength of bonded assemblies have been introduced. Nondestructive methods for testing and evaluating bonded structures are now reported in the following.

### Nondestructive methods

Nondestructive methods can be used to test and evaluate bonded assemblies after the manufacturing process or during maintenance operations. NDE methods have been widely studied in the literature. Many bibliographical reviews have been written by authors such

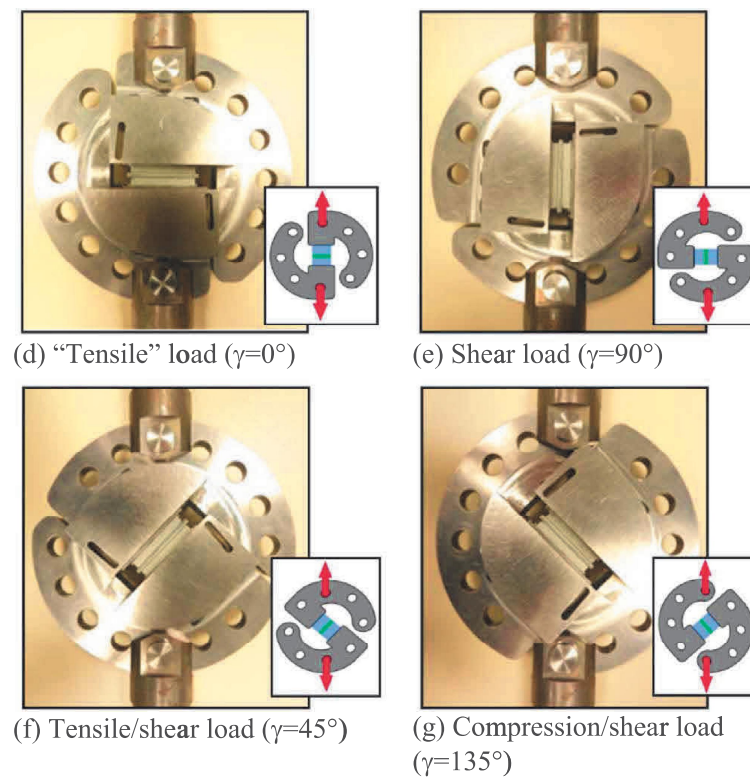


Figure 1.6 – Representation of the Arcan mounting for different angular positions to induce tensile, shear and compressive stresses in the adhesive bonding. Fig. taken from Ref. 35.

as Guyott *et al.*,<sup>11</sup> Light *et al.*,<sup>41</sup> Adams *et al.*,<sup>12,13,42</sup> Ehrhart *et al.*<sup>14</sup> and Bode *et al.*<sup>43</sup> In addition, a large number of PhD theses contain bibliographical studies that cover numerous NDE methods to evaluate adhesive bonding: Pialucha,<sup>44</sup> Ecault,<sup>45</sup> Michaloudaki,<sup>46</sup> Lourme,<sup>47</sup> Le Crom - Levasseur,<sup>48</sup> Baudot,<sup>49</sup> Ehrhart,<sup>50</sup> Siryabe,<sup>10</sup> and Zabbal.<sup>51</sup> The objective of this section is to give an overview of existing methods for non-destructively evaluating bonded assemblies. First of all, three main types of methods are presented. First, techniques that take advantage of the rather low-frequency resonances (up to a few tens of kHz) of the structure are introduced (tap test, membrane resonance). Secondly, infrared thermography methods (vibrothermography, pulsed thermography, lock-in) are presented. Thirdly, laser shock techniques, used to quantify the mechanical strength of a structural bond, are studied [Laser Bond Inspection (LBI), Laser Adhesion Test (LASAT)]. Finally, other methods that can be found in the literature, in particular to detect disbonds, are briefly introduced. Concerning the ultrasonic NDE methods (linear and non-linear), these are presented in detail in Sec. 1.3.

Firstly, methods based on structure resonances at relatively low frequencies (up to a few tens of kHz) are generally referred to in the literature as *sonic vibrations*.<sup>11,13,42</sup> The most common one in the industry and the easiest to implement is the *tap test*.<sup>52</sup> This technique consists of impacting a structure with a calibrated hammer. If the frequency emitted after impact is different from the reference measurement made on a healthy structure then a void or a disbond can be detected. Indeed, the modification of the local stiffness of the structure, caused by a defect located close to the surface, leads to a change in the resonant properties of the sample. This control method remains qualitative, local (in generation and detection) and relative (need for a reference acquisition on an undamaged structure). Other methods based on structure resonances have been grouped together, notably by Guyott *et al.*,<sup>11</sup> under the name of *membrane resonance*. The general idea is that the structure won't vibrate in the same way in places with or without disbonding. Indeed, the substrate above a disbond can be modeled as a disc, bound to the rest of the structure by certain boundary conditions, which has a resonant frequency different from that of the whole structure. The objective of this method is therefore to vibrate the structure at low frequencies and to succeed in detecting the resonance frequencies characteristic of defects (disbonds, voids). Commercial systems exploiting this phenomenon were developed before the 1990s: *Fokker Bond Tester*, *Harmonic Bond Tester* developed by Boeing.<sup>11,53,54</sup> However, methods based on structural resonances do not allow the detection of small defects because the frequencies used are relatively low (up to a few tens of kHz). Moreover, these methods are limited to the detection of voids, disbonding<sup>55</sup> but do not allow to quantify

the mechanical strength of bonded structures.

Secondly, many papers have been written on infrared thermography methods for non-destructive testing. In particular, there is a detailed literature review by Ciampa *et al.*<sup>56</sup> on NDT methods applied to aerospace structures. Three main techniques can be distinguished according to the type of heat flow generation and detection: *vibrothermography*, *pulsed thermography* and *lock-in thermography*. These are all active and not passive thermography methods as they require external heat flow generation. In *vibrothermography*, the generation of this flow is achieved by vibrating the structure. These mechanical vibrations dissipate energy into heat.<sup>57,58</sup> This heat flux is then detected using an infrared camera. Gao *et al.*<sup>59</sup> has used this technique to detect cracks in the fan blades of aircraft engines. Zhu and Guo<sup>60</sup> were able to visualize disbonds in a bonded assembly (aluminum/cork) using vibrothermography. Rantala *et al.*<sup>61</sup> used this technique to detect voids, cracks and also to evaluate the quality of a CFRP/CFRP (Carbon Fiber Reinforced Polymer) bonded assembly. Pulsed thermography differs from vibrothermography by the fact that the heat flow is not generated by mechanical vibrations but by strong light pulses that heat the surface of the part by photothermal effect.<sup>62,63</sup> Flash or halogen lamps can be used to generate this heat flow. The pulse duration can vary from a few hundred microseconds to a few tens of milliseconds depending on the thermal properties of the materials inspected and the depth of the imperfections to be examined.<sup>56</sup> Then, an infrared camera is used to measure the surface temperature of the part in order to detect possible defects. Indeed, temperature gradients can be caused by discontinuities in thermal conduction due to voids, disbonds or porosities within the controlled structure. *Lock-in thermography* consists in generating the heat flow no longer by a high intensity light pulse (*pulsed thermography*) but by an amplitude modulation of this light energy as a function of time. This allows to generate thermal waves of different frequencies within the medium to be controlled. Scientific work has been carried out on bonded assemblies using this type of thermographic methods.<sup>64–66</sup> However, infrared thermography does not currently make possible to quantify the mechanical strength of a bonded structure, but allows to inspect the parts for finding defects such as cracks, voids, etc. For example, in 2017, the Safran group inaugurated an automated NDT process called “IRIS” (Infra Red Inspection System)<sup>e</sup> which used infrared thermography. This device allowed the inspection of composite panels with complex geometries, large sizes (3 to 12 m<sup>2</sup>) and variable thicknesses.

---

e. Automated NDT solution using infrared thermography (IRIS): [URL link](#) [Accessed on 08/05/2020].

Third, a promising method for quantifying the mechanical strength of bonded assemblies is laser shock. This technique is based on the generation of a shock wave in the material by a laser pulse of very high energy (above 10 J per pulse<sup>67</sup>) and duration of a few nanoseconds. This laser pulse creates a plasma on the surface of the material which, by expanding under pressure, generates a shock wave in the medium. This generation can be carried out either in direct irradiation [Fig. 1.7(a)], or in confined regime [confinement of the plasma by a layer of water as shown in Fig. 1.7(b)]. A significant amount of research has been conducted from the early 1980s to evaluate the mechanical strength of bonded assemblies with laser-generated shock waves. Two technologies, based on the same principle, can be cited:

- Laser Bond Inspection (LBI) developed by LSP Technologies and Boeing;<sup>f</sup>
- LASer Adhesion Test (LASAT).<sup>g</sup>

The LBI technology is commercialized by LSP Technologies and allows to detect weak adhesive bonds. Nevertheless, this method requires to glue on the surface of the structure an EMAT sensor and a protective film.<sup>h</sup> The operator must then press the inspection head onto the surface before performing the laser shock measurement. According to the designer, this method allows to distinguish between good and bad bonding. LASAT technology is also based on the generation of a laser shock wave. A literature review, written by Berthe *et al.*,<sup>68</sup> gives an interesting overview of this technology. It can be used either to quantify the practical adhesion of a coating deposited on the surface of a material, or to quantify the mechanical strength of a bonded assembly. Several PhD theses have been conducted on this topic: Ecault,<sup>45</sup> Fabre,<sup>69</sup> Ehrhart<sup>14</sup> and Bardy.<sup>70</sup> In 2018, Ducouso *et al.*<sup>67</sup> successfully applied this laser shock technique to quantify the mechanical strength of bonded aeronautical assemblies (TA6V4/epoxy/3D woven composite). The LASAT technology is therefore interesting because it strongly stresses the bonded assembly to test its mechanical strength. However, it must be ensured that this method remains nondestructive (does not degrade the substrates and the adhesive) when used to quantify the practical adhesion of a bonded assembly.

Finally, in the scientific literature, there are still many other methods than those presented so far to try to non-destructively control adhesive bonding. Especially, it is possible to cite the techniques of holography,<sup>71</sup> shearography,<sup>72</sup> acoustic emission<sup>73</sup> or radiography

---

f. LSP Technologies: [URL link](#) [Accessed on 08/05/2020].

g. Demonstration video of the LASAT at the Process and Engineering in Mechanics and Materials (PIMM) laboratory (2018): [URL link](#) [Accessed on 09/09/2020].

h. Demonstration video of the LBI method developed by LSP Technologies (2014): [URL link](#) [Accessed on 08/05/2020].

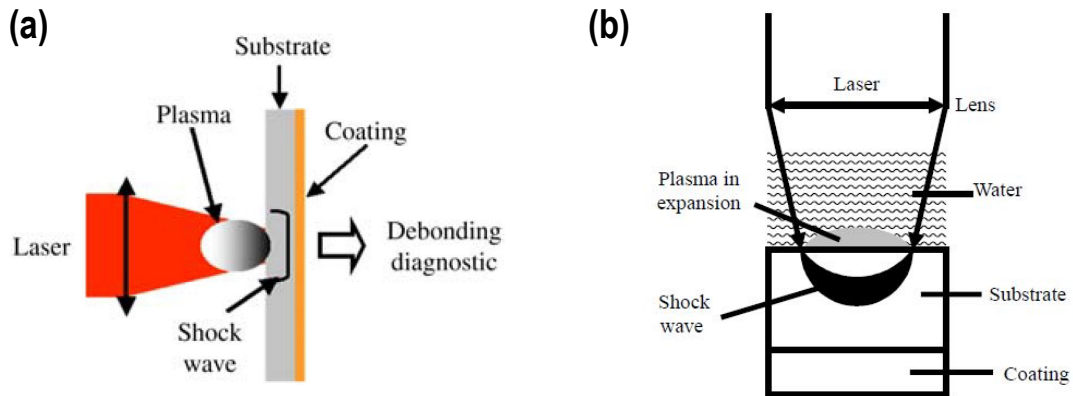


Figure 1.7 – Generation of a laser shock in: (a) direct irradiation and (b) confined regime. Fig. taken from Ref. 68.

methods (X-ray or  $\gamma$ ).<sup>74,75</sup> These methods can be used to detect disbonds, but none of them has yet been able to quantify the mechanical strength of a bonded structure.

An overview of NDE methods for inspecting bonded assemblies was presented (infrared thermography, laser shock, etc.). It can be noted that a significant amount of scientific work has been carried out on this topic over the last few decades. This scientific activity reflects the major interest in finding a nondestructive method for inspecting bonded structures. In the next section, the ultrasonic NDE methods are detailed.

### 1.3 Ultrasonic nondestructive evaluation methods for bonded structures

A large number of nondestructive methods have been presented previously for testing and evaluating bonded assemblies. Ultrasonic methods are detailed in this section. Indeed, elastic waves are good candidates for testing bonded structures because of their mechanical interactions with the adhesive bonding. Ultrasonic NDE methods can be performed either in *contact* with the assembly to be inspected or *non-contact*. For *contact methods*, generation and detection are most commonly performed by one or more piezoelectric transducers (single or multi-elements) that are held in contact with the surface through a coupling liquid or gel. This ensures good ultrasound transmission between the transducer and the medium to be controlled. For *non-contact methods*, several techniques can be used. The first concerns the generation and detection of ultrasound in

immersion. The transducers and the part to be controlled are immersed, totally or partially, in a tank usually filled with water. The second brings together methods using air-coupled transducers for generation and/or detection. The third includes techniques using ElectroMagnetic Acoustic Transducer (EMAT) transducers that allow ultrasound to be generated or detected in materials that must necessarily be electrically conductive. Finally, the generation and detection of ultrasound can be performed with lasers.

In the following, methods based on linear bulk waves and then on guided waves are presented. Next, non-linear ultrasonic methods are introduced (harmonic generation, mixing of non-collinear waves, etc.).

### 1.3.1 Linear ultrasonic nondestructive evaluation methods using bulk waves

For the ultrasonic inspection of bonded structures, nondestructive methods using bulk waves have been widely studied in the literature. The conventional NDT techniques in *pulse-echo* or *pitch-catch* modes, which are usually used to detect cracks or voids in parts, are difficult to apply for the detection of cohesive and adhesive defects in bonded structures. Indeed, these methods are efficient when there is a high impedance ratio between the medium where the wave propagates and the defect; which is not necessarily the case for bonded assemblies. For this reason, much work has been carried out to try to modify and adapt these methods to the NDE of adhesive bonding.

First, approaches using *pulse-echo* methods for monitoring bonded structures are presented. Then, *pitch-catch* methods in transmission (generation and detection on both sides of the assembly to be inspected) and in reflection (generation and detection on the same side) are introduced.

#### Pulse-echo

Pulse-echo methods generally involve generating and detecting ultrasound at normal incidence, relative to the surface, with a single transducer. Usually, these methods are used to detect defects such as voids, open cracks oriented parallel to the surface, etc. The calculation of the time of flight then allows to locate the defect knowing the propagation velocities of the elastic waves in the medium. This conventional approach is not directly applicable to the inspection of bonded assemblies. Numerous works have therefore been carried out to improve this technique for the NDE of adhesive bonding, in particular with contact methods.<sup>76–80</sup> For instance, Tattersall<sup>76</sup> used all the information contained in the reflected

signal (amplitude, phase) and not just the presence or absence of a reflected signal, as it is done in conventional pulse-echo techniques. Chang *et al.*<sup>77</sup> studied the frequency spectra of signals measured in the pulse-echo mode on single-coated aluminum bonded specimens with different mechanical properties. Mojškerc *et al.*<sup>80</sup> were interested in the amplitudes of several echoes reflected on a glass (8 mm)/adhesive (3.2 mm)/polymer (2 mm) assembly to evaluate the quality of the bonded joint. These presented techniques do not allow to quantify the mechanical strength of bonded assemblies. However, they can be used to detect disbonds, porosities or voids using suitable signal processing methods (Fourier transform, filtering, convolution, etc.).

#### **Pitch-catch**

Pitch-catch methods differ from pulse-echo methods in that generation and detection are generally not performed by the same transducer. This makes it possible to perform measurements in transmission (when generation and detection are located on opposite sides of the part to be inspected) or in reflection (when generation and detection are located on the same side).

Concerning the pitch-catch methods in transmission, Siryabe *et al.*<sup>10,81</sup> have used an immersion technique called the *Ultrasonic Plane Wave Transmission Coefficient* (UPWTC), on aluminum/epoxy/aluminum bonded structures (see Fig. 1.8). Different surface treatments (degreasing, sandblasting, silanisation, etc.) and different adhesive curing times were used to modulate the mechanical strength of the bonded assemblies. Then, solving an inverse problem from the experimental and theoretical transmission coefficients, as a function of the frequency and angle of incidence of the plane wave on the surface, made it possible to identify the apparent elastic coefficients of the epoxy layer. The apparent anisotropy of the adhesive was then used as an indicator of poor practical adhesion between the substrates and the adhesive. This method was applied to bonded samples with an adhesive thickness of about one millimeter. In the aeronautical industry, the adhesive thicknesses are thinner (on the order of a few tens or hundreds of micrometers). In 2017, Wu *et al.*<sup>82</sup> implemented a transmission method using air-coupled transducers. The layout of the experimental set-up used is quite similar to that of Siryabe *et al.* presented in Fig. 1.8 (transmitter and receiver on either side of the sample with the possibility of changing the angle of incidence of the wave by rotating the sample). The contactless measurements were carried out in air. The bonded assemblies consisted of two composite plates bonded together with a thin layer of epoxy (20  $\mu\text{m}$ ). The frequency spectra (between 0.5 and 1 MHz) of the experimental signals received after propagation in the

sample were studied for different angles of incidence and for different curing times (from 1 to 10 hours). The authors showed, theoretically and experimentally, that it was possible to follow the polymerization time and thus the evolution of the normal  $K_N$  and transverse  $K_T$  interfacial stiffnesses, that were proposed to model the bonding, by looking at the frequency shifts of some well-chosen resonance peaks obtained on the frequency spectra.

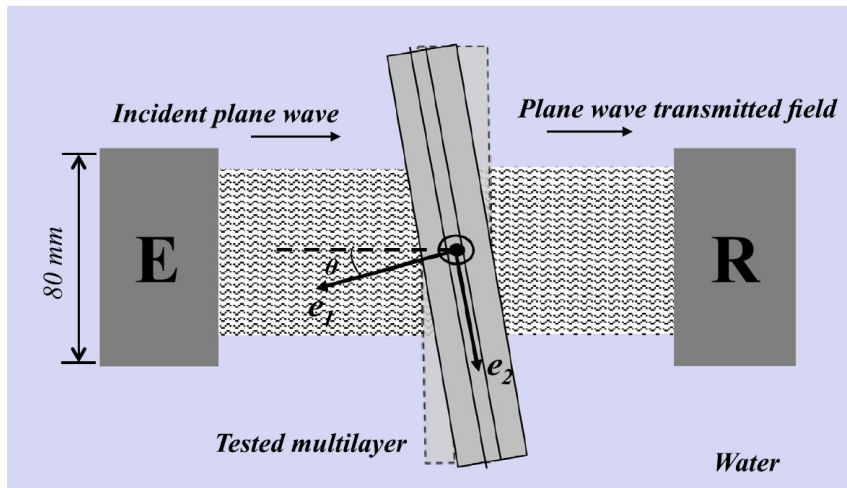


Figure 1.8 – Experimental transmission set-up used by Siryabe<sup>10</sup> on an aluminum/epoxy/aluminum bonded assembly. Fig. taken from Ref. 81.

These transmission methods are interesting but difficult to apply in an industrial context. Indeed, only one surface of the assembly to be inspected is, most of the time, accessible. The use of pitch-catch methods in reflection is therefore relevant to non-destructively inspect industrial bonded structures. A significant number of papers have been published on this topic since the 1980s.<sup>16,18,19,44,83–94</sup> These publications deal with the study of the evolution of the reflection coefficients of longitudinal and/or transverse waves as a function of their angles of incidence with respect to the substrate/adhesive interface. The study of these reflection coefficients is generally carried out in the frequency domain to determine the frequencies most sensitive to the mechanical strength of the bonded assembly. In addition, normal and transverse interfacial stiffnesses are often used to model the interface. In 2003, Baltazar *et al.*<sup>94</sup> developed an inversion method, based on the previous work of Lavrentyev and Rokhlin<sup>90</sup> and Wang *et al.*,<sup>93</sup> to determine the acoustic, geometric and interfacial properties of an isotropic layer of adhesive between

two known substrates. The properties of this layer included: thickness, attenuation coefficients within the adhesive, Lamé coefficients, density and complex interfacial stiffnesses (normal and transverse). The developed inversion method was based on the frequency spectra obtained in reflection at normal and oblique incidences. The objective of this method was to be able to detect separately cohesive defects (in the adhesive layer) and adhesive defects (at the substrate/adhesive interface). This algorithm has been experimentally tested on an aluminum/epoxy/aluminum bonded assembly whose interfaces had been degraded in the presence of an aggressive environment (saturated solution of NaCl at 68°C). The normal interfacial stiffness  $K_N$  was considered infinite and the imaginary part of the transverse interfacial stiffness  $K_T$  was considered null. The inversion method was used to identify the real part of  $K_T$  as well as the other parameters presented above.

NDE linear methods using bulk waves for inspecting bonded assemblies were presented and some were detailed. Ultrasonic techniques using guided waves are now introduced below.

#### 1.3.2 Linear ultrasonic nondestructive evaluation methods using guided waves

To control and evaluate bonded assemblies, guided wave methods remaining in the linear domain, have been intensively investigated. Several types of guided waves exist and can be used for NDE purposes. First of all, ultrasonic methods are based on the propagation of Rayleigh waves, which were discovered in 1887 by Lord Rayleigh. These waves are guided by a single free surface of an elastic solid and penetrate in a thickness approximately equivalent to one wavelength. The polarization of these waves is elliptical. Rayleigh waves are said to be *non-dispersive* when their propagation velocities depend essentially on the material properties and not on the frequency. There are also elastic waves guided by a medium bounded by two parallel free surfaces (plate-like guide): Shear Horizontal (SH) guided waves and Lamb waves. SH guided waves are the result of the multi-reflections on the two free surfaces of the plate of the SH bulk waves polarized horizontally, i.e., polarized in a direction perpendicular to the wave propagation plane. Lamb waves are the result of the multi-reflections on the two free surfaces of vertically polarized bulk waves, i.e., polarized in the wave propagation plane. These elastic waves can have longitudinal or transverse (shear) polarizations.

First, NDE methods using Rayleigh waves and then SH guided waves applied to bonded assemblies are presented. Secondly, developed techniques using Lamb waves and more particularly zero-group-velocity (ZGV) Lamb modes are described.

### Rayleigh waves and SH guided waves

Regarding methods based on Rayleigh wave propagation to inspect bonded assemblies, Rokhlin *et al.*<sup>95</sup> used an experimental device to generate a Rayleigh wave on a metal substrate (300 mm-long, 70 mm-wide and 30 mm-thick). This Rayleigh wave then propagated to a steel/epoxy (25  $\mu\text{m}$ )/steel bonding interface before being detected. The authors concluded that the phase velocity of the guided wave propagating at the interface and the transmission loss coefficient are parameters correlated to the mechanical strength of the bonded joint. Singher<sup>96</sup> used an experimental set-up to generate a Rayleigh wave on the surface of an aluminum plate using a piezoelectric contact transducer. This wave then propagated at an aluminum/epoxy (100  $\mu\text{m}$ )/aluminum bonding interface before being detected by a Michelson interferometer (see Fig. 1.9). The modulation of the mechanical strength of the bonded joint was obtained by different surface treatments (mechanical, chemical, etc.) of the substrates. The author of this paper has shown that there is a good correlation between the velocity of the guided waves at the interface and the mechanical strength of the adhesive bonding. However, this work using Rayleigh wave generation and detection<sup>95,96</sup> did not allow to quantify the practical adhesion of bonded assemblies.

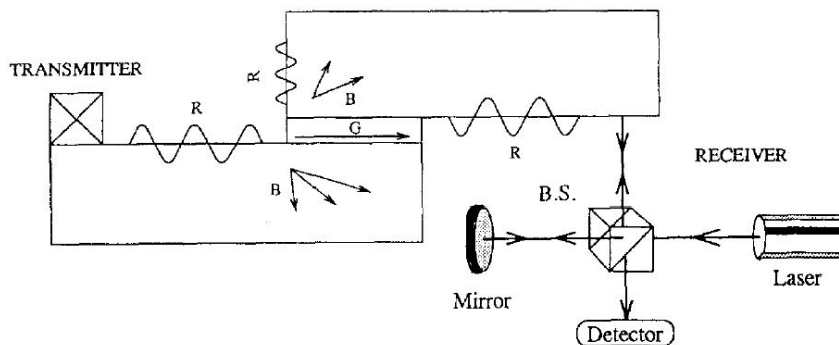


Figure 1.9 – Experimental set-up used by Singher (Fig. taken from Ref. 96) with (contact) generation and (non-contact) detection of Rayleigh waves on aluminum substrates. R (Rayleigh wave), B (bulk wave), G (guided wave), B.S. (beam splitter).

About the NDE methods using SH guided waves, Lourme,<sup>47</sup> Le Crom *et al.*<sup>48,97,98</sup> and Castaings<sup>99</sup> have used these waves to non-destructively evaluate adhesive bonding. Indeed, Le Crom<sup>48</sup> indicated that these SH guided waves are sensitive to the shear properties of bonded assemblies because of their polarization in a direction perpendicular to the plane of wave propagation. These guided waves therefore appear to be good candidates for inspecting bonded structures. Le Crom and Castaings<sup>97,98</sup> have studied numerically [Fig. 1.10(a)] and experimentally [Fig. 1.10(b)] these SH guided waves on aluminum (3 mm)/epoxy (0.2 mm)/composite (1.2 mm) bonded structures. Their results showed that the SH<sub>0</sub> and SH<sub>1</sub> modes have a strong potential to quantify the shear stiffness of this type of bonded assembly. On the other hand, the SH<sub>2</sub> mode was not used to test the cohesive properties of the bond because it was highly sensitive to the physical and mechanical properties of the substrates (aluminum and composite) as well as their thicknesses. Castaings<sup>99</sup> studied the sensitivity of SH guided waves, including the SH<sub>0</sub> mode, to the cohesive properties of the adhesive and the interface properties of a single lap joint between two 3 mm-thick aluminum bonded plates. An inverse problem was then solved to determine the shear modulus of the adhesive layer and the shear interface stiffness  $K_T$  of the bonded joint from the results of numerical modeling and experimental measurements. Castaings stated in the conclusion of the paper that the experimental conditions were perfect for obtaining good results (aluminum plates with known mechanical properties, known thicknesses, etc.); which is rarely the case in an industrial context for example. In addition, further studies need to be carried out to test this method on bonded assemblies composed of composite material substrates.

#### **Lamb waves and ZGV resonances**

Lamb waves have been the subject of numerous research studies to evaluate non-destructively bonded assemblies. These are waves guided in a medium bounded by two parallel free surfaces (plate-like guide). Lamb waves are the result of the multi-reflections of longitudinal and transverse polarized bulk waves in the medium. Symmetric (S) and antisymmetric (A) modes, satisfying the Rayleigh-Lamb equation, can be represented by dispersion curves linking the frequency to the wavenumber. When the group velocity of one of these modes goes to zero, there is a resonance that can be classified into one of two categories according to its wavenumber  $k$ : thickness resonances ( $k = 0$ ) or local resonances ( $k \neq 0$ ). When the wavenumber  $k$  is zero, the wavelength is infinite, so the whole surface vibrates in phase. When the wave number is not equal to zero, the wavelength is finite and the resonance is therefore localized; these are zero-group-velocity

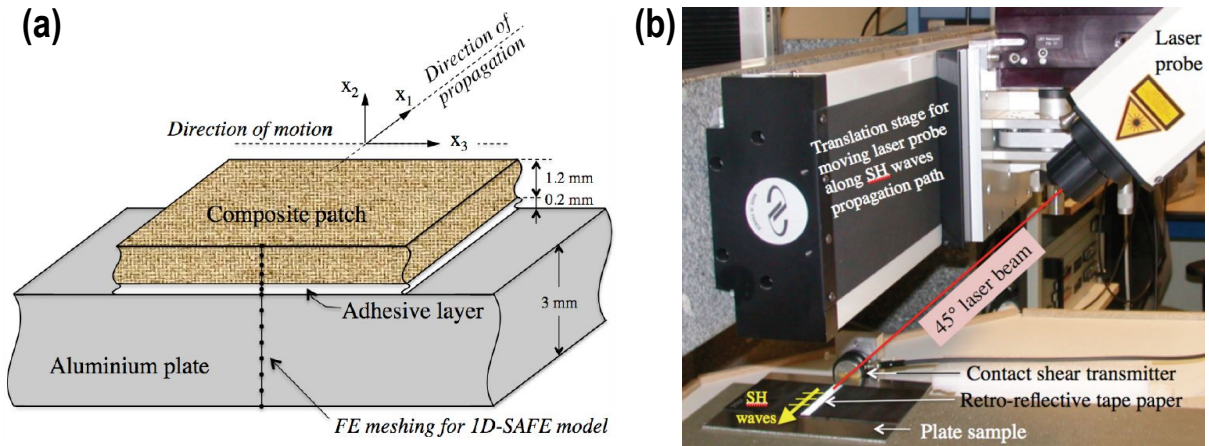


Figure 1.10 – (a) Schematic diagram of the aluminum/epoxy/composite trilayer studied by Le Crom and Castaings using one-dimensional semi-analytical finite element code (SAFE). (b) Picture of the experimental set-up used to generate and detect SH guided waves and to measure the phase velocities of the different modes. Fig. taken from Ref. 98.

(ZGV) resonances. First, methods based on Lamb waves to evaluate bonded assemblies are presented. Secondly, techniques based on ZGV resonances are discussed.

Regarding methods using Lamb waves, Kundu *et al.*<sup>100</sup> studied the detection of kissing bond defects between two glass plates compressed together by hydraulic pressure. Experiments conducted in pitch-catch mode in immersion showed that most Lamb modes are insensitive to the kissing bond. However, in their studied case, only the  $A_1$  mode is strongly affected by this defect for phase velocities lower than 4 km/s. Mori *et al.*<sup>101,102</sup> were interested in the reflection and transmission of Lamb waves at an imperfect butt joint. In 2013, they showed that the reflection and transmission of the  $A_0$  and  $S_0$  modes at the joint depended on frequency and different interface stiffnesses following numerical studies by Modal Decomposition Method (MDM) and Hybrid Finite Element Method (HFEM). Then in 2016, experiments were carried out on two 2.5 mm-thick aluminum plates bonded end-to-end with different bonding conditions. From the measured transmission coefficients, the interfacial stiffnesses could be identified. A correlation between these determined stiffnesses and the bonding conditions of the different prepared samples was noted. Siryabe *et al.*<sup>103</sup> studied the transmission of Lamb waves at a 0.2 mm-thick adhesive joint and a simple overlap between two 3 mm-thick aluminum bonded plates.

Two bonded assemblies with different mechanical properties were manufactured: a *reference* assembly (with surface preparation) and another sample with potentially low practical adhesion (without surface preparation). Two-dimensional finite element simulations and experiments including air-coupled transducers were performed. The normal  $K_N$  and transverse  $K_T$  interfacial stiffnesses of the numerical model were adjusted so that the simulated transmission coefficients as a function of the frequency of the  $A_0$  and  $S_0$  modes were in agreement with those measured experimentally. The results showed that the use of Lamb waves in transmission can be interesting to quantify the mechanical strength of this type of bonded structure (simple overlap). Gauthier *et al.*<sup>104</sup> were interested in classifying aluminum (5 mm)/epoxy (0.5 mm) bilayers according to their level of practical adhesion. Several samples were manufactured with different surface treatments and different epoxy curing times. Several levels of adhesion were separated by comparing the experimental dispersion curves with those simulated by finite element method (FEM). However, normal and transverse interfacial stiffnesses were assumed to be equal; which remains a hypothesis to be tested. The authors indicated that their next step was to study an aluminum/epoxy/aluminum trilayer to be more representative of a real structural bonding and that the resolution of an inverse problem should be carried out to determine interfacial stiffnesses more precisely.

There is a limitation to the dispersion curves of Lamb waves for the NDE of bonded assemblies. Indeed, several authors,<sup>105–109</sup> including Lowe and Cawley,<sup>106</sup> specified that these dispersion curves were very sensitive to the physical and mechanical properties as well as to the thickness of the substrates. Moreover, Nagy *et al.*<sup>107</sup> or Dwen,<sup>109</sup> indicated that these dispersion curves were relatively unaffected by the modification of: the properties of the adhesive layer, its thickness, and the substrate/adhesive interface conditions. Thus, another technique consists in using zero-group-velocity (ZGV) resonances, of the bonded assembly, to attempt to quantify its mechanical strength. Indeed, these ZGV resonances have several advantages. Firstly, they have a finite wavelength so they are spatially localized. Secondly, their quality factor is high, so the ZGV resonances are spectrally narrow.

About the scientific work on ZGV Lamb modes, Cho *et al.*<sup>110</sup> have estimated the quality of a bonded structure, composed of aluminum (3 mm)/epoxy (0.09 mm)/aluminum (3 mm), from ZGV resonance frequencies. Generation and detection of ZGV modes were carried out experimentally using laser beams. Samples with and without surface preparation were manufactured and then mechanically tested in order to be able to compare the

ZGV resonance frequencies between high and low mechanical strength. The lowest resonance frequency showed a good sensitivity to the bond quality. In 2014, Mezil *et al.*<sup>111</sup> used an analytical model to calculate Lamb modes in a symmetrical bilayer structure where the bonding interface was modeled by normal and transverse interfacial stiffnesses ( $K_N$  and  $K_T$ , respectively). This model demonstrated that the resonance frequencies of the symmetrical ZGV modes were dependent on  $K_N$  and those of the antisymmetrical modes on  $K_T$ . In addition, experiments were conducted on a glass/glass bilayer. The bonding agents between these two plates were water, oil and salol. The thicknesses of these layers were considered negligible compared to those of the substrates. Generation and detection were performed by laser. This local and non-contact method allowed the estimation of normal and transverse interfacial stiffnesses from the calculated and measured ZGV resonance frequencies. In 2015, Mezil *et al.*<sup>112</sup> focused their work on a trilayer duralumin (1.5 mm)/epoxy (0.035 mm)/duralumin (1.5 mm) in order to take the thickness of the adhesive into account. An adhesive rheological model, shown in Fig. 1.11(a), was used to numerically calculate the dispersion curves to derive the ZGV resonance frequencies. Experiments with laser generation and detection on either side of the structure were carried out. In a first step, the thickness of the adhesive layer was measured by time-of-flight measurement. Then, the experimentally obtained ZGV resonance frequencies were used to identify the values of the interfacial stiffnesses to be imposed in the model to ensure a good theory/experiment agreement [see Fig. 1.11(b)]. This paper shows the interest of ZGV resonances to quantify the mechanical strength of bonded structure with a local and contactless method. However, some limitations are expressed by the authors of the article. First, the thickness of the substrates and especially the thickness of the adhesive layer must be known to determine the interfacial stiffnesses. Indeed, the ZGV resonances are sensitive to the thicknesses of the different components of the assembly. Secondly, the developed method must be extended to a larger number of samples of different natures in terms of the materials used and/or the thicknesses taken into account. Destructive mechanical tests could also be carried out to compare the results of this nondestructive method with destructive one. Finally, Bruno, who participated in the elaboration of this article,<sup>112</sup> concludes his PhD thesis<sup>113</sup> by indicating that it would be interesting to couple non-linear methods with ZGV resonance measurements; for example by stressing the bonded assembly.

### 1.3. Ultrasonic nondestructive evaluation methods for bonded structures

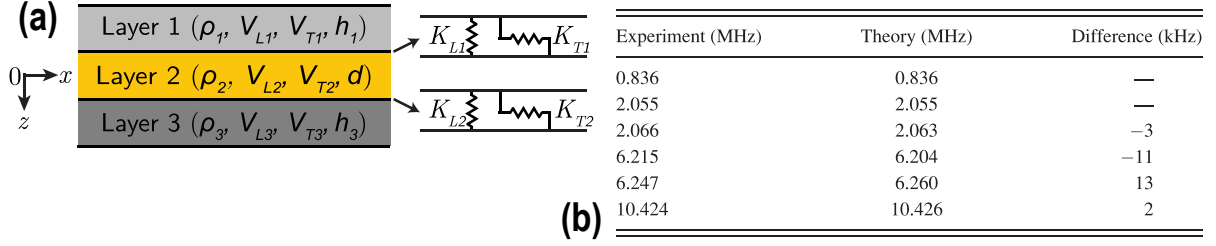


Figure 1.11 – Figure and table taken from Ref. 112: (a) geometry of the trilayer model used to compute the dispersion curves following the approach proposed by Vlasie and Rousseau,<sup>114</sup> (b) comparison between experimental and theoretical ZGV resonance frequencies.

#### 1.3.3 Non-linear ultrasonic nondestructive evaluation methods

When linear ultrasonic NDE methods are insensitive or ineffective for evaluating bonded assemblies, non-linear ultrasonic methods are another class of methods that can be of interest. Non-linear acoustics concerns the propagation of elastic waves in a non-linear medium which causes signal distortion, pseudo-periodic behaviour or chaotic behaviour. As Saidoun pointed out,<sup>115</sup> there are three different non-linear mechanisms: *geometric*, *material* and *contact* non-linearities. First, *geometric non-linearities* are usually caused by large deformation amplitudes. Second, *material non-linearities* are those corresponding to a non-linear stress/strain relationship (i.e., taking higher order terms into account in the Hooke's law). Third, there are *contact non-linearities*, notably referred as *Contact Acoustics Nonlinearity* (CAN) in the literature. Solodov *et al.*<sup>116</sup> define CAN as an asymmetry of interfacial stiffness (higher stiffness when the two solids are in compression with each other and lower or zero stiffness when they tend to move apart). This phenomenon can be activated when an elastic wave is applied to a bonding interface, which can lead to the generation of harmonics.

In this part, different NDE methods based on non-linear ultrasound are discussed. First, the methods of harmonic generation, second harmonic imaging and non-collinear wave mixing are presented. Secondly, non-linear ultrasonic techniques using heat flow modulation and phase modulation are introduced.

#### Harmonic generation

The principle of harmonic generation consists in exciting the bonded assembly with, for example, a very high amplitude acoustic signal. Thus, harmonics (integer multiples of

the excitation frequency) are generated. This non-linear method can therefore potentially provide access to information that is not accessible by remaining in the linear domain. Berndt and Green<sup>117</sup> studied the generation of harmonics in transmission and immersion at a bonding interface between two aluminum plates. Four samples were prepared under a heated press by varying the adhesive curing time to modulate the mechanical strength of the bonded structure. The experimental set-up consisted of a transducer with a nominal frequency of 5 MHz followed by a lens to focus the high amplitude ultrasonic waves at the bonding interface. A 10 MHz center frequency transducer was used to receive the signal. The authors of the paper noticed that the more the adhesive is cured, the more the amplitudes of the generated harmonics (especially the second harmonic) decrease. However, Berndt and Green indicated that these non-linearities are not primarily related to the bonding interface. Indeed, according to them, they could also be caused by wave propagation within the adhesive. It was therefore difficult with this method to separate the different types of the observed non-linearities. Brotherhood *et al.*<sup>118</sup> sought to detect defects, such as kissing bonds, by generating high amplitude ultrasonic waves experimentally. Samples consisting of two aluminum blocks, separated by 2 mm-thick adhesive layer, were tested at different compression loading intensities. The experiments were carried out in transmission and immersion. Ultrasonic waves were generated at a frequency of 1.85 MHz and then detected by a transducer with a center frequency of 5 MHz. The Fast Fourier Transform (FFT) of the received signal made it possible to plot the evolution of the amplitude ratio between the second harmonic and the fundamental frequency as a function of the compression loading. The authors noted that as the compression loading decreased, the amplitude ratio (second harmonic to fundamental) increased. They explained this by the fact that there was a large asymmetry between the compressive and tensile stiffness at the interface when the surfaces of the aluminum blocks were simply in contact or when the compressive loading was very low. Yan *et al.*<sup>119</sup> used an experimental device quite similar to the one of Brotherhood *et al.*<sup>118</sup> where two cylindrical blocks of aluminum separated, or not, by an adhesive layer were compressed (pressures between 0.1 and 11.2 MPa). On the other hand, the generation and detection of ultrasound were not performed in immersion but in contact, see Fig. 1.12. One of the conclusions of the paper was that the majority of non-linearities were caused by the generation and amplification of the acoustic signal.

Liu *et al.*<sup>120</sup> went further in the search for the origins of non-linearities. Their objective was to evaluate the influence of different experimental parameters (signal amplification, transducers, coupling conditions, etc.) on the generation of harmonics. Indeed, in order

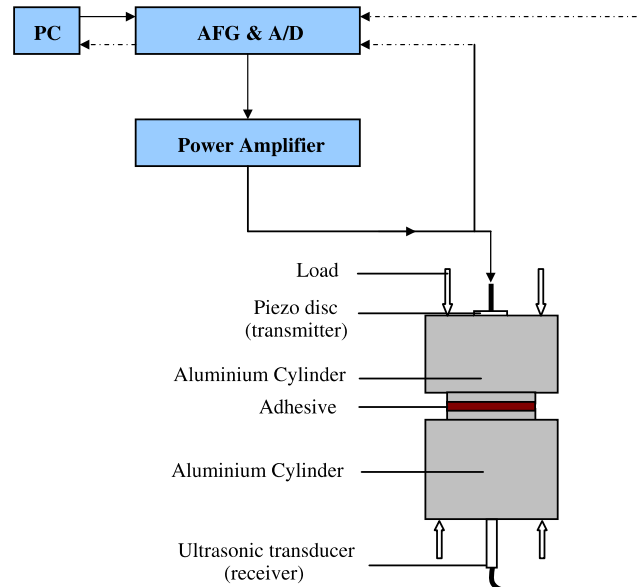


Figure 1.12 – Schematic of the experimental set-up used by Yan *et al.* (Fig. taken from Ref. 119) for the generation of high-amplitude ultrasonic waves.

to have access to the non-linearities essentially caused by the bonding interface, it was necessary to identify those caused by the assembly itself and to try to minimize them if possible. The authors of this paper used an amplified 3.6 MHz center frequency signal to excite a piezoelectric cell bonded to the surface of a healthy aluminum block (no damage was done). Ultrasound was received from the other side of the medium by a contact piezoelectric transducer (using a coupling gel). In the same way as Brotherhood *et al.*,<sup>118</sup> Liu *et al.* realized that strong non-linearities are caused by signal generation and amplification. They showed that the force with which the receiving piezoelectric transducer was pressed against the workpiece had an influence on the measured non-linearities. In addition, the alignment of the receiving piezoelectric transducer with respect to the transmitting piezoelectric cell could change the measurement of the non-linearities. Finally, the authors showed that the choice of the windowing (Hann window, Gaussian window, rectangular window, etc.) to perform the Fast Fourier Transform (FFT) of the time signals had its importance in the measurement of non-linearities. Thus, this article highlighted the difficulties encountered when measurements by harmonic generation are carried out. Shui *et al.*<sup>121</sup> have used this non-linear technique to non-destructively evaluate aluminum (6.5 mm)/epoxy (less than 1 mm)/aluminum (6.5 mm) bonded assembly subjected to loading cycles, as shown in Fig. 1.13.

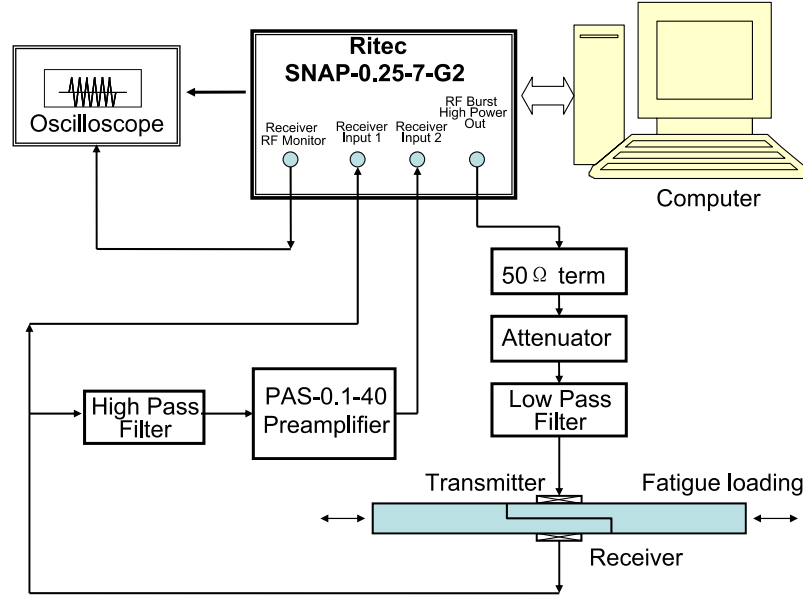


Figure 1.13 – Diagram of the experimental set-up used by Shui *et al.*<sup>121</sup> for the generation of harmonics on bonded specimens subjected to fatigue.

The authors found that the measured *Acoustic Non-linearity Parameter* (ANP) increased with the number of fatigue cycles. This ANP parameter, which was noted  $\beta$  in the paper, was equal to

$$\beta = \frac{8A_2}{A_1^2 h k^2}, \quad (1.1)$$

with  $A_2$  the amplitude of the second harmonic,  $A_1$  the amplitude of the fundamental,  $h$  the propagation distance and  $k$  the wavenumber. Shui *et al.* have also developed a theoretical model to calculate the evolution of the acoustic non-linearity parameter (ANP) as a function of the number of fatigue cycles. However, the theoretical model was not fully consistent with the experimental data. The authors pointed out that many effects (material non-linearities, attenuation, etc.) were not taken into account in the theory, which could explain the discrepancies observed with the experiment. Biwa and Ishii<sup>122</sup> and then Ishii *et al.*<sup>123</sup> were interested to theoretically model the generation of the second harmonic caused by non-linearities at the interfaces of a multilayer structure. These different interfaces were modeled by non-linear stiffnesses. The theoretical calculations were performed by considering a monochromatic longitudinal polarized wave at normal incidence on the multilayer structure. Thus, the expressions of the amplitudes of the second harmonic of the reflected and transmitted waves as a function of frequency were obtained.

Several experimental and theoretical work on the generation of harmonics, as a non-linear ultrasonic NDE method applied to bonded assemblies, have been presented. Interest is now focused on second harmonic imaging techniques.

### Second harmonic imaging

Concerning second harmonic imaging, the studies that are presented do not all directly concern the examination of bonded assemblies. However, these may potentially be of interest for the NDE of adhesive bonding. Yun *et al.*<sup>124</sup> have developed a method for evaluating *Contact Acoustic Nonlinearity* (CAN) at the interface between two solids. The performed experiment consisted of two aluminum blocks compressed with each other for different loading levels (0 MPa, 20 MPa and 40 MPa). Several reflection measurements (in pitch-catch mode) followed by a suitable post-processing step were used to obtain an image of the second harmonic along the interface. This method could be used to image closed cracks that are difficult to visualize using linear ultrasonic methods.

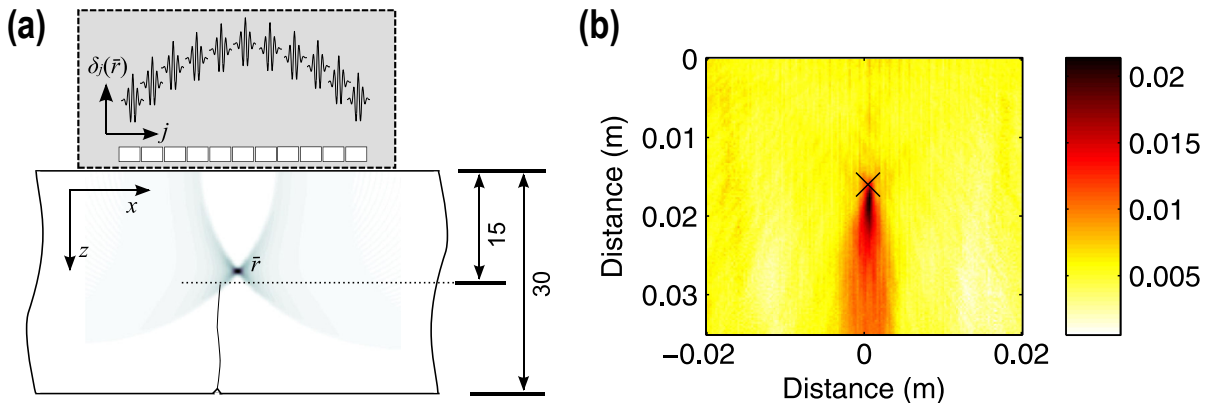


Figure 1.14 – Figures extracted from Potter *et al.*<sup>125</sup> (a) schematic of the experimental set-up consisting of the multi-element transducer in contact with the surface of the aluminum alloy part having a closed through crack, (b) visualization of the crack with the non-linear imaging method presented in the paper.

Potter *et al.*<sup>125</sup> have imaged closed cracks using a multi-element transducer. In a first time, the focusing of the ultrasonic waves, at several points in the medium to be imaged, was performed at the emission by imposing different delay laws. In a second time, a *Full Matrix Capture* (FMC) was performed and then delay laws were imposed in a post-processing step. These two methods were equivalent in terms of linear acoustics because a defect was detected with the same amplitude in both cases. However, in non-linear

acoustics, the two methods did not give the same result. Indeed, focusing the ultrasound at the emission generated harmonics, which was not the case when the focusing was done in a post-processing step. Thus, the authors of the paper have plotted the difference between the energy obtained with a focusing at emission and a focusing in post-processing. This method made it possible to image a closed crack in an aluminum alloy sample, see Fig. 1.14, that could not be visualized with a linear ultrasonic method.

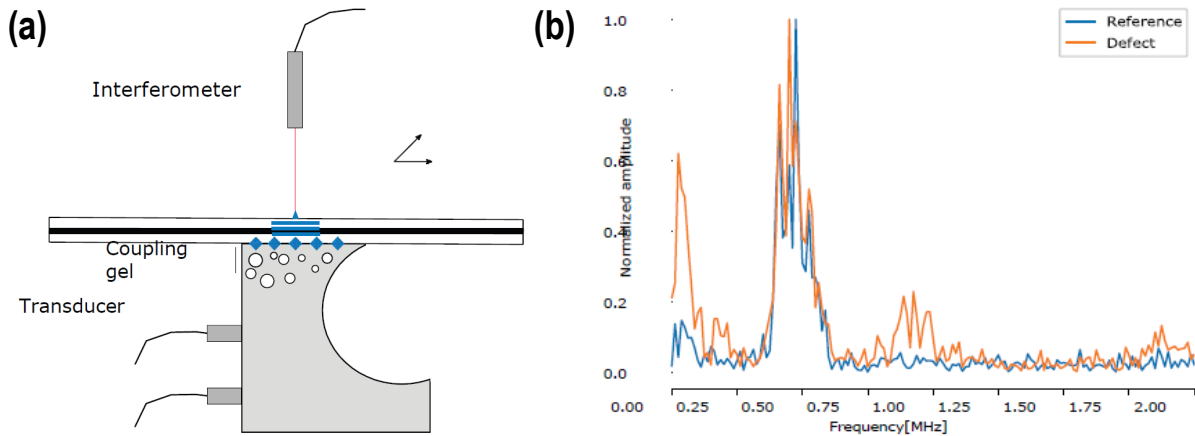


Figure 1.15 – Figures from Zabbal *et al.*:<sup>126</sup> (a) representation of the chaotic cavity transducer used to generate high amplitude plane waves, (b) Fourier transforms of the signals measured on bonded assemblies [aluminum(5 mm)/epoxy (0.1 mm)/aluminum(5 mm)] with and without defect (denoted “Defect” and “Reference”, respectively).

A second harmonic imaging technique dedicated to the NDE of bonded assemblies has been developed by Zabbal *et al.*<sup>126</sup> This method is based on a chaotic cavity transducer, as shown in Fig. 1.15(a), to generate plane waves of high amplitudes that will interact with the bonding. The measurement of the non-linear parameter  $\beta = A_2/A_1$ , with  $A_1$  ( $A_2$ ) the maximum amplitude of the fundamental (second harmonic), has allowed to detect bonding defects, as illustrated in Fig. 1.15(b).

### Non-collinear wave mixing

The non-collinear wave mixing is another non-linear technique than those previously discussed (generation of harmonics, second harmonic imaging). The objective is to make two non-collinear waves of different frequencies interact in a medium with non-linear mechanical properties where the superposition law does not apply. Thus, a third wave

resulting from this interaction will be scattered. The non-collinear wave mixing has been studied by Zhang *et al.*,<sup>127</sup> see Fig. 1.16. They modeled analytically and numerically the interaction of two shear waves at an imperfect interface that allowed a longitudinal wave to scatter in a certain direction. As Escobar-Ruiz *et al.*<sup>128</sup> pointed out, several advantages exist. First of all, there is spectral separation because the frequencies of the two incident waves and the scattered wave are different. In addition, the polarizations of the incident and scattered waves are not the same, which ensures a mode separation. Then, there is spatial separation because the interaction between the two incident waves is limited to a particular area and the scattered wave propagates in a different direction from the two incident waves. However, Zhang *et al.*<sup>127</sup> specified that the mixing of non-collinear waves can be sensitive to interface imperfections but also to non-linearities in the bulk of the adhesive. Croxford *et al.*<sup>129</sup> used this technique to detect non-linearities in a material (here an aluminum alloy) caused by plastic deformation or fatigue defects. Blanloeuil, in his PhD thesis,<sup>130</sup> simulated by finite elements the mixing of non-collinear waves at: a contact interface between two solids (pp. 111–124) and a closed crack (pp. 125–135). His numerical work has clearly demonstrated the generation of a longitudinal wave when two shear waves interact at oblique incidence in a zone with non-linear mechanical properties. Demčenko *et al.*<sup>131</sup> detected kissing bond between two PVC sheets ( $228 \times 72.5 \times 25 \text{ mm}^3$ ) held in contact with each other. The experiment was carried out in immersion with a longitudinal wave and a transverse wave in oblique incidence on one side of the assembly to be controlled. The longitudinal wave scattered on the other side was then measured to detect this interface defect. In 2017, Ju *et al.*<sup>132</sup> developed a non-collinear wave-mixing technique to monitor the degradation of a bonded joint between two aluminum blocks. The method required access to only one surface of the bonded joint. In addition, the method was performed with piezoelectric transducers in contact with one of the aluminum surfaces. A longitudinal wave (5 MHz) and a shear wave (3.5 MHz) interacted in the adhesive layer to generate a shear wave which was then detected. Experimental measurements were performed on bonded assemblies for different levels of thermal aging (oven drying of the bonded assemblies at a constant temperature of 170°C and variable exposure time ranging from 0 to 10 hours). The use of this non-collinear wave mixing technique allowed to follow the evolution of the degradation of the adhesive joint. However, it seems that the method detailed in the article of Ju *et al.* did not distinguish between disbonding defects, interface defects (kissing bond, weak adhesive bond) and cohesive defects within the adhesive.

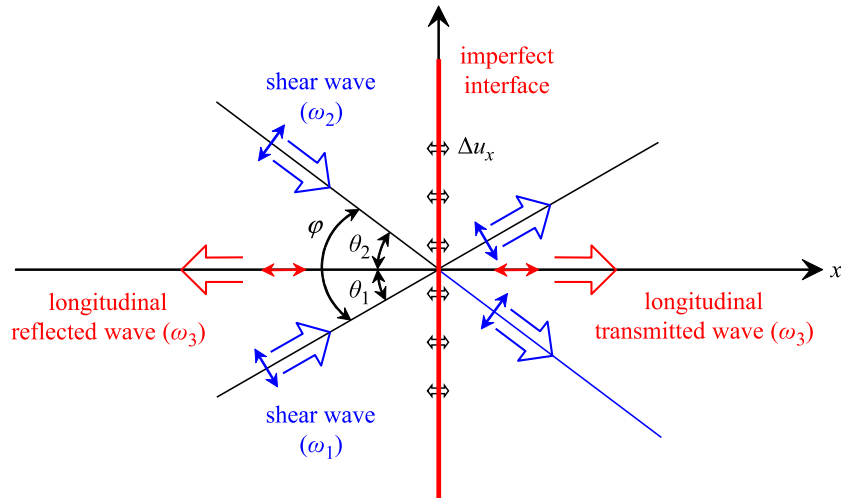


Figure 1.16 – Schematic from Zhang *et al.*<sup>127</sup> on the non-collinear wave mixing at an imperfect interface.

To conclude this first part on non-linear ultrasonic methods, harmonic generation seems to be an interesting technique for the NDE of bonded assemblies. However, it is difficult to separate the non-linearities generated by the assembly itself (generation, signal amplification, etc.) from the non-linearities generated by an imperfect bonding interface. Concerning second harmonic imaging techniques, these have been used in particular to visualize closed cracks in solid medium. Finally, the non-collinear wave mixing admits many advantages compared to the generation of harmonics. Indeed, as previously mentioned, this technique allows spectral, modal and spatial separation because the objective is to make two non-collinear waves (of different frequencies) interact in a medium with non-linear mechanical properties; where the superposition principle does not apply. Thus, a third wave resulting from this interaction will be scattered. This non-linear method can therefore be potentially interesting for the NDE of bonded assemblies. The second part concerning non-linear ultrasonic methods of bonded assemblies now focuses on heat flow modulation techniques and phase modulation methods (addition of a low-frequency excitation).

### Heat flux modulation and phase modulation

The non-linear method that is discussed in this part is the heat flow modulation. This technique was used by Mezil<sup>133,134</sup> to detect cracks in a glass plate. As can be seen in Fig. 1.17, two laser beams were focused at the same location on the crack. One of the

### 1.3. Ultrasonic nondestructive evaluation methods for bonded structures

beams was amplitude modulated at a rather low-frequency  $f_L$  ( $\sim$  Hz) to allow the crack to open and close successively. A second laser beam was amplitude modulated at a higher frequency  $f_H$  ( $\sim$  kHz) to generate ultrasonic waves. The fact that the crack opened and closed regularly resulted in the frequency modulation of the reflected and transmitted waves on either side of the crack. This allowed the crack to be detected. This non-linear heat flow modulation technique was therefore relevant for this type of application. However, the use of this method to evaluate bonded assemblies remains to be studied.

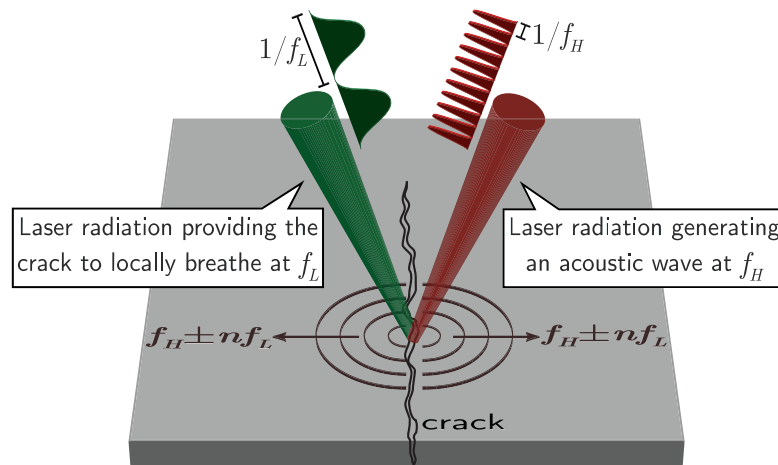


Figure 1.17 – Diagram of the principle of the heat flux modulation taken from the PhD thesis of Mezil.<sup>133</sup>

The second non-linear method using a modulation is about the phase modulation. This technique consists of performing an ultrasonic measurement at high-frequency by adding a low-frequency modulation. The interaction between these two waves of different frequencies can be used to detect defects that are difficult to observe with linear NDE methods. Scientific work has been carried out with this non-linear technique to detect cracks (Donksoy and Sutin<sup>135</sup>) but also bonding defects. Goursolle, in his PhD thesis,<sup>136</sup> studied phase modulation on two aluminum blocks, 20 mm and 8 mm-thick, bonded together with a 0.5 mm-thick layer of epoxy. The interaction between a high-frequency wave ( $\sim$  15 MHz) and a low-frequency wave ( $\sim$  2 MHz) was used to measure the  $\beta$  non-linearity coefficient of the assembled materials (see Fig. 1.18). The measurements were performed on a healthy and degraded bonded structures. Goursolle's objective was not to quantify the mechanical strength of the bonded assembly but to determine the overall non-linearity coefficient of the aluminum substrate. He noted that for a healthy bond, the good transmission of the low-frequency wave from one aluminum block to the other

allowed a better determination of the  $\beta$  coefficient than when the bond was of poorer quality. Rokhlin *et al.*<sup>137</sup> have studied aluminum/epoxy/aluminum bonded assemblies with different levels of degradation. The picture of the experimental assembly is shown in Fig. 1.19. Ultrasonic measurements were performed in contact with the structure and in reflection (normal and oblique incidence) at 10 MHz. The low-frequency modulation ( $\sim 50$  Hz) was carried out by a shaker firmly fixed on one of the substrates of the bonded assembly. The results obtained are shown in Fig. 1.19. The solid lines represent the spectra obtained for measurements at normal incidence and the dashed lines for those at oblique incidence. The amplitudes of the frequency modulation index increased as the bonded structure became more and more degraded. Rokhlin *et al.*<sup>137</sup> concluded that this method can detect the degradation of adhesive bonding. However, few indications on the nature of these degradations are explained in the article. This method remains qualitative and has not been used to quantify the mechanical strength of bonded assemblies.

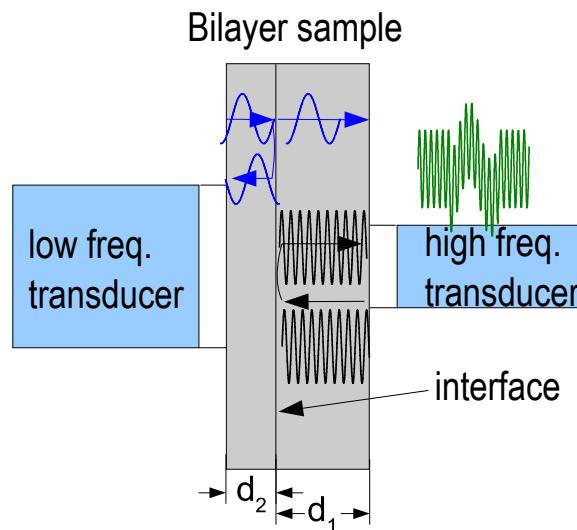


Figure 1.18 – Diagram of the principle used by Goursolle<sup>136</sup> to measure the coefficient of non-linearity of bonded samples using phase modulation. Fig. taken from Ref. 136 (translated from French to English).

The non-linear methods of heat flow modulation and phase modulation have been presented. These scientific studies, whose applications have not always been oriented towards the evaluation of bonded assemblies, are interesting non-linear methods for the NDE of bonded structures.

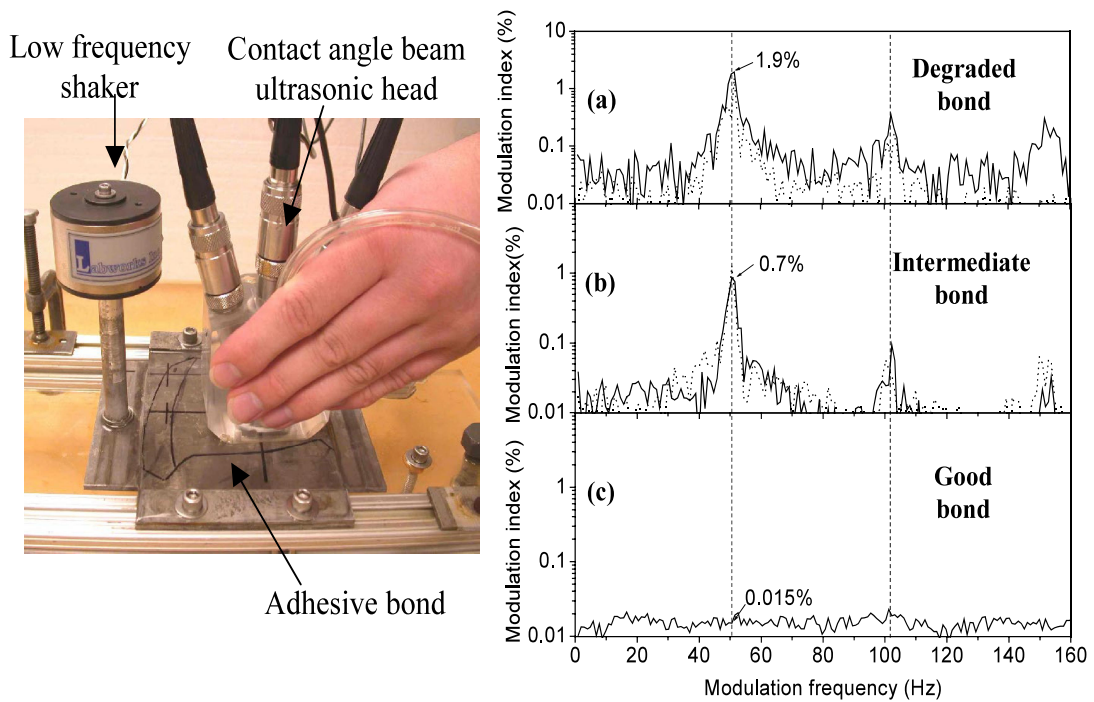


Figure 1.19 – Extract from Rokhlin *et al.*:<sup>137</sup> picture of the experimental set-up (left) and results obtained (right) for different degradations of the bonded samples.

## 1.4 Conclusion

Adhesive bonding, rather than riveting or welding, makes it possible to lighten aeronautical structures. This weight saving leads to a reduction in engine fuel consumption and greenhouse gas emissions. Nevertheless, the fact that there is a lack of nondestructive methods to certify the mechanical strength of bonded aeronautical assemblies raises safety issues. This is why it is essential to develop nondestructive techniques for testing and evaluating bonded assemblies. First of all, the objective of this bibliographical study was to define the terminology used concerning bonded assemblies. The distinction between the terms *adhesion* and *adherence* (or *practical adhesion*) was introduced. Then, the bonding defects (disbond, cohesive defect, adhesive defect) as well as the failures generated (cohesive, adhesive, mixed) were presented. Next, an overview of destructive (tensile tests, shear tests, etc.) and nondestructive methods (infrared thermography, laser shock, etc.) was provided. The *Laser Adhesion Test* (LASAT) seems promising for quantifying the mechanical strength of bonded assemblies.<sup>67</sup> It remains to ensure that the

latter evaluation methods is nondestructive, i.e., that the propagation of the shock wave does not damage the substrates and the adhesive. The second part of this literature review focused on linear and non-linear ultrasonic NDE methods. The linear methods were classified according to the type of waves used: bulk waves or guided waves. The studies of Siryabe *et al.*<sup>81</sup> with bulk waves or Mezil *et al.*<sup>112</sup> with guided waves (ZGV resonances) were notably detailed. Finally, the last part dealt with NDE methods using non-linear ultrasound. Several methods of the literature were introduced, e.g., harmonic generation, second harmonic imaging, non-collinear wave mixing, heat flux modulation, phase modulation. This literature review was an opportunity to study numerous scientific works concerning the NDE of bonded assemblies. It also helps realizing the truly large number of articles written on this topic as well as the numerous methods developed to non-destructively evaluate bonded structures.

Before presenting, in the chapters 3 and 4, the two methods based on laser ultrasonic experiments and developed during this PhD work to non-destructively evaluate bonded structures, the next chapter presents the derivation of a semi-analytic resolution of the laser-based generation of ultrasounds in a multilayer structure accounting for optical, thermal and mechanical coupling conditions. Not only this semi-analytic simulation method is the key to the NDE method in Chap. 3, but it is intended to be general enough to be used for many different cases of assembly, as it is demonstrated next.

## Chapter 2

# Semi-analytic simulations of laser-generated ultrasounds in a multilayer structure

### Contents

---

2.1	Introduction . . . . .	43
2.2	Geometry and assumptions . . . . .	44
2.3	Electromagnetic problem . . . . .	46
2.3.1	Formulation of the electromagnetic problem . . . . .	46
2.3.2	Propagation of the electromagnetic waves in the multilayer structure . . . . .	47
2.3.3	Determination of the power density $Q$ . . . . .	49
2.4	Heat diffusion problem . . . . .	50
2.4.1	Homogeneous solutions of the heat equation . . . . .	52
2.4.2	Particular solutions of the heat equation . . . . .	53
2.4.3	Application of the boundary conditions . . . . .	54
2.5	Elastodynamic problem . . . . .	56
2.5.1	Homogeneous solutions of the elastodynamic equations . . . . .	57
2.5.2	Particular solutions of the elastodynamic equations . . . . .	59
2.5.3	Application of the boundary conditions . . . . .	59
2.6	Numerical simulation results . . . . .	61
2.6.1	Analysis of the guided elastic waves in an aluminum alloy plate . . . . .	62
2.6.2	Bilayer/trilayer with interfacial stiffnesses . . . . .	63
2.6.3	Bilayer with the heat source at the interface . . . . .	65
2.7	Conclusion . . . . .	65

---

## Abstract

Laser-generated elastic waves, of great interest for the nondestructive evaluation (NDE) of material and mechanical structures, have been the subject of numerous experimental, theoretical and numerical studies to describe the opto-acoustic generation process, involving electromagnetic, thermal and elastic fields and their couplings in matter. Among the numerical methods for solving this multiphysical problem, the semi-analytic approach is one of the most relevant for obtaining fast and accurate results, when analytic solutions exist. In this chapter, a multilayer model is proposed to successively solve electromagnetic, thermal and elastodynamic problems. The optical penetration of the laser line source, as well as thermal conduction and convection, are accounted for. Optical, thermal and mechanical coupling conditions are considered between the upper and lower media of the multilayer. The simulation of laser-generated ultrasounds in multilayer structures (presented in this chapter) is of interest for the development of nondestructive evaluation methods of complex structures, such as bonded assemblies in aeronautics (as discussed in Chap. 3).

---

This work was submitted to the *J. Acoust. Soc. Am.*:

R. Hodé, M. Ducouso, N. Cuvillier, V. Gusev, V. Tournat and S. Raetz, “Laser ultrasonics in a multilayer structure: Semi-analytic model and simulated examples,” *J. Acoust. Soc. Am.* (submitted on December 11, 2020).

## 2.1 Introduction

Laser-generated ultrasounds are of great interest for the nondestructive evaluation (NDE) of material and mechanical structures. In aeronautics, the non-contact feature of this laser inspection is a significant advantage over more conventional techniques such as piezoelectric transducers with coupling agent. Furthermore, the opto-acoustic generation in the thermoelastic regime<sup>138,139</sup> ensures the integrity of the structure after the laser pulse impact. In the literature, laser-generated elastic waves<sup>140</sup> in metals were experimentally observed in the thermoelastic regime by Scruby *et al.*<sup>141</sup> Then, the theoretical basis was formulated by Rose,<sup>142</sup> where the thermoelastic generation at the surface of a half-space was represented by a point-source, called the surface center of expansion (SCOE) by the author.

Following this seminal work, simulations of laser-generated ultrasounds in elastic media have been carried out using analytic or semi-analytic approaches. Dubois *et al.*<sup>143</sup> reported an analytic one-dimensional model taking the optical penetration effect into account. Coulette *et al.*<sup>144</sup> simulated elastic waves propagation in a bilayer of cylindrical symmetry with a semi-analytic model. The structure was composed of two orthotropic and homogeneous plates which were perfectly coupled [continuity of displacements and elastic forces (stresses) at the interface between the two media]. The optical reflection at the interface and the thermal diffusion were neglected in their numerical calculations. Murray *et al.*<sup>145</sup> used a similar approach based on the Hankel and Laplace transforms to simulate elastic waves propagating in an isotropic plate perfectly coupled to a semi-infinite medium. Cheng *et al.*<sup>146</sup> extended the work of Murray *et al.*<sup>145</sup> to isotropic layered plates, using the transfer matrix method.<sup>147</sup> The structure was illuminated by an axisymmetric laser source, but the optical penetration and the thermal diffusion were not considered. Audoin and Guilbaud,<sup>148</sup> Meri,<sup>149</sup> Perton,<sup>150</sup> and Raetz<sup>151</sup> gradually developed a semi-analytic model, based on the Fourier transform, to simulate acoustic waves generated by a laser line source. Specifically, Perton<sup>150</sup> modeled a bilayer structure composed of two orthotropic, homogeneous and viscoelastic plates perfectly coupled, with the plane strain hypothesis. The transmission of electromagnetic waves in the two media were considered, but reflections at the interface and the rear surface of the bilayer were neglected. Thermal conduction was also accounted for by considering three thermal waves: two propagating in the first medium and only one in the second (reflections at the rear surface were neglected).

Other numerical approaches such as finite element<sup>152,153</sup> or finite difference methods<sup>154</sup>

have also been used to simulate laser-generated ultrasounds in the thermoelastic regime. These numerical methods are well suited for the simulation of elastic waves in media with complex geometry. However, they require more computing power than semi-analytic calculations. This can be a drawback when numerous simulations have to be performed for inverse problem solving, for instance. Hence, when analytic solutions can be found for wave propagation in media with simple geometry, the semi-analytic approach is the most appropriate choice to obtain accurate results quickly.

In this chapter, a semi-analytic model is described where electromagnetic (Sec. 2.3), thermal (Sec. 2.4) and elastodynamic (Sec. 2.5) problems are successively solved to obtain the displacement field in the upper and lower media of a multilayer structure. The geometry and the main assumptions about the optical, thermal and mechanical properties of the layers are detailed in Sec. 2.2. Numerical results are presented in Sec. 2.6 to give examples of simulations that can be performed with this semi-analytic model.

## 2.2 Geometry and assumptions

The geometry of the multilayer structure is illustrated in Fig. 2.1. The multilayer is composed of two solid media I and II of thicknesses  $h_1$  and  $h_2$ , respectively, and two semi-infinite media (0 and III) which are assumed to be air. The origin of the Cartesian coordinate system ( $O$ ,  $\mathbf{x}_1$ ,  $\mathbf{x}_2$ ) is located at the upper-surface of the medium I. Note that in the previous definition of the coordinate system and for the remainder, a bold letter stands for a vector. The layers are considered to be of infinite dimension in the  $\mathbf{x}_2$ - and  $\mathbf{x}_3$ -directions. The incident tilted laser line source is oriented along the  $\mathbf{x}_3$ -direction. Thus, the electromagnetic, thermal and mechanical problems are solved in 2D. Sublayers, with a total thickness of  $\Delta h$ , can be inserted between media I and II and are denoted by the uppercase letter “EM” in Fig. 2.1 for the electromagnetic problem, by “T” in Fig. 2.2 for the thermal problem and by “M” in Fig. 2.3 for the mechanical problem. These sublayers will be taken into account later in the coupling conditions between media I and II. The main assumptions made for the optical, thermal and mechanical properties of the layers are introduced below.

In Sec. 2.3, all layers are assumed electromagnetically linear, isotropic and homogeneous. This means that the dielectric constant  $\varepsilon$  and magnetic permeability  $\mu$  are scalar quantities and not position-dependent. The materials constituting the layers should therefore not be birefringent, or at least have a negligible birefringence. These constants are also assumed to be independent of the temperature but related to the angular frequency  $\omega_0$

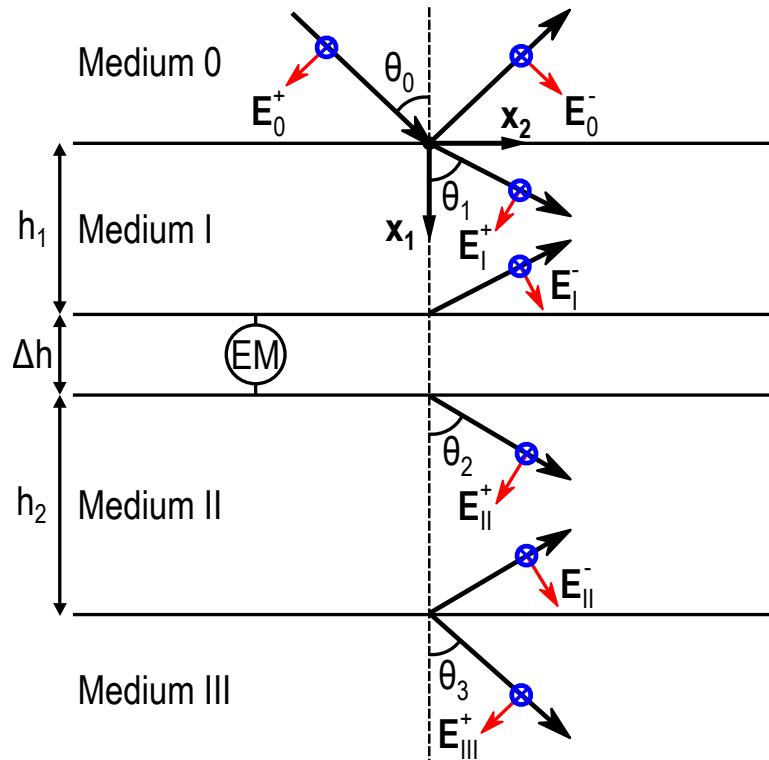


Figure 2.1 – The geometry of the multilayer structure is represented with the two semi-infinite media (0 and III) and the media I and II of thicknesses  $h_1$  and  $h_2$ , respectively. The uppercase letter “EM” symbolizes the sublayers, with a total thickness of  $\Delta h$ , that can be inserted between media I and II. The black arrows represent the  $\mathbf{k}$ -wave vectors and the red (blue) arrows indicate the electric vectors  $\mathbf{E}$  (magnetic vectors  $\mathbf{H}$ ).

of the assumed monochromatic electromagnetic field. Moreover, the electric and magnetic polarization fields are not taken into account. In addition, the electric charge density  $\rho_q$  is supposed to be zero. This is a valid assumption, especially for metals, because  $\rho_q$  decays exponentially with time (relaxation time of the order of  $10^{-18}$  s, see p. 736 of Ref. 155). This hypothesis implies that the divergence of the electric displacement is zero,  $\nabla \cdot \mathbf{D} = 0$ , as is the convection current density:  $\mathbf{j}_v = \mathbf{0}$ .

In Sec. 2.4, the thermal properties of the solid media are assumed linear, homogeneous and orthotropic, with  $\mathbf{x}_1$  and  $\mathbf{x}_2$  as principal axes. Thermal conduction in the solid layers and convection phenomena at the upper surface of medium I (at  $x_1 = 0$ ) and the lower surface of medium II (at  $x_1 = H$  with  $H = h_1 + \Delta h + h_2$ ) are considered.

In Sec. 2.5, the mechanical properties of solid media are assumed linear, homogeneous, viscoelastic and orthotropic, with  $\mathbf{x}_1$  and  $\mathbf{x}_2$  as principal axes. Elastic waves propagating in semi-infinite media (0 and III) are neglected. Furthermore, the plane strain hypothesis is used ( $\frac{\partial}{\partial x_3} = 0$ ) because the layers and the laser line source are considered to be of infinite dimension in the  $\mathbf{x}_3$ -direction.

## 2.3 Electromagnetic problem

In this section, the method for solving the electromagnetic problem in the multilayer structure, represented in Fig. 2.1, is detailed. Our work focuses on the simulation of laser-ultrasonic experiments performed in the thermoelastic regime. Thus, the aim is to obtain the power density  $Q$  of the energy dissipated into heat in the different media, following the approach of Born and Wolf.<sup>155</sup> The power density  $Q$  will then be used as the source term for the heat equation defined in Sec. 2.4.

### 2.3.1 Formulation of the electromagnetic problem

Under the assumptions presented in Sec. 2.2, and using the Maxwell's equations, the electric vector  $\mathbf{E}$  in the multilayer structure must satisfy the Helmholtz equation

$$\nabla^2 \mathbf{E} + k^2 \mathbf{E} = 0, \quad (2.1)$$

with the complex wavenumber

$$k = k' + jk'', \quad k' = \Re\left(\frac{\omega_0}{c_0} n\right) \text{ and } k'' = \Im\left(\frac{\omega_0}{c_0} n\right). \quad (2.2)$$

### 2.3. Electromagnetic problem

---

In Eq. (2.2), the constant  $c_0$  is equal to the speed of light in vacuum,  $j$  is the imaginary number, the  $\Re$  ( $\Im$ ) symbol corresponds to the real (imaginary) part and  $n$  is the complex refractive index defined by the relation

$$n = n' + jn'', \quad n' = \Re(n) \text{ and } n'' = \Im(n). \quad (2.3)$$

In the literature,  $n''$  is often called the extinction coefficient<sup>156</sup> or the attenuation index.<sup>155</sup> The complex refractive index  $n$  is also equal to

$$n = \sqrt{\mu\varepsilon_c} = \sqrt{\mu \left( \varepsilon + j \frac{4\pi\sigma}{\omega_0} \right)}, \quad (2.4)$$

with  $\varepsilon_c$  the complex dielectric constant,  $\varepsilon$  the dielectric constant,  $\mu$  the magnetic permeability and  $\sigma$  the optical conductivity.

#### 2.3.2 Propagation of the electromagnetic waves in the multilayer structure

In Fig. 2.1, a plane electromagnetic wave is incident on the medium I with an angle of incidence equal to  $\theta_0$ . The incident electromagnetic wave is linearly polarized and the electric vector  $\mathbf{E}_0^+$  is in the plane  $(\mathbf{x}_1, \mathbf{x}_2)$ . This implies that the magnetic vector  $\mathbf{H}_0^+$  is in the  $\mathbf{x}_3$ -direction [case of transverse magnetic (TM) waves]. Using Snell's laws, the electromagnetic waves that are reflected and transmitted in the different layers can be defined, as illustrated in Fig. 2.1. The analytic expressions of the electric vectors, in the different media at a point of vector position  $\mathbf{x}$ , are

$$\mathbf{E}_0 = \mathbf{E}_0^+ e^{-j(\omega_0 t - \mathbf{k}_0^+ \cdot \mathbf{x})} + \mathbf{E}_0^- e^{-j(\omega_0 t - \mathbf{k}_0^- \cdot \mathbf{x})}, \quad (2.5a)$$

$$\mathbf{E}_I = \mathbf{E}_I^+ e^{-j(\omega_0 t - \mathbf{k}_I^+ \cdot \mathbf{x})} + \mathbf{E}_I^- e^{-j(\omega_0 t - \mathbf{k}_I^- \cdot \mathbf{x})}, \quad (2.5b)$$

$$\mathbf{E}_{II} = \mathbf{E}_{II}^+ e^{-j(\omega_0 t - \mathbf{k}_{II}^+ \cdot \mathbf{x})} + \mathbf{E}_{II}^- e^{-j(\omega_0 t - \mathbf{k}_{II}^- \cdot \mathbf{x})}, \quad (2.5c)$$

$$\mathbf{E}_{III} = \mathbf{E}_{III}^+ e^{-j(\omega_0 t - \mathbf{k}_{III}^+ \cdot \mathbf{x})}. \quad (2.5d)$$

with

$$\mathbf{E}_0^+ = E_0^+ \begin{bmatrix} \sin \theta_0 \\ -\cos \theta_0 \end{bmatrix}, \quad \mathbf{k}_0^+ = k_0 \begin{bmatrix} \cos \theta_0 \\ \sin \theta_0 \end{bmatrix}, \quad \mathbf{E}_0^- = E_0^- \begin{bmatrix} \sin \theta_0 \\ \cos \theta_0 \end{bmatrix}, \quad \mathbf{k}_0^- = k_0 \begin{bmatrix} -\cos \theta_0 \\ \sin \theta_0 \end{bmatrix},$$

$$\begin{aligned}
 \mathbf{E}_I^+ &= E_I^+ \begin{bmatrix} \sin \theta_1 \\ -\cos \theta_1 \end{bmatrix}, \quad \mathbf{k}_I^+ = k_I \begin{bmatrix} \cos \theta_1 \\ \sin \theta_1 \end{bmatrix}, \quad \mathbf{E}_I^- = E_I^- \begin{bmatrix} \sin \theta_1 \\ \cos \theta_1 \end{bmatrix}, \quad \mathbf{k}_I^- = k_I \begin{bmatrix} -\cos \theta_1 \\ \sin \theta_1 \end{bmatrix}, \\
 \mathbf{E}_{II}^+ &= E_{II}^+ \begin{bmatrix} \sin \theta_2 \\ -\cos \theta_2 \end{bmatrix}, \quad \mathbf{k}_{II}^+ = k_{II} \begin{bmatrix} \cos \theta_2 \\ \sin \theta_2 \end{bmatrix}, \quad \mathbf{E}_{II}^- = E_{II}^- \begin{bmatrix} \sin \theta_2 \\ \cos \theta_2 \end{bmatrix}, \quad \mathbf{k}_{II}^- = k_{II} \begin{bmatrix} -\cos \theta_2 \\ \sin \theta_2 \end{bmatrix}, \\
 \mathbf{E}_{III}^+ &= E_{III}^+ \begin{bmatrix} \sin \theta_3 \\ -\cos \theta_3 \end{bmatrix}, \quad \mathbf{k}_{III}^+ = k_{III} \begin{bmatrix} \cos \theta_3 \\ \sin \theta_3 \end{bmatrix}.
 \end{aligned} \tag{2.6}$$

The analytic expressions of the magnetic vectors are obtained using the relation

$$\mathbf{H} = \sqrt{\frac{\varepsilon_c}{\mu}} \mathbf{s} \times \mathbf{E}, \quad \text{with } \mathbf{s} = \frac{\mathbf{k}}{\|\mathbf{k}\|}. \tag{2.7}$$

Thus, the magnetic vectors in the different media, with  $i = \{0, I, II\}$ , are equal to

$$\mathbf{H}_i = -n_i/\mu_i (E_i^+ e^{j\mathbf{k}_i^+ \cdot \mathbf{x}} + E_i^- e^{j\mathbf{k}_i^- \cdot \mathbf{x}}) e^{-j\omega_0 t} \mathbf{x}_3, \tag{2.8a}$$

$$\mathbf{H}_{III} = -n_{III}/\mu_{III} E_{III}^+ e^{-j(\omega_0 t - \mathbf{k}_{III}^+ \cdot \mathbf{x})} \mathbf{x}_3. \tag{2.8b}$$

To determine the amplitudes  $E_0^-$ ,  $E_I^+$ ,  $E_I^-$ ,  $E_{II}^+$ ,  $E_{II}^-$  and  $E_{III}^+$ , six boundary conditions are applied, ensuring the continuity of the projected electric field along the  $\mathbf{x}_2$ -axis and the projected magnetic field along the  $\mathbf{x}_3$ -axis at each interfaces between the different media. At  $x_1 = 0$  and  $x_1 = H$ , these boundary conditions lead to the writing of Eqs. (2.9a, 2.9b, 2.9d, 2.9e). Between media I and II, the boundary conditions are expressed in Eq. (2.9c), using the transfer matrix method (pp. 26–60 in Ref. 157). This transfer matrix  $[L^{EM}]$ , defined in Appendix A.1.4, takes into account the propagation of electromagnetic waves in the sublayers located between media I and II.

$$\mathbf{E}_0|_{x_1=0} \cdot \mathbf{x}_2 = \mathbf{E}_I|_{x_1=0} \cdot \mathbf{x}_2, \tag{2.9a}$$

$$\mathbf{H}_0|_{x_1=0} \cdot \mathbf{x}_3 = \mathbf{H}_I|_{x_1=0} \cdot \mathbf{x}_3, \tag{2.9b}$$

$$\begin{bmatrix} \mathbf{E}_I \cdot \mathbf{x}_2 \\ \mathbf{H}_I \cdot \mathbf{x}_3 \end{bmatrix}_{x_1=h_1} = [L^{EM}]_{2 \times 2} \begin{bmatrix} \mathbf{E}_{II} \cdot \mathbf{x}_2 \\ \mathbf{H}_{II} \cdot \mathbf{x}_3 \end{bmatrix}_{x_1=h_1+\Delta h}, \tag{2.9c}$$

$$\mathbf{E}_{II}|_{x_1=H} \cdot \mathbf{x}_2 = \mathbf{E}_{III}|_{x_1=H} \cdot \mathbf{x}_2, \tag{2.9d}$$

$$\mathbf{H}_{II}|_{x_1=H} \cdot \mathbf{x}_3 = \mathbf{H}_{III}|_{x_1=H} \cdot \mathbf{x}_3. \tag{2.9e}$$

Using the Eqs. (2.5a–2.5d) and Eqs. (2.8a, 2.8b) in the calculation of the boundary conditions [Eqs. (2.9a–2.9e)], it follows that the linear system to solve in order to determine

### 2.3. Electromagnetic problem

---

the ratio of the amplitudes of the reflected/transmitted electromagnetic waves to the amplitude of the incident electromagnetic wave is

$$\begin{bmatrix} A_{11}^E & A_{12}^E & A_{13}^E & 0 & 0 & 0 \\ A_{21}^E & A_{22}^E & A_{23}^E & 0 & 0 & 0 \\ 0 & A_{32}^E & A_{33}^E & A_{34}^E & A_{35}^E & 0 \\ 0 & A_{42}^E & A_{43}^E & A_{44}^E & A_{45}^E & 0 \\ 0 & 0 & 0 & A_{54}^E & A_{55}^E & A_{56}^E \\ 0 & 0 & 0 & A_{64}^E & A_{65}^E & A_{66}^E \end{bmatrix} \begin{bmatrix} R_0^- \\ R_1^+ \\ R_1^- \\ R_{II}^+ \\ R_{II}^- \\ R_{III}^+ \end{bmatrix} = \begin{bmatrix} \cos \theta_0 \\ -n_0/\mu_0 \\ 0 \\ 0 \\ 0 \\ 0 \end{bmatrix}. \quad (2.10)$$

In order to obtain a well-conditioned matrix, where the coefficients  $A_{ij}^E$  are detailed in Appendix A.1.2, the unknowns of Eq. (2.10) are written as

$$\begin{aligned} R_0^- &= \frac{E_0^-}{E_0^+}, R_1^+ = \frac{E_1^+}{E_0^+}, R_1^- = \frac{E_1^-}{E_0^+} e^{\beta_I(\theta_1) \frac{h_1}{2}}, \\ R_{II}^+ &= \frac{E_{II}^+}{E_0^+} e^{-\beta_{II}(\theta_2) \frac{h_1 + \Delta h}{2}}, R_{II}^- = \frac{E_{II}^-}{E_0^+} e^{\beta_{II}(\theta_2) \frac{h}{2}}, R_{III}^+ = \frac{E_{III}^+}{E_0^+}, \end{aligned} \quad (2.11)$$

with the inverse expressions of the optical penetrations which are equal to<sup>158</sup>

$$\beta_I(\theta_1) = 2 [k_1' \Im(\cos \theta_1) + k_1'' \Re(\cos \theta_1)], \quad (2.12a)$$

$$\beta_{II}(\theta_2) = 2 [k_{II}' \Im(\cos \theta_2) + k_{II}'' \Re(\cos \theta_2)]. \quad (2.12b)$$

The amplitudes of the electromagnetic waves are now determined and will be used to obtain the power density  $Q$  of the energy dissipated into heat in the media.

#### 2.3.3 Determination of the power density $Q$

The power density  $Q$  is obtained by applying the Poynting theorem and by assuming that the convection current density  $\mathbf{j}_v$  is equal to zero (see the hypothesis formulated Sec. 2.2). Therefore,

$$Q = -\nabla \cdot \langle \mathbf{S} \rangle, \quad (2.13)$$

with the time average of the Poynting vector

$$\langle \mathbf{S} \rangle = \frac{c_0}{8\pi} \Re(\mathbf{E} \times \overline{\mathbf{H}}). \quad (2.14)$$

In Eq. (2.14),  $\overline{\mathbf{H}}$  is the conjugate of the magnetic vector  $\mathbf{H}$ . Finally, using the Eqs. (2.5a–2.5d) and Eqs. (2.8a, 2.8b), the expressions of the power density  $Q$  in media I and II are

$$Q_{\text{I}}(x_1) = I_0 \Lambda_{\text{I}}(\theta_1) [ |R_{\text{I}}^+|^2 e^{-\beta_{\text{I}}(\theta_1)x_1} + |R_{\text{I}}^-|^2 e^{\beta_{\text{I}}(\theta_1)(x_1-h_1)} ], \quad (2.15a)$$

$$Q_{\text{II}}(x_1) = I_0 \Lambda_{\text{II}}(\theta_2) [ |R_{\text{II}}^+|^2 e^{-\beta_{\text{II}}(\theta_2)[x_1-(h_1+\Delta h)]} + |R_{\text{II}}^-|^2 e^{\beta_{\text{II}}(\theta_2)(x_1-H)} ], \quad (2.15b)$$

with  $I_0 = c_0 |E_0^+|^2 / (8\pi)$  the intensity of the incident electromagnetic wave and

$$\Lambda_{\text{I}}(\theta_1) = \beta_{\text{I}}(\theta_1) \Re(\overline{n}_{\text{I}} \cos \theta_1) / \mu_{\text{I}}, \quad (2.16a)$$

$$\Lambda_{\text{II}}(\theta_2) = \beta_{\text{II}}(\theta_2) \Re(\overline{n}_{\text{II}} \cos \theta_2) / \mu_{\text{II}}, \quad (2.16b)$$

which, multiplied by the squared modulus of the ratio  $R_i^+$  ( $R_i^-$ ), stands for the intensity transmission (reflection) of an electromagnetic plane wave under oblique incidence. The power densities  $Q_{\text{I}}(x_1)$  and  $Q_{\text{II}}(x_1)$  will be used in Sec. 2.4 as the source terms for the heat equation.

## 2.4 Heat diffusion problem

The aim of this section is to determine the temperature fields in media I and II by considering heat conduction. Therefore, the heat equation to be solved is

$$\nabla \cdot (\underline{\lambda} \nabla T) + Q(x_1, x_2, t) = \rho c_p \frac{\partial T}{\partial t}, \quad (2.17)$$

with  $\underline{\lambda}$  the second-order tensor of thermal conductivity,  $T$  the temperature field,  $Q$  the power density defined in Sec. 2.3,  $\rho$  the density and  $c_p$  the specific heat. Note that here the power density  $Q$  depends on  $x_1$  and also on  $x_2$  to consider the lateral distribution of intensity of the incident laser line source.<sup>158</sup> Assuming that the media are homogeneous, the tensor of thermal conductivity in Eq. (2.17) is taken out of the divergence operator to obtain

#### 2.4. Heat diffusion problem

---

$$\underline{\lambda} \nabla^2 T + Q(x_1, x_2, t) = \rho c_p \frac{\partial T}{\partial t}. \quad (2.18)$$

In addition, each layer is assumed to be orthotropic, with  $\mathbf{x}_1$  and  $\mathbf{x}_2$  as principal axes, so the thermal conductivity tensor is written as a diagonal matrix

$$\underline{\lambda} = \begin{bmatrix} \lambda_{11} & 0 \\ 0 & \lambda_{22} \end{bmatrix}. \quad (2.19)$$

The heat equation will be solved in the Fourier domain by considering harmonic solutions. Therefore, Eq. (2.18) gives

$$D_{11} \frac{\partial^2 \hat{T}}{\partial x_1^2} - (j\omega + D_{22} k_2^2) \hat{T} = -\frac{1}{\rho c_p} \hat{Q}(x_1, k_2, \omega), \quad (2.20)$$

with thermal diffusivities  $D_{11} = \frac{\lambda_{11}}{\rho c_p}$  and  $D_{22} = \frac{\lambda_{22}}{\rho c_p}$ . The convention chosen for the double Fourier transform in space  $x_2$  and time  $t$  (denoted by the hat “ $\hat{\phantom{x}}$ ”) is given by

$$\hat{T}(x_1, k_2, \omega) = \frac{1}{2\pi} \iint_{-\infty}^{+\infty} T(x_1, x_2, t) e^{-j(\omega t - k_2 x_2)} dt dx_2. \quad (2.21)$$

The source term  $\hat{Q}(x_1, k_2, \omega)$ , expressed in the Fourier domain in Eq. (2.20), is equal to

$$\hat{Q}(x_1, k_2, \omega) = Q(x_1) F(\omega) G(x_1, k_2), \quad (2.22)$$

with  $Q(x_1)$  the power density determined in Sec. 2.3.  $F(\omega)$  and  $G(x_1, k_2)$  are the Fourier transforms of the pulse distributions in time and space,  $f(t)$  and  $g(x_1, x_2)$ , respectively. Their expressions are here considered to be

$$\begin{aligned} F(\omega) &= \frac{1}{\sqrt{2\pi}} \int_{-\infty}^{+\infty} f(t) e^{-j\omega t} dt \\ &= \frac{1}{\sqrt{2\pi}} e^{-\tau_p^2 \omega^2 / (16 \ln 2)}, \end{aligned} \quad (2.23a)$$

$$\begin{aligned} G(x_1, k_2) &= \frac{1}{\sqrt{2\pi}} \int_{-\infty}^{+\infty} g(x_1, x_2) e^{jk_2 x_2} dx_2 \\ &= \frac{1}{\sqrt{2\pi} \cos \theta} e^{-a_s^2 k_2^2 / (16 \ln 2 \cos^2 \theta)} e^{jk_2 x_1 \tan \theta}, \end{aligned} \quad (2.23b)$$

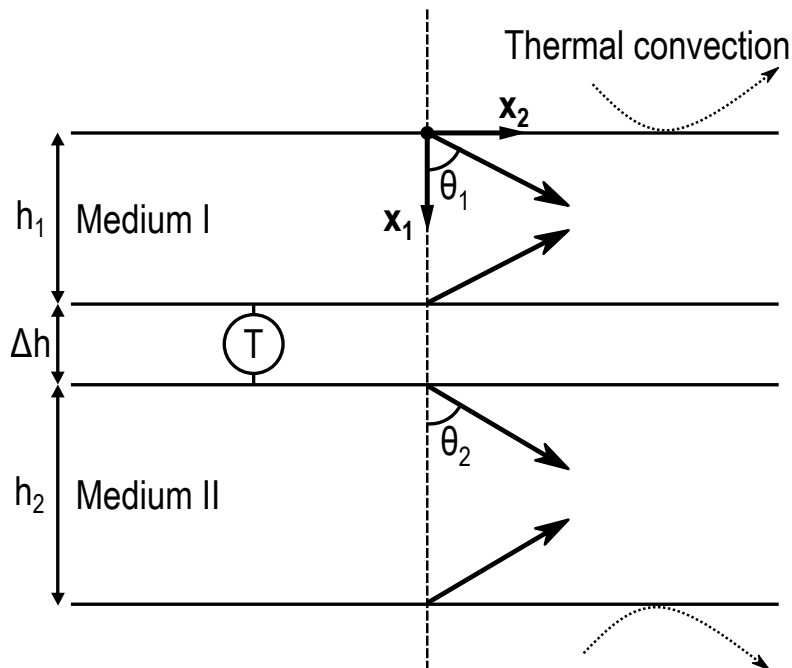


Figure 2.2 – Illustration of the multilayer structure used to solve the thermal diffusion problem. The uppercase letter “T” denotes the sublayers that can be inserted between media I and II. The black arrows represent the wave vectors of the thermal waves propagating in the  $\pm x_1$ -direction. The two dotted arrows indicate the thermal convection at the upper surface of medium I and the lower surface of medium II.

with  $\tau_p$  the pulse duration at half maximum (FWHM) of the Gaussian function  $f(t)$  and  $a_s$  the source width at half maximum (FWHM) of the tilted Gaussian beam mathematically represented by  $g(x_1, x_2)$ .<sup>158</sup> The angle  $\theta$  refers to the angle between the  $x_1$ -direction and the direction of refraction in the medium in which the heat diffusion problem is solved. Homogeneous and particular solutions are searched to solve Eq. (2.20) in media I and II and are detailed in the following.

### 2.4.1 Homogeneous solutions of the heat equation

In each layer  $i = \{I, II\}$ , homogeneous solutions  $\hat{T}_h^i$  of the heat equation, expressed without the source term  $-\frac{1}{\rho c_p} \hat{Q}^i(x_1, k_2, \omega)$  in Eq. (2.20), are sought in the form

$$\hat{T}_h^i(x_1, k_2, \omega) = \hat{T}_h^{i\pm}(k_2, \omega) e^{\pm \Gamma_1^i x_1}. \quad (2.24)$$

## 2.4. Heat diffusion problem

---

By injecting Eq. (2.24) into the homogeneous heat equation, we obtain

$$\left[ D_{11}^i \Gamma_1^{i2} - (j\omega + D_{22}^i k_2^2) \right] \hat{T}_h^{i\pm}(k_2, \omega) e^{\pm \Gamma_1^i x_1} = 0, \quad (2.25)$$

which results in

$$\Gamma_1^i = \sqrt{\frac{j\omega + D_{22}^i k_2^2}{D_{11}^i}}. \quad (2.26)$$

Therefore, the homogeneous solutions are the sum of two thermal waves that propagate in the  $\pm x_1$ -direction, as illustrated in Fig. 2.2 and given by

$$\hat{T}_h^i(x_1, k_2, \omega) = \hat{T}_h^{i+}(k_2, \omega) e^{-\Gamma_1^i x_1} + \hat{T}_h^{i-}(k_2, \omega) e^{\Gamma_1^i x_1}, \quad (2.27)$$

with the coefficients  $\hat{T}_h^{i+}(k_2, \omega)$  and  $\hat{T}_h^{i-}(k_2, \omega)$  to be determined later using the boundary conditions.

### 2.4.2 Particular solutions of the heat equation

Particular solutions  $\hat{T}_p^i$  are searched in the form of the source terms specified in Eqs. (2.15a, 2.15b) for media I and II, which gives

$$\begin{aligned} \hat{T}_p^{\text{I}}(x_1, k_2, \omega) &= \hat{T}_p^{\text{I}+}(k_2, \omega) e^{-\beta_1(\theta_1)x_1} e^{jk_2 \tan \theta_1 x_1} \\ &\quad + \hat{T}_p^{\text{I}-}(k_2, \omega) e^{\beta_1(\theta_1)(x_1-h_1)} e^{-jk_2 \tan \theta_1 x_1}, \end{aligned} \quad (2.28a)$$

$$\begin{aligned} \hat{T}_p^{\text{II}}(x_1, k_2, \omega) &= \hat{T}_p^{\text{II}+}(k_2, \omega) e^{-\beta_{\text{II}}(\theta_2)[x_1-(h_1+\Delta h)]} e^{jk_2 \tan \theta_2 x_1} \\ &\quad + \hat{T}_p^{\text{II}-}(k_2, \omega) e^{\beta_{\text{II}}(\theta_2)(x_1-H)} e^{-jk_2 \tan \theta_2 x_1}. \end{aligned} \quad (2.28b)$$

Then, Eqs. (2.28a, 2.28b) are fed into the heat equation (2.20) to obtain the four coefficients

$$\hat{T}_p^{i+} = -\frac{\hat{Q}_i^+}{\rho^i c_p^i} \left[ D_{11}^i [\beta_i(\theta_i) - jk_2 \tan \theta_i]^2 - (j\omega + D_{22}^i k_2^2) \right]^{-1}, \quad (2.29a)$$

$$\hat{T}_p^{i-} = -\frac{\hat{Q}_i^-}{\rho^i c_p^i} \left[ D_{11}^i [\beta_i(\theta_i) - jk_2 \tan \theta_i]^2 - (j\omega + D_{22}^i k_2^2) \right]^{-1}, \quad (2.29b)$$

with the power densities  $Q_i^+$  and  $Q_i^-$  expressed as a function of the parameters  $I_0$ ,  $\Lambda_i(\theta_i)$  and  $|R_i^\pm|$  given in Sec. 2.3

$$\hat{Q}_i^+ = I_0 \Lambda_i(\theta_i) |R_i^+|^2 F(\omega) G(k_2), \quad (2.30a)$$

$$\hat{Q}_i^- = I_0 \Lambda_i(\theta_i) |R_i^-|^2 F(\omega) G(k_2). \quad (2.30b)$$

Note that here the Fourier transform of the pulse distribution in space  $G(k_2)$  [defined in Eq. (2.23b) and in Appendix A.2.1] is only a function of  $k_2$  because the dependence in  $x_1$  has already been taken into account in the expressions of the particular solutions  $\hat{T}_p^i$  [Eqs. (2.28a, 2.28b)].

### 2.4.3 Application of the boundary conditions

As mentioned in Sec. 2.4.1, the boundary conditions are applied to determine the four coefficients  $\hat{T}_h^{i+}(k_2, \omega)$  and  $\hat{T}_h^{i-}(k_2, \omega)$  of the homogeneous solutions. At  $x_1 = 0$  and  $x_1 = H$ , the heat fluxes are conserved and the thermal convection is taken into account with the heat transfer coefficient  $h_c$ . Hence, using the Fourier's law and the Newton's law,<sup>159</sup> it gives

$$\lambda_{11}^I \left. \frac{\partial \hat{T}_I}{\partial x_1} \right|_{x_1=0} = h_c \left( \hat{T}_I \Big|_{x_1=0} - \hat{T}_\infty \right), \quad (2.31)$$

$$\lambda_{11}^{II} \left. \frac{\partial \hat{T}_{II}}{\partial x_1} \right|_{x_1=H} = -h_c \left( \hat{T}_{II} \Big|_{x_1=H} - \hat{T}_\infty \right), \quad (2.32)$$

with  $\hat{T}_\infty$  the double Fourier transform of the temperature when  $x_1$  approaches infinity. Furthermore, if heat diffusion losses are neglected in the  $\mathbf{x}_2$ -direction for each  $i$ -th sublayer and  $\Gamma_1^i h_i \ll 1$  is assumed, i.e., thermally-thin sublayer, with  $\Gamma_1^i$  defined in Eq. (2.26) and  $h_i$  the thickness of the  $i$ -th sublayer, the heat flux is conserved between media I and II, resulting in

$$\lambda_{11}^I \left. \frac{\partial \hat{T}_I}{\partial x_1} \right|_{x_1=h_1} = \lambda_{11}^{II} \left. \frac{\partial \hat{T}_{II}}{\partial x_1} \right|_{x_1=(h_1+\Delta h)}. \quad (2.33)$$

However, the temperature field may be discontinuous, which results in

## 2.5. Elastodynamic problem

---

$$\lambda_{11}^I \left. \frac{\partial \hat{T}_I}{\partial x_1} \right|_{x_1=h_1} = \frac{\hat{T}_{II} \Big|_{x_1=(h_1+\Delta h)} - \hat{T}_I \Big|_{x_1=h_1}}{R_c}, \quad (2.34)$$

with  $R_c$  the thermal resistance defined as

$$R_c = \sum_{i=1}^{N_{\text{sublayers}}} \frac{h_i}{\lambda_{11}^i}, \quad (2.35)$$

with  $N_{\text{sublayers}}$  the total number of sublayers between media I and II and  $\lambda_{11}^i$  the thermal conductivity of each sublayer. By replacing the temperature field in the boundary conditions [Eqs. (2.31–2.34)] by the sum of the homogeneous and particular solutions given in Eqs. (2.27, 2.28a, 2.28b), we obtain the following linear system:

$$\begin{bmatrix} A_{11}^T & A_{12}^T & 0 & 0 \\ A_{21}^T & A_{22}^T & A_{23}^T & A_{24}^T \\ A_{31}^T & A_{32}^T & A_{33}^T & A_{34}^T \\ 0 & 0 & A_{43}^T & A_{44}^T \end{bmatrix} \begin{bmatrix} \hat{T}_h^{I+} \\ * \hat{T}_h^{I-} \\ * \hat{T}_h^{II+} \\ * \hat{T}_h^{II-} \end{bmatrix} = \begin{bmatrix} B_1^T \\ B_2^T \\ B_3^T \\ B_4^T \end{bmatrix}. \quad (2.36)$$

To obtain a well-conditioned matrix, the coefficients  $A_{ij}^T$  and  $B_i^T$  are detailed in Appendix A.2.2 and the unknowns of Eq. (2.36), with the symbol “\*”, are written as<sup>150</sup>

$$\begin{aligned} * \hat{T}_h^{I-} &= \hat{T}_h^{I-} e^{\Gamma_1^I h_1}, & * \hat{T}_h^{II+} &= \hat{T}_h^{II+} e^{-\Gamma_1^{II}(h_1+\Delta h)}, \\ * \hat{T}_h^{II-} &= \hat{T}_h^{II-} e^{\Gamma_1^{II} H}. \end{aligned} \quad (2.37)$$

Finally, the temperature fields  $\hat{T}^I(x_1, k_2, \omega)$  and  $\hat{T}^{II}(x_1, k_2, \omega)$  are fully determined by the expressions

$$\begin{aligned} \hat{T}^I(x_1, k_2, \omega) &= \hat{T}_h^{I+}(k_2, \omega) e^{-\Gamma_1^I x_1} \\ &\quad + * \hat{T}_h^{I-}(k_2, \omega) e^{\Gamma_1^I(x_1-h_1)} + \hat{T}_p^I(x_1, k_2, \omega), \end{aligned} \quad (2.38a)$$

$$\begin{aligned} \hat{T}^{II}(x_1, k_2, \omega) &= * \hat{T}_h^{II+}(k_2, \omega) e^{-\Gamma_1^{II}[x_1-(h_1+\Delta h)]} \\ &\quad + * \hat{T}_h^{II-}(k_2, \omega) e^{\Gamma_1^{II}(x_1-H)} + \hat{T}_p^{II}(x_1, k_2, \omega). \end{aligned} \quad (2.38b)$$

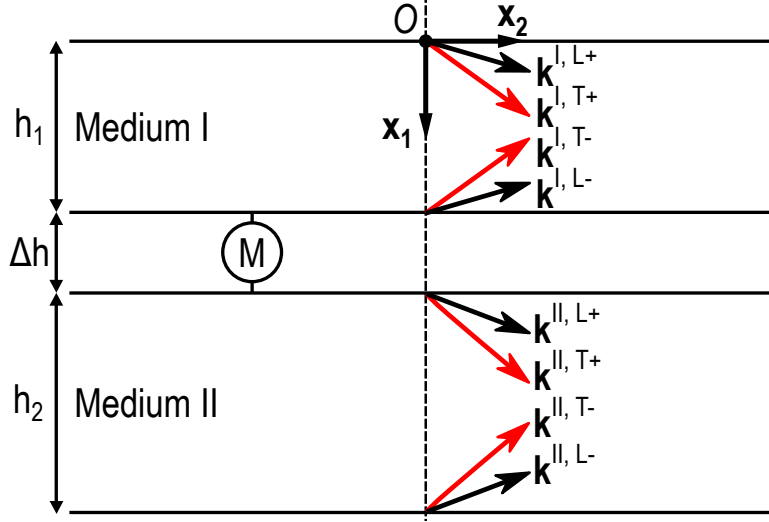


Figure 2.3 – Representation of the multilayer structure used to solve the elastodynamic problem. The uppercase letter “M” denotes the sublayers that can be inserted between media I and II to mechanically couple these two media. The black (red) arrows represent the wave vectors of the longitudinal (transverse) polarized waves propagating in the  $\pm x_1$ -direction.

## 2.5 Elastodynamic problem

The absorption of electromagnetic waves by the layers, as well as the thermal diffusion, have been detailed in Sec. 2.3 and Sec. 2.4, respectively. These two physical phenomena are at the origin of the elastic wave generation that occurs in the multilayer represented in Fig. 2.3. The elastodynamic problem is addressed in this section. Under the assumptions presented in Sec. 2.2 and the small perturbation hypothesis, the equation of motion is

$$\rho \frac{\partial^2 \mathbf{u}}{\partial t^2}(x_1, x_2, t) = \nabla \cdot \underline{\underline{\sigma}}(x_1, x_2, t), \quad (2.39)$$

with  $\rho$  the density,  $\mathbf{u}$  the displacement vector and  $\underline{\underline{\sigma}}$  the Cauchy stress tensor. Using the Hooke’s law, the stress tensor is equal to

$$\underline{\underline{\sigma}}(x_1, x_2, t) = \underline{\underline{C}} : \underline{\underline{\varepsilon}}(x_1, x_2, t) - \underline{\underline{C}} : \underline{\underline{\alpha}} \Delta T(x_1, x_2, t), \quad (2.40)$$

with  $\underline{\underline{C}}$  the fourth-order stiffness tensor,  $\underline{\underline{\varepsilon}}$  the second-order strain tensor,  $\underline{\underline{\alpha}}$  the second-order thermal expansion tensor and  $\Delta T$  the elevation of temperature in the medium.

## 2.5. Elastodynamic problem

---

Media I and II are assumed to be orthotropic with  $\mathbf{x}_1$  and  $\mathbf{x}_2$  as principal axes. In Voigt notation, Eq. (2.40) gives

$$\begin{bmatrix} \sigma_{11} \\ \sigma_{22} \\ \sigma_{12} \end{bmatrix} = \begin{bmatrix} C_{11} & C_{12} & 0 \\ C_{12} & C_{22} & 0 \\ 0 & 0 & C_{66} \end{bmatrix} \left( \begin{bmatrix} \varepsilon_{11} \\ \varepsilon_{22} \\ 2\varepsilon_{12} \end{bmatrix} - \begin{bmatrix} \alpha_{11} \\ \alpha_{22} \\ 0 \end{bmatrix} \Delta T \right), \quad (2.41)$$

with  $\varepsilon_{ij} = \frac{1}{2} \left( \frac{\partial u_i}{\partial x_j} + \frac{\partial u_j}{\partial x_i} \right)$ . Viscoelastic attenuation can be introduced by considering complex elastic coefficients with the imaginary part related to the attenuation. For the Kelvin-Voigt model

$$\underline{\underline{C}}^* = \underline{\underline{C}} + j\omega\underline{\underline{\eta}}, \quad (2.42)$$

with  $\underline{\underline{\eta}}$  the fourth-order viscosity tensor. To lighten the notations, the elastic coefficients are written without the symbol “\*” in the following. The use of Eq. (2.40) in Eq. (2.39) and the projection of Eq. (2.39) onto  $\mathbf{x}_1$ -axis and  $\mathbf{x}_2$ -axis yields the following elastodynamic equations in the Fourier domain:

$$C_{11} \frac{\partial^2 \hat{u}_1}{\partial x_1^2} - jk_2 (C_{12} + C_{66}) \frac{\partial \hat{u}_2}{\partial x_1} \quad (2.43a)$$

$$+ (\rho\omega^2 - C_{66}k_2^2) \hat{u}_1 = C_{\alpha_1} \frac{\partial \hat{T}}{\partial x_1},$$

$$C_{66} \frac{\partial^2 \hat{u}_2}{\partial x_1^2} - jk_2 (C_{12} + C_{66}) \frac{\partial \hat{u}_1}{\partial x_1} \quad (2.43b)$$

$$+ (\rho\omega^2 - C_{22}k_2^2) \hat{u}_2 = -jk_2 C_{\alpha_2} \hat{T},$$

with  $C_{\alpha_1} = C_{11}\alpha_{11} + C_{12}\alpha_{22}$ ,  $C_{\alpha_2} = C_{12}\alpha_{11} + C_{22}\alpha_{22}$ . In this section, the convention for the double Fourier transform, in space  $x_2$  and time  $t$ , is the same as the one given in Eq. (2.21). The solution of Eqs. (2.43a, 2.43b) is the sum of the homogeneous solution  $\hat{\mathbf{u}}_h(x_1, k_2, \omega)$  and the particular solution  $\hat{\mathbf{u}}_p(x_1, k_2, \omega)$  as detailed in the following sections.

### 2.5.1 Homogeneous solutions of the elastodynamic equations

The solutions of the homogeneous elastodynamic equations, Eqs. (2.43a, 2.43b) without the source terms  $C_{\alpha_1} \frac{\partial \hat{T}}{\partial x_1}$  and  $-jk_2 C_{\alpha_2} \hat{T}$ , are sought in the form of

$$\hat{\mathbf{u}}_h(x_1, k_2, \omega) = \hat{\mathbf{U}}_h(k_2, \omega)e^{-jk_1x_1}. \quad (2.44)$$

By injecting Eq. (2.44) in the homogeneous elastodynamic equations (2.43a, 2.43b), we obtain

$$\begin{bmatrix} a_{11} - k_1^2 C_{11} & -k_1 a_{12} \\ -k_1 a_{12} & a_{22} - k_1^2 C_{66} \end{bmatrix} \begin{bmatrix} \hat{U}_{1h} \\ \hat{U}_{2h} \end{bmatrix} = \begin{bmatrix} 0 \\ 0 \end{bmatrix}, \quad (2.45)$$

with  $a_{11} = \rho\omega^2 - k_2^2 C_{66}$ ,  $a_{22} = \rho\omega^2 - k_2^2 C_{22}$ , and  $a_{12} = k_2 (C_{12} + C_{66})$ . Then, by imposing that the determinant of the  $2 \times 2$  matrix of Eq. (2.45) is zero, we get the quadratic equation

$$aX^2 + bX + c = 0, \quad (2.46)$$

with  $X = k_1^2$  and the coefficients of the quadratic equation:  $a = C_{11}C_{66}$ ,  $b = -(C_{11}a_{22} + C_{66}a_{11} + a_{12}^2)$ ,  $c = a_{11}a_{22}$ . The two solutions of Eq. (2.46) are

$$X_{\pm} = \frac{-b \pm \sqrt{b^2 - 4ac}}{2a}, \quad (2.47a)$$

which gives four eigenvalues for the wavenumber  $k_1$ . Thus, the homogeneous solution is the linear combination of two longitudinal (L) and two transverse (T) polarized waves, which are travelling along the positive and negative directions of the  $\mathbf{x}_1$ -axis as illustrated in Fig. 2.3 and defined by the equation

$$\begin{aligned} \hat{\mathbf{u}}_h(x_1, k_2, \omega) = & \sum_{n=\{L,T\}} A^{n+} \hat{\mathbf{U}}_h^{n+}(k_2, \omega)e^{-jk_1^n x_1} \\ & + A^{n-} \hat{\mathbf{U}}_h^{n-}(k_2, \omega)e^{jk_1^n x_1}. \end{aligned} \quad (2.48)$$

In Eq. (2.48),  $k_1^L = \sqrt{X_-}$  and  $k_1^T = \sqrt{X_+}$  are the projections of the longitudinal and transverse wave vectors along the  $\mathbf{x}_1$ -axis, respectively. In addition,  $A^{n\pm}$  refer to the wave amplitudes that are subsequently determined by applying the boundary conditions and  $\hat{\mathbf{U}}_h^{n\pm}$  are the eigenvectors that are equal to

$$\hat{\mathbf{U}}_h^{n\pm}(k_2, \omega) = \begin{bmatrix} \hat{U}_{1h}^{n\pm} \\ \hat{U}_{2h}^{n\pm} \end{bmatrix} = \begin{bmatrix} a_{22} - (k_1^n)^2 C_{66} \\ \pm k_1^n a_{12} \end{bmatrix}. \quad (2.49a)$$

### 2.5.2 Particular solutions of the elastodynamic equations

The particular solutions are searched following the form of the source terms  $C_{\alpha_1} \frac{\partial \hat{T}}{\partial x_1}$  and  $-jk_2 C_{\alpha_2} \hat{T}$  of Eqs. (2.43a, 2.43b). Therefore, using the analytic expression of the temperature fields  $\hat{T}$  in media I and II, given in Eqs. (2.38a, 2.38b), the particular solutions are

$$\hat{\mathbf{u}}_p^I = \hat{\mathbf{U}}_{p\Gamma}^{I+} e^{-\Gamma_1^I x_1} + \hat{\mathbf{U}}_{p\Gamma}^{I-} e^{\Gamma_1^I (x_1 - h_1)} \quad (2.50a)$$

$$+ \hat{\mathbf{U}}_{p\beta}^{I+} e^{-\beta_1(\theta_1) x_1} e^{jk_2 \tan \theta_1 x_1} + \hat{\mathbf{U}}_{p\beta}^{I-} e^{\beta_1(\theta_1)(x_1 - h_1)} e^{-jk_2 \tan \theta_1 x_1},$$

$$\hat{\mathbf{u}}_p^{II} = \hat{\mathbf{U}}_{p\Gamma}^{II+} e^{-\Gamma_1^{II} [x_1 - (h_1 + \Delta h)]} + \hat{\mathbf{U}}_{p\Gamma}^{II-} e^{\Gamma_1^{II} (x_1 - H)} \quad (2.50b)$$

$$+ \hat{\mathbf{U}}_{p\beta}^{II+} e^{-\beta_1(\theta_2) [x_1 - (h_1 + \Delta h)]} e^{jk_2 \tan \theta_2 x_1} + \hat{\mathbf{U}}_{p\beta}^{II-} e^{\beta_1(\theta_2)(x_1 - H)} e^{-jk_2 \tan \theta_2 x_1}.$$

To obtain the four vectors  $\hat{\mathbf{U}}_{p\beta}^{I+}$ ,  $\hat{\mathbf{U}}_{p\beta}^{I-}$ ,  $\hat{\mathbf{U}}_{p\beta}^{II+}$  and  $\hat{\mathbf{U}}_{p\beta}^{II-}$ , which are related to the optical penetration of the electromagnetic waves in media I and II, each term of Eqs. (2.50a, 2.50b) is injected into the elastodynamic equations (2.43a, 2.43b). Thus, four linear systems with the form

$$\begin{bmatrix} a_{11}^i + C_{11}^i (\beta_i - jk_2 \tan \theta_i)^2 & \pm ja_{12}^i (\beta_i - jk_2 \tan \theta_i) \\ \pm ja_{12}^i (\beta_i - jk_2 \tan \theta_i) & a_{22}^i + C_{66}^i (\beta_i - jk_2 \tan \theta_i)^2 \end{bmatrix} \begin{bmatrix} \hat{U}_{1p\beta}^{i\pm} \\ \hat{U}_{2p\beta}^{i\pm} \end{bmatrix} = \begin{bmatrix} -C_{\alpha_1}^i (\beta_i - jk_2 \tan \theta_i) (\pm \hat{T}_p^{i\pm}) \\ -jk_2 C_{\alpha_2}^i \hat{T}_p^{i\pm} \end{bmatrix}, \quad (2.51)$$

have to be solved, with  $i = \{I, II\}$ . The same procedure is applied to calculate the four vectors  $\hat{\mathbf{U}}_{p\Gamma}^{I+}$ ,  $\hat{\mathbf{U}}_{p\Gamma}^{I-}$ ,  $\hat{\mathbf{U}}_{p\Gamma}^{II+}$  and  $\hat{\mathbf{U}}_{p\Gamma}^{II-}$  of Eqs. (2.50a, 2.50b), which are linked to the thermal diffusion in media I and II. Four other linear systems have to be solved (see Appendix A.3.2 for more detailed).

### 2.5.3 Application of the boundary conditions

The homogeneous and particular solutions of the elastodynamic equations (2.43a, 2.43b) have been determined in Sec. 2.5.1 and Sec. 2.5.2. Consequently, the last step is to apply the boundary conditions to find the eight amplitudes  $A_1^{n\pm}$ , with  $n = \{L, T\}$  and  $i = \{I, II\}$ , of the eight elastic waves that propagate in media I and II. In Fig. 2.3, the upper surface of medium I (at  $x_1 = 0$ ) and the lower surface of medium II (at  $x_1 = H$ ) are considered as free surfaces. Thus, four boundary conditions are given by

$$\hat{\sigma}_{11}^I \Big|_{x_1=0} = \hat{\sigma}_{12}^I \Big|_{x_1=0} = 0, \quad (2.52)$$

$$\hat{\sigma}_{11}^{\text{II}}|_{x_1=H} = \hat{\sigma}_{12}^{\text{II}}|_{x_1=H} = 0. \quad (2.53)$$

Using the mechanical coupling between media I and II, four other boundary conditions are

$$\begin{bmatrix} \hat{u}_1^{\text{I}} \\ \hat{u}_2^{\text{I}} \\ \hat{\sigma}_{11}^{\text{I}} \\ \hat{\sigma}_{12}^{\text{I}} \end{bmatrix}_{x_1=h_1} = [L^M]_{4 \times 4} \begin{bmatrix} \hat{u}_1^{\text{II}} \\ \hat{u}_2^{\text{II}} \\ \hat{\sigma}_{11}^{\text{II}} \\ \hat{\sigma}_{12}^{\text{II}} \end{bmatrix}_{x_1=h_1+\Delta h}, \quad (2.54)$$

with  $[L^M]$  the transfer matrix (pp. 53–60 in Ref. 157) used to couple the displacements  $(\hat{u}_1, \hat{u}_2)$  and the stresses  $(\hat{\sigma}_{11}, \hat{\sigma}_{12})$  from medium I at  $x_1 = h_1$ , to medium II at  $x_1 = h_1 + \Delta h$ . The sublayers that can be inserted between media I and II will be taken into account through this transfer matrix. For instance, if we assume the continuity of displacements and stresses at the interface between media I and II (with  $\Delta h = 0$ ), then  $[L^M]$  is equal to the identity matrix. For more complex cases, the expression of the transfer matrix is detailed in Appendix A.3.4. Then, Eqs. (2.52–2.54) have to be solved to obtain the eight amplitudes of the elastic waves, taking care that the matrices are well-conditioned [as it was done in Eqs. (2.36, 2.37)].<sup>150</sup> The complete solution in media I and II is equal to the linear combination of the homogeneous and particular solutions

$$\hat{\mathbf{u}}^i(x_1, k_2, \omega) = \hat{\mathbf{u}}_h^i(x_1, k_2, \omega) + \hat{\mathbf{u}}_p^i(x_1, k_2, \omega). \quad (2.55)$$

Finally, a double inverse Fourier transform in space  $x_2$  and time  $t$  is performed to find the temporal solutions of the displacement field  $u_i(x_1, x_2, t)$ , with  $i = \{1, 2\}$ . Numerically, this double integration is carried out according to the approach proposed by Bouchon and Aid,<sup>160</sup> as well as Weaver *et al.*<sup>161,162</sup> The complex angular frequency  $\omega^* = \omega - j\delta_\omega$  is used to slightly shift the analytic solutions in the imaginary plane to avoid the poles of the Rayleigh-Lamb waves. Then, the small positive constant  $\delta_\omega$  is removed after the double integration by multiplying the final result by  $e^{\delta_\omega t}$ :

$$u_i(x_1, x_2, t) = \frac{e^{\delta_\omega t}}{2\pi} \iint_{-\infty}^{+\infty} \hat{u}_i(x_1, k_2, \omega^*) e^{j(\omega t - k_2 x_2)} d\omega dk_2. \quad (2.56)$$

The semi-analytic method for solving electromagnetic, thermal and elastodynamic problems was fully presented in sections 2.3, 2.4 and 2.5, respectively. Examples of numerical results obtained with this simulation technique are presented below.

## 2.6. Numerical simulation results

Table 2.1 – Optical, thermal and mechanical properties of the aluminum alloy (Al), SCHOTT N-BK7<sup>®</sup> glass and titanium (Ti).

	Al	N-BK7	Ti
$n'$ (@ 532 nm) <sup>163</sup>	1.468	1.519	2.479
$n''$ (@ 532 nm) <sup>163</sup>	8.949	$7.761 \cdot 10^{-9}$	3.351
$\mu$	1.	1.	1.
$\lambda_{11}$ (W m <sup>-1</sup> K <sup>-1</sup> )	$1.5 \cdot 10^2$	1.1	$2.0 \cdot 10^1$
$\lambda_{22}$ (W m <sup>-1</sup> K <sup>-1</sup> )	$1.5 \cdot 10^2$	1.1	$2.0 \cdot 10^1$
$c_p$ (J kg <sup>-1</sup> K <sup>-1</sup> )	$9.0 \cdot 10^2$	$8.6 \cdot 10^2$	$5.0 \cdot 10^2$
$\alpha_{11} = \alpha_{22}$ (K <sup>-1</sup> )	$2.5 \cdot 10^{-5}$	$8.3 \cdot 10^{-6}$	$1.1 \cdot 10^{-5}$
$C_{11}$ (GPa)	$1.10 \cdot 10^2$	$9.18 \cdot 10^1$	$1.62 \cdot 10^2$
$C_{12}$ (GPa)	$5.69 \cdot 10^1$	$2.38 \cdot 10^1$	$6.90 \cdot 10^1$
$C_{22}$ (GPa)	$1.10 \cdot 10^2$	$9.18 \cdot 10^1$	$1.80 \cdot 10^2$
$C_{66}$ (GPa)	$2.65 \cdot 10^1$	$3.40 \cdot 10^1$	$4.67 \cdot 10^1$
$\rho$ (kg m <sup>-3</sup> )	$2.70 \cdot 10^3$	$2.51 \cdot 10^3$	$4.54 \cdot 10^3$

## 2.6 Numerical simulation results

In this section, numerical results obtained with this semi-analytic model are reported. Some simulation parameters are unchanged for the three examples that are presented later: the time range  $t \in [0, 16.384] \mu\text{s}$  with the discretization step  $\Delta t = 8.0 \cdot 10^{-3} \mu\text{s}$ ; the position range  $x_2 \in [-81.92, 81.92] \text{mm}$  with the discretization step  $\Delta x_2 = 8.0 \cdot 10^{-2} \text{mm}$ . Hence, the maximum angular frequency  $\omega$  is equal to  $3.927 \cdot 10^2 \text{rad} \mu\text{s}^{-1}$  (maximum frequency of 62.5 MHz) and the maximum wavenumber  $k_2$  to  $3.927 \cdot 10^1 \text{rad} \text{mm}^{-1}$ . Furthermore, the incident electromagnetic wave is defined by: the pulse duration  $\tau_p = 8 \text{ns}$ , the source width  $a_s = 0.2 \text{mm}$ , the intensity  $I_0 = 0.2 \text{J} \text{mm}^{-1}$ , the angle of incidence  $\theta_0 = 0^\circ$  and the electromagnetic wavelength  $\lambda_{\text{opt}} = 532 \text{nm}$ . Concerning the thermal parameters, the external temperature is set to  $T_\infty = 293.15 \text{K}$ , and the heat transfer coefficient is imposed to  $h_c = 25 \text{W} \text{m}^{-2} \text{K}^{-1}$ . Using these settings, three examples of the use of the developed semi-analytic model are described hereafter. The optical, thermal and mechanical properties of the material used for the simulations are given in Tab. 2.1.

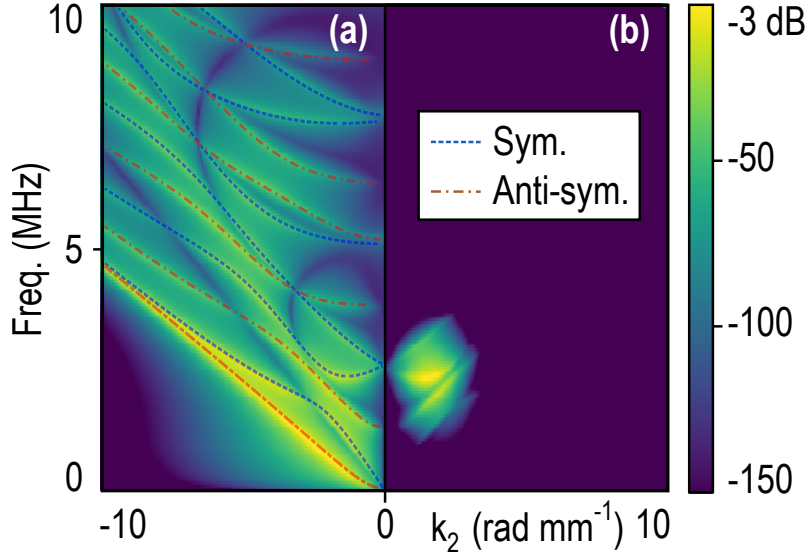


Figure 2.4 – Zoom views of  $f$ – $k$  diagrams (in dB), for a 1.23 mm-thick aluminum alloy plate at  $x_1 = 1.23$  mm, for two different laser sources. (a) Gaussian laser pulse ( $\tau_p = 8$  ns,  $a_s = 0.2$  mm). (b) Modulated laser source in time (tone burst of 2.5 MHz central frequency) and space (phase mask of  $1.5$  rad mm $^{-1}$  central wavenumber). A good agreement is obtained with the dispersion curves simulated with the commercial software “CIVA 2020” in dashed (dash-dotted) lines for symmetric (antisymmetric) modes.

### 2.6.1 Analysis of the guided elastic waves in an aluminum alloy plate

The first example is the frequency–wavenumber ( $f$ – $k$ ) diagrams depicting the normalized spectral density in dB,

$$\frac{|\hat{u}_1^I(x_1, k_2, \omega^*)|^2}{\max_{k_2, \omega^*} |\hat{u}_1^I(x_1, k_2, \omega^*)|^2}, \quad (2.57)$$

of a 1.23 mm-thick aluminum alloy plate for two different laser sources. In Fig. 2.4(a), the  $f$ – $k$  diagram is obtained for a Gaussian laser pulse of duration  $\tau_p = 8$  ns and source width  $a_s = 0.2$  mm. The Fourier transforms of the pulse distribution in time and space are given by the expressions of  $F(\omega)$  and  $G(x_1, k_2)$  with  $\theta_0 = 0^\circ$  in Eqs. (2.23a) and (2.23b), respectively. Before applying the double inverse Fourier transform introduced in Eq. (2.56), the displacement  $\hat{u}_i(x_1, k_2, \omega^*)$  can indeed be used to analyze the dispersion of the waves guided along the  $\mathbf{x}_2$ -direction. In the case of a free plate, the modes shown in Fig. 2.4(a)

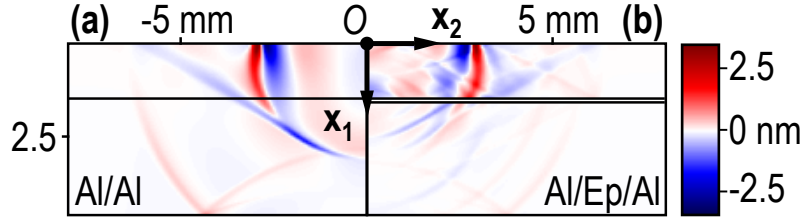


Figure 2.5 – Normal displacements  $u_1(x_1, x_2, t)$  simulated at  $t = 1 \mu\text{s}$  in: (a) a bilayer Al (1.5 mm)/Al (3.1 mm) and (b) a trilayer Al (1.5 mm)/Epoxy (0.1 mm)/Al (3.0 mm).

correspond to the Lamb modes. Note that this  $f$ – $k$  diagram contains, on top of the dispersive features of the modes, the information about their detectability with an interferometer sensitive only to the normal component of the displacement of the free surface. This Gaussian laser pulse allows to excite a large number of Lamb modes because of the broadband content of  $F(\omega)$  and  $G(x_1, k_2)$ . In order to excite specific modes only, the laser source can be modulated in time and space to select a particular area in the  $f$ – $k$  diagram, as shown in Fig. 2.4(b). This can be easily implemented in the model by changing the expressions of  $F(\omega)$  and  $G(x_1, k_2)$  by the Fourier transform of the desired laser source modulated in time and space. To obtain the  $f$ – $k$  diagram presented in Fig. 2.4(b), a tone burst of 2.5 MHz central frequency and a phase mask of  $1.5 \text{ rad mm}^{-1}$  central wavenumber  $k_2$  were used.

The calculation time to obtain  $\hat{u}_i(x_1, k_2, \omega^*)$ , at a given  $x_1$  position and for all the values of  $\omega^*$  and  $k_2$  vectors, is equal to  $1 \text{ min } 37 \text{ s} \pm 6 \text{ s}$  (with an Intel® Core™ i7-6500U CPU @ 2.5 GHz, 16.0 GB RAM). The time domain signals as a function of  $x_2$  can be obtained by applying the double inverse Fourier transform of  $\hat{u}_i(x_1, k_2, \omega^*)$ , which only adds 0.2 s to the previous calculation time.

Among other useful applications, the possibility, offered by the semi-analytic model proposed here, to analyze the influence of  $F(\omega)$  and  $G(x_1, k_2)$  on simulated  $f$ – $k$  diagrams is of interest to help design the temporal and spatial profiles of the laser source to excite and detect specific Lamb modes. This type of analysis can be performed on more complex structures such as those presented below.

### 2.6.2 Bilayer/trilayer with interfacial stiffnesses

The second example deals with a bilayer composed of two aluminum alloy (Al) plates of 1.5 and 3.1 mm [Fig. 2.5(a)] and a trilayer Al (1.5 mm)/Epoxy (0.1 mm)/Al (3.0 mm)

[Fig. 2.5(b)]. The normal displacement  $u_1(x_1, x_2, t)$ , generated by a Gaussian laser pulse of duration  $\tau_p = 8$  ns and source width  $a_s = 0.2$  mm, is obtained by solving numerically Eq. (2.56) for  $x_1 \in [0, 4.6$  mm], with the positive constant  $\delta_\omega = 0.4$  rad  $\mu\text{s}^{-1}$ . The snapshot of the normal displacement at  $t = 1$   $\mu\text{s}$  is represented in Fig. 2.5. The heat source is located at the origin of the Cartesian coordinate system because the optical penetration depth in aluminum is equal to  $1/\beta = 4.7$  nm (@  $\theta_0 = 0^\circ$  and  $\lambda_{\text{opt}} = 532$  nm).

In Fig. 2.5(a), two distributions of normal and transverse interfacial stiffnesses (see Appendix A.3.4), equal to  $K_N = K_T = \infty$  kN mm<sup>-3</sup>, are inserted between the two Al plates. Thus, a perfect continuity of displacements and stresses is imposed at the interface, which explains the full transmission of the elastic waves between media I and II. At the free surface of the top Al plate (at  $x_1 = 0$ ), the Rayleigh wave with the largest normal displacement (more than 2.5 nm in this simulation, see the color bar) is visible. In the bulk of the bilayer, the fastest wave (in red), which is reflected at the free surface of the lower Al plate (at  $x_1 = 4.6$  mm), corresponds to the longitudinal wave. The slowest bulk wave is the transverse wave (in blue). The head wave is also simulated and corresponds to the plane wave that is generated at the critical angle  $\theta_{\text{crit}} = \arcsin(\sqrt{C_{66}/C_{11}}) = 29.4^\circ$ , with the elastic coefficients  $C_{11}$  and  $C_{66}$  given in Tab. 2.1.

In Fig. 2.5(b), three sublayers are inserted between the two Al plates: two distributions of normal and transverse interfacial stiffnesses (see Appendix A.3.4) equal to  $K_{N_1} = K_{T_1} = \infty$  kN mm<sup>-3</sup>, a 0.1 mm-thick epoxy layer and two other interfacial stiffness distributions equal to  $K_{N_2} = K_{T_2} = \infty$  kN mm<sup>-3</sup>. The epoxy layer is assumed to be isotropic with a density of  $2.1 \cdot 10^3$  kg m<sup>-3</sup> and elastic coefficients  $C_{11} = 4.2$  GPa and  $C_{12} = 3.3$  GPa. Contrary to the bilayer Al/Al in Fig. 2.5(a), elastic waves are transmitted but also reflected by the epoxy layer.

This second example demonstrates the opportunities of the proposed model to predict/interpret the effect of imperfect bonding (by modifying the values of interfacial stiffnesses) on the detectable elastic waves in a bonded multilayer structure. Possible applications of this semi-analytic model could be the simulation of laser-generated ultrasounds in structural bonding. Indeed, quantifying the mechanical strength of bonds is a major issue in aeronautics. These simulations could allow to understand the influence of a weak bond on the detected ultrasonic signature. Moreover, these fast and accurate simulations could enable the resolution of inverse problems requiring the optimization of various key parameters related to the mechanical strength of adhesive bonding.

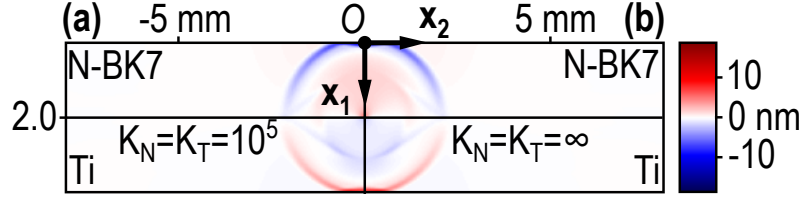


Figure 2.6 – Normal displacements  $u_1(x_1, x_2, t)$  simulated at  $t = 0.35 \mu\text{s}$  in a bilayer glass (2 mm)/Ti (2 mm) with interfacial stiffnesses equal to: (a)  $K_N = K_T = 10^5 \text{ kN mm}^{-3}$  and (b)  $K_N = K_T = \infty \text{ kN mm}^{-3}$ .

### 2.6.3 Bilayer with the heat source at the interface

The third example, in Fig. 2.6, is about a bilayer structure composed of a 2 mm-thick glass plate (SCHOTT N-BK7<sup>®</sup>) perfectly coupled to a 2.0 mm-thick titanium plate of orthotropic mechanical properties. To ensure the continuity of displacements and stresses at the interface, two distributions of normal and transverse interfacial stiffnesses are added and equal to  $K_N = K_T = 10^5 \text{ kN mm}^{-3}$  in Fig. 2.6(a) and  $K_N = K_T = \infty \text{ kN mm}^{-3}$  in Fig. 2.6(b). The heat source is located at the interface between the two media because the incident electromagnetic wave is mainly absorbed in the titanium plate. Indeed, the complex part of the refractive index  $n''$  is approximately  $10^9$  times higher for the titanium than for the glass plate (see Tab. 2.1). Moreover, the normal displacement  $u_1$  is similar in the two cases presented in Fig. 2.6(a) and (b) because large values of interfacial stiffnesses ( $K_N = K_T = 10^5 \text{ kN mm}^{-3}$ ) are sufficient to ensure a perfect continuity of displacements and stresses at the interface between the two media. Furthermore, longitudinal bulk waves are mainly generated in the  $x_1$ -direction and the sign of the normal displacement is positive (negative) in the titanium (glass) plate. Transverse bulk waves and head waves are clearly visible (in blue) in the titanium plate.

This third example illustrates the fact that this model can be used to simulate a thermoelastic source at the interface between two media and not only at the upper surface of medium I, as previously shown in the first and second examples.

## 2.7 Conclusion

Laser-generated ultrasounds are simulated in a multilayer structure using a semi-analytic approach detailed in this chapter. Electromagnetic, thermal and elastodynamic problems are successively solved to obtain the displacement fields in the upper and lower media of

the structure. A tilted laser line source, of infinite length in the  $\mathbf{x}_3$ -axis, is considered. The optical transmission and reflection of the incident laser beam are calculated to obtain the power densities dissipated into heat and used as source terms for solving the heat diffusion problem. The amplitudes of the thermal waves are obtained by considering conduction and convection phenomena. Then, analytic solutions of the displacement field due to the thermal expansion are determined in the Fourier domain. Finally, a double numerical inverse Fourier transform in space and time is performed to find the displacement field in the time domain.

In this 2D model, layered plates with parallel surfaces are considered and it is assumed that the generation of ultrasounds occurs only in the upper and lower media, i.e., the generation of ultrasounds in the sublayers should be negligible. The model has been applied to three different cases showing just a glance of the possibilities such a model provides for forecasting, designing or else analyzing the elastic waves generated and detected by lasers in multilayer structures. Note that this model, as long as the thermoelastic process of ultrasound generation is at major play, is not limited to millimetric-in-thickness structure nor to the MHz frequency range. In addition, it can be extended to a 3D geometry in order to simulate ultrasound generation with thermoelastic sources that are no longer assumed to be of infinite length in the  $\mathbf{x}_3$ -direction. This will obviously make the formulas presented in this chapter more complex (the wavenumber  $k_3$  must be added) and will necessarily increase the calculation time; which is about 1 min 37 s  $\pm$  6 s for a 2D geometry at a given  $x_1$  position. However, this approach could be of real interest for simulating laser-generated ultrasounds in multilayer structures with thermoelastic sources of complex 3D shape.

As pointed out in the second example above, the fast and accurate simulations with the developed model could enable the resolution of inverse problems requiring the optimization of various key parameters related to the mechanical strength of adhesive bonding. The next chapter is dedicated to such applications of the semi-analytic model.

## Chapter 3

# Plane wave synthesis and inverse problem for nondestructive evaluation of adhesive bondings

### Contents

---

3.1	Introduction . . . . .	69
3.2	Plane wave synthesis for the nondestructive evaluation of adhesive bondings	70
3.2.1	Description of the plane wave synthesis . . . . .	71
3.2.2	Application for the nondestructive evaluation of adhesive bondings	73
3.3	Solving the direct problem . . . . .	74
3.3.1	Analytic formulation . . . . .	74
3.3.2	Semi-analytic model . . . . .	75
3.3.3	Results of semi-analytic simulations . . . . .	78
3.4	Resolution of inverse problems with simulated data . . . . .	78
3.5	Resolution of inverse problems with experimental data . . . . .	85
3.5.1	Sample preparation . . . . .	85
3.5.2	Experimental set-up . . . . .	86
3.5.3	Simple case of the free-standing plate . . . . .	87
3.5.4	Quantification and differentiation of two adhesive bonding conditions: nominal and degraded . . . . .	91
3.6	Conclusion . . . . .	92

---

## Abstract

A laser ultrasonic method is proposed for the nondestructive evaluation of bonded assemblies, based on the analysis of elastic plane waves reflected from the bonding interface. Plane waves are numerically synthesized from experimentally detected cylindrical waves. Several angles of incidence with respect to the bonding interface are achieved by varying the delay in the synthesis step. An inverse problem using these plane waves is then solved to identify the normal and transverse interfacial stiffnesses that model the mechanical coupling between two bonded media. The developed method is first validated with semi-analytic simulated input data where Gaussian noise has been added (semi-analytic model presented in Chap. 2). Next, the method is applied using signals acquired on an aluminum alloy plate and on assemblies (with and without adhesion defects) made of two aluminum alloy plates bonded by an aeronautical structural epoxy adhesive film. The identified values of interfacial stiffnesses enable to distinguish the three samples and to obtain quantitative values to characterize the adhesive bonding.

---

This work was submitted to the J. Acoust. Soc. Am.:

R. Hodé, S. Raetz, N. Chigarev, J. Blondeau, N. Cuvillier, V. Gusev, M. Ducouso and V. Tournat, “Laser ultrasonics in a multilayer structure: Plane wave synthesis and inverse problem for nondestructive evaluation of adhesive bondings,” J. Acoust. Soc. Am. (submitted on December 11, 2020).

## 3.1 Introduction

In this chapter, a laser ultrasonic method is developed for the quantitative NDE of adhesive bonding. This work is based on the synthesis of elastic plane waves developed by Reverdy and Audoin.<sup>164,165</sup> This post-processing method was originally designed to find the elastic coefficients of isotropic or anisotropic plates using laser-generated ultrasound. The times of flight of the synthesized plane waves were used to solve an inverse problem based on the Christoffel equation. This method is here applied to identify the mechanical coupling conditions between two bonded elastic media with known elastic coefficients. Not only the times of flight but also the amplitudes of the synthesized reflected plane waves are gathered for different angles of incidence with respect to the bonding interface. An inverse problem is then solved to identify the normal and transverse interfacial stiffnesses used to model the bonding.

The outline of this chapter is introduced as follows. In Sec. 3.2, the post-processing method to synthesize plane waves is described and the application of this technique for the NDE of adhesive bonding is presented. In Sec. 3.3, two methods are introduced to simulate the amplitudes of the synthesized plane waves reflected from the here-investigated interface between two bonded media. The choice of the semi-analytic approach to solve the direct problem is justified and numerical results are provided. In Sec. 3.4, the algorithm used to solve the inverse problem in order to identify the values of normal and transverse interfacial stiffnesses, which model the mechanical coupling between two bonded media, is detailed. The identification process is first validated using simulated data to which noise has been added. Then, the inverse problem is solved using experimental data acquired for a free-standing aluminum alloy plate and for two bonded assemblies (Al/Epoxy/Al), with and without adhesion defects, in Sec. 3.5. The epoxy layer was, in both cases, an industrial aeronautical adhesive. Both assemblies, similar in geometry and constituents, yet different in adhesion level, were undistinguishable when evaluated with conventional ultrasonic inspection techniques. The identification of the interfacial stiffnesses with the proposed method is eventually presented. Its ability to non-destructively characterize adhesive bondings and therefore to distinguish different adhesion levels is demonstrated.

## 3.2 Plane wave synthesis for the nondestructive evaluation of adhesive bondings

One advantage of laser ultrasound generation in the thermoelastic regime is that the surface of the inspected material is not locally degraded, in contrast to the ablation regime. However, the elastic waves generated in this regime are of relatively low amplitudes, which can make optical signal detection difficult and result in a relatively poor signal-to-noise ratio. For these reasons, different techniques have been developed to increase the amplitude of laser-generated ultrasound and to improve the directivity pattern of opto-acoustic sources. Plane wave generation is one of the methods to address this issue.

For absorbing material, the easiest way to experimentally generate non-destructively plane waves in laser ultrasonics is to use a thermoelastic source with lateral dimensions very large compared to the achievable wavelength. The limit of that approach is that only plane waves propagating in a direction normal to the generation surface are made possible. Two main experimental techniques allowing to steer the propagation direction of plane waves along any angle are reported in the literature. One approach is based on a moving laser source that continuously sweeps the surface of a medium at subsonic, transonic or supersonic velocities. Berthelot *et al.*<sup>166</sup> applied this technique for the experimental generation of plane waves in a freshwater tank. The mobile thermoacoustic source on the water surface was created by the reflection of a laser beam from a rotating mirror. Ing *et al.*<sup>167</sup> used an acousto-optic cell working under the Bragg mode to generate a moving laser source at the surface of an aluminum half-cylinder. Another approach to launch plane waves is based on a set of photoacoustic sources separated in space and time. These laser ultrasonic methods are close to those developed in conventional ultrasound with the use of phased array transducers.<sup>168</sup> Steckenrider *et al.*<sup>169</sup> used the propagation of one laser pulse in an optical delay system, consisting of a White cell cavity<sup>170</sup> and a graded beamsplitter, to generate up to ten spatially and temporally separated laser sources. Another technique that requires only one laser beam was based on the redirection of a laser pulse into several optical fibers of different lengths, resulting in phase shifts.<sup>171–173</sup> Furthermore, multiple laser beams were also used to design a phased array of laser sources. Noroy *et al.* carried out experiments with a multiple beam Q-switched Nd:YAG laser capable of delivering sixteen optical pulses. Laser-generated ultrasonic phased array were performed by the authors in the ablation regime,<sup>174</sup> and in the thermoelastic regime.<sup>175,176</sup> Murray *et al.*<sup>177</sup> followed a similar approach with ten Nd:YAG lasers cavities.

Although laser-generated plane waves are experimentally achievable, these techniques are difficult to realize in practice and require the use of more complicated systems than those with two laser beams, i.e., one for ultrasound generation and one for detection. Therefore, an alternative approach, based on the synthesis of plane waves in a post-processing step, has been chosen and is detailed in the following.

#### 3.2.1 Description of the plane wave synthesis

To synthesize plane waves from divergent laser-generated ultrasound, a method has been developed by Reverdy and Audoin.<sup>164,165</sup> They have used it to measure the elastic coefficients of anisotropic materials by solving an inverse problem based on the Christoffel equation. The first step of this technique is the acquisition of temporal signals. A laser line source, of infinite length in the  $\mathbf{x}_3$ -direction, is moved over the sample surface in  $2N + 1$  positions with a constant  $\delta x$ -step. At each  $i \in [-N, N]$  position, laser-generated ultrasound are emitted in the sample and the normal displacement of the surface is measured at the  $i = 0$  position. Therefore, for each generation location, a temporal signal  $s_i(t)$  is recorded. The second step deals with the post-processing of the acquired data to synthesize plane waves. A constant time delay  $\delta t$  is imposed between the signals  $s_i(t)$  and  $s_{i+1}(t)$ . Then, a sum on all the signals is achieved to obtain:

$$s(t) = \sum_{i=-N}^N s_i(t + i\delta t), \quad (3.1)$$

where  $s(t)$  corresponds to the signal that would have been experimentally recorded, at the  $i = 0$  position, if a phased array of laser sources had generated plane waves in the linear domain, i.e when the superposition principle is valid. The time delay  $\delta t$  is directly linked to the steering angle  $\varphi_n$ , of the synthesized plane wave of  $n$ -polarization, given by

$$\sin(\varphi_n) = \frac{k_s}{k_n}, \quad n = \{\text{L}, \text{T}\}, \quad (3.2)$$

with L and T denoting the longitudinal and transverse polarizations of the elastic waves, respectively. The wavenumber  $k_s = \omega \delta t / \delta x$  is defined by  $\omega$  the angular frequency,  $\delta x$  the fixed spatial step and  $\delta t$  the time delay which is an adjustable parameter. The wavenumber of the synthesized plane wave is equal to  $k_n = \omega / c_n$  with  $c_n$  the phase velocity of the wave having a  $n$ -polarization. Then, the times of flight (TOF) and the amplitudes of the synthesized plane waves are obtained by convolving the signal  $s(t)$  with a complex Morlet wavelet.<sup>164</sup> To identify the elastic coefficients of an anisotropic plate,

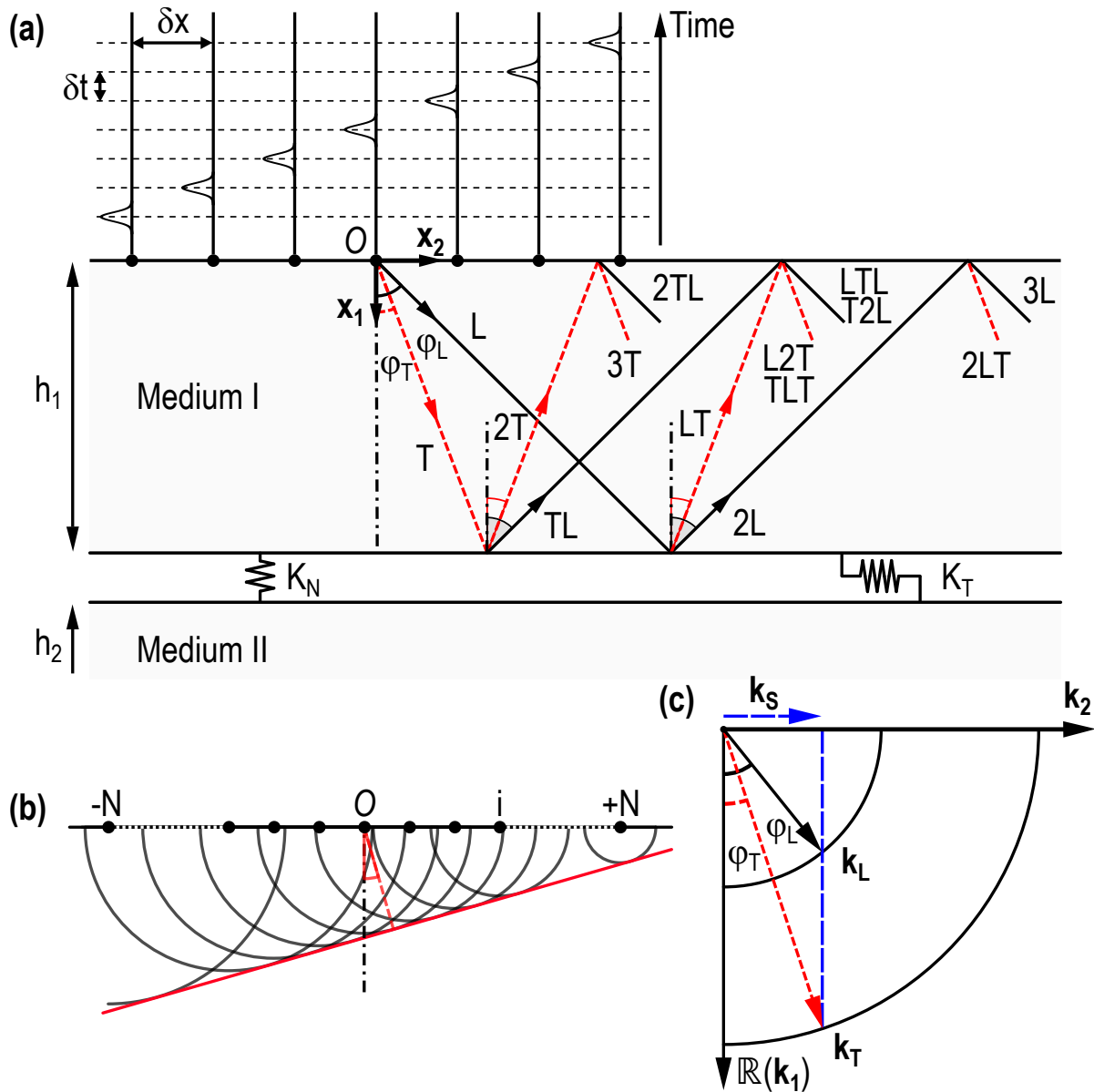


Figure 3.1 – (a) Representation of the elastic plane waves that are synthesized in the medium I. First, a laser line source, of infinite length in the  $x_3$ -direction, is moved over the sample surface in  $2N + 1$  positions with a constant  $\delta x$ -step. Secondly, a time delay  $\delta t$  is applied between the laser pulses, in post-processing, to synthesized longitudinal (L) and transverse (T) plane waves. (b) The application of delays between the  $2N + 1$  sources leads to constructive and destructive interferences between the divergent elastic waves, resulting in the generation of a plane wave. (c) Slowness diagram of the longitudinal and transverse plane waves that are synthesized by imposing the wave vector  $k_s = \omega \delta t / \delta x$  with  $\omega$  the angular frequency.

the TOF of the synthesized plane waves was measured either in transmission<sup>164</sup> or in reflection.<sup>165</sup>

### 3.2.2 Application for the nondestructive evaluation of adhesive bondings

In this chapter, the aim is to quantify the mechanical strength of structural adhesive bonding using this technique. Thus, not only the arrival times, but also the amplitudes of the plane waves reflected from the bonding interface, are considered. Indeed, the studied structure is represented in Fig. 3.1(a) and is composed of an elastic plate of thickness  $h_1$  bonded on a thicker medium of thickness  $h_2$ . Both media are assumed to be linear, homogeneous and isotropic. In addition,  $h_2$  is assumed to be much larger than  $h_1$ ; hence the lower elastic medium is modeled acoustically as a half-space, i.e., the following treatment is applied over a measurement time ensuring that no wave reflected from the bottom surface of the lower medium is in the signal. Furthermore, the acoustic wavelengths that are considered later are assumed to be greater than the thickness of the adhesive joint. Thus, normal ( $K_N$ ) and transverse ( $K_T$ ) distributions of interfacial stiffnesses, illustrated by springs in Fig. 3.1(a), are used to model the bonding.<sup>178–180</sup> This modeling is deduced from the simplification of the transfer matrix formalism,<sup>147,157</sup> detailed in the Appendix B. It allows to couple displacements and stresses between media I and II.

The sum of all the signals  $s_i(t + i\delta t)$ , in Eq. (3.1), is illustrated in Fig. 3.1(b). The application of time delay  $\delta t$ , in a post-processing step, leads to constructive and destructive interferences that result in the synthesis of plane waves. As shown in the slowness diagram in Fig. 3.1(c), the choice of the wavenumber  $k_s$  in Eq. (3.2), linked to the ratio  $\delta t/\delta x$ , favors the generation of a longitudinal plane wave L and a transverse one T of defined steering angles  $\varphi_n$ . Therefore, the synthesized plane waves that propagate in the medium I are represented in Fig. 3.1(a). Two incident plane waves L and T are reflected from the interface according to Snell's laws. Thus, the longitudinal plane wave L is reflected as a wave that retains the same polarization [which is noted 2L in Fig. 3.1(a)] and a wave with a polarization conversion (LT). It is the same for the incident transverse plane wave T which is reflected as a transverse (2T) and longitudinal (TL) plane waves. Then, these four waves are reflected from the free surface of the medium I, in  $x_1 = 0$ , and so on.

The interest of using this technique is that the amplitudes of the reflected waves are related to the reflection coefficients from the bonding interface. In fact, the expressions of these coefficients are defined by the mechanical properties of media I and II but also by

the coupling conditions at the interface. Thus, a modification of the mechanical coupling between two media leads to an evolution of the reflection coefficients and consequently to a change in the amplitudes of the reflected plane waves.

The strategy adopted in this chapter is to solve an inverse problem to find the normal ( $K_N$ ) and transverse ( $K_T$ ) interfacial stiffnesses with the amplitudes of the reflected plane waves. This requires the calculation of the direct problem, i.e., finding the amplitudes of the reflected plane waves by knowing the interfacial stiffnesses. This will be detailed in the following section.

### 3.3 Solving the direct problem

Two approaches were studied to solve the direct problem: one based on analytic formulas taking the directivity pattern of an array of thermoelastic sources into account and another based on semi-analytic simulations to numerically solve the electromagnetic, thermal and elastodynamic problems. These two methods will be presented in Sec. 3.3.1 and 3.3.2, respectively. In addition, the choice of the second method rather than the first, for the subsequent resolution of the inverse problem, will be justified.

#### 3.3.1 Analytic formulation

The first approach to solve the direct problem was to calculate the amplitudes of the reflected plane waves using analytic formulas, as reported in the literature.<sup>176,181,182</sup> The goal was to find the theoretical amplitudes, as a function of the steering angle  $\varphi_n$  defined in Eq. (3.2), of all plane waves reflected from the bonding interface illustrated in Fig. 3.1(a): 2L, LT, TL, 2T, etc. Assuming that both the bonding interface and the observation point are in the far field, the amplitudes of these reflected plane waves can be obtained by considering the directivity pattern of the array of thermoelastic sources, the propagation path of plane waves, the reflections from the bonding interface (see Appendix C for detailed calculations of the reflection coefficients) and the laser detection at the free surface of medium I. However, in the cases we are studying, the observation point is in the near field of the thermoelastic sources because the thickness of the medium I is of the order of a millimeter. It implies that the directivity pattern of the thermoelastic sources, notably calculated in the far field by Raetz *et al.*,<sup>183</sup> cannot be used here. In addition, this analytic approach leads to complicated formulas where a multitude of plane wave reflections have to be accounted for. Indeed, as shown in Fig. 3.1(a), an incident plane wave is reflected

### 3.3. Solving the direct problem

---

as two plane waves of different polarization at each reflection from the bonding interface or the upper free surface of the medium I. Hence, the number of analytic formulas to calculate all the reflected plane waves increases rapidly with time.

For all these reasons, another approach has been selected to solve the direct problem. The choice was made to use semi-analytic simulations to numerically solve the electromagnetic, thermal and elastodynamic problems. This method, presented in Sec. 3.3.2 and fully described in Chap. 2, provides fast and accurate simulated data. Moreover, it allows solving the multiphysical problem without using the far-field assumption, unlike the previous approach based on directivity patterns of opto-acoustic sources.

#### 3.3.2 Semi-analytic model

The resolution of the direct problem, i.e., the simulation of laser-generated ultrasound in the bonded structure, is achieved with the semi-analytic method presented in Chap. 2. This numerical approach is notably inspired by the studies of Audoin *et al.*<sup>148,184</sup> Our proposed semi-analytic model provides accurate results in a relatively short computing time compared to other numerical techniques, such as the Finite Element Method (FEM)<sup>152,153</sup> or the Finite Difference Method (FDM).<sup>154</sup> Accuracy and rapidity are two advantages of real interest for inverse problem solving and justify this choice for the cases studied in this chapter. Obviously, if more complex geometries than layered plates with parallel surfaces have to be investigated, the FEM or the FDM should be preferred.

The possibilities offered by the semi-analytic model, detailed in Chap. 2, are numerous. It is of primary importance to depict with the model the whole physics involved in the generation and propagation of the laser-generated elastic waves, as close to reality as possible, in order to get reliable quantitative information about the bonding. To ensure this, the proposed model allows to consider a tilted laser line source, of infinite length in the  $\mathbf{x}_3$ -axis. The temporal and spatial Gaussian profiles of this thermoelastic source are taken into account. The electromagnetic transmission and reflection of the incident laser beam in the multilayer are calculated and the optical penetration is accounted for. The solution to the electromagnetic problem allows to obtain the power densities dissipated into heat which is used as source terms for solving the heat diffusion problem. Conduction and convection phenomena are considered to find the amplitudes of the thermal waves that are diffusing in the structure. Then, analytic solutions of the displacement fields generated by the thermal expansion are determined in the Fourier domain. Subsequently, a double numerical inverse Fourier transform in space and time is performed to find

the displacement field in the time domain. The thermal coupling between media I and II is obtained with a thermal resistance which is defined from the thermal properties of all the sublayers inserted between media I and II. Electromagnetic and mechanical coupling conditions are taken into account with transfer matrices.<sup>147,157</sup> This extended semi-analytic model, although restricted to two-dimensional geometries for now, has been thought to allow the simulation of the propagation of laser-generated elastic waves in multilayer structures made of any materials respecting the assumptions listed in Sec. 2.2.

In sections 3.4 and 3.5, this numerical model is applied to solve inverse problems involving bonded aluminum substrates. Thus, further assumptions are formulated for the resolution of electromagnetic, thermal and elastodynamic problems.

First, perfect electromagnetic and thermal coupling between media I and II is assumed. Indeed, the thermoelastic source remains localized at the surface of medium I because (i) the optical penetration depth of a normal incident laser beam in aluminum is equal to 4.7 nm along the  $\mathbf{x}_1$ -axis (@  $\lambda_{\text{opt}} = 532$  nm) and (ii) the thermal penetration depth is equal to  $\sqrt{2D_{11}/\omega} = 2.0$   $\mu\text{m}$  with the thermal diffusivity of aluminum  $D_{11} = 62$   $\mu\text{m}^2$   $\mu\text{s}^{-1}$  and the angular frequency  $\omega = 2\pi f$  rad  $\mu\text{s}^{-1}$ , with  $f = 5$  MHz. Both optical and thermal penetration depths are negligible compared to the thickness of the medium I, which is of the order of a millimeter. Thus, perfect conditions of electromagnetic and thermal coupling are imposed between media I and II because none of these waves will interact with the bonding interface.

Secondly, the mechanical coupling between two aluminum substrates is modeled with normal ( $K_N$ ) and transverse ( $K_T$ ) interfacial stiffnesses<sup>178</sup> [shown in Fig. 3.1(a)]. This model results from the simplification of the transfer matrix<sup>147,157</sup> that links displacements and stresses between the upper and lower surfaces of an elastic plate. For a layer with homogeneous, linear and isotropic mechanical properties, the complete transfer matrix is given in Appendix B. Assuming that the acoustic wavelengths are large with respect to the adhesive joint thickness, this transfer matrix can be simplified into an identity matrix having two extra-diagonal terms:  $K_N$  and  $K_T$ . It implies a continuity of stresses ( $\sigma_{11}$ ,  $\sigma_{12}$ ) and a discontinuity of displacements ( $u_1$ ,  $u_2$ ) at the interface between media I and II at  $x_1 = h_1$  [see Fig. 3.1(a)], which gives

$$\sigma_{11}^I|_{x_1=h_1} = \sigma_{11}^{II}|_{x_1=h_1} = K_N(u_1^{II}|_{h_1} - u_1^I|_{h_1}), \quad (3.3)$$

$$\sigma_{12}^I|_{x_1=h_1} = \sigma_{12}^{II}|_{x_1=h_1} = K_T(u_2^{II}|_{h_1} - u_2^I|_{h_1}). \quad (3.4)$$

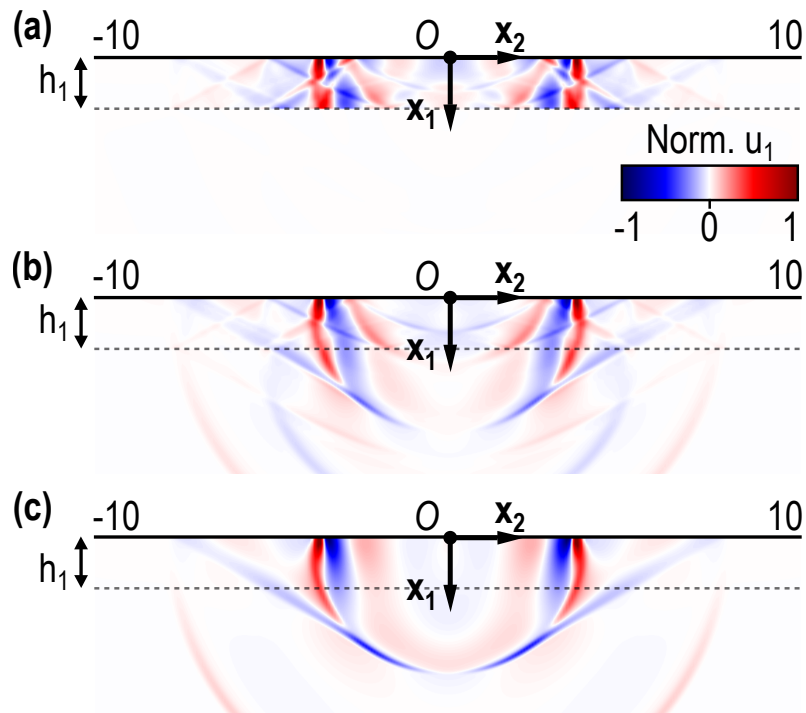


Figure 3.2 – Results of semi-analytic simulations in three different cases. Snapshots at  $t = 1.25 \mu\text{s}$  of the normalized normal displacement  $u_1$  in a bi-layer structure with normal and transverse interfacial stiffnesses [illustrated in Fig. 3.1(a)] equal to (a)  $K_N = K_T = 10^{-3} \text{ kN mm}^{-3}$  for the decoupling case, (b)  $K_N = 10^3 \text{ kN mm}^{-3}$  and  $K_T = 10^1 \text{ kN mm}^{-3}$  for the intermediate coupling, (c)  $K_N = K_T = 10^5 \text{ kN mm}^{-3}$  for the high mechanical coupling between media I and II.

### 3.3.3 Results of semi-analytic simulations

Numerical results achieved with this semi-analytic model are plotted in Fig. 3.2. Note that the dashed horizontal gray line stands for the interface between media I and II. The bilayer structure is composed of an aluminum plate, of thickness  $h_1 = 1.45$  mm, mechanically coupled to a semi-infinite aluminum medium. Both media are considered homogeneous, linear and isotropic of density  $\rho = 2.7 \cdot 10^3 \text{ kg m}^{-3}$  and elastic coefficients equal to  $C_{11} = 109.9$  GPa and  $C_{66} = 26.5$  GPa. Concerning the thermoelastic source, a normal incident laser line pulse, of infinite length along the  $\mathbf{x}_3$ -axis, is considered. The pulse duration is equal to  $\tau_p = 8$  ns, which corresponds to the full width at half maximum (FWHM) of the temporal Gaussian profile. The width of the laser line source along the  $\mathbf{x}_2$ -axis is equal to  $a_s = 0.2$  mm, which corresponds to the FWHM of the spatial Gaussian profile. Three cases are simulated for different values of normal and transverse interfacial stiffnesses. The first case is the simulation of the normalized normal displacement  $u_1(x_1, x_2, t)$  with  $K_N = K_T = 10^{-3} \text{ kN mm}^{-3}$ . This is equivalent to a mechanical decoupling between media I and II, i.e., ultrasonic waves are fully reflected from the interface, as shown in Fig. 3.2(a). The second case deals with an intermediate mechanical coupling with  $K_N = 10^3 \text{ kN mm}^{-3}$  and  $K_T = 10^1 \text{ kN mm}^{-3}$ . In Fig. 3.2(b), simulated elastic waves are reflected from the interface at  $x_1 = h_1$  and are also transmitted into the medium II. The third case is the simulation of ultrasonic propagation when  $K_N = K_T = 10^5 \text{ kN mm}^{-3}$ , which corresponds to a high mechanical coupling. Since the two media are the same, a total transmission of the elastic waves at the interface is observed in Fig. 3.2(c). This simulation is analogous to what would have been obtained in an elastic half-space.

Such numerical results obtained with the semi-analytic model are the basis of the here-proposed method to solve the inverse problem in order to obtain quantitative estimate of the adhesive bonding through values of  $K_N$  and  $K_T$ .

## 3.4 Resolution of inverse problems with simulated data

An inverse method is proposed to identify the values of interfacial stiffnesses,  $K_N$  and  $K_T$ , using the amplitudes of the synthesized plane waves reflected from the bonding interface. The method is illustrated in Fig. 3.3, and is based on the two previous sections: the plane wave synthesis in Sec. 3.2 and the resolution of the direct problem in Sec. 3.3. First of all, the plane wave synthesis is applied on a B-scan which depends on time  $t$  and position  $x_2$ . A large number of delays  $\delta t$  are imposed on these temporal signals to

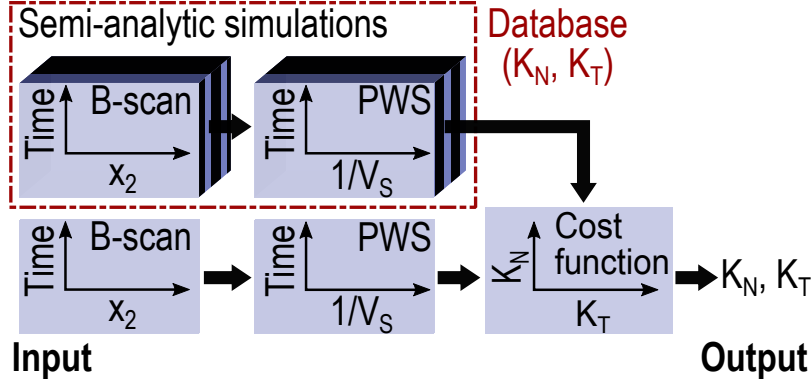


Figure 3.3 – Diagram of the method to solve the inverse problem. The input data is a B-scan where the plane wave synthesis (PWS) is applied. It is then compared to a database of semi-analytic simulations for different values of interfacial stiffnesses. The minimum of the cost function is finally searched to identify the values of  $K_N$  and  $K_T$  which gives the lowest mean squared error (MSE) between the input and the database.

synthesize plane waves with different steering angles  $\varphi_n$  with  $n = \{L, T\}$ . The adjustable parameter to control this angle is defined as  $1/V_S = \delta t/\delta x$  in Fig. 3.3, with  $\delta x$  the fixed spatial step of the B-scan along the  $\mathbf{x}_2$ -axis and  $\delta t$  the delay that can be modified. This input data is then compared to a database resulting of a set of semi-analytic simulations with different values of interfacial stiffnesses  $K_N$  and  $K_T$ . Thus, the normal and transverse interfacial stiffnesses are identified by finding the minimum of a cost function which will be defined in the following.

The algorithm presented in Fig. 3.3 is tested with simulated input data before being used with experimental input data in Sec. 3.5. This ensures that the inverse method works with input signals which have known interfacial stiffnesses. Furthermore, these simulated temporal signals were noised to get closer to experimentally measured waveforms. Three cases have been studied with different values of normal and transverse interfacial stiffnesses to represent three main situations: low, intermediate and high mechanical coupling between media I and II. The first case deals with low values of interfacial stiffnesses equal to  $K_N = K_T = 10^{-3} \text{ kN mm}^{-3}$ . In this specific situation, the mechanical coupling is so weak that the elastic waves are fully reflected from the interface and no waves are transmitted in the medium II [see simulation results in Fig. 3.2(a)]. Hence, this simulation is similar to that obtained for laser-generated ultrasound in an aluminum plate. Concerning the input data of the algorithm, a B-scan is simulated with the semi-analytic model (introduced in

Chap. 2) succinctly presented in the Sec. 3.3.2. A Gaussian noise is applied to the temporal signals to be closer to an experimental case with a signal-to-noise ratio  $\text{SNR} \approx 20$  dB. Then, the plane wave synthesis is applied on these temporal signals following the sum introduced in Eq. (3.1). The delay  $\delta t$ , between the signals  $s_i(t)$  and  $s_{i+1}(t)$ , is applied in the Fourier domain by multiplying the fast Fourier transform of  $s_i(t)$  by  $e^{j\omega i\delta t}$  with  $j$  the imaginary number,  $\omega$  the angular frequency and  $i \in [-N, N]$  the source position shown in Fig. 3.1(b). For each steering angle imposed by the delay  $\delta t$ , the summed signal  $s(t)$  is convolved with a complex Morlet wavelet having a center frequency of 5 MHz and a bandwidth at -3 dB equal to 4 MHz. This allows to detect the time of flight and the amplitudes of the synthesized plane waves reflected from the interface. As the laser pulse generates wide-band ultrasonic waves, the convolution by the complex Morlet wavelet acts as a band-pass filter to avoid considering high-frequency waves whose wavelengths are too short for the model of the bonded assembly with interfacial stiffnesses to be accurate. By varying the parameter  $1/V_S = \delta t/\delta x$  between  $\pm 0.2 \mu\text{s mm}^{-1}$  with a  $3.2 \cdot 10^{-3} \mu\text{s mm}^{-1}$  step, 129 steering angles are imposed. It allows to synthesize longitudinal plane waves with steering angles  $\varphi_L$  up to  $\pm 90^\circ$  and transverse plane waves with  $\varphi_T$  between  $\pm 40^\circ$ . Indeed, beyond this angle, transverse waves of relatively low amplitudes are generated according to the directivity pattern of a thermoelastic source.<sup>141</sup> These post-processed signals are then compared to a database composed of 1089 semi-analytic simulations with different values of  $K_N$  and  $K_T$  from  $10^{-3}$  to  $10^5 \text{ kN mm}^{-3}$ , with a step of  $10^{0.25} \text{ kN mm}^{-3}$ . It takes about 30 hours to compute this complete database on a laptop (Intel<sup>®</sup> Core<sup>™</sup> i7-6500U CPU @ 2.5 GHz, 16 GB RAM). Comparisons are made using a cost function based on the mean squared error (MSE) between the results of the plane wave synthesis applied on the input data and on the simulations of the database.

For the first studied case, where the input values are equal to  $K_N = K_T = 10^{-3} \text{ kN mm}^{-3}$  [simulation in Fig. 3.2(a)], the cost function is provided in Fig. 3.4(a). The identified values of  $K_N$  and  $K_T$  are found when this function is minimum. This is represented by the red rectangle in Fig. 3.4(a), considering an uncertainty margin of  $\pm 0.1$  dB on the minimum value of the cost function. This margin is chosen to account for uncertainties due to the addition of noise to the input data, which results in very small local variations of the cost function compared to those observed at a more global scale. The identified values of  $K_N$  and  $K_T$  are reported in Tab. 3.1. In this case, the cost function is effectively the lowest for low values of interfacial stiffnesses in the range  $[10^{-3}, 10^{-0.5}] \text{ kN mm}^{-3}$  for  $K_N$  and  $[10^{-3}, 10^{-0.75}] \text{ kN mm}^{-3}$  for  $K_T$ . The fact that the identified values are within a given

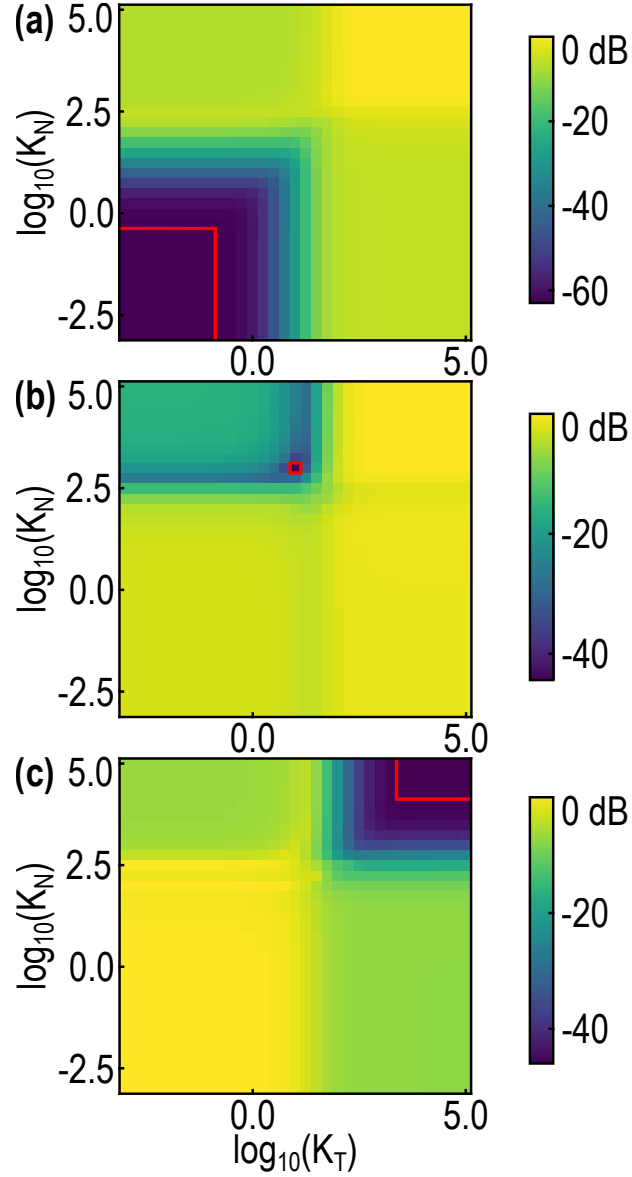


Figure 3.4 – Cost functions (in dB) obtained when the plane wave synthesis is applied on simulated B-scans, with the addition of noise, for interfacial stiffnesses equal to: (a)  $K_N = K_T = 10^{-3} \text{ kN mm}^{-3}$ , (b)  $K_N = 10^3 \text{ kN mm}^{-3}$  and  $K_T = 10^1 \text{ kN mm}^{-3}$ , (c)  $K_N = K_T = 10^5 \text{ kN mm}^{-3}$ . The red rectangles indicate the location of the minimum of each cost function with an uncertainty margin of  $\pm 0.1 \text{ dB}$ .

Table 3.1 – Results obtained by solving the inverse problem with noisy simulations as input data. Three different cases are processed for input values of  $K_N$  and  $K_T$  given in  $\text{kN mm}^{-3}$ : low, intermediate and high mechanical coupling between media I and II. The interfacial stiffnesses identified using the minima of the cost functions are reported below.

Simu. data	Input data		Identified parameters	
	$K_N$	$K_T$	$K_N$	$K_T$
Low coupling	$10^{-3}$	$10^{-3}$	$[10^{-3}, 10^{-0.5}]$	$[10^{-3}, 10^{-0.75}]$
Int. coupling	$10^3$	$10^1$	$10^3$	$10^1$
High coupling	$10^5$	$10^5$	$[10^{4.25}, 10^5]$	$[10^{3.75}, 10^5]$

range is due to the added noise, as already discussed, but also to the fact that the reflection coefficients of the interface are not sensitive enough to small variations in mechanical coupling when interfacial stiffnesses are already low (i.e., less than  $1 \text{ kN mm}^{-3}$ ). For the intermediate mechanical coupling case, where the cost function is plotted in Fig. 3.4(b), it is different. The minimum of the cost function is precisely equal to the value of the input interfacial stiffnesses which are equal to  $K_N = 10^3 \text{ kN mm}^{-3}$  and  $K_T = 10^1 \text{ kN mm}^{-3}$ . Thus, the reflection coefficients are highly sensitive to a change of mechanical coupling in this range of interfacial stiffnesses. For the high mechanical coupling case, the cost function is represented in Fig. 3.4(c). The identified values of interfacial stiffnesses are in the range  $[10^{4.25}, 10^5] \text{ kN mm}^{-3}$  for  $K_N$  and  $[10^{3.75}, 10^5] \text{ kN mm}^{-3}$  for  $K_T$ . This is consistent with the input values of interfacial stiffnesses that were equal to  $K_N = K_T = 10^5 \text{ kN mm}^{-3}$ . As in the case of low mechanical coupling, the reflection coefficients are less sensitive to small variations of mechanical coupling when interfacial stiffnesses are already high (i.e., more than  $1 \text{ MN mm}^{-3}$ ); that is why the identified values are given within a particular range in Tab. 3.1.

The results of the plane wave synthesis applied on simulated data, with the addition of Gaussian noise, are shown in Fig. 3.5 for different values of  $K_N$  and  $K_T$ . The times of flight of the synthesized plane waves 2L, LT, TL and 2T [see Fig. 3.1(a) for the denomination] are plotted for the different cases. The visual analysis to relate the amplitudes of the reflected plane waves to the values of  $K_N$  and  $K_T$  can be difficult to perform with the naked eye because of (i) the high number of plane waves that are reflected by the bonding interface in some cases and (ii) the complexity of analyzing the variations from one image

3.4. Resolution of inverse problems with simulated data

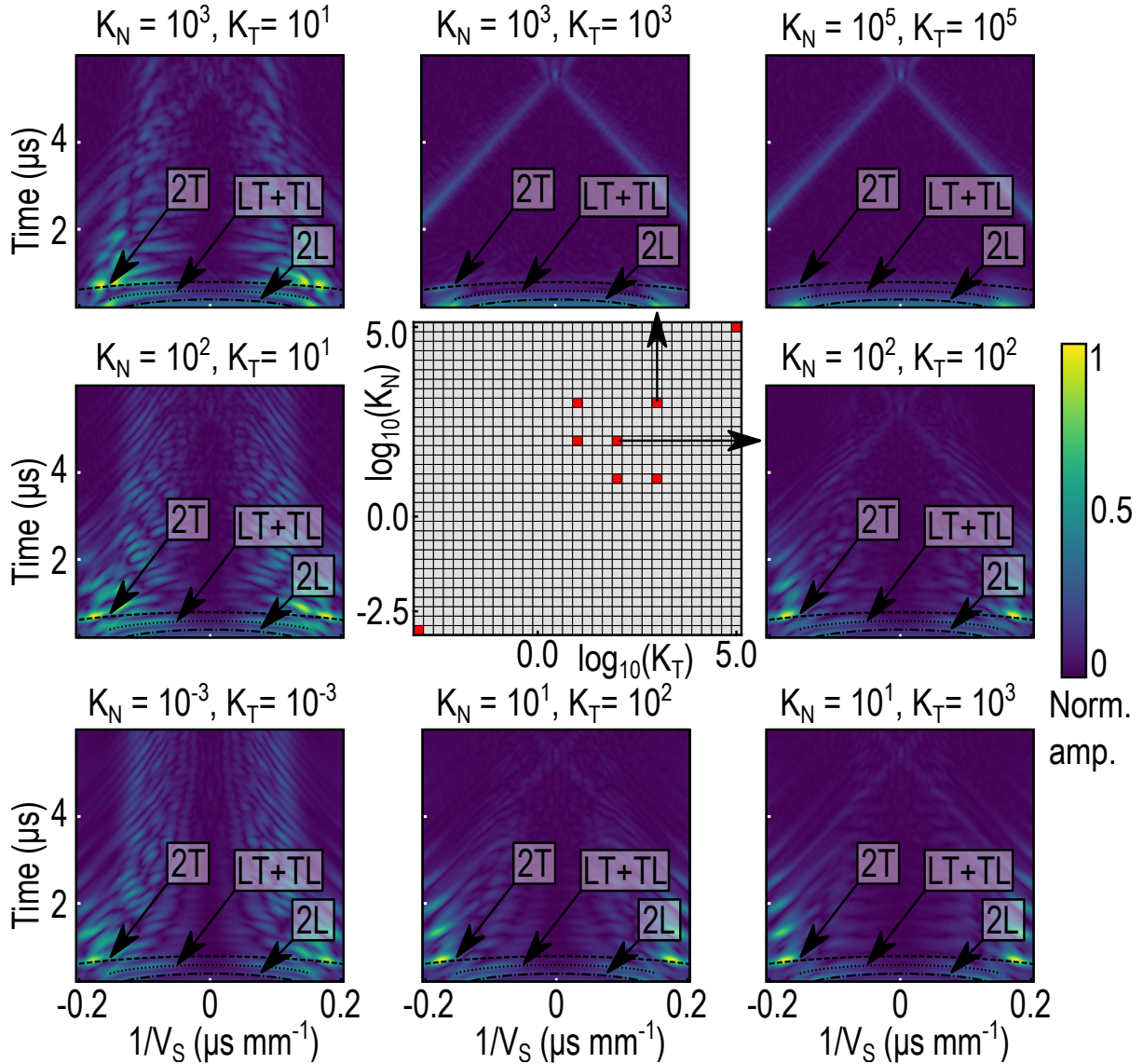


Figure 3.5 – Results of the plane wave synthesis applied on simulated data, with the addition of Gaussian noise, for different values of  $K_N$  and  $K_T$  (8 different cases). The times of flight of the reflected synthesized plane waves are identified as: dash-dotted line for the 2L longitudinal plane wave, dashed line for the 2T transverse plane wave and dotted line for the sum of the LT and TL plane waves.

to another without a suitable comparison tool. Therefore, the strategy adopted here is to numerically compare the input data with all the simulations included in the database to solve the inverse problem.

The interest of using the plane wave synthesis to compare the input data to the database and not to directly compare the B-scans (as it could be thought by looking at Fig. 3.3) is

justified for two main reasons. First, the application of the plane wave synthesis implies a sum on all temporal signals [see Eq. (3.1)] of the B-scan between  $\pm 16$  mm (on 401 positions in the  $\mathbf{x}_2$ -direction). Thus, the sum of these signals leads to the reduction of the noise level, as observed experimentally when temporal signals are averaged to improve the signal-to-noise ratio. Indeed, the noisy parts of temporal signals that do not contribute to the synthesis of plane waves are reduced and the signals that lead to the synthesis of plane waves are amplified.

Secondly, this post-processing technique allows to filter the contribution of surface acoustic waves, here essentially Rayleigh waves, which propagate at the free surface of the medium I in the  $\pm \mathbf{x}_2$ -direction and do not interact with the bonding. This enables to analyze mainly plane waves which are synthesized from bulk waves reflected from the bonding interface and which contain the necessary information concerning the mechanical coupling conditions between the two bonded media. The only contributions of Rayleigh waves to the signals plotted in Fig. 3.5 are visible for the cases  $K_N = K_T = 10^3 \text{ kN mm}^{-3}$  and  $K_N = K_T = 10^5 \text{ kN mm}^{-3}$  (top right of Fig. 3.5). They correspond to the two inclined lines that crossed when  $1/V_S = 0$  at  $t_R = 5.5 \mu\text{s}$ . They are due to the fact that after this time  $t_R$ , no Rayleigh wave is visible on the B-scan. Thus, following the sum of all temporal signals when no delay is applied ( $1/V_S = 0$ ) and due to the convolution of this sum with the complex Morlet wavelet (see p. 80) a spot is visible at the intersection of these two inclined lines. Moreover, the slopes of these two lines are equal to the minimum and maximum positions of the B-scan ( $\pm 16$  mm). Their intersections with the  $1/V_S$ -axis (when  $t = 0$ ) are equal to  $\pm 1/V_R$  with  $V_R$  the Rayleigh wave speed. In addition, the time  $t_R$  at  $1/V_S = 0$  is equal to the absolute value of the slope of the line divided by  $V_R$ . These observations are visible only on these two cases because of the normalization of the figures. Indeed, for really high values of  $K_N$  and  $K_T$ , almost no wave is reflected from the bonding interface. Hence, the normalization is only done by the contribution of the source at very short time which makes these two lines visible at the top right of Fig. 3.5. The advantage of the plane wave synthesis is therefore to filter the Rayleigh wave contributions, even if the fact that the B-scan is bounded in the direction  $\mathbf{x}_2$  leads to the observation of inclined lines. However, they are not critical to the study of the synthesized plane waves reflected from the bonding interface because (i) these two inclined lines are also visible on the signals included in the database due to the same bounded simulated B-scans between  $\pm 16$  mm in the  $\mathbf{x}_2$ -direction and (ii) the positions of these two lines do not interfere with the reflected plane waves containing the information about the adhesive bonding unlike the case of the B-scans where the Rayleigh waves interfere

with reflective waves. This is why the plane wave synthesis is used to solve the inverse problem.

In this section, the results with simulated input data have been presented and it has been shown that the algorithm, illustrated in Fig. 3.3, allows the identification of interfacial stiffnesses from the amplitudes of the synthesized plane waves. In the following section, experimental input data is used to find the values of  $K_N$  and  $K_T$ .

## 3.5 Resolution of inverse problems with experimental data

The inverse problems were solved, in Sec. 3.4, to identify the values of normal and transverse interfacial stiffnesses from simulated signals. In this section, the algorithm presented in Fig. 3.3 is run with experimental input data. The aim is to identify two key parameters ( $K_N$  and  $K_T$ ) that model and characterize the practical adhesion between media I and II.

### 3.5.1 Sample preparation

Laser ultrasonic measurements have been performed on three samples. The first specimen was a 1.23 mm-thick aluminum alloy plate of aeronautical quality (6061 grade, Good-Fellow, United Kingdom) of lateral dimensions  $150 \times 150 \text{ mm}^2$ . Two other samples were composed of a 1.45 mm-thick 6061 aluminum alloy plates bonded with an aeronautical structural adhesive film (AF 191, 3M<sup>™</sup>, United States) on a 20 mm-thick aluminum alloy substrate. The lateral dimensions of these bonded assemblies were similar to those of the first aluminum plate. With regard to the manufacturing process, the aluminum alloy surfaces were first degreased with ethanol. Then, between the 1.45 mm-thick plate and the thicker substrate, strips of material about 5 mm-wide were placed on the edges of the surfaces. These strips were used to prevent the glue from leaking during curing and to control the thickness of the epoxy layer (equal to  $150 \mu\text{m}$ ). Next, a constant pressure was applied during curing with spring clamps, calibrated at 65 N, and homogeneously distributed around the sample.<sup>67</sup> One bonded sample was manufactured without defects (later called “nominal”), and another with an interfacial bonding defect between the top aluminum alloy plate (Al) and the epoxy layer. This degradation was introduced by applying one layer of release agent (R.A.) [Frekote<sup>®</sup> 44-NC<sup>™</sup> (Henkel, Germany)], with a clean lint-free cloth, on the degreased aluminum alloy surface.<sup>185</sup> This R.A. layer had the

effect of degrading the practical adhesion between the Al plate and the adhesive. This protocol led to a significant reduction in the structural mechanical strength of the bonding interface, while maintaining a mechanical coupling between two parts; they were not detached.

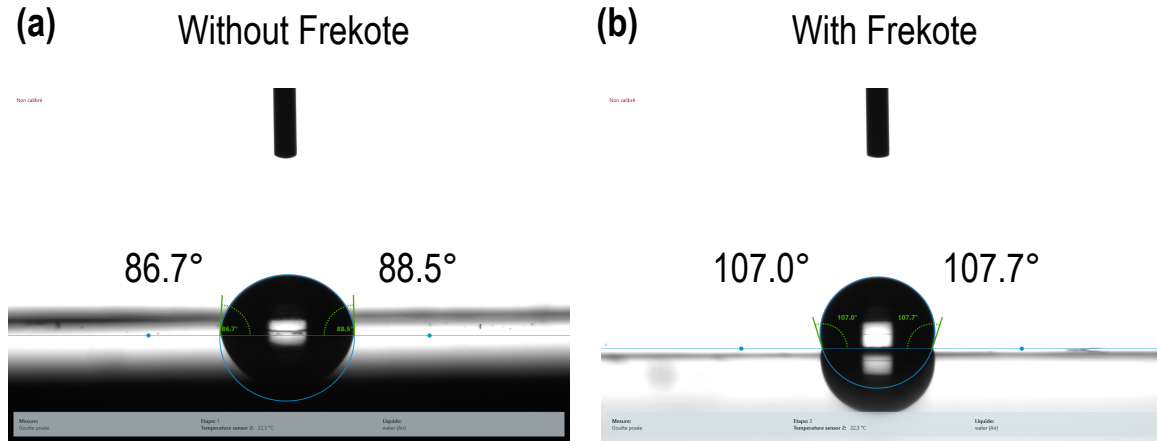


Figure 3.6 – Water droplet on an aluminum surface (a) without and (b) with one layer of Frekote.

For instance, in Fig. 3.6, a water droplet was deposited on an aluminum surface with and without one layer of Frekote. We can see that when the surface is not coated with Frekote, the contact angle is less than  $90^\circ$ . However, when the surface is coated with Frekote, the contact angle is greater than  $90^\circ$ . Thus, the layer of Frekote makes the aluminum surface more hydrophobic. These two bonded samples, with and without bonding defects, were cured simultaneously in a laboratory oven at  $150^\circ\text{C}$  for 3 hours with ramps up and down (heating and cooling) of  $2^\circ\text{C min}^{-1}$ . The longitudinal static strengths were measured of the order of 20 MPa for the nominal bond and 2 MPa for the sample with adhesion defects. These two bonded assemblies could not be distinguished by acoustic microscopy measurements carried out at 30 MHz.

### 3.5.2 Experimental set-up

A laser ultrasonic set-up, represented in Fig. 3.7, was used to acquire the experimental B-scans of the three specimens. A Q-switched Nd:YAG laser (InnoLas Laser GmbH, Germany, SpitLight Compact 400, 532 nm) delivering 8 ns pulses of 200 mJ, with a repetition rate of 10 Hz, was used to generate ultrasonic waves in the samples. The laser beam was first attenuated, using a  $\lambda/2$  plate to adjust the intensity, in order to remain in the

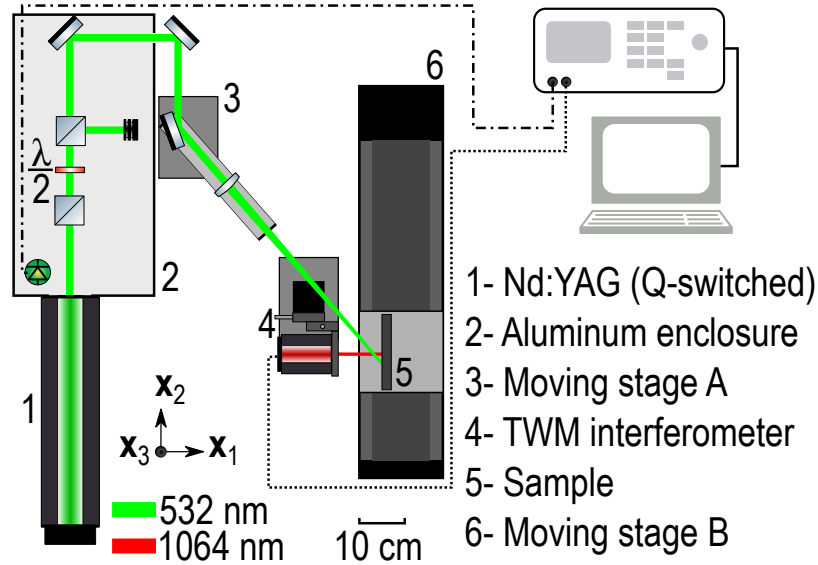


Figure 3.7 – Laser ultrasonic set-up for the acquisition of experimental B-scan.

thermoelastic (nondestructive) regime. It was then focused onto the surface sample with a cylindrical lens to obtain a line source oriented along the  $x_3$ -axis of about 10 mm. The Gaussian profile along the  $x_2$ -axis had a full width at half maximum (FWHM) equal to 0.2 mm. To acquire each B-scan, this laser line source was successively displaced to the  $2N + 1$  positions with the moving stage A, shown in Fig. 3.7. The spatial step  $\delta x$  along the  $x_2$ -axis was equal to 0.08 mm. Thus, the line source was moved to 401 positions over a total length of 32 mm. The normal displacement of the surface was measured with a two-wave mixing interferometer (Tecnar, Canada, TWM Laser Ultrasound Detector, 1064 nm, bandwidth 0.7–40 MHz). The laser detection spot, with a diameter at half maximum (FWHM) of 0.6 mm, was always positioned at the center of the generation sources array. Temporal signals were recorded with a Teledyne LeCroy HDO4054A oscilloscope and transferred to a computer for post-processing. The photodiode, at the output of the Nd:YAG laser cavity, was used to trigger the detection of the interferometer signal by the oscilloscope. For each laser line source position, 500 temporal signals were averaged to increase the signal-to-noise ratio ( $\text{SNR} \approx 20$  dB).

### 3.5.3 Simple case of the free-standing plate

For the aluminum alloy plate of thickness 1.23 mm, the experimental B-scan acquired with this set-up is represented in Fig. 3.8(b). A good agreement is qualitatively observed between the experiment and the simulation performed with the semi-analytic model, as

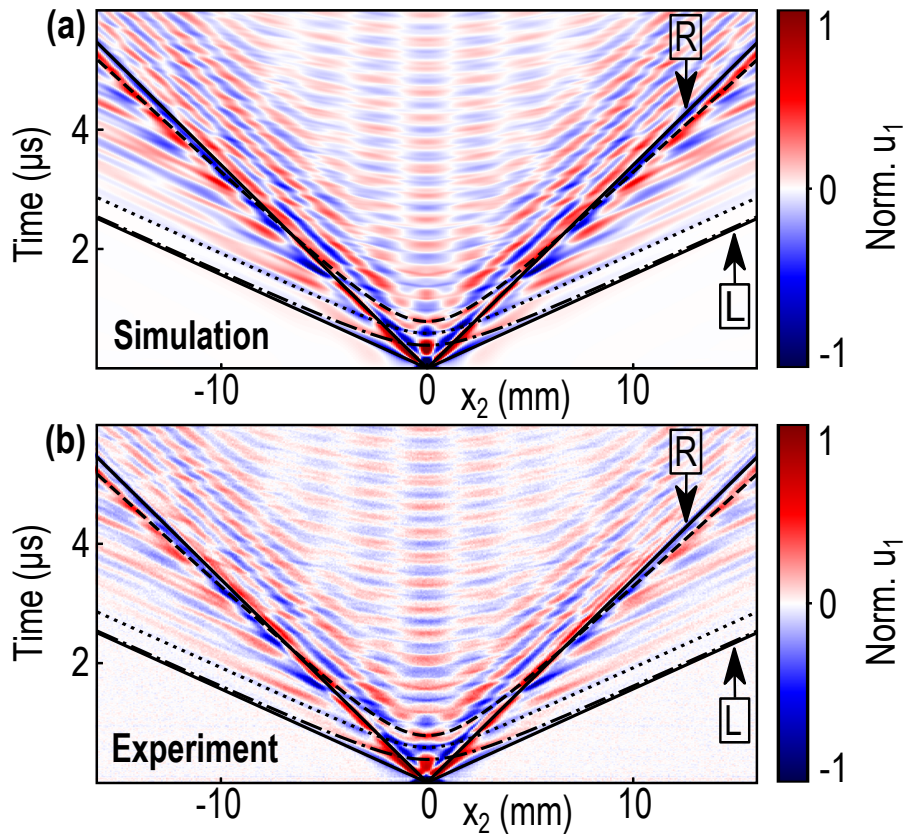


Figure 3.8 – Comparisons between simulation and experiment for the 1.23 mm-thick aluminum alloy plate. (a) Simulated B-scan obtained with the semi-analytic model described in Chap. 2. The normalized normal displacements at the top surface of the aluminum alloy plate are simulated as a function of time and position  $x_2$ . (b) Experimental B-scan measured with the set-up presented in Fig. 3.7. The longitudinal wave (L) and the Rayleigh wave (R) are identified with solid lines.

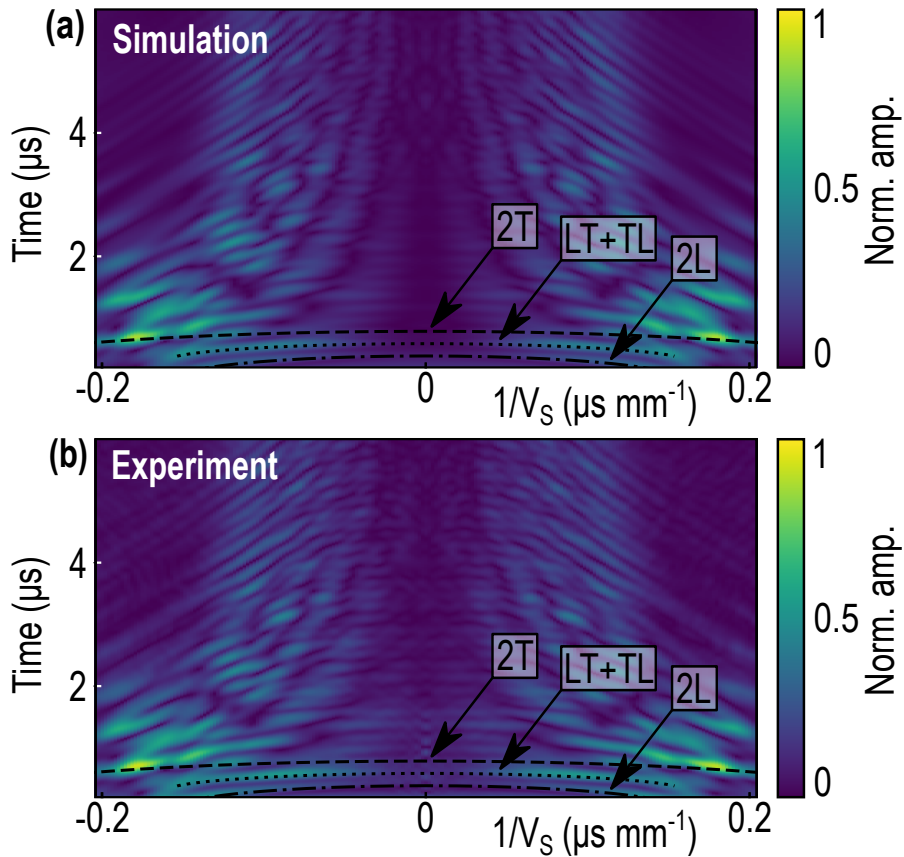


Figure 3.9 – Comparisons between simulation and experiment for the 1.23 mm-thick aluminum alloy plate. (a-b) Results of the plane wave synthesis applied on the simulated [Fig. 3.8(a)] and experimental [Fig. 3.8(b)] B-scans, respectively. The times of flight of the reflected synthesized plane waves are identified as: dash-dotted line for the 2L longitudinal plane wave, dashed line for the 2T transverse plane wave and dotted line for the sum of the LT and TL plane waves [previously illustrated in Fig. 3.1(a)].

shown in Fig. 3.8(a). The plane wave synthesis was then applied on these numerical and experimental B-scans following the same process and parameters as those presented in the previous section. The results are plotted in Fig. 3.9(a) and (b) for the simulation and the experiment, respectively. On these figures, the synthesized plane waves, illustrated in Fig. 3.1(a), can be identified using their times of flight. For instance, four reflected plane waves (2L, LT, TL, 2T) are represented in Fig. 3.9(a) and (b). As time increases, more and more plane waves are synthesized as an incident plane wave is reflected in two waves of longitudinal and transverse polarizations at each interface. This complicates the signal analysis because the total number of synthesized plane waves in the medium I is equal to  $2^{r+1}$ , with  $r$  the number of reflections. It is exactly for this reason that the amplitudes of the reflected plane waves were not analyzed separately, but a strategy based on inverse problem solving using all the reflected plane waves was adopted.

Following the same approach as presented in Sec. 3.4, inverse problems were solved to identify the interfacial stiffnesses ( $K_N$  and  $K_T$ ) of these three samples: the aluminum alloy plate and both bonded assemblies with and without adhesion defects. The experimental B-scans acquired with the laser ultrasonic set-up, shown in Fig. 3.7, were used as input data for the algorithm presented in Fig. 3.3. Then, the plane wave synthesis was applied on these temporal signals and compared to the database composed of 1089 semi-analytic simulations with different values of  $K_N$  and  $K_T$  from  $10^{-3}$  to  $10^5$  kN mm $^{-3}$ , with a step of  $10^{0.25}$  kN mm $^{-3}$ . These comparisons were based on the mean squared error (MSE) to obtain the  $K_N$  and  $K_T$  dependent cost functions plotted in Fig. 3.10. The red rectangles indicate the minimum of each cost function with an uncertainty margin of  $\pm 0.1$  dB. The identified values of  $K_N$  and  $K_T$  are reported in Tab. 3.2. For the aluminum alloy plate, the identified values are comprised between  $10^{-3}$  and  $10^{0.75}$  kN mm $^{-3}$  for  $K_N$ , and  $10^{-3}$  and  $10^{0.5}$  kN mm $^{-3}$  for  $K_T$ . This is consistent with the case presented in Sec. 3.4 where the algorithm was tested on simulated data with really low values of interfacial stiffnesses equal to  $K_N = K_T = 10^{-3}$  kN mm $^{-3}$ . The cost function was represented in Fig. 3.4(a) and this result is close to what is observed for the experimental case in Fig. 3.10(a). This first result allows to validate the method on a simple experimental case (free-standing plate) before applying the algorithm on bonded assemblies. It is important to note here that numerous physical phenomena must be accounted for in the simulations to obtain such results with experimental data. In particular, the thermal diffusion should be taken into account in the simulation, otherwise the inverse problem (not shown here) does not converge to  $K_N$  and  $K_T$  in low value ranges but gives values of  $K_N$  and  $K_T$  about  $10^{1.5}$  kN mm $^{-3}$ .

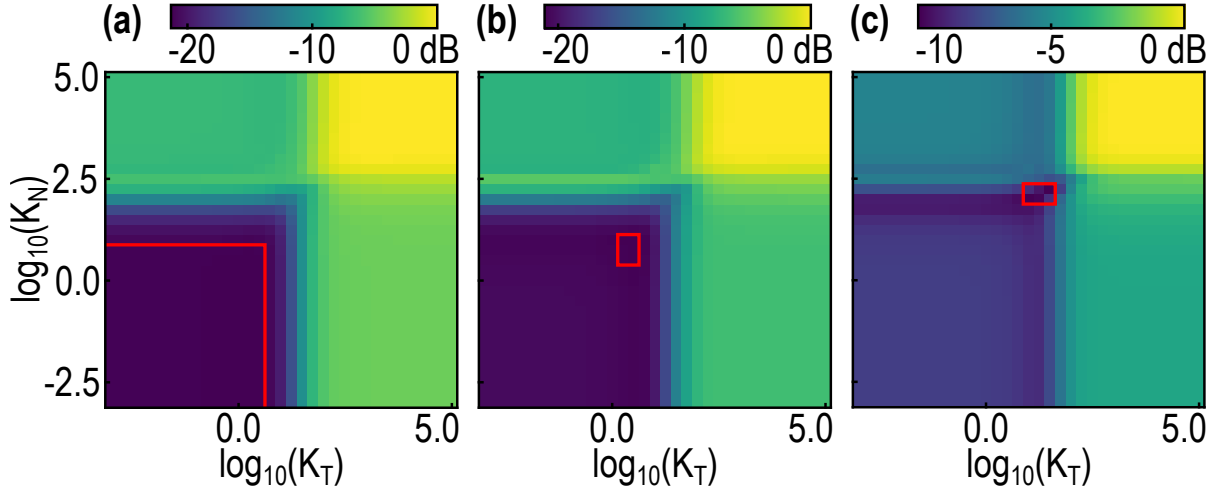


Figure 3.10 – Cost functions obtained when experimental B-scans of (a) an aluminum alloy plate, bonded assemblies Al/Ep/Al (b) with and (c) without release agent, are used as input data for the algorithm shown in Fig. 3.3. The red rectangles indicate the minimum of each cost function with an uncertainty margin of  $\pm 0.1$  dB.

### 3.5.4 Quantification and differentiation of two adhesive bonding conditions: nominal and degraded

The results are plotted in Fig. 3.10(b) for the bonded sample with adhesion defects and Fig. 3.10(c) for the nominal bonding. The identified values of  $K_N$  and  $K_T$  are reported in Tab. 3.2. For the degraded bonding, with the layer of release agent at one interface, the identified values are comprised between  $10^{0.5}$  and  $10^1$   $\text{kN mm}^{-3}$  for  $K_N$ , and  $10^{0.25}$  and  $10^{0.5}$   $\text{kN mm}^{-3}$  for  $K_T$ . For the nominal bonding, the identified values are higher and comprised between  $10^2$  and  $10^{2.25}$   $\text{kN mm}^{-3}$  for  $K_N$ , and  $10^1$  and  $10^{1.5}$   $\text{kN mm}^{-3}$  for  $K_T$ . Therefore, the method enables these two bonded samples to be distinguished, as it can be seen from the cost functions in Fig. 3.10(b) and (c). For the bonded sample with adhesion defects, the identified values of  $K_N$  and  $K_T$  are close to those achieved for the free-standing aluminum alloy plate. This is due to the fact that the lack of adhesion caused by the layer of release agent results in weaker mechanical coupling which has an effect on the amplitudes of the reflected plane waves, making the method sensitive to this type of degradation. Furthermore, in Fig. 3.10, the minimum of the cost function is higher for the nominal bonding (-10 dB) than for the two other cases (-20 dB). A possible explanation is that the adhesive layer has an influence on the experimental temporal signals that is not

Table 3.2 – The interfacial stiffnesses identified by solving the inverse problem with experimental B-scans as input data in the three different experimental cases: aluminum alloy plate, adhesive bonding Al/Ep./Al with release agent (R.A.) and without (called nominal bonding).

Exp. data	Input data		Identified parameters	
	$K_N$	$K_T$	$K_N$	$K_T$
Alu. plate	-	-	$[10^{-3}, 10^{0.75}]$	$[10^{-3}, 10^{0.5}]$
Bond. with R.A.	-	-	$[10^{0.5}, 10^1]$	$[10^{0.25}, 10^{0.5}]$
Nom. bond.	-	-	$[10^2, 10^{2.25}]$	$[10^1, 10^{1.5}]$

fully captured by the simulations of the database. Indeed, the modeling of the bonding was voluntarily chosen with only two effective parameters related to the mechanical strength of the bonding, to avoid the identification of a large set of parameters. In fact, to solve the inverse problem with a finer modeling of the bonding,<sup>112,114</sup> eight parameters must be considered: two interfacial stiffnesses for the upper interface (medium I/adhesive), two others for the lower interface (adhesive/medium II), and four parameters for the adhesive layer [one for the thickness, two for the elastic coefficients (if the adhesive is assumed to be isotropic), and one for the mass density]. To give an order of magnitude, considering thirty values for each of the eight parameters, 656.1 billion simulations of laser-generated ultrasound have to be performed to generate the database used for the algorithm presented in Fig. 3.3 (compared to the 1089 simulations required in this chapter). By keeping calculation time within a reasonable range, the model used here and limited to the variation of two key parameters,  $K_N$  and  $K_T$ , demonstrates the ability to quantitatively distinguish the three studied specimens from a simplified, although physically justified, model.

### 3.6 Conclusion

A laser ultrasonic method has been presented for the NDE of adhesive bonding. Elastic plane waves are synthesized with several steering angles with respect to the bonding interface. The synthesized plane waves are used to solve an inverse problem to identify normal and transverse interfacial stiffnesses ( $K_N, K_T$ ) that model the mechanical coupling between two bonded substrates. The developed algorithm is first validated with input

### 3.6. Conclusion

---

data simulated with a semi-analytic model, where Gaussian noise was added. Next, experimental signals acquired on an aluminum alloy plate and on two bonded assemblies (with and without adhesion defects) are used as input data. This method allows to distinguish these three specimens by finding the minima of cost functions based on the differences between the input data and a database composed of semi-analytic simulations for a large set of  $K_N$  and  $K_T$ . It is remarkable to note that solving inverse problems directly by comparing simulated and experimental B-scans do not lead to accurate results. This is due to the fact that the plane wave synthesis artificially improves the SNR and, above all, effectively filters the Rayleigh waves out of the bulk waves that actually contain the information about the bonding.

Concerning the limits of this approach, the mechanical properties of the bonded substrates must be known to obtain accurate simulations of the ultrasound propagation necessary for the creation of the database. Furthermore, this method provides average values of  $K_N$  and  $K_T$  for the scanned area (32 mm in our experiments); no local bonding defects can be detected. The next chapter is dedicated to propose a NDE method to locally quantify adhesive bondings. It is important to note that, in the method proposed in this chapter, the top plate where the laser generation and detection are performed must be free of imperfections as it is assumed in the model. However, the imperfections can be easily detected since the detection of elastic waves with shorter times of flight than those reflected from the bonding interface would be a sign of such imperfections. One way to quantify the practical adhesion even in the case with imperfections could be to use windowed experimental and simulated B-scans where the influence of the reflections from these imperfections would have been gated out.

In terms of prospects, other methods of comparison between the input data and the database could be tested, such as SSIM (Structural Similarity)<sup>186,187</sup> or others. Moreover, this presented method could be implemented with an even more complete semi-analytic model taking the thickness, the elastic coefficients and the mass density of the adhesive into account. The introduction of new parameters will greatly complicate the resolution of the inverse problem by considerably increasing the number of simulations required to create the database (see Sec. 3.5). A thoughtful analysis of the parameter dependencies/independencies in their effect to the solution of the inverse problem could eventually permit to decrease the number of degrees of freedom in the minimization process. Succeeding in doing so would allow to consider reflected plane waves of higher frequencies (above 5 MHz) and therefore would ensure to obtain a more accurate description of the bonded assembly.



## Chapter 4

# Nondestructive evaluation of structural adhesive bonding using the attenuation of zero-group-velocity Lamb modes

### Contents

---

4.1	Introduction . . . . .	97
4.2	Dispersion curves in a bilayer structure . . . . .	98
4.3	Presentation of the samples, the laser-ultrasonic set-up and experimental measurements . . . . .	100
4.3.1	Presentation of the samples . . . . .	100
4.3.2	Description of the laser-ultrasonic set-up . . . . .	101
4.3.3	Experimental measurements . . . . .	101
4.4	Damping of local resonances . . . . .	103
4.5	2D maps of a trilayer assembly with inhomogeneously distributed defects .	107
4.6	Conclusion . . . . .	109

---

## Abstract

A laser ultrasonic method is proposed for the local nondestructive evaluation (NDE) of structural adhesive bonding. Zero-group-velocity (ZGV) resonances were generated and detected in five trilayer assemblies composed of two asymmetric aluminum alloy plates bonded with an epoxy adhesive. Cohesive and adhesive defects were introduced to degrade the practical adhesion. The attenuation of the temporal signal of ZGV resonances was found to provide sufficient information to discriminate between strong and weak bonding. Two metrics characterizing the attenuation were identified, which allow us to evaluate quantitatively the differences between the manufactured samples. A 2D scan of a trilayer assembly with different bond defects demonstrates the imaging capability of this all-optical NDE method.

---

This work was published in *Appl. Phys. Lett.* (see Ref. 185):

R. Hodé, S. Raetz, J. Blondeau, N. Chigarev, N. Cuvillier, V. Tournat, and M. Ducouso, “Nondestructive evaluation of structural adhesive bonding using the attenuation of zero-group-velocity Lamb modes,” *Appl. Phys. Lett.* **116**(10), 104101(2020) doi: [10.1063/1.5143215](https://doi.org/10.1063/1.5143215).

## 4.1 Introduction

In industrial applications, bonded assemblies must withstand a mechanical load that is defined by the manufacturer. In the following, if this level is satisfied, the bonding will be qualified as strong, if not, as weak. However, even for weak bonding, the adhesion is not null in practice. Thus, it is difficult for a nondestructive evaluation (NDE) to differentiate between weak and strong bonding. It has already been discussed in Chap. 1 that a large number of NDE methods have been investigated to evaluate qualitatively or quantitatively the mechanical strength (practical adhesion) of bonded assemblies.

One of the most promising quantitative techniques is based on laser-generated shock waves, often referred to as a laser shock adhesion test (LASAT).<sup>68</sup> In this method, a high dynamical and mechanical tensile stress is applied to a bonded joint with shock waves. Ducouso *et al.*<sup>67</sup> succeeded in quantifying the practical adhesion of a trilayer bonded assembly (TA6V4 titanium alloy/epoxy/3D-woven composite) thanks to this method. One identified limitation of this technique, notably highlighted by Ehrhart *et al.*,<sup>188</sup> is that the process must be thoughtfully calibrated so that other parts of the structure are not degraded by the propagation of the shock waves. Ultrasonic techniques, which are absolutely nondestructive, have not yet been developed to overcome this potential limitation of LASAT in quantifying bonded assemblies.

Of the nondestructive ultrasonic techniques discussed in Chap. 1, various approaches based on the reflection<sup>76,77,85,94</sup> or transmission<sup>81,82</sup> of bulk waves at imperfect interfaces have been proposed. However, the small impedance differences between strong and weak bonds make the detection of imperfect interfaces difficult and force to use accurate post-processing methods in order to identify key metrics that characterize the mechanical strength of adhesive bonding.<sup>76,77,81,82,85,94</sup> As the method proposed in the previous chapter, other ultrasonic methods based on non-linear phenomena of bulk waves<sup>126</sup> or on measuring guided waves<sup>98,99,105,189,190</sup> allow to obtain an average value for the practical adhesion along a joint. To achieve better defect localization, zero-group-velocity (ZGV) Lamb modes<sup>191,192</sup> have been studied.<sup>111,193–195</sup> Mezil *et al.*<sup>112</sup> carried out theoretical and experimental investigations of a symmetrical trilayer composed of two duralumin plates bonded with an epoxy adhesive. They found that the frequencies of the ZGV modes are sensitive to the quality of the bonding. Thus, these ZGV modes are good candidates for nondestructively evaluating the interfacial stiffnesses that model the mechanical coupling between the bonded layers. These local resonances can be applied in a wider context for NDE.<sup>196–200</sup>

In this chapter, the attenuation characteristics of ZGV Lamb modes, as well as their frequencies, were used quantitatively to distinguish between strongly and weakly bonded samples. Laser ultrasonic measurements were made of five asymmetric trilayer assemblies (aluminum alloy/epoxy/aluminum alloy) with different mechanical strengths. The samples were clearly discriminated thanks to the frequency and the attenuation of the ZGV modes. Quantitative metrics were obtained from the attenuation characteristics, paving the way for a local quantified assessment of the practical adhesion using a contactless nondestructive method.

## 4.2 Dispersion curves in a bilayer structure

For a thin elastic plate with two parallel free surfaces, Lamb waves can propagate and are polarized in the sagittal plane.<sup>201</sup> There are symmetrical and anti-symmetrical modes, which are the solutions of the Rayleigh–Lamb equations. These propagation modes are represented in the  $\omega - k$  space by dispersion curves, where  $\omega$  is the angular frequency and  $k$  the wavenumber. In particular, ZGV Lamb modes occur when the group velocity vanishes (i.e.,  $d\omega/dk = 0$ ) for a finite value of  $k \neq 0$ . In this case, the energy is locally trapped under the ultrasonic source. A ZGV mode, therefore, behaves as a sharp local resonance of the plate at a well-defined frequency.

For two elastic plates mechanically coupled through an adhesive layer, ZGV modes may also occur and are strongly influenced by the mechanical strength of the coupling. Simulations of the dispersion curves have been used to observe the frequencies of the ZGV modes, which are referred to as ZGV frequencies in the following. When the acoustic wavelength is large compared to the adhesive thickness,<sup>114,178,202</sup> a bilayer model can be used to represent the bonded assembly [Fig. 4.1(a)]. In our case, both plates are considered to be homogeneous and isotropic.  $h_1$  is the thickness of the thinner plate and  $h_2$  the thickness of the thicker one. The bonded joint is modeled by normal ( $K_N$ ) and transverse ( $K_T$ ) interfacial stiffnesses per unit area.

The dispersion curves were obtained numerically [Fig. 4.1(b)] for two different cases, based on the approach of Jones and Whittier.<sup>178</sup> First, the top aluminum alloy plate Al<sub>1</sub> with thickness  $h_1$  is considered alone, i.e.,  $K_N = K_T = 0 \text{ kN mm}^{-3}$ . Symmetrical and anti-symmetrical modes are plotted as dashed and dashed dotted lines, respectively, in Fig. 4.1(b). Between 0 and 3 MHz, a unique ZGV mode occurs at a frequency of 1.96 MHz, as indicated by the white triangle. Secondly, coupling between the two plates is imposed by choosing  $K_N = K_T = 10 \text{ kN mm}^{-3}$ . The dispersion curves are represented

## 4.2. Dispersion curves in a bilayer structure

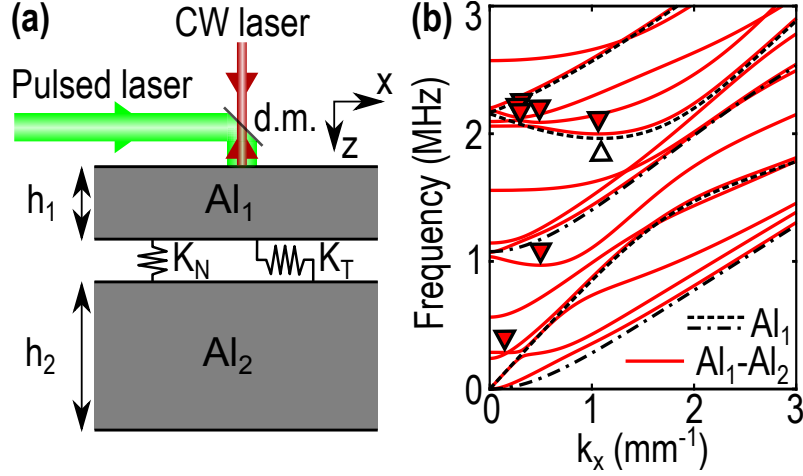


Figure 4.1 – (a) Schematic diagram of the generation and detection laser paths and of the bilayer model used to simulate the dispersion curves. d.m.: dichroic mirror.  $K_N$ ,  $K_T$ : the normal and transverse interfacial stiffnesses per unit area. (b) The dispersion curves of the top aluminum alloy plate alone ( $Al_1$ ) are represented as dashed and dashed dotted lines for symmetrical and anti-symmetrical Lamb modes, respectively. The dispersion curves obtained for mechanical coupling between  $Al_1$  and  $Al_2$ , with  $K_N = K_T = 10 \text{ kN mm}^{-3}$ , are represented as solid lines. ZGV resonances are indicated by white and red triangles.

as red solid lines in Fig. 4.1(b). In this example, there are more guided modes and ZGV modes (shown by red inverted triangles) in the bilayer assembly than for the single plate. Therefore, the theory predicts that with the higher interfacial stiffnesses, there will be several ZGV modes with similar frequencies due to this mechanical coupling. As a result and as already shown theoretically and experimentally in Ref. 112, any change in the mechanical coupling between the two plates will lead to a modification of the dispersion curves and hence, of the ZGV resonance frequencies. Here, we experimentally investigate this ZGV feature for five different bonded samples by analyzing the attenuation of the ZGV modes as a function of time. The samples are now introduced.

## 4.3 Presentation of the samples, the laser-ultrasonic set-up and experimental measurements

### 4.3.1 Presentation of the samples

The first specimen,  $Al_1$ , was a 6061 aluminum alloy plate (GoodFellow, United Kingdom), 1.5 mm-thick, and of lateral dimensions  $150 \times 150 \text{ mm}^2$ . All the other samples were composed of two 6061 aluminum alloy plates, 1.5 mm and 3.0 mm-thick. These plates, of lateral dimensions similar to those of  $Al_1$ , were bonded with a structural adhesive film AF 191 (3M™, United States). During manufacturing, the surfaces of the aluminum alloy plates were first degreased with ethanol. Next, strips of material about 5 mm-wide were placed on the edges of the surfaces, between the two plates, to control the thickness of the epoxy layer (equal to  $150 \mu\text{m}$ ) and to prevent the glue from leaking during curing, as previously done for the samples studied in Chap. 3. Then, 16 spring clamps calibrated at 65 N were homogeneously distributed around the sample to maintain a constant pressure during curing.<sup>67</sup> In the nominal case, the bonded sample (subsequently referred to as Nom) was fully cured at  $150^\circ\text{C}$  for 3 hours.

To simulate cohesive and adhesive defects,<sup>16</sup> two kinds of degradation were implemented. The first was the reduction of the curing time by 50% to lower the cohesive strength of the adhesive. This half-cured sample is labeled  $C_{.50\%}$ . The other type of degradation was the application, with a clean lint-free cloth, of one layer of release agent (R.A.) [Frekote® 44-NC™ (Henkel, Germany)] to a degreased aluminum alloy surface, as in Chap. 3 (see Fig. 3.6). This layer of release agent disrupted the practical adhesion between the substrate and the fully cured adhesive. The two parts did not become detached, but the structural mechanical strength of the interface of the bonding is significantly reduced using such protocol. Three samples were produced with this adhesive defect. The first,  $R.A._1$ , had one layer of release agent between the first (thin) aluminum plate and the epoxy layer. The second,  $R.A._2$ , had the release agent at the interface between the adhesive and the second (thick) aluminum plate. For the third,  $R.A._{1-2}$ , both aluminum plates were coated with one layer of Frekote, which affected both interfaces (Table 4.1). All the bonded samples (except the half-cured sample,  $C_{.50\%}$ ) were cured simultaneously in a laboratory oven at  $150^\circ\text{C}$  for 3 hours with ramps up and down (heating and cooling) of  $2^\circ\text{C min}^{-1}$ .  $C_{.50\%}$  was cured at  $125^\circ\text{C}$  for 1.5 hours with the same ramps up and down. The longitudinal static strengths were measured to be of the order

### 4.3. Presentation of the samples, the laser-ultrasonic set-up and experimental measurements

of 20 MPa for the nominal bonding and 10 MPa (2 MPa) for a sample with cohesive (adhesive) defects. The specimens were indistinguishable in conventional immersion ultrasonic measurements in reflection at 15 MHz (see the C-scan in reflection at 15 MHz of the four samples, represented in Fig. 4.2).

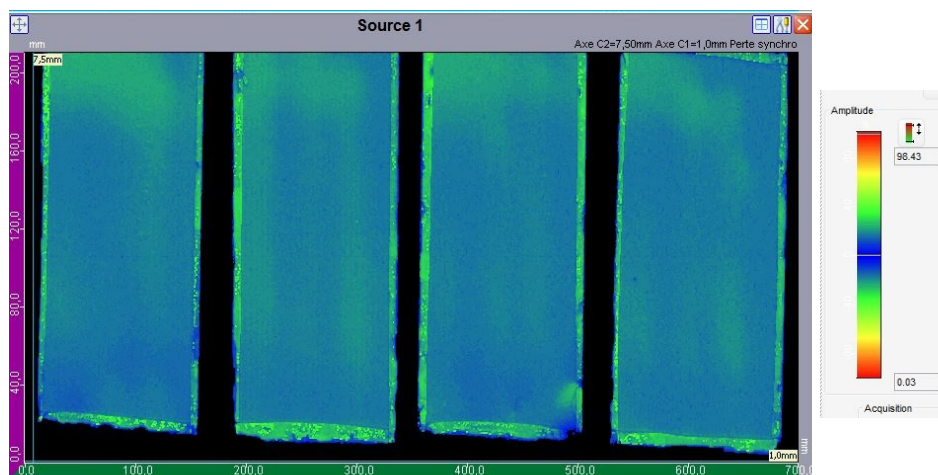


Figure 4.2 – Conventional immersion ultrasonic measurements (C-scan) in reflection at 15 MHz for the bonded samples R.A.<sub>1</sub>, C.<sub>50%</sub>, R.A.<sub>2</sub> and Nom. (from left to right).

#### 4.3.2 Description of the laser-ultrasonic set-up

For the evaluation of these five bonded samples, the laser ultrasonic set-up described in the Chap.3 (see Fig. 3.7) was used. To remain in the thermoelastic (nondestructive) regime, the pump beam was attenuated and then focused onto the surface of the thinnest aluminum plate of the bonded samples [see Fig. 4.1(a)]. The beam diameter was adjusted to maximize the amplitude of the  $S_1S_2$ -ZGV resonance, with the full width at half maximum of the excitation spot approximately equal to half the wavelength of the  $S_1S_2$ -ZGV mode<sup>196</sup> of the thin plate. The normal displacement of the surface was measured with the same two-wave mixing interferometer.

#### 4.3.3 Experimental measurements

For each sample, the generation and the detection laser spots were superimposed [Fig. 4.1(a)] and swept onto 11 positions with a 1 mm-step in the  $x$ -direction. For each measurement point, 500 temporal signals were averaged to increase the signal-to-noise

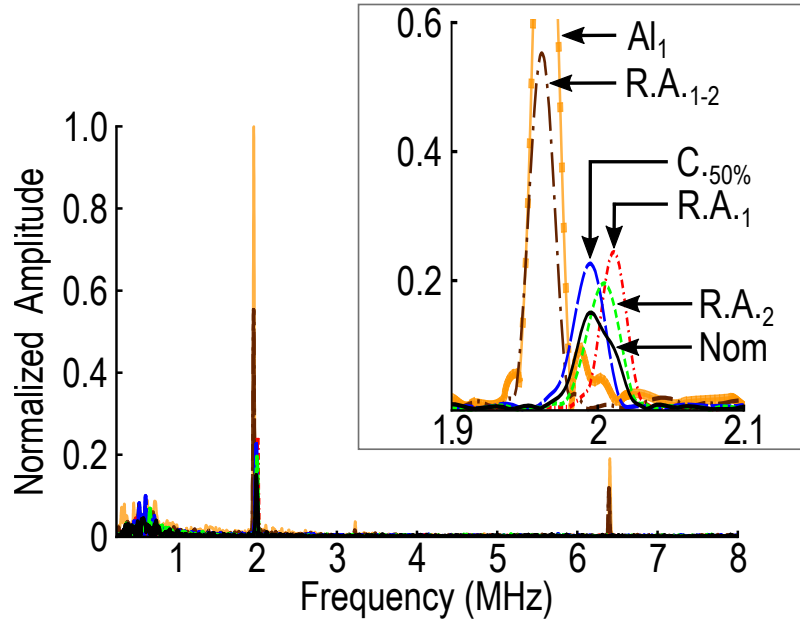


Figure 4.3 – Experimental frequency spectra in the range 0–8 MHz and around 2 MHz (inset) measured in reflection with the set-up presented in Fig. 4.1(a).

ratio. The fast Fourier transform algorithm was used to process these time-domain signals (Fig. 4.3). These frequency spectra are normalized with respect to the maximum amplitude of the  $S_1S_2$ -ZGV resonance, around 2 MHz, of the 1.5 mm-thick aluminum alloy plate. Since the measurements are reproducible over the 11 positions of the scans (the standard deviations of the measured ZGV frequencies are equal to 1 kHz), only one spectrum per sample is plotted in Fig. 4.3 for clarity. In the range 0–8 MHz, there are three main peaks around 2, 3, and 6 MHz. Near 3 and 6 MHz, resonance frequencies are visible only for the Al<sub>1</sub> and R.A.<sub>1-2</sub> samples (the orange solid line with square markers and the brown loosely dashed dotted line, respectively). Thanks to the theoretical dispersion curves, the resonance at  $\sim 3$  MHz is identified as a thickness mode of the 1.5 mm-thick plate and the one at  $\sim 6$  MHz with the  $S_3S_6$ -ZGV mode of the 1.5 mm-thick plate. At  $\sim 2$  MHz, all the samples have similar but different ZGV frequencies, as can be seen from the inset in Fig. 4.3. The maximum amplitudes of the peaks also depend on the curing time of the adhesive and on the release agent between the interfaces. Furthermore, notice that for the nominal bonded sample (black solid line labeled Nom), there is not a sharp unique ZGV peak, rather two very close resonance frequencies, as identified theoretically. We discuss later why this observation can be extended to R.A.<sub>1</sub>, C.<sub>50%</sub>, and R.A.<sub>2</sub>.

Experimental measurements were also performed with a set-up in transmission, i.e.,

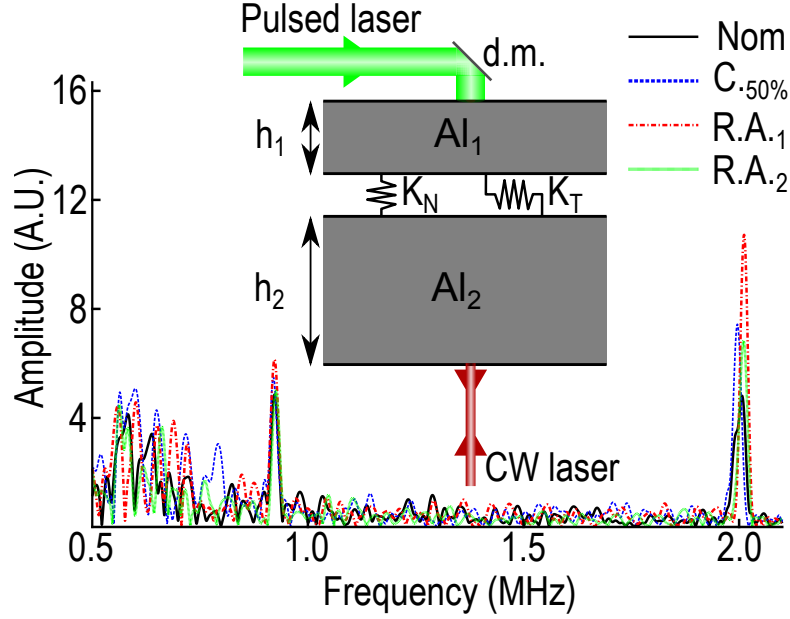


Figure 4.4 – Experimental frequency spectra with a set-up in transmission, i.e., where the generation laser spot is focused on the top aluminum alloy plate  $Al_1$  and the detection laser spot is focused on the bottom aluminum alloy plate  $Al_2$ .

where the generation laser spot is focused on the top aluminum alloy plate  $Al_1$  and the detection laser spot is focused on the bottom aluminum alloy plate  $Al_2$ . In this configuration, we detect the ZGV mode around 0.9 MHz (see experimental spectra in Fig. 4.4) that is predicted in the simulated dispersion curves represented in Fig. 4.1(b). However, these measurements with a transmission configuration are not considered in the following for two main reasons. First, the cut-off frequency of the high-pass filter of the interferometer is equal to 0.7 MHz, which is close to 0.9 MHz. Thus, this can disturb the measurements of this ZGV mode. Secondly, measurements in transmission are not always possible in an industrial context. Therefore, we prefer to carry out measurements with a set-up in reflection because it requires access to only one surface.

## 4.4 Damping of local resonances

The damping of local resonances measured with the reflection configuration (see the experimental set-up in Fig. 4.1(a) and experimental frequency spectra in Fig. 4.3) provides sufficient information for discriminating the differently prepared samples. The magnitudes of the ZGV modes as a function of time (to a logarithmic scale) are shown in Fig. 4.5(a).

These curves were obtained after filtering the temporal signals with a bandpass filter (Butterworth, order 4, lower and higher cutoff frequencies of 1.5 MHz and 2.5 MHz, respectively) around the ZGV frequency. This filter was chosen for its flat magnitude response in the bandwidth of interest. Typical filtered signals are plotted in Fig. 4.5(b) for the aluminum alloy plate and for the nominal bonded sample. Then, signal envelopes were extracted with the Hilbert transform and their magnitudes are displayed in decibels. For each sample, the average attenuation for the 11 measurement points is plotted and the standard deviation is represented with shaded error bars in Fig. 4.5(a). For the aluminum alloy plate, the  $S_1S_2$ -ZGV resonance decreases as a function of  $t^{-1/2}$ , which agrees with the results of Prada *et al.*<sup>203</sup>, who analytically derived this power law decay:

$$u(t) = G_0 t^{-1/2} e^{-t/\tau_1} \cos(\omega_0 t + \phi), \quad (4.1)$$

where  $u(t)$  is the normal displacement of the surface at the center of the generation laser spot.  $G_0$  is related to the efficiency of the laser-ultrasound generation. It depends on several parameters that are described in Ref. 203, especially the Fourier transform of the spatial and temporal profiles of the laser pulse.  $\omega_0$  and  $\phi$  are the ZGV angular frequency and the phase, respectively. The time constant  $\tau_1$  is for viscoelastic losses, which lead to the exponential decay of the amplitude. For the aluminum alloy plate, this parameter is large ( $\bar{\tau}_1 = 840 \mu\text{s}$ ; Table 4.1), so that attenuation is mainly due to the  $t^{-1/2}$  factor. As explained by Prada *et al.*,<sup>203</sup> this power law decay is due to energy that is not trapped under the source, which can, thus, propagate at non-zero group velocity in the medium.

When this model is used to fit the other experimental curves, there are some discrepancies, notably for the bonded samples R.A.<sub>1</sub>, C.<sub>50%</sub>, R.A.<sub>2</sub>, and Nom. To address this issue, an additional term is proposed for Eq. (4.1). It is based on the previous theoretical and experimental observations that the resonance is due to two or more ZGV modes [Fig. 4.1(b) and inset of Fig. 4.3], particularly the black solid curve for the nominal bonded sample. We consider here that the attenuation is due to a beating phenomenon between two close resonances. Assuming that the frequencies have the same phase and amplitude but different frequencies,  $\omega_1$  and  $\omega_2$ , their sum is equivalent to an oscillating signal modulated in amplitude by a cosine function. The angular frequency of the oscillating signal ( $\omega_m$ ) is the mean of  $\omega_1$  and  $\omega_2$  and the decreasing term is the cosine function, which depends on the slight difference between the frequencies  $\delta\omega = \omega_2 - \omega_1$ . Therefore, we have

$$u(t) = G_0 t^{-1/2} e^{-t/\tau_1} \cos\left(\frac{\delta\omega t}{2}\right) \cos(\omega_m t + \phi). \quad (4.2)$$

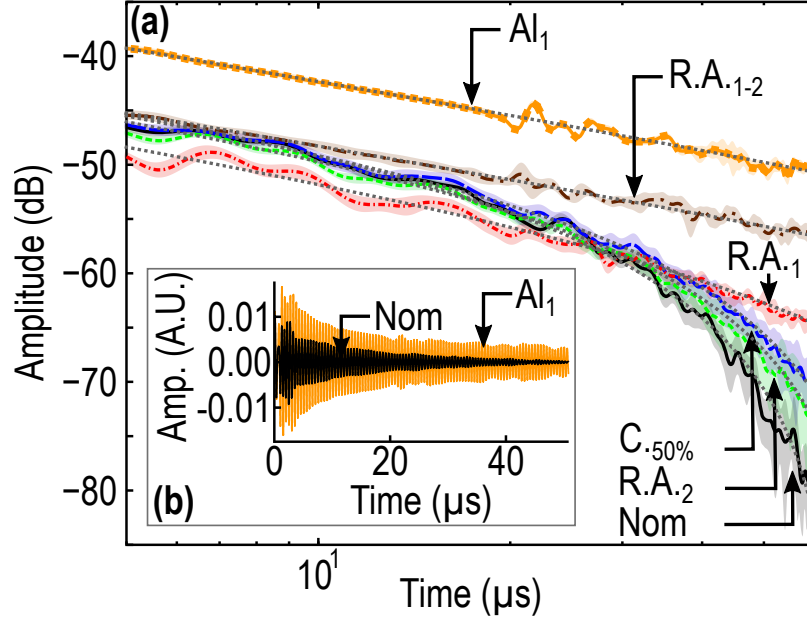


Figure 4.5 – (a) Experimental attenuation as a function of time to a logarithmic scale. For each sample, the average attenuation for the 11 measurement points is plotted and the standard deviation is represented with shaded error bars. The fitting lines with Eq. (4.2) are represented with dotted lines. (b) Temporal signals acquired from the aluminum alloy plate and from the nominal bonded sample after filtering the data with a bandpass filter around the ZGV frequency at  $\sim 2$  MHz.

The fits of the experimental data with this formula, based on a least-squares minimization method, are represented by the dotted lines in Fig. 4.5(a). There is a relatively good agreement [see the root-mean-square error (RMSE) of the fits in Table 4.1].

For each sample, the average values and the standard deviations of the metrics  $G_0$ ,  $\tau_1$ ,  $\delta\omega$ , and  $\omega_m$  for the 11 measurement points are listed in Table 4.1. The RMSEs of the fit obtained with Eqs. (4.1) and (4.2) are similar for  $Al_1$  and  $R.A._{1-2}$ . However, the RMSE is higher when the experimental attenuation is fitted with Eq. (4.1) rather than with Eq. (4.2). For instance, the RMSE increases by +1%, +27%, +35%, and +42%, respectively, for  $R.A._1$ ,  $C_{.50\%}$ ,  $R.A._2$ , and  $Nom$  when Eq. (4.1) is used instead of Eq. (4.2). Thus, the experimental attenuation is fitted with Eq. (4.2).

To discriminate between the different samples, the metrics  $\tau_1$  and  $\delta\omega$  are considered because of their significant sensitivity to bond defects. For the  $Al_1$  and  $R.A._{1-2}$  samples, the attenuation is mainly due to the power law decay  $t^{-1/2}$ . Moreover, note that when Frekote is applied on both sides, the assembly behaves as a freestanding plate. For

Table 4.1 – Properties of the samples and fitted values for the attenuation. The bars indicate averages for 11 measurement points.  $\sigma$  is the standard deviation.

	Al <sub>1</sub>	R.A. <sub>1-2</sub>	R.A. <sub>1</sub>	C. <sub>50%</sub>	R.A. <sub>2</sub>	Nom
Adhesive curing	–	✓	✓	50%	✓	✓
Interface 1 <sup>a</sup>	–	Frekote	Frekote	✓	✓	✓
Interface 2 <sup>b</sup>	–	Frekote	✓	✓	Frekote	✓
$\overline{G_0}$ (mm $\mu\text{s}^{1/2}$ )	0.025	0.012	0.009	0.013	0.012	0.013
$\sigma/\overline{G_0}$ (%)	3%	5%	7%	4%	8%	7%
$\overline{\tau_1}$ ( $\mu\text{s}$ )	840	960	102	85	87	63
$\sigma/\overline{\tau_1}$ (%)	23%	7%	17%	27%	34%	23%
$\overline{\delta\omega}/(2\pi)$ (kHz)	0.5	0.5	2.1	6.4	6.8	7.7
$\sigma/\overline{\delta\omega}$ (%)	96%	92%	56%	7%	9%	4%
$\overline{\omega_m}/(2\pi)$ (MHz)	1.964	1.962	2.010	1.992	2.002	1.998
$\sigma/\overline{\omega_m}$ (%)	<0.1%	<0.1%	<0.1%	<0.1%	<0.1%	<0.1%
$\overline{\text{RMSE}}$ ( $10^{-3}$ ) <sup>c</sup>	0.7	0.3	0.2	0.3	0.3	0.4

<sup>a</sup> Interface 1: Aluminum alloy plate Al<sub>1</sub> (1.5 mm-thick)/adhesive layer.

<sup>b</sup> Interface 2: Adhesive layer/aluminum alloy plate Al<sub>2</sub> (3.0 mm-thick).

<sup>c</sup> Root-mean-square error of the fit.

the samples R.A.<sub>1</sub>, C.<sub>50%</sub>, R.A.<sub>2</sub>, and Nom, the decrease of the amplitude as a function of time is also due to viscoelastic losses, with the time constant  $\tau_1$ , and to the beating phenomenon, with the parameter  $\delta\omega$ . The Nom sample has the lowest  $\tau_1$  (i.e., viscoelastic losses play a major role) and the highest  $\delta\omega$  (i.e., the beating phenomenon has a large influence on the attenuation).

Although interface 1 is coated with Frekote for both R.A.<sub>1</sub> and R.A.<sub>1-2</sub>, they have different attenuation profiles. This may be because the layer of release agent does not detach the substrate from the adhesive. The two parts are still mechanically coupled, even if this coupling is weak compared to the nominal case. For R.A.<sub>1</sub>, only one interface is degraded, while for R.A.<sub>1-2</sub>, two interfaces are degraded. The amount of release agent for R.A.<sub>1-2</sub> was twice as high than for R.A.<sub>1</sub>. This may explain why R.A.<sub>1-2</sub> behaves more like the top Al<sub>1</sub> plate alone than R.A.<sub>1</sub>.

Thus, the attenuation characteristics in Fig. 4.5 combined with this identification method allow us to distinguish the different bonded samples and to determine the key metric values that provide a quantification of these differences.

## 4.5 2D maps of a trilayer assembly with inhomogeneously distributed defects

The method was finally tested on a trilayer assembly with two adhesive defects. It had four  $75 \times 75 \text{ mm}^2$  zones: two without defects (denominated as previously Nom), one with an adhesive defect R.A.<sub>1</sub> and another with R.A.<sub>2</sub>. 2D maps were produced for the ZGV frequency and attenuation over an area of  $80 \times 48 \text{ mm}^2$ , which covers the four regions. In Fig. 4.6(a), the frequency  $\omega_m$  is plotted versus position. There is clearly no distinct zone with different frequencies, as may be expected. Rather,  $\omega_m$  changes continuously across the four regions. These interesting monotonous variations show that the effects of a localized adhesive defect spread away from the defect zone. In contrast,  $\tau_1$  [Fig. 4.6(b)] and  $\delta\omega$  [Fig. 4.6(c)], vary non-monotonously across the four regions. The centers of the Nom areas have the highest  $\delta\omega$  (as encountered previously; Table 4.1). Assuming, as for the homogeneous samples, that  $\delta\omega$  is high where the bonding is actually nominal, Fig. 4.6(c), thus, shows that the Nom zones are not homogeneous, which strengthens our hypothesis that the effect of a limited adhesive defect is hardly local. Surprisingly,  $\tau_1$  is not the lowest in these parts of the Nom areas where  $\delta\omega$  is high, which is in contrast with the results in Table 4.1. Note also that a peak is observed in the spectra at  $\sim 1.9 \text{ MHz}$

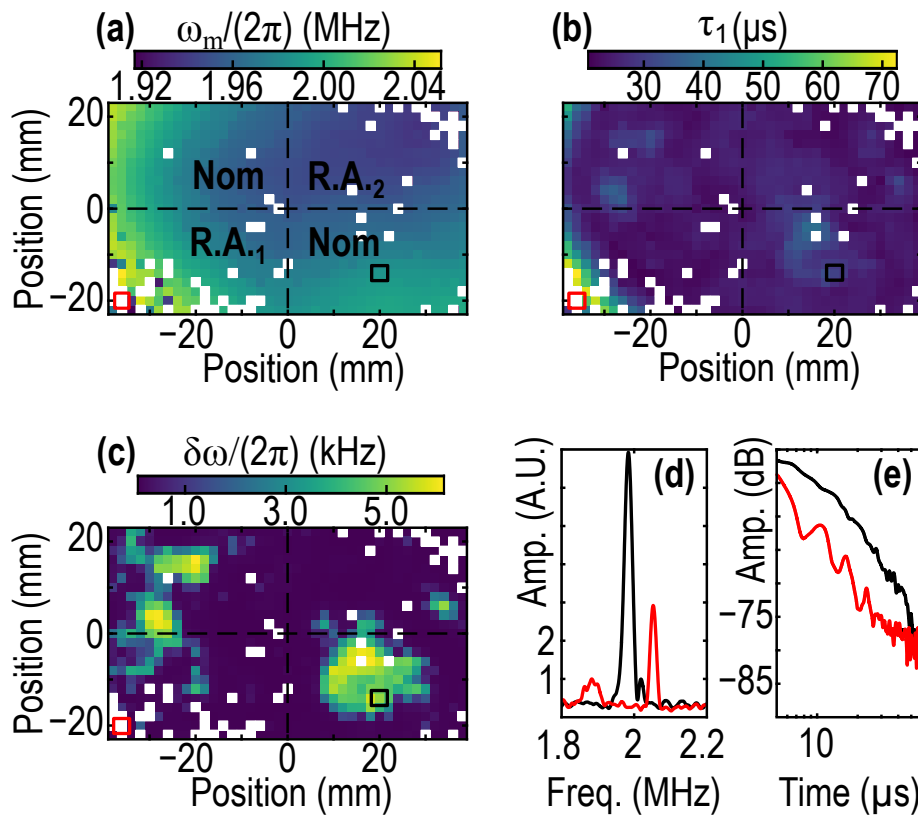


Figure 4.6 – 2D maps of the metrics of the trilayer sample split into four zones: (a)  $\omega_m$ , (b)  $\tau_1$ , and (c)  $\delta\omega$ . When the RMSE of a fit is higher than  $0.4 \times 10^{-3}$  (maximum value of the previous results for the bonded samples; Table 4.1), the point is rejected and replaced by a white square. (d) Frequency spectra and (e) attenuation of the signals for the red and black boxes in the maps.

[Fig. 4.6(d)], which is absent for the homogeneous samples. This peak gives rise to the beating phenomenon [Fig. 4.6(e)] for a larger  $\delta\omega$  than assumed for the minimization.

Two possible reasons may explain why the effects of a localized adhesive defect spread away from its initial deposition area. First, the release agent could migrate from its initial deposition area during curing. This could explain why a continuous change of the ZGV resonance frequency is observed in Fig. 4.6(a). Second, the differences in the practical adhesion in the four areas could lead to residual stresses in the inhomogeneous sample. Therefore, a localized adhesive defect could affect a wider area. Although these unexpected results remain to be explained fully, the metrics  $\tau_1$  and  $\delta\omega$  have undoubtedly enabled the nondestructive imaging of adhesive bonds with inhomogeneously distributed defects.

## 4.6 Conclusion

We have proposed a laser-based method for generating and detecting ZGV modes so that we can locally evaluate trilayer assemblies with both cohesive and adhesive defects. By studying the attenuation of ZGV resonances, we have been able to discriminate the different samples thanks to the determination of quantitative metrics ( $\tau_1$  and  $\delta\omega$ ). Finally, the imaging ability of this contactless method has been demonstrated with a bonded sample with and without adhesive defects. The root causes of the differences in our results for homogeneously and inhomogeneously distributed defects should be further investigated, since understanding these could pave the way for quantitative assessments of adhesive bonding with this nondestructive all-optical technique. Laser ultrasonic methods that use non-linear interactions<sup>134,204</sup> could be a valuable approach to improving further the imaging of adhesive bonds.



# General conclusion

In this PhD thesis, laser ultrasonic methods have been investigated for the nondestructive evaluation (NDE) of bonded aeronautical assemblies. The main objective of this work was to develop NDE methods to identify quantitative parameters to discriminate structural bonded structures of different mechanical strengths. To this end, laser-generated and detected elastic waves in bonded assemblies have been studied both numerically and experimentally. Indeed, laser ultrasonic methods are well suited to industrial applications, especially because of the non-contact nature of the measurements.

First of all, a literature review concerning the NDE of adhesive bonding was presented in Chap. 1. After introducing the terms related to bonding as well as the defects encountered, an overview of destructive and non-destructive methods was given. Linear and non-linear ultrasonic methods were presented and discussed. This part illustrates the lack of a NDE method to quantify the mechanical strength of structural bonded assemblies despite the strong industrial need.

Then, a semi-analytic model was described in Chap. 2 to simulate the propagation of laser-generated ultrasounds in a multilayer structure, which is suitable for modeling a bonded assembly. This 2D model allows to calculate the displacement fields in the upper and lower media (media I and II, respectively) of the multilayer when a tilted laser line source is incident on it. Electromagnetic, thermal and elastodynamic problems are successively solved to model the optoacoustic source in the thermoelastic regime and the elastic waves generated by the thermal expansion of the material. The optical penetration of the incident laser beam into the multilayer is considered. The power densities dissipated by heating, which are used as source terms to solve the heat diffusion problem, are calculated with the amplitudes of the electromagnetic waves transmitted and reflected in the structure. The thermal problem is then solved to obtain the temperature field by considering the phenomena of conduction and convection. The displacement field is calculated in the Fourier domain where analytic solutions can be found. At that point, dispersion curves can be directly evaluated in plate-like structures. A double numerical inverse Fourier transform can also be performed to obtain the displacement field in the temporal and space domains. Sublayers can be inserted between the upper and lower media of the structure and are modeled with the transfer matrix method which considers the

electromagnetic, thermal and elastodynamic coupling conditions between media I and II. This allows fast and accurate results for solving the direct problem, i.e., to obtain the displacement fields in the upper and lower media when material properties are known. Simulated examples are provided to show just a brief overview of the results that can be obtained with this developed semi-analytic model. First, laser-generated elastic waves are simulated in a bilayer structure composed of two aluminum alloy (Al) plates mechanically coupled at the interface with two distributions of normal and transverse interfacial stiffnesses ( $K_N$  and  $K_T$ , respectively). The optoacoustic source is localized at the free surface of the upper medium due to the really low value of the optical penetration depth in aluminum alloy ( $1/\beta = 4.7\text{ nm}$ ). Secondly, simulations are also performed by taking the thickness of an epoxy layer between two Al plates into account. Thirdly, a heat source is simulated at the interface between two media when the incident laser beam is mainly absorbed in the lower medium compared to the upper one. Concerning the limitations of this developed semi-analytic approach, layered plates with parallel surfaces must be considered and the generation of ultrasounds in the sublayers should be neglected compared to the one in media I and II. One of the main perspectives of this work is to extend this 2D model to 3D geometries. This will necessarily complicate the calculations because a new space dimension must be taken into account. However, the methodology to solve the electromagnetic, thermal and elastodynamic problems will be similar. This approach could be of interest to simulate laser-generated ultrasounds when the 3D shape of the laser source is complex (as it will be discussed in the “*Perspectives*” section). The semi-analytic model described in Chap. 2 has been used in the next chapter to simulate the databases needed to solve inverse problems.

Indeed, in Chap. 3, a laser ultrasonic method has been proposed to identify normal ( $K_N$ ) and transverse ( $K_T$ ) interfacial stiffnesses that model two bonded aluminum alloy media when the wavelength is large compared to the adhesive thickness. This technique is based on the resolution of inverse problems using the reflection of elastic plane waves that are synthesized for several angles of incidence with respect to the bonding interface. A post-processing method is used to synthesize plane waves, from the propagation of laser-generated cylindrical bulk waves, because of the experimental difficulties to generate plane wave in laser ultrasonics. A validation of the developed method is first performed on simulated input data, obtained with the semi-analytic model presented in Chap. 2, and where Gaussian noise has been added. Then, it is applied on an aluminum alloy (Al) plate and on two bonded assemblies Al/Epoxy/Al (with and without adhesion defects) which are manufactured with structural epoxy adhesive films. This method allows to

discriminate the three samples and to identify quantitative parameters of  $K_N$  and  $K_T$ . These values are obtained by finding the minima of cost functions that correspond to the differences [measured with the mean squared error (MSE)] between the experimental input data and the database composed of semi-analytic simulations for a large set of  $K_N$  and  $K_T$  (from  $10^{-3}$  kN mm $^{-3}$  to  $10^5$  kN mm $^{-3}$ ). This developed technique allows to obtain average values of  $K_N$  and  $K_T$  for the scanned area (32 mm in our experimental cases). However, no local defects can be detected with such a technique and the upper propagation medium must be free of imperfections. In addition, the optical, thermal and mechanical properties of the bonded substrates must be known in order to obtain a database with accurate numerical simulations to solve the inverse problem. It is remarkable to note that solving inverse problems directly by comparing simulated and experimental B-scans do not lead to accurate results. This is due to the fact that the plane wave synthesis artificially improves the SNR and, above all, effectively filters the Rayleigh waves out of the bulk waves that actually contain the information about the bonding.

Concerning the perspectives of the work presented in Chap. 3, more parameters could be identified by solving the inverse problem (thickness of the adhesive, elastic coefficients of the adhesive, mass density of the adhesive, etc.) in order to have a better characterization of the bonded assembly. However, increasing the number of parameters to be identified will greatly complicate the problem and generate a very long computation time to obtain the database. To give an idea, with two parameters to be identified ( $K_N$  and  $K_T$ ), 1089 cases were simulated to generate the database (33 values for  $K_N$  and the same for  $K_T$ ). It takes about 30 hours to compute this complete database on a laptop (Intel<sup>®</sup> Core<sup>™</sup> i7-6500U CPU @ 2.5 GHz, 16 GB RAM). Following this logic, the addition of a single parameter multiplies by 33 the number of computation hours, which leads to more than 40 days to calculate the database with 3 parameters. Modeling a bonded assembly by considering: the thickness of the adhesive, its density, its two elastic coefficients (if considered isotropic) and the normal and transverse interfacial stiffnesses at the upper and lower interfaces leads to 8 parameters to be identified, without taking into account the viscoelastic phenomena. It would take more than 4 million years to compute the whole database with the same computer! Thus, to perform such calculations, three possible options could be studied. The first one could be to parallelize the calculations of the different cases in order to greatly reduce the computation time of the database (because each case is independent). The second one could be to reduce the computation time of each case (which is currently about 1 min and 45 sec): (i) by further optimizing the numerical code and (ii) by using even more powerful computers or computing clusters.

The last improvement could be not to compute the whole database but only the cases necessary for the minimization algorithm to find the minimum of the cost function. The problem that may appear with this technique is the identification of local minima and not global minima; this does not happen when the complete database is computed. The successful implementation of the proposed improvements would allow the identification of more parameters related to the bonded assembly and, therefore, to describe it more precisely.

In Chap. 4, a second approach has been proposed for the NDE of structural adhesive bonding. Contrary to the NDE method presented in Chap. 3, this one allows a local measurement by using the attenuation of zero-group-velocity (ZGV) Lamb modes, which are sharp local resonances at well-defined frequencies. ZGV resonances are experimentally generated and detected in five trilayer assemblies composed of two asymmetric aluminum alloy plates bonded with an epoxy structural adhesive film. Cohesive and adhesive defects were introduced to degrade the practical adhesion of these bonded samples. The temporal attenuations of ZGV resonances allow to discriminate the different bonded samples and to identify two quantitative metrics ( $\tau_1$  and  $\delta\omega$ ) related to these attenuation profiles. Then, to demonstrate the imaging ability of this all-optical method, a 2D scan of a trilayer assembly with and without adhesive defects is performed. This allows to image different area on the bonded sample by looking at the temporal attenuation parameters in addition to the ZGV resonance frequencies. Differences were observed between the measurements carried out on samples with homogeneously distributed bonding defects and with the latter sample having inhomogeneously distributed bonding defects, i.e., with several types of adhesive defects on the same bonding. A beat phenomenon was observed between two resonance frequencies much more distant than those observed on homogeneous samples, where the beat phenomenon was visible between two close resonance frequencies ( $\delta\omega$  around few kHz). Concerning the perspectives, two tracks may be investigated to explain the reason(s) for the differences observed between bonded samples with homogeneously and inhomogeneously distributed defects. The first one concerns the study of the migration of the release agent (Frekote<sup>®</sup> 44-NC<sup>™</sup>) which is used to create adhesive defects during manufacturing. Research is needed to understand the behavior of the release agent during curing and whether it could migrate from its initial area of deposition to another part of the bond during this process. The second one is the study of the formation of residual stresses after curing when several different bonding defects are introduced in the same bonded assembly. This could explain the differences observed when the bonding defects are homogeneously or inhomogeneously distributed for each

sample. These two perspectives could be studied to obtain an even finer understanding of the results obtained.

To conclude, a semi-analytic model and two NDE methods of bonded assemblies have been developed during this PhD thesis. The semi-analytic model, although used in one of its simplest form in the first NDE method for solving the inverse problem, aims at being general for simulating the propagation of elastic waves in multilayer assemblies with the abilities to take into account: (i) anisotropic materials, as far as the assumption of the two-dimensional problem holds; (ii) electromagnetic, thermal and mechanical unconventional boundary conditions (discontinuities); (iii) asymmetric volume distribution in 2D of the absorbed electromagnetic power density. The code is shared and will be continuously corrected, if needed, and improved/completed by me and the research team involved in the PhD work. The two NDE methods have been demonstrated to give quantitative metrics allowing to distinguish between, and characterize, bonded assemblies of different adhesion levels where classic ultrasonic techniques failed to observe a difference. Each method has its specific feature of characterization which will drive their usage: on the one hand, the global adhesion level of an assembly is made possible from a scan of the generation laser with the plane-wave-synthesis-based method; on the other hand, the adhesion level local mapping of an assembly is made possible from a scan of the sample with the ZGV-mode-based one. Regarding the more general prospects, non-linear methods also appear to be of real interest. Preliminary work has already been started and is presented below, in the last section of this manuscript.



# Perspectives

In this PhD thesis, two linear methods have been developed and are presented in this manuscript. Concerning the perspectives, non-linear methods are also of real interest for the NDE of bonded assemblies. Indeed, the identification of non-linear parameters could provide access to information not accessible by linear methods in order to characterize bonded assemblies. Preliminary work has been started during this PhD thesis and needs to be pursued in the future. Two main classes of non-linear methods have been identified. The first one is the addition of external modulations (low-frequency modulation or pressure modulation) to mechanically load the bonding and to couple this with laser ultrasonic measurements. The second one is to shape the laser source to focus ultrasounds at the bonding interface. A patent application has been filed on this latter idea. These two non-linear approaches are introduced in the following.

## External modulations

The approach concerning the addition of external modulations is divided in two proposed methods: (i) low-frequency modulation and (ii) pressure modulation. These techniques could be of interest for the NDE of bonded aeronautical structures such as Outlet Guide Vanes (OGV) which are located in the secondary flow of an aircraft turbine engine, behind fan blades.<sup>a</sup> A representative sample to study the bonding of a hood to the body of the OGV is given in Fig. P.1(a) and (b). This bonded assembly is interesting for testing non-linear NDE methods, especially because of the cavity present under the aluminum hood [see Fig. P.1(b)]. The low-frequency and pressure modulation methods are introduced below.

### Low-frequency modulation

The approach concerning the low-frequency modulation consists of exciting the first bending mode of the hood of the OGV sample [see Fig. P.1(c)] by means of a piezoelectric cell and at the same time performing laser ultrasonic measurements above the bonded

---

a. Video to show how an aircraft engine works. [URL link](#) [Accessed on 09/17/2020]

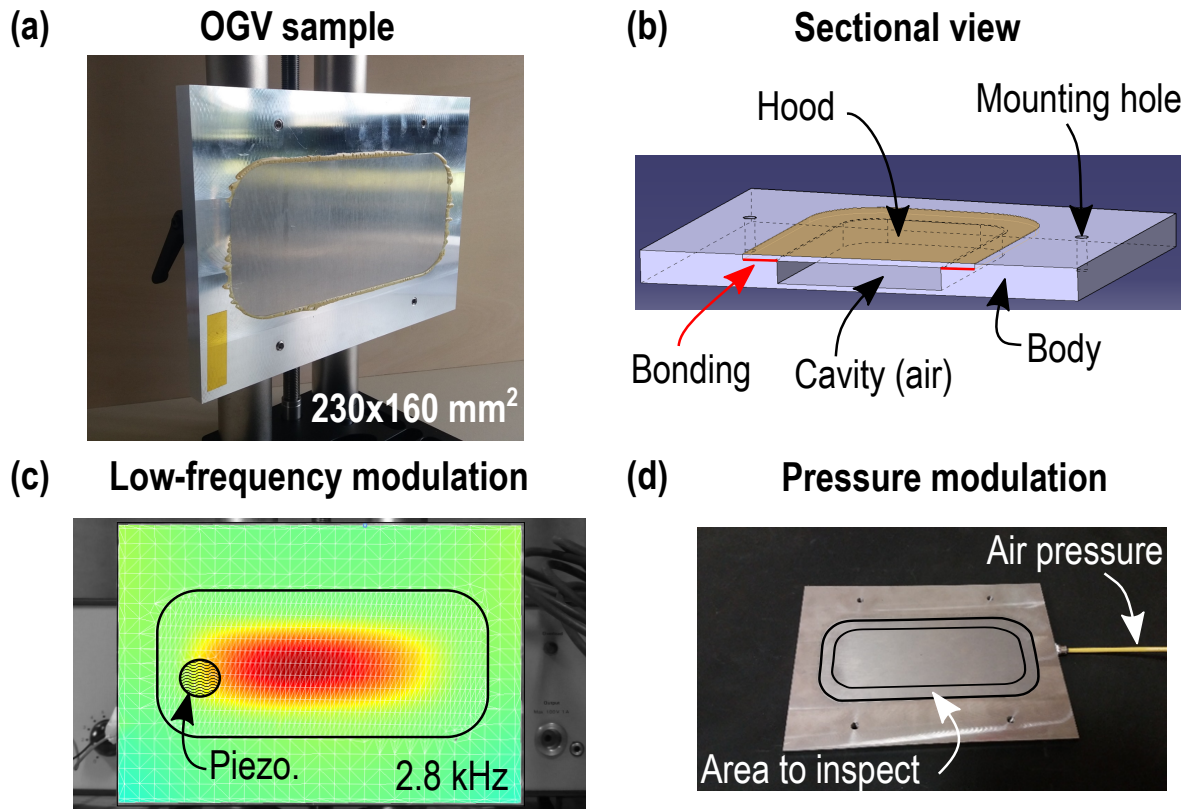


Figure P.1 – (a) Picture of the Outlet Guide Vane (OGV) sample. (b) CAD of the sectional view of the OGV sample composed of an aluminum alloy hood bonded to an aluminum alloy body. (c) Visualization of the first resonance mode of the aluminum alloy hood with excitation by a piezoelectric cell and measurement by scanning laser vibrometry. (d) Picture of the OGV sample with compressed air supply.

part. This low-frequency modulation is used to create a cyclic stress modulation at the bonding [represented in red in Fig. P.1(b)] to mechanically load this part of the sample. Scanning laser vibrometry measurements have been carried out on this OGV sample to obtain the experimental resonance frequency of the first bending mode [measured at 2.8kHz, see measured displacement field in Fig. P.1(c)]. The future plan is to perform laser ultrasonic measurements above the bonding, with and without the addition of this low-frequency excitation, to see if this cyclic modulation allows the observation of non-linear phenomena.

## Pressure modulation

The approach concerning the pressure modulation consists in injecting compressed air into the cavity of the specimen [see Fig. P.1(b) and (d)] in order to apply pressure on the hood and thus on the bonding. The idea is to apply stages at different pressure levels. For each pressure stage, laser ultrasonic measurements above the bonding will be performed. The pressure regulator as well as the other pneumatic elements have been ordered, delivered and installed. A Python script has been developed to control the pressure level numerically. A first pressurization test of the cavity has already been carried out. Hence, the aim is now to perform laser ultrasonic measurements, with and without this pressurization, above the bonding [see the area to inspect in Fig. P.1(d)].

Another approach, which does not rely on the addition of external modulations but on the focusing of laser-generated ultrasounds, is introduced hereafter.

## Focusing of laser-generated ultrasounds

The aim of this technique is to focus laser-generated bulk waves at the bonding interface to locally increase the amplitude of ultrasounds and to potentially observe non-linear effects. A patent application has been filed on this idea. In order to focus laser-generated ultrasounds, the laser source is proposed to be shaped. Indeed, there is a zone in the depth of the material where all the waves generated at different points of a thoughtful-shaped thermoelastic surface source will converge at the same time. The simplest case is the case of an isotropic medium where the shape is a ring. In that case, the principle is therefore to dimension the ring (inner radius, outer radius) so that the focus of ultrasounds is achieved at the bonding. An illustration of the proposed method in the case of an isotropic medium I is presented in Fig. P.2(a). The directivity pattern of the laser source is needed to define the geometry of the ring in order to focus ultrasounds at angles where the amplitudes of bulk waves are the highest. For instance, with the directivity pattern shown in Fig. P.2(b), the amplitudes of transverse waves are the largest at  $\pm 30^\circ$ .

From a technical point of view, this ring-shaped laser source is generated using a Spatial Light Modulator (SLM). The principle is to illuminate this diffractive optics with an incident laser beam. This beam is then reflected and refocused using a lens. The different phase delays imposed during the reflection from the SLM will create, in the focal plane of the lens, an image obtained by diffraction. Examples of images obtained with this device are presented in Fig. P.2(c) and (d). The ring-shaped laser source is also shown in

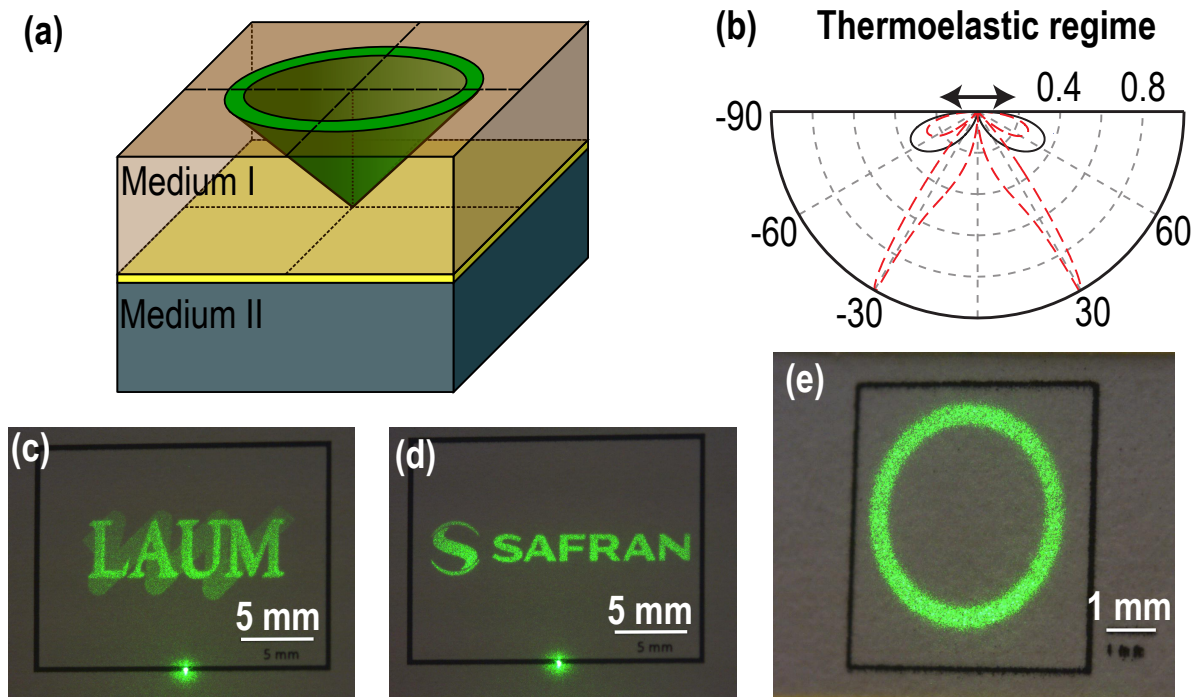


Figure P.2 – (a) Schematic diagram of the proposed method to focus ultrasounds with a ring-shaped laser source in an isotropic medium. (b) Directivity pattern of a laser source in the thermoelastic regime. Figure extracted from the PhD Thesis of S. Raetz (p. 24 in Ref. 151). Longitudinal (transverse) waves are represented by solid (dashed) lines. (c)–(d) Images obtained with the SLM. (e) Ring-shaped laser source obtained with the SLM.

Fig. P.2(e). The experimental set-up integrating the SLM, presented in Fig. P.3, has been prepared. Elements such as the beam expander, the CMOS camera, the dichroic mirror, etc. have been ordered and installed. The SLM has been calibrated and a Python script has been developed to control it. A camera, which is connected to the computer, is used to measure the dimensions of the ring based on a developed image processing algorithm.

The objective is now to test this technique on bonded assemblies. It is necessary to define and experiment the appropriate ring size to focus ultrasonic waves at the bonding interface. One of the expected results is to observe the generation of second harmonics as experimentally detected by Zabbal *et al.*<sup>126</sup> with a chaotic cavity transducer.

To conclude, preliminary work has been started during the PhD thesis concerning the development of non-linear methods in laser ultrasonics. Further numerical and experimental studies are needed to determine the potential of the proposed approaches: (i) external

modulations and (ii) focusing of laser-generated ultrasounds. This provides interesting prospects concerning the development of laser ultrasonic non-linear methods for the NDE of bonded assemblies.

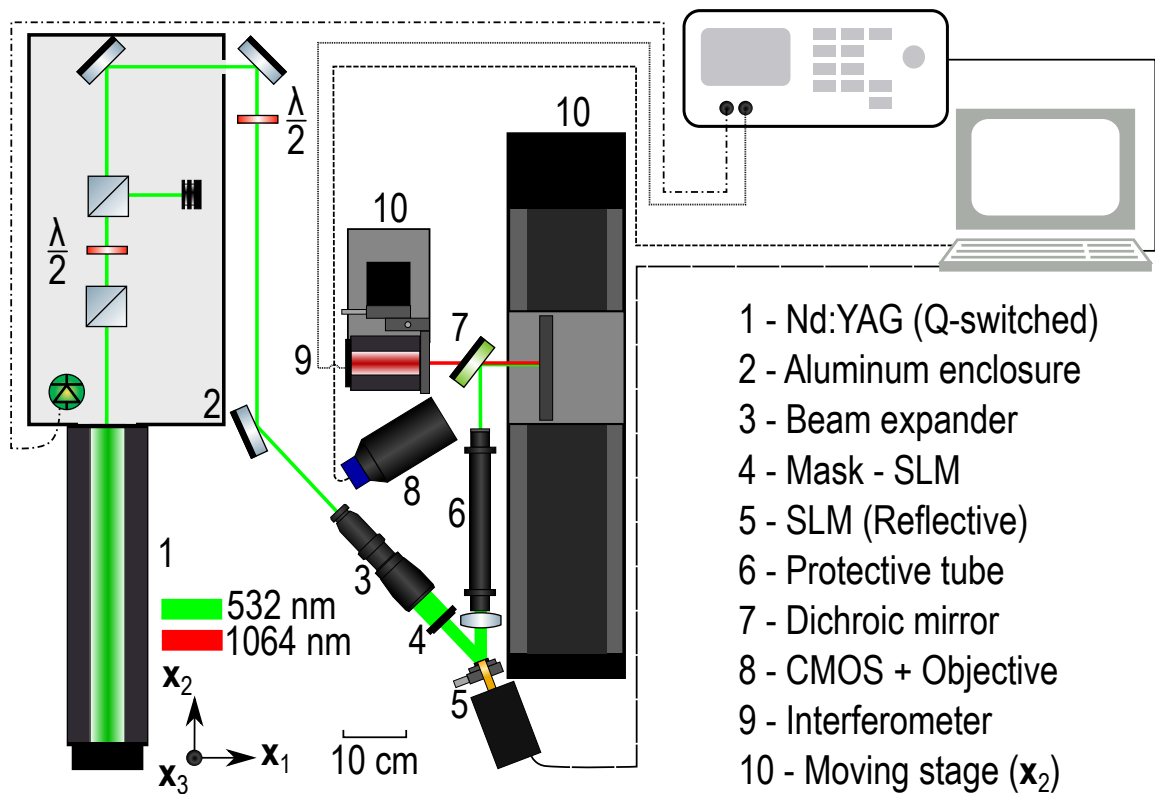


Figure P.3 – Experimental set-up with the Spatial Light Modulator (SLM).



# Résumé de la thèse

Actuellement, l'allègement des structures aéronautiques est un enjeu industriel majeur, notamment pour des raisons environnementales. Afin de réduire les émissions de gaz à effet de serre, celles-ci doivent devenir plus légères pour diminuer la consommation en carburant des moteurs. L'utilisation du collage comme technique d'assemblage permet de répondre à ce besoin de gain de masse. En effet, par rapport aux méthodes plus conventionnelles telles que le soudage ou le rivetage, le collage présente de nombreux avantages. Tout d'abord, l'assemblage par collage ne nécessite pas l'ajout de rivets qui viennent alourdir la structure. De plus, aucun perçage, synonyme de concentration des contraintes, ne doit être effectué dans les pièces à assembler. Ensuite, le collage permet d'assurer une meilleure répartition des contraintes entre les structures assemblées ; ce qui garantit une transmission plus homogène des efforts mécaniques. D'autre part, c'est l'une des techniques les plus performantes pour assembler des structures fabriquées en matériaux composites ayant un rapport résistance/masse élevé répondant à ce besoin d'allègement.

Bien que le collage présente de nombreux avantages vis-à-vis des techniques plus conventionnelles (rivetage, soudage, etc.), il n'existe pas à ce jour de méthodes non destructives permettant de quantifier et de certifier la tenue mécanique des assemblages collés. Cela pose donc de véritables problèmes de sécurité et de certification auprès des agences aériennes telles que la *Federal Aviation Administration* (FAA) ou encore l'*Agence Européenne de la Sécurité Aérienne* (EASA). Par conséquent, un fort intérêt doit être porté au développement de méthodes d'évaluation non destructive des assemblages aéronautiques collés. Cela permettrait de lever l'un des derniers verrous technologiques limitant actuellement le développement de cette technique d'assemblage dans l'industrie aéronautique.

Dans cette thèse, des méthodes ultrasons-laser pour l'évaluation non destructive (END) des assemblages aéronautiques collés sont étudiées. En effet, le caractère sans contact de cette technique optique pour générer et détecter des ultrasons est un atout majeur pour des applications industrielles. L'objectif principal de ce travail est de développer des méthodes END pour identifier des paramètres quantitatifs permettant de discriminer des collages ayant des tenues mécaniques différentes. Pour cela, la propagation d'ondes élastiques

générées et détectées par laser dans les assemblages collés est étudiée numériquement et expérimentalement.

Tout d'abord, une étude bibliographique est présentée dans le Chap. 1 concernant les méthodes END d'assemblages collés existantes dans la littérature. Suite à l'introduction des termes relatifs au collage ainsi que des défauts rencontrés dans ce type d'assemblage, un aperçu des méthodes destructives et non destructives est donné. Les méthodes par ultrasons dans les domaines linéaire et non linéaire sont présentées et discutées. Cette partie illustre l'absence d'une méthode END permettant de quantifier la tenue mécanique des collages structuraux malgré le fort besoin industriel.

Un modèle semi-analytique développé au cours de la thèse est ensuite décrit au Chap. 2. Celui-ci permet de simuler la propagation d'ultrasons générés par laser dans une structure multicouche, permettant de modéliser un assemblage collé. Avec ce modèle 2D, les champs de déplacement dans les milieux supérieur et inférieur du multicouche (respectivement les milieux I et II) sont calculés. La génération laser peut être simulée en prenant en compte une ligne source laser avec un certain angle d'incidence par rapport à la normale à la surface. Les problèmes électromagnétique, thermique et élastodynamique sont successivement résolus pour modéliser la source optoacoustique en régime thermoélastique ainsi que les ondes élastiques générées par l'expansion thermique des matériaux. La pénétration optique du faisceau laser incident dans le multicouche est prise en compte. Les densités de puissance dissipées en chaleur sont calculées à partir des amplitudes des ondes électromagnétiques transmises et réfléchies dans la structure. Ces densités de puissance dissipées sont ensuite utilisées comme termes sources pour résoudre le problème thermique. La résolution de celui-ci permet d'obtenir les champs de température en considérant les phénomènes de conduction et de convection thermique. Puis, les champs de déplacement dans les milieux I et II sont calculés dans l'espace de Fourier où des solutions analytiques peuvent être trouvées. Enfin, une double transformée de Fourier inverse (en temps et en espace) est effectuée numériquement pour obtenir les champs de déplacement dans les domaines temporel et spatial. Des couches intermédiaires peuvent être insérées entre les milieux supérieur et inférieur de la structure et sont modélisées à l'aide de matrices de transfert qui simulent les conditions de couplage électromagnétique, thermique et élastodynamique entre ces milieux I et II. Ce modèle semi-analytique permet d'obtenir des résultats rapides et précis pour résoudre le problème direct, c'est-à-dire pour obtenir les champs de déplacement dans les milieux supérieur et inférieur lorsque les propriétés optiques, thermiques et mécaniques des matériaux sont connues.

Des exemples de simulation sont fournis dans le Chap. 2 pour donner un bref aperçu

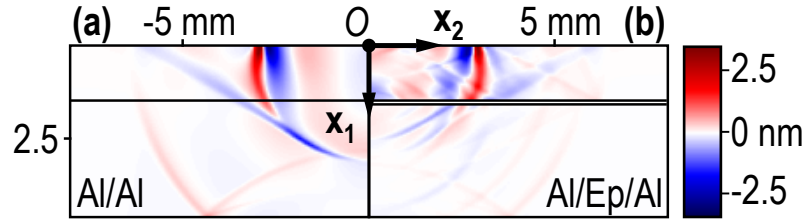


FIGURE R.1 – Déplacement normal  $u_1(x_1, x_2, t)$  simulé à  $t = 1 \mu\text{s}$  pour : (a) un bicouche Al (1,5 mm)/Al (3,1 mm) et (b) un tricouche Al (1,5 mm)/Epoxy (0,1 mm)/Al (3,0 mm).

des résultats obtenus avec le modèle semi-analytique développé au cours de cette thèse. Premièrement, les ondes élastiques générées par laser sont simulées dans une structure bicouche composée de deux plaques en alliage d'aluminium (Al) couplées mécaniquement au niveau de l'interface par deux distributions surfaciques de raideurs normales ( $K_N$ ) et transverses ( $K_T$ ). Les déplacements normaux simulés sont représentés Fig. R.1(a) lorsque des valeurs infinies sont choisies pour les raideurs interfaciales  $K_N$  et  $K_T$ . Cela implique une parfaite continuité des déplacements et des contraintes à l'interface entre les deux milieux. Ainsi, les ondes élastiques générées par laser à la surface du milieu supérieur sont entièrement transmises vers le milieu inférieur. Deuxièmement, des simulations sont réalisées en prenant en compte l'épaisseur d'une couche de colle entre deux plaques en alliage d'aluminium [voir Fig. R.1(b)]. Troisièmement, une source optoacoustique est simulée à l'interface entre deux milieux lorsque le faisceau laser incident est principalement absorbé dans le milieu inférieur par rapport au milieu supérieur. En ce qui concerne les limites de cette approche semi-analytique, les milieux solides composant le multicouche doivent avoir des surfaces parallèles et la génération d'ultrasons dans les sous-couches doit être négligée par rapport à celle dans les milieux I et II. L'une des principales perspectives de ce travail est d'étendre ce modèle 2D aux géométries 3D. Cela compliquera nécessairement les calculs car une nouvelle dimension spatiale doit être prise en compte. Cependant, la méthodologie pour résoudre les problèmes électromagnétique, thermique et élastodynamique sera similaire. Cette approche pourrait avoir un intérêt concernant la simulation d'ultrasons générés par laser lorsque la forme 3D de la source laser est complexe (comme cela est introduit dans le dernier paragraphe de ce résumé). Le modèle semi-analytique décrit dans le Chap. 2 a ensuite été utilisé dans le chapitre suivant pour simuler les bases de données nécessaires à la résolution de problèmes inverses.

En effet, une première méthode ultrasons-laser a été développée pour l'évaluation non destructive d'assemblages collés. Celle-ci est présentée dans le Chap. 3 de ce manuscrit.

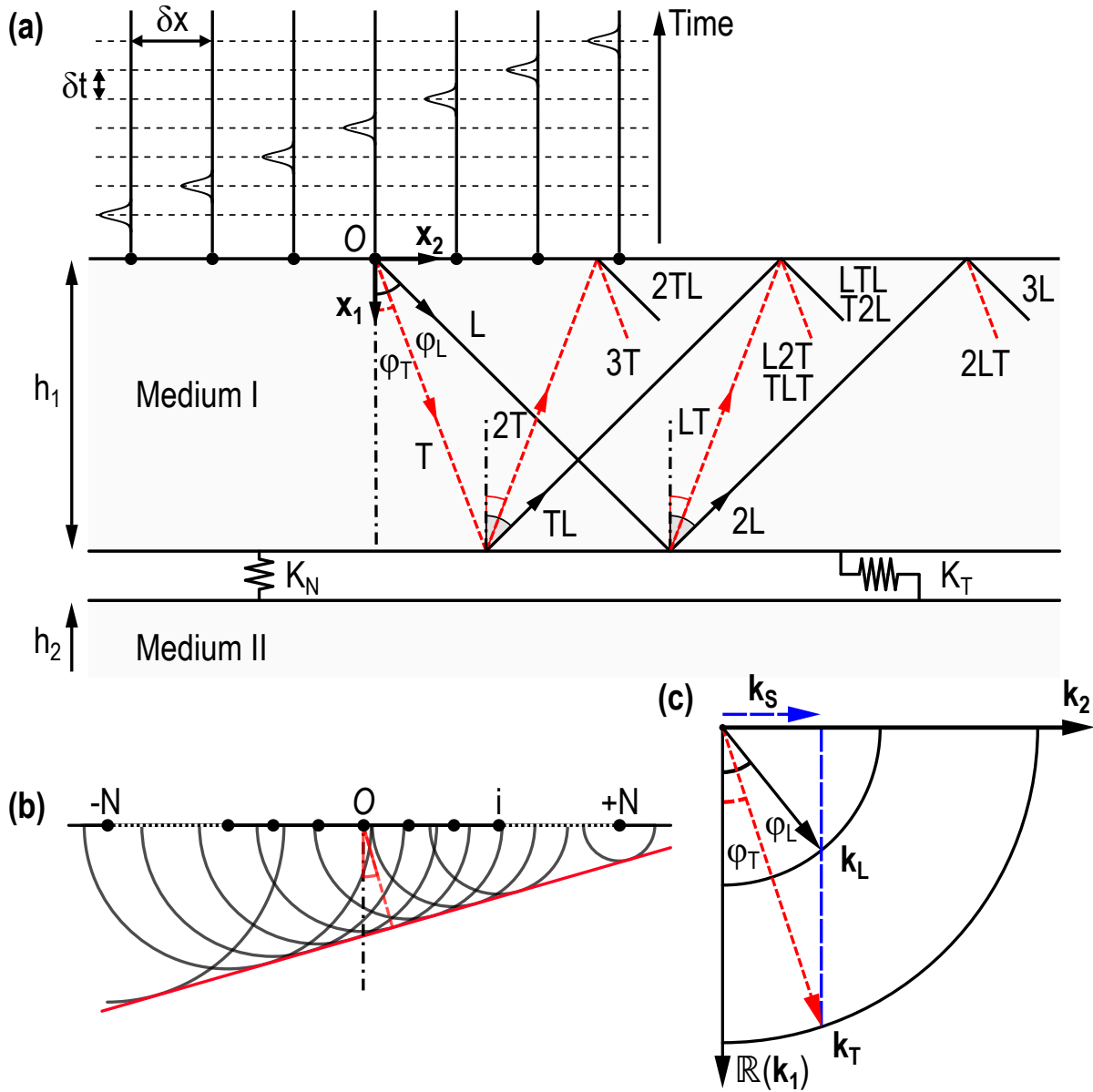


FIGURE R.2 – (a) Représentation des ondes planes synthétisées dans le milieu I. Tout d’abord, une ligne source laser de longueur infinie dans la direction  $\mathbf{x}_3$  est déplacée à la surface de l’échantillon en  $2N + 1$  positions avec un pas constant  $\delta x$  selon la direction  $\mathbf{x}_2$ . Puis, des retards à l’émission  $\delta t$  sont appliqués entre les différentes impulsions laser, dans une étape de post-traitement, afin de synthétiser des ondes planes longitudinales (L) et transversales (T). (b) L’application de retards à l’émission entre les  $2N + 1$  sources conduit à des interférences constructives et destructives entre les ondes divergentes entraînant la génération d’une onde plane. (c) Diagramme des lenteurs des ondes planes longitudinales et transversales qui sont synthétisées en imposant le vecteur d’onde  $k_s = \omega \delta t / \delta x$  avec  $\omega$  la fréquence angulaire.

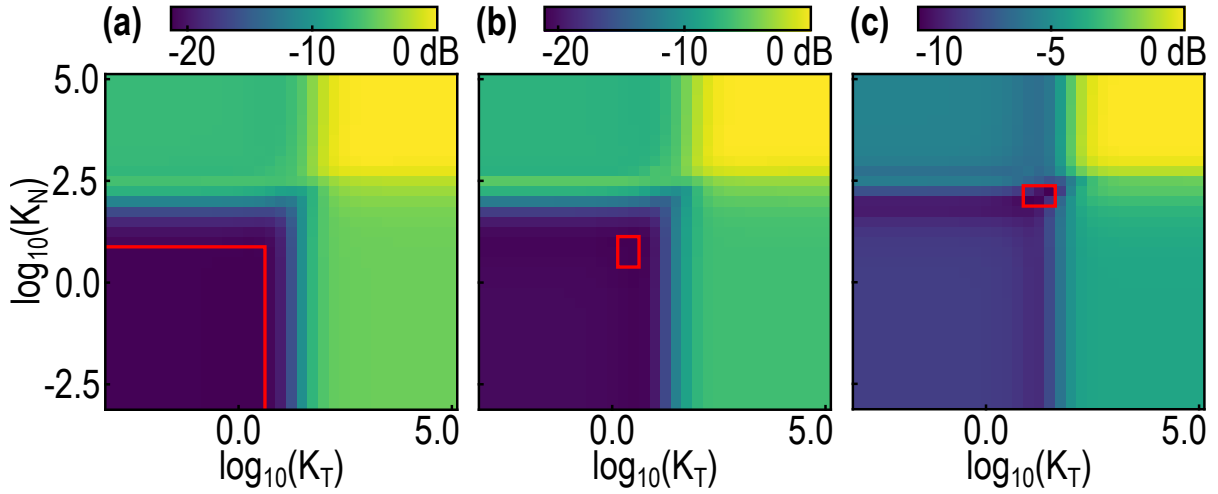


FIGURE R.3 – Fonctions coût obtenues lorsque les B-scans expérimentaux mesurés sur (a) une plaque d’alliage d’aluminium et deux assemblages collés Al/Ep/Al [(b) avec et (c) sans agent de démoulage] sont utilisés comme données d’entrée de l’algorithme permettant de résoudre le problème inverse. Les rectangles rouges indiquent les minima de chaque fonction coût avec une marge d’incertitude de  $\pm 0,1$  dB.

Elle permet d’identifier des raideurs interfaciales normales ( $K_N$ ) et transverses ( $K_T$ ) qui modélisent le collage lorsque les longueurs d’onde considérées sont grandes devant l’épaisseur du joint de colle. La méthode développée est basée sur la résolution de problèmes inverses à partir de la réflexion d’ondes planes synthétisées pour différents angles d’incidence par rapport à l’interface de collage. Une méthode de post-traitement est utilisée pour synthétiser ces ondes planes à partir de la propagation d’ondes de volume cylindriques générées par laser (voir Fig. R.2). Cette étape est réalisée en post-traitement en raison des difficultés expérimentales inhérentes à la génération d’ondes planes en ultrasons-laser. Une validation de la méthode développée est tout d’abord effectuée sur des données d’entrée simulées où un bruit Gaussien a été ajouté pour s’approcher d’un cas expérimental. Ces données simulées ont été obtenues avec le modèle semi-analytique présenté au Chap. 2. Ensuite, la méthode est appliquée sur une plaque en alliage d’aluminium (Al) et sur deux assemblages collés Al/Epoxy/Al (avec et sans défauts d’adhérence). Ces échantillons collés sont fabriqués à partir de films adhésifs structuraux en époxy. La méthode développée permet de discriminer les trois échantillons et d’identifier des paramètres quantitatifs de raideurs interfaciales  $K_N$  et  $K_T$  suite à la résolution de problèmes inverses. Ces valeurs

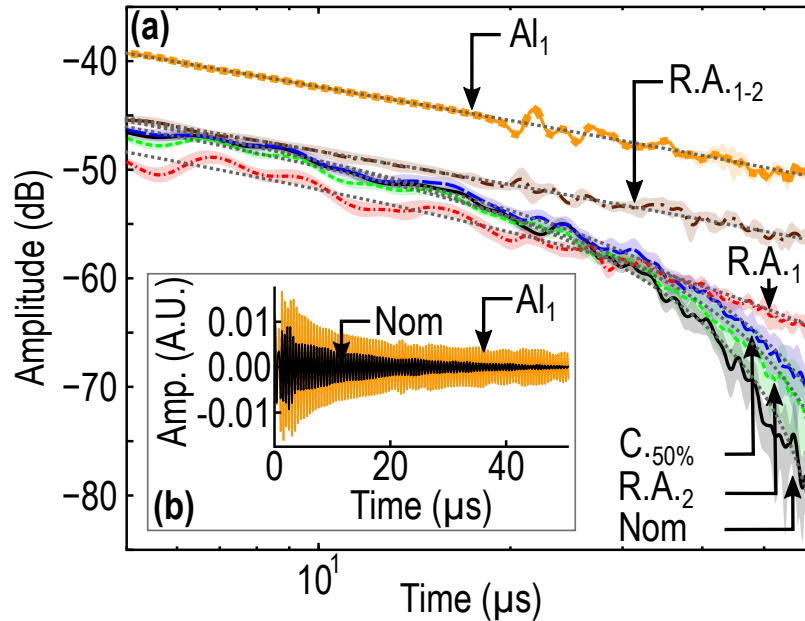


FIGURE R.4 – (a) Atténuations expérimentales en fonction du temps selon une échelle logarithmique. Pour chaque échantillon, l’atténuation moyenne pour les 11 points de mesure est tracée et l’écart type est représenté par des barres d’erreur en transparence. Les courbes obtenues suite à l’identification des paramètres d’atténuation sont représentées par des lignes pointillées. (b) Signaux temporels mesurés, pour la plaque en alliage d’aluminium (Al) et pour l’assemblage collé nominal (Nom), après filtrage des données avec un filtre passe-bande centré à  $\sim 2$  MHz autour de la fréquence de résonance ZGV.

sont obtenues en trouvant les minima des fonctions coût, représentées Fig. R.3, qui correspondent aux différences entre les données expérimentales d’entrée et la base de données composée de simulations semi-analytiques pour un grand nombre de valeurs de  $K_N$  et  $K_T$  (de  $10^{-3}$  kN mm $^{-3}$  à  $10^5$  kN mm $^{-3}$ ). Cette technique permet d’obtenir des valeurs moyennes de  $K_N$  et  $K_T$  pour la zone scannée (32 mm dans nos cas expérimentaux).

Une seconde approche a été proposée pour l’évaluation non destructive d’assemblages collés. Elle est présentée dans le Chap. 4. Contrairement à la méthode précédente, détaillée dans le Chap. 3, celle-ci permet une mesure locale en utilisant l’atténuation de modes de Lamb à vitesse de groupe nulle (ZGV), qui sont des résonances locales à des fréquences bien définies. Des mesures expérimentales sont réalisées sur cinq assemblages tricouches composés de deux plaques asymétriques, en alliage d’aluminium, collées par un film adhésif structural en époxy. Des défauts de cohésion, obtenus en diminuant le

temps de polymérisation de l'adhésif, et des défauts d'adhésion, créés à l'aide d'un agent démoulant, sont introduits pour dégrader la tenue mécanique de ces échantillons collés. Puis, les résonances ZGV sont générées et détectées expérimentalement pour ces différents échantillons collés. Les atténuations temporelles de ces résonances locales permettent de discriminer les différents échantillons collés (voir Fig. R.4) et d'identifier deux paramètres quantitatifs ( $\tau_1$  et  $\delta\omega$ ) liés à ces profils d'atténuation.

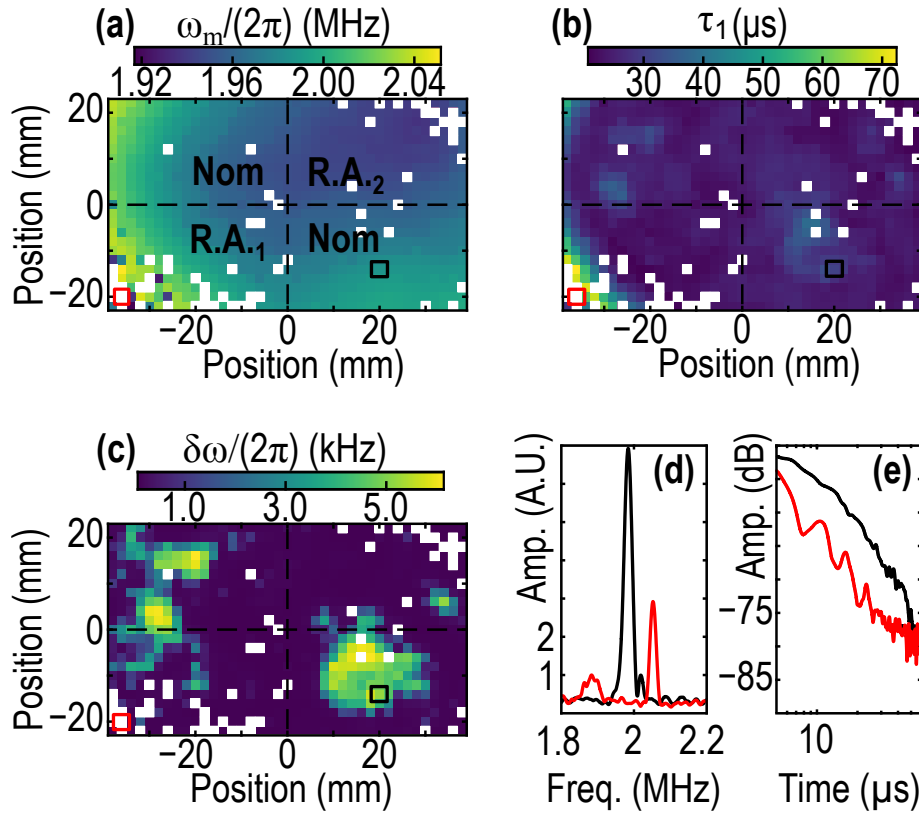


FIGURE R.5 – Cartographies 2D des paramètres identifiés [(a)  $\omega_m$ , (b)  $\tau_1$ , et (c)  $\delta\omega$ ] sur l'assemblage collé Al/Ep/Al divisé en quatre zones : deux zones nominales (Nom), une zone avec une couche d'agent de démoulage à l'interface supérieure (R.A.<sub>1</sub>) et une zone avec une couche d'agent de démoulage à l'interface inférieure (R.A.<sub>2</sub>). Lorsque le RMSE du fit est supérieur à  $0,4 \times 10^{-3}$  (valeur maximale obtenue pour les assemblages collés testés), le point est rejeté et remplacé par un carré blanc. (d) Spectres de fréquence et (e) atténuation des signaux temporels aux positions indiquées par les cases rouges et noires représentées sur les cartographies (a)–(c).

Pour démontrer la capacité d'imagerie de cette méthode entièrement optique, un balayage 2D d'un assemblage collé Al/Epoxy/Al (avec et sans défauts de collage) est effectué. Cela permet d'imager différentes zones sur l'échantillon collé en examinant les paramètres d'atténuation temporelle en plus des fréquences de résonance ZGV [voir Fig. R.5(a)–(c)]. Des différences ont été observées entre les mesures effectuées sur des échantillons présentant des défauts de collage répartis de manière homogène et sur ce dernier échantillon où les défauts de collage sont distribués de manière inhomogène, c'est-à-dire avec plusieurs types de défauts de collage sur le même échantillon. Un phénomène de battement a notamment été observé entre deux fréquences de résonance beaucoup plus éloignées [voir Fig. R.5(d) et (e)] que celles observées sur des échantillons homogènes, où le phénomène de battement était visible entre deux fréquences de résonance proches (environ quelques kHz).

Pour conclure, un modèle semi-analytique et deux méthodes END d'assemblages collés ont été développées au cours de cette thèse. Le modèle semi-analytique, bien qu'utilisé dans l'une de ses formes les plus simples dans la première méthode END pour résoudre les problèmes inverses, vise à être général. En effet, celui-ci permet de simuler la propagation d'ondes élastiques dans des structures multicouches avec la possibilité de prendre en compte : (i) des matériaux anisotropes dans la mesure où l'hypothèse du problème bidimensionnel se vérifie ; (ii) des conditions limites électromagnétiques, thermiques et mécaniques non conventionnelles (c'est-à-dire des discontinuités) ; (iii) des distributions volumiques asymétriques en 2D de la densité de puissance électromagnétique dissipée sous forme de chaleur. Le code est partagé et sera continuellement corrigé, si nécessaire, et amélioré/complété par moi et l'équipe de recherche impliquée dans ce travail de thèse. Il a été démontré que les deux méthodes END développées donnent accès à des paramètres quantitatifs permettant de distinguer et de caractériser des assemblages collés ayant des tenues mécaniques différentes, lorsque les techniques ultrasonores classiques ne le permettent pas. Chaque méthode a sa propre caractéristique de mesure qui déterminera son utilisation. D'une part, le niveau d'adhérence global d'un assemblage est rendu possible par un balayage du laser de génération avec la méthode basée sur la synthèse de fronts plans d'ondes. D'autre part, la cartographie locale du niveau d'adhérence d'un assemblage peut être réalisée par un balayage de l'échantillon avec la méthode basée sur la génération de modes ZGV. En ce qui concerne les perspectives plus générales de ces travaux de thèse, les méthodes non linéaires semblent également présenter un réel intérêt.

Des travaux préliminaires ont déjà été entrepris, notamment concernant la focalisation

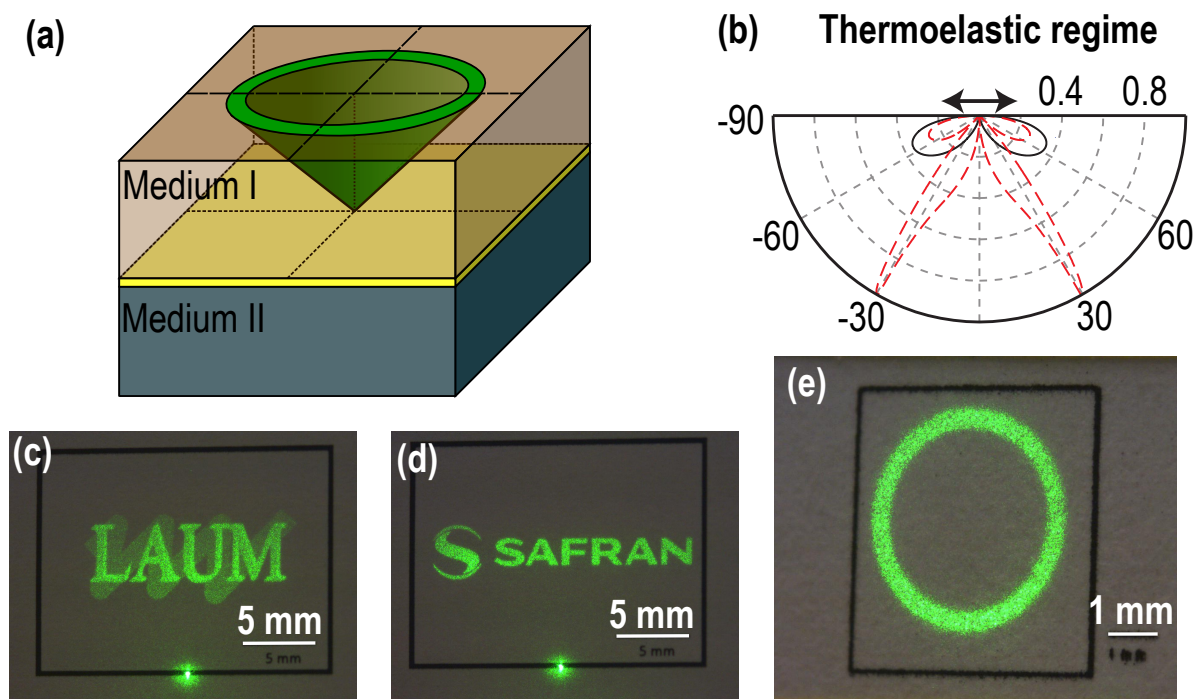


FIGURE R.6 – (a) Schéma de la méthode proposée pour focaliser les ultrasons générés par laser au niveau du collage en utilisant, par exemple dans le cas d'un matériau isotrope, une source laser en forme d'anneau. (b) Diagramme de directivité d'une source laser en régime thermoélastique. Figure extraite de la thèse de S. Raetz (p. 24 de la Ref. 151). Les ondes longitudinales (transversales) sont représentées par des lignes continues (pointillées). (c)–(d) Images obtenues avec le Spatial Light Modulator (SLM). (e) Source laser en forme d'anneau obtenue avec le SLM.

d'ondes de volume en utilisant une source laser en forme d'anneau [voir Fig. R.6(a)]. L'objectif de cette technique est de venir focaliser les ondes de volume, générées par laser, au niveau de la zone collée. Cette focalisation permettra d'augmenter localement l'amplitude des ultrasons et d'observer éventuellement des effets non linéaires. Une demande de brevet a été déposée concernant ce principe de mesure pour l'END des assemblages collés. Afin de focaliser les ultrasons générés par laser, la forme adéquate de la source optoacoustique est obtenue à l'aide d'un modulateur spatial de lumière [Spatial Light Modulator (SLM)]. La réflexion d'un faisceau laser collimaté sur cette optique diffractive permet d'obtenir à la surface de l'échantillon inspecté des faisceaux lasers présentant des profils géométriques complexes [voir Fig. R.6(c) et (d)]. La source laser en forme d'anneau, à utiliser dans le

cas d'un matériau isotrope, est quant à elle représentée Fig. R.6(e). Le but est donc de dimensionner l'anneau (rayon intérieur, rayon extérieur) de façon à ce que la focalisation des ultrasons s'opère au niveau du collage. Cela offre des perspectives intéressantes concernant le développement de méthodes ultrasons-laser non linéaires pour l'évaluation non destructive des assemblages aéronautiques collés.

# Appendices



# Appendix A

## Semi-analytic model: additional calculations

In this appendix, additional equations are provided to complement the semi-analytic model described in Chap. 2. Details of calculations are given concerning the resolution of electromagnetic (Sec. A.1), thermal (Sec. A.2) and elastodynamic (Sec. A.3) problems.

### A.1 Electromagnetic problem

In order to simulate laser-generated ultrasounds in a multilayer structure, the first part of the semi-analytic model, presented in Chap. 2, is to solve the electromagnetic problem (see Sec. 2.3). The aim is to obtain the power density  $Q$  of the energy dissipated by heat in the different media. This term is then used as the source term for the heat equation defined in Sec. 2.4.

#### A.1.1 Obtaining the Helmholtz equation

In Sec. 2.3, the Helmholtz equation (Eq. 2.1) is solved to find the electric vector  $\mathbf{E}$  and the magnetic vector  $\mathbf{H}$  in the multilayer structure. To obtain this Helmholtz equation, the Maxwell's equations are used:

$$\nabla \times \mathbf{H} - \frac{1}{c_0} \frac{\partial \mathbf{D}}{\partial t} = \frac{4\pi}{c_0} \mathbf{j}, \quad (\text{A.1a})$$

$$\nabla \times \mathbf{E} + \frac{1}{c_0} \frac{\partial \mathbf{B}}{\partial t} = 0, \quad (\text{A.1b})$$

$$\nabla \cdot \mathbf{D} = 4\pi \rho_q, \quad (\text{A.1c})$$

$$\nabla \cdot \mathbf{B} = 0. \quad (\text{A.1d})$$

with  $\mathbf{E}$  the electric vector,  $\mathbf{D}$  the electric displacement,  $\mathbf{H}$  the magnetic vector,  $\mathbf{B}$  the magnetic induction,  $\mathbf{j}$  the electric current density,  $\rho_q$  the electric charge density,  $c_0$  the

speed of light in vacuum and  $t$  the time. The curl of a vector is denoted “ $\nabla \times$ ” and the divergence “ $\nabla \cdot$ ” with “ $\nabla$ ” the nabla operator. These four Maxwell’s equations [Eqs. (A.1a–A.1d)] are extracted from the book of Born and Wolf (pp. 1–2 in Ref. 155), which is written in the Gaussian unit system.<sup>a</sup> Under the assumptions introduced in Sec. 2.2, the constitutive relations (pp. 3 and 9 in Ref. 155) are given by

$$\mathbf{j} = \mathbf{j}_c + \mathbf{j}_v, \quad (\text{A.2a})$$

$$\mathbf{D} = \varepsilon \mathbf{E}, \quad (\text{A.2b})$$

$$\mathbf{B} = \mu \mathbf{H}, \quad (\text{A.2c})$$

with  $\mathbf{j}_c = \sigma \mathbf{E}$  the conduction current density,  $\sigma$  the optical conductivity,  $\varepsilon$  the dielectric constant and  $\mu$  the magnetic permeability. In Eq. (A.2a), the convection current density  $\mathbf{j}_v = 0$  because the electric charge density  $\rho_q$  is assumed to be zero in Sec. 2.2. Hence, the time derivative of Eq. (A.1a) gives

$$\nabla \times \frac{\partial \mathbf{H}}{\partial t} = \frac{\varepsilon}{c_0} \frac{\partial^2 \mathbf{E}}{\partial t^2} + \frac{4\pi\sigma}{c_0} \frac{\partial \mathbf{E}}{\partial t}, \quad (\text{A.3})$$

and the curl of Eq. (A.1b):

$$\nabla \times \frac{\partial \mathbf{H}}{\partial t} = -\frac{c_0}{\mu} (\nabla(\nabla \cdot \mathbf{E}) - \nabla^2 \mathbf{E}). \quad (\text{A.4})$$

The assumption that  $\rho_q = 0$  also implies that  $\nabla \cdot \mathbf{E} = 0$ . Thus, Eqs. (A.3, A.4) lead to

$$\nabla^2 \mathbf{E} = \frac{\mu}{c_0^2} \left( \varepsilon \frac{\partial^2 \mathbf{E}}{\partial t^2} + 4\pi\sigma \frac{\partial \mathbf{E}}{\partial t} \right). \quad (\text{A.5})$$

The electromagnetic field is assumed to be monochromatic, with the angular frequency  $\omega_0$ , and the convention  $(\mathbf{E} = \mathbf{E}_i e^{-j(\omega_0 t - \mathbf{k}_i \cdot \mathbf{x})})$ <sup>b</sup> is used to obtain:

---

a. Gaussian units are widely used in electromagnetic. According to Milton and Schwinger (p. 347 in Ref. 205), one of the advantage of this unit system is that “the electric and magnetic fields,  $\mathbf{E}$ ,  $\mathbf{D}$ ,  $\mathbf{B}$ ,  $\mathbf{H}$ , have the same units”. Moreover, the dielectric constant  $\varepsilon$  and the magnetic permeability  $\mu$  are dimensionless in the Gaussian unit system and correspond to the relative permittivity  $\varepsilon_r$  and the relative permeability  $\mu_r$  in SI units, respectively. To convert physical quantities from Gaussian units to SI units, one can refer to the Appendix A of Ref. 206 (pp. 673–676).

b. For electromagnetic plane waves, the convention is chosen to be  $e^{-j(\omega t - \mathbf{k} \cdot \mathbf{x})}$  which is often used in electromagnetic books. This is the only part in this manuscript where this convention is used. For thermal and mechanical plane waves, the convention is  $e^{j(\omega t - \mathbf{k} \cdot \mathbf{x})}$ .

### A.1. Electromagnetic problem

---

$$\nabla^2 \mathbf{E} + \left( \frac{\omega_0}{c_0} \right)^2 \underbrace{\mu \left( \varepsilon + j \frac{4\pi\sigma}{\omega_0} \right)}_{\varepsilon_c} \mathbf{E} = 0. \quad (\text{A.6})$$

In Eq. (A.6), the term  $\frac{\omega_0}{c_0}$  is the wavenumber in vacuum and  $\varepsilon_c = \varepsilon + j \frac{4\pi\sigma}{\omega_0}$  is the complex permittivity. Hence, the expression of the Helmholtz equation, given in Ref. 155 (p. 737) and in Eq. 2.1, is:

$$\boxed{\nabla^2 \mathbf{E} + k^2 \mathbf{E} = 0}, \quad (\text{A.7})$$

with the complex wavenumber  $k = \frac{\omega_0}{c_0} n$ , also written

$$k = k' + jk'' \text{ with } k' = \Re \left( \frac{\omega_0}{c_0} n \right), k'' = \Im \left( \frac{\omega_0}{c_0} n \right), \quad (\text{A.8})$$

and  $n$  the complex refractive index given by

$$n = n' + jn'' \text{ with } n' = \Re(n) \text{ and } n'' = \Im(n), \quad (\text{A.9})$$

with the  $\Re$  ( $\Im$ ) symbol which corresponds to the real (imaginary) part. In the literature,  $n''$  is often called the extinction coefficient<sup>156</sup> or the attenuation index.<sup>155</sup> The complex refractive index  $n$  is also equal to

$$n = \sqrt{\mu \varepsilon_c} = \sqrt{\mu \left( \varepsilon + j \frac{4\pi\sigma}{\omega_0} \right)}. \quad (\text{A.10})$$

Squaring these two expressions of  $n$  in Eqs. (A.9, A.10), leads to

$$\left\{ \begin{array}{l} n^2 = n'^2 - n''^2 + 2jn'n'', \end{array} \right. \quad (\text{A.11a})$$

$$\left\{ \begin{array}{l} n^2 = \mu \left( \varepsilon + j \frac{4\pi\sigma}{\omega_0} \right). \end{array} \right. \quad (\text{A.11b})$$

Finally, the equalization of the real and imaginary parts gives the dielectric constant  $\varepsilon$  and the optical conductivity  $\sigma$  as a function of  $n'$ ,  $n''$ ,  $\mu$  and  $\omega_0$ :

$$\left\{ \begin{array}{l} \varepsilon = \frac{n'^2 - n''^2}{\mu}, \end{array} \right. \quad (\text{A.12a})$$

$$\left\{ \begin{array}{l} \sigma = \frac{\omega_0 n' n''}{2\pi\mu}. \end{array} \right. \quad (\text{A.12b})$$

### A.1.2 Coefficients $A_{ij}^E$

In Sec. 2.3.2, the linear system to solve in order to determine the ratio of the amplitudes of the reflected/transmitted electromagnetic waves to the amplitude of the incident electromagnetic wave is

$$\begin{bmatrix} A_{11}^E & A_{12}^E & A_{13}^E & 0 & 0 & 0 \\ A_{21}^E & A_{22}^E & A_{23}^E & 0 & 0 & 0 \\ 0 & A_{32}^E & A_{33}^E & A_{34}^E & A_{35}^E & 0 \\ 0 & A_{42}^E & A_{43}^E & A_{44}^E & A_{45}^E & 0 \\ 0 & 0 & 0 & A_{54}^E & A_{55}^E & A_{56}^E \\ 0 & 0 & 0 & A_{64}^E & A_{65}^E & A_{66}^E \end{bmatrix} \begin{bmatrix} R_0^- \\ R_I^+ \\ R_I^- \\ R_{II}^+ \\ R_{II}^- \\ R_{III}^+ \end{bmatrix} = \begin{bmatrix} \cos \theta_0 \\ -n_0/\mu_0 \\ 0 \\ 0 \\ 0 \\ 0 \end{bmatrix}. \quad (\text{A.13})$$

In order to obtain a well-conditioned matrix, the unknowns of Eq. (A.13) are written as

$$\begin{aligned} R_0^- &= \frac{E_0^-}{E_0^+}, R_I^+ = \frac{E_I^+}{E_0^+}, R_I^- = \frac{E_I^-}{E_0^+} e^{\beta_I(\theta_1) \frac{h_1}{2}}, \\ R_{II}^+ &= \frac{E_{II}^+}{E_0^+} e^{-\beta_{II}(\theta_2) \frac{h_1 + \Delta h}{2}}, R_{II}^- = \frac{E_{II}^-}{E_0^+} e^{\beta_{II}(\theta_2) \frac{h}{2}}, R_{III}^+ = \frac{E_{III}^+}{E_0^+}, \end{aligned} \quad (\text{A.14})$$

with the inverse expressions of the optical penetrations which are equal to<sup>158</sup>

$$\beta_I(\theta_1) = 2 [k_I' \Im(\cos \theta_1) + k_I'' \Re(\cos \theta_1)], \quad (\text{A.15a})$$

$$\beta_{II}(\theta_2) = 2 [k_{II}' \Im(\cos \theta_2) + k_{II}'' \Re(\cos \theta_2)]. \quad (\text{A.15b})$$

The coefficients  $A_{ij}^E$ , in Eq. (A.13), are given by

$$A_{11}^E = \cos \theta_0, \quad A_{12}^E = \cos \theta_1, \quad A_{13}^E = -e^{-\frac{\beta_I(\theta_1) h_1}{2}} \cos \theta_1, \quad (\text{A.16})$$

$$A_{21}^E = n_0/\mu_0, \quad A_{22}^E = -n_I/\mu_I, \quad A_{23}^E = -n_I e^{-\frac{\beta_I(\theta_1) h_1}{2}} / \mu_I, \quad (\text{A.17})$$

$$A_{32}^E = -e^{-\frac{\beta_I(\theta_1) h_1}{2}} e^{\gamma_I(\theta_1) h_1} \cos \theta_1, \quad (\text{A.18})$$

$$A_{33}^E = e^{-\gamma_I(\theta_1) h_1} \cos \theta_1, \quad (\text{A.19})$$

$$A_{34}^E = (L_{11}^E \cos \theta_2 + L_{12}^E n_{II}/\mu_{II}) e^{\gamma_{II}(\theta_2)(\Delta h + h_1)}, \quad (\text{A.20})$$

$$A_{35}^E = (-L_{11}^E \cos \theta_2 + L_{12}^E n_{II}/\mu_{II}) e^{-\frac{\beta_{II}(\theta_2) h_2}{2}} e^{-\gamma_{II}(\theta_2)(\Delta h + h_1)}, \quad (\text{A.21})$$

$$A_{42}^E = -n_I e^{-\frac{\beta_I(\theta_1) h_1}{2}} e^{\gamma_I(\theta_1) h_1} / \mu_I, \quad (\text{A.22})$$

### A.1. Electromagnetic problem

---

$$A_{43}^E = -n_I e^{-\gamma_I(\theta_1)h_1} / \mu_I, \quad (\text{A.23})$$

$$A_{44}^E = (L_{21}^E \cos \theta_2 + L_{22}^E n_{II} / \mu_{II}) e^{j\gamma_{II}(\theta_2)(\Delta h + h_1)}, \quad (\text{A.24})$$

$$A_{45}^E = (-L_{21}^E \cos \theta_2 + L_{22}^E n_{II} / \mu_{II}) e^{-\frac{\beta_{II}(\theta_2)h_2}{2}} e^{-j\gamma_{II}(\theta_2)(\Delta h + h_1)}, \quad (\text{A.25})$$

$$A_{54}^E = -e^{-\frac{\beta_{II}(\theta_2)h_2}{2}} e^{jH\gamma_{II}(\theta_2)} \cos \theta_2, \quad (\text{A.26})$$

$$A_{55}^E = e^{-jH\gamma_{II}(\theta_2)} \cos \theta_2, \quad A_{56}^E = e^{jHk_{III} \cos \theta_3} \cos \theta_3, \quad (\text{A.27})$$

$$A_{64}^E = n_{II} e^{-\frac{\beta_{II}(\theta_2)h_2}{2}} e^{jH\gamma_{II}(\theta_2)} / \mu_{II}, \quad (\text{A.28})$$

$$A_{65}^E = n_{II} e^{-jH\gamma_{II}(\theta_2)} / \mu_{II}, \quad A_{66}^E = -n_{III} e^{jHk_{III} \cos \theta_3} / \mu_{III}. \quad (\text{A.29})$$

#### A.1.3 Obtaining the power density $Q$ with Poynting's theorem

In Sec. 2.3.3, to determine the power density  $Q$  which is the source term of the heat equation in Eq. (2.17), the Poynting's theorem is applied. The detailed calculation to quickly obtain this theorem is recalled and is based on the book of Born and Wolf.<sup>155</sup> First, the Maxwell's equation [Eq. (A.1a)] and the constitutive relations, introduced in Eqs. (A.2b) and (A.2a) with the conduction current density  $\mathbf{j}_c = \sigma \mathbf{E}$ , are considered and result in

$$\nabla \times \mathbf{H} = \frac{1}{c_0} \underbrace{\left( \varepsilon + j \frac{4\pi\sigma}{\omega_0} \right)}_{\varepsilon_c} \frac{\partial \mathbf{E}}{\partial t} + \frac{4\pi}{c_0} \mathbf{j}_v, \quad (\text{A.30})$$

with  $\varepsilon_c$  the complex permittivity. Using the identity:

$$\mathbf{H} \cdot (\nabla \times \mathbf{E}) - \mathbf{E} \cdot (\nabla \times \mathbf{H}) = \nabla \cdot (\mathbf{E} \times \mathbf{H}), \quad (\text{A.31})$$

and replacing the terms  $\nabla \times \mathbf{H}$  by Eq. (A.30) and  $\nabla \times \mathbf{E}$  by the Maxwell's equation [Eq. (A.1b)], with the constitutive relation given in Eq. (A.2c), we obtain the Poynting's theorem:

$$\frac{1}{4\pi} \left( \mu \mathbf{H} \cdot \frac{\partial \mathbf{H}}{\partial t} + \varepsilon_c \mathbf{E} \cdot \frac{\partial \mathbf{E}}{\partial t} \right) = -\frac{c_0}{4\pi} \nabla \cdot (\mathbf{E} \times \mathbf{H}) - \mathbf{E} \cdot \mathbf{j}_v \quad (\text{A.32})$$

Assuming that the convection current density  $\mathbf{j}_v = \mathbf{0}$  (hypothesis defined in Sec. 2.2) and that the time average (denoted by “ $\langle \rangle$ ”) of Eq. (A.32) is realized over a period which is large compared to the fundamental optical period  $2\pi/\omega_0$  (see p. 34 in Ref. 155), we obtain

$$\boxed{Q = -\nabla \cdot \langle \mathbf{S} \rangle}, \quad (\text{A.33})$$

with  $Q$  the power density equals to the time average of the term on the left of Eq. (A.32):

$$Q = \frac{1}{4\pi} \left\langle \mu \mathbf{H} \cdot \frac{\partial \mathbf{H}}{\partial t} + \varepsilon_c \mathbf{E} \cdot \frac{\partial \mathbf{E}}{\partial t} \right\rangle, \quad (\text{A.34})$$

and  $\langle \mathbf{S} \rangle$  the time average of the Poynting vector (p. 35 in Ref. 155) which is equal to

$$\langle \mathbf{S} \rangle = \frac{c_0}{8\pi} \Re(\mathbf{E} \times \bar{\mathbf{H}}). \quad (\text{A.35})$$

In Eq. (A.35),  $\Re$  refers to the real part of  $\mathbf{E} \times \bar{\mathbf{H}}$ ,  $\mathbf{E}$  is the electric vector and  $\bar{\mathbf{H}}$  is the conjugate of the magnetic vector  $\mathbf{H}$ .

#### A.1.4 Detailed calculation of the transfer matrix $[L_i^{EM}]_{2 \times 2}$

In Sec. 2.3.2, the transfer matrix  $[L^{EM}]$  associated to the electromagnetic boundary condition between media I and II, introduced in Eq. (2.9c), is expressed as

$$[L^{EM}]_{2 \times 2} = \prod_{i=1}^{N_{\text{sublayers}}} [L_i^{EM}]_{2 \times 2}, \quad (\text{A.36})$$

with  $[L_i^{EM}]$  the transfer matrix of the  $i$ -th sublayer and  $N_{\text{sublayers}}$  the total number of sublayers which are between media I and II. For a given sublayer of thickness  $h_i$ , as the one represented in Fig. A.1, the projections of the electric vector  $\mathbf{E}_i \cdot \mathbf{x}_2$  and magnetic vector  $\mathbf{H}_i \cdot \mathbf{x}_3$  are linked between the upper and lower surfaces (of local coordinates  $x_1 = -h_i$  and  $x_1 = 0$ , respectively) by the relation:

$$\begin{bmatrix} \mathbf{E}_i \cdot \mathbf{x}_2 \\ \mathbf{H}_i \cdot \mathbf{x}_3 \end{bmatrix}_{x_1=-h_i} = [L_i^{EM}]_{2 \times 2} \begin{bmatrix} \mathbf{E}_i \cdot \mathbf{x}_2 \\ \mathbf{H}_i \cdot \mathbf{x}_3 \end{bmatrix}_{x_1=0}. \quad (\text{A.37})$$

To obtain the transfer matrix  $[L_i^{EM}]_{2 \times 2}$ , the methodology presented in Ref. 157 (pp. 53–60) to find the transfer matrix for elastic waves is applied for electromagnetic waves. For the  $i$ -th sublayer, the projections of the electric vector  $\mathbf{E}_i$  along the  $\mathbf{x}_2$ -axis and the magnetic vector  $\mathbf{H}_i$  along the  $\mathbf{x}_3$ -axis, without the time  $t$  and the position  $x_2$  dependencies (i.e., without the term  $e^{-j(\omega_0 t - k_i \sin \theta_i x_2)}$ ), are equal to

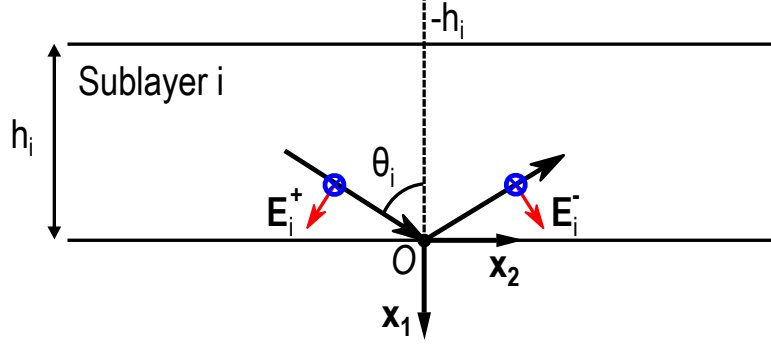


Figure A.1 – Geometry of the  $i$ -th sublayer of thickness  $h_i$ . The black arrows represent the  $\mathbf{k}_i$ -wave vectors and the red (blue) arrows indicate the electric vectors  $\mathbf{E}_i$  (magnetic vectors  $\mathbf{H}_i$ ).

$$\mathbf{E}_i \cdot \mathbf{x}_2 = \cos \theta_i \left( -E_i^+ e^{jk_i \cos \theta_i x_1} + E_i^- e^{-jk_i \cos \theta_i x_1} \right), \quad (\text{A.38})$$

$$\mathbf{H}_i \cdot \mathbf{x}_3 = -\frac{n_i}{\mu_i} \left( E_i^+ e^{jk_i \cos \theta_i x_1} + E_i^- e^{-jk_i \cos \theta_i x_1} \right), \quad (\text{A.39})$$

with  $\theta_i$  the angle of propagation of the electromagnetic wave with respect to the  $\mathbf{x}_1$ -axis,  $k_i$  the complex wavenumber given in Eq. (2.2),  $n_i$  the refractive index defined in Eq. (2.3) and  $\mu_i$  the magnetic permeability of the  $i$ -th sublayer. Using Euler's formula:

$$\begin{aligned} -E_i^+ e^{jk_i \cos \theta_i x_1} + E_i^- e^{-jk_i \cos \theta_i x_1} &= -j \left( E_i^+ + E_i^- \right) \sin(k_i \cos \theta_i x_1) \\ &\quad - \left( E_i^+ - E_i^- \right) \cos(k_i \cos \theta_i x_1), \end{aligned} \quad (\text{A.40})$$

$$\begin{aligned} E_i^+ e^{jk_i \cos \theta_i x_1} + E_i^- e^{-jk_i \cos \theta_i x_1} &= \left( E_i^+ + E_i^- \right) \cos(k_i \cos \theta_i x_1) \\ &\quad + j \left( E_i^+ - E_i^- \right) \sin(k_i \cos \theta_i x_1). \end{aligned} \quad (\text{A.41})$$

Therefore, Eqs. (A.38) and (A.39) can be written in the form

$$\mathbf{E}_i \cdot \mathbf{x}_2 = -\cos \theta_i \left[ j \sin(k_i \cos \theta_i x_1) \left( E_i^+ + E_i^- \right) + \cos(k_i \cos \theta_i x_1) \left( E_i^+ - E_i^- \right) \right], \quad (\text{A.42})$$

$$\mathbf{H}_i \cdot \mathbf{x}_3 = -\frac{n_i}{\mu_i} \left[ \cos(k_i \cos \theta_i x_1) \left( E_i^+ + E_i^- \right) + j \sin(k_i \cos \theta_i x_1) \left( E_i^+ - E_i^- \right) \right]. \quad (\text{A.43})$$

We can now evaluate Eqs. (A.42) and (A.43) at  $x_1 = 0$ , which gives the linear system:

$$\begin{bmatrix} \mathbf{E}_i \cdot \mathbf{x}_2 \\ \mathbf{H}_i \cdot \mathbf{x}_3 \end{bmatrix}_{x_1=0} = \begin{bmatrix} 0 & -\cos \theta_i \\ -\frac{n_i}{\mu_i} & 0 \end{bmatrix} \begin{bmatrix} E_i^+ + E_i^- \\ E_i^+ - E_i^- \end{bmatrix}, \quad (\text{A.44})$$

and at the position  $x_1 = -h_i$ , which gives

$$\begin{bmatrix} \mathbf{E}_i \cdot \mathbf{x}_2 \\ \mathbf{H}_i \cdot \mathbf{x}_3 \end{bmatrix}_{x_1=-h_i} = \begin{bmatrix} j \sin(k_i \cos \theta_i h_i) \cos \theta_i & -\cos(k_i \cos \theta_i h_i) \cos \theta_i \\ -\cos(k_i \cos \theta_i h_i) \frac{n_i}{\mu_i} & j \sin(k_i \cos \theta_i h_i) \frac{n_i}{\mu_i} \end{bmatrix} \begin{bmatrix} E_i^+ + E_i^- \\ E_i^+ - E_i^- \end{bmatrix}. \quad (\text{A.45})$$

By inverting the linear system given in Eq. (A.44), we obtain

$$\begin{bmatrix} E_i^+ + E_i^- \\ E_i^+ - E_i^- \end{bmatrix} = \begin{bmatrix} 0 & -\frac{n_i}{\mu_i} \\ -\cos \theta_i & 0 \end{bmatrix} \begin{bmatrix} \mathbf{E}_i \cdot \mathbf{x}_2 \\ \mathbf{H}_i \cdot \mathbf{x}_3 \end{bmatrix}_{x_1=0}, \quad (\text{A.46})$$

and by reinjecting this expression into Eq. (A.45), we finally get the expression of the transfer matrix  $[L_i^{EM}]_{2 \times 2}$  for the  $i$ -th sublayer:

$$\begin{bmatrix} \mathbf{E}_i \cdot \mathbf{x}_2 \\ \mathbf{H}_i \cdot \mathbf{x}_3 \end{bmatrix}_{x_1=-h_i} = \underbrace{\begin{bmatrix} \cos(k_i \cos \theta_i h_i) & -j \sin(k_i \cos \theta_i h_i) \frac{\cos \theta_i \mu_i}{n_i} \\ -j \sin(k_i \cos \theta_i h_i) \frac{n_i}{\cos \theta_i \mu_i} & \cos(k_i \cos \theta_i h_i) \end{bmatrix}}_{[L_i^{EM}]_{2 \times 2}} \begin{bmatrix} \mathbf{E}_i \cdot \mathbf{x}_2 \\ \mathbf{H}_i \cdot \mathbf{x}_3 \end{bmatrix}_{x_1=0}. \quad (\text{A.47})$$

If  $h_i$  equals zero, this transfer matrix is equal to the identity matrix, as expected to ensure perfect continuity of the projections of electric and magnetic vectors along the  $\mathbf{x}_2$ -axis and  $\mathbf{x}_3$ -axis, respectively.

## A.2 Heat diffusion problem

### A.2.1 Laser pulse distributions in time and space

In Eq. (2.23a), the laser pulse distribution in time is equal to

$$f(t) = \frac{2}{\tau_p} \sqrt{\frac{\ln 2}{\pi}} e^{-4 \ln 2 \frac{t^2}{\tau_p^2}}, \quad (\text{A.48})$$

with  $\tau_p$  the pulse duration at half maximum (FWHM) of the Gaussian function. Hence, the Fourier transform of  $f(t)$  is given by

$$F(\omega) = \frac{1}{\sqrt{2\pi}} \int_{-\infty}^{+\infty} f(t) e^{-j\omega t} dt = \frac{1}{\sqrt{2\pi}} e^{-\tau_p^2 \omega^2 / (16 \ln 2)}. \quad (\text{A.49})$$

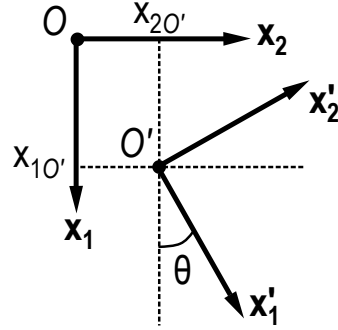


Figure A.2 – Representation of the Cartesian coordinate system  $(O', \mathbf{x}'_1, \mathbf{x}'_2)$  translated and rotated through an angle  $\theta$  to the Cartesian coordinate system  $(O, \mathbf{x}_1, \mathbf{x}_2)$ .

In the semi-analytic model presented in Chap. 2, an incident tilted laser line source of infinite dimension in the  $\mathbf{x}_3$ -direction is considered (see Sec. 2.2). To model this tilted laser line source, a Gaussian function is written in the Cartesian coordinate system  $(O', \mathbf{x}'_1, \mathbf{x}'_2)$ , as shown in Fig. A.2, with  $\theta$  the angle between the  $\mathbf{x}_1$ -direction and the direction of refraction in the medium in which the heat diffusion problem is solved (i.e., the  $\mathbf{x}'_1$ -direction) and  $(x_{1O'}, x_{2O'})$  the coordinates of the origin  $O'$  in the Cartesian coordinate system  $(O, \mathbf{x}_1, \mathbf{x}_2)$ . In the Cartesian coordinate system  $(O', \mathbf{x}'_1, \mathbf{x}'_2)$ , the laser line source distribution in space is equal to

$$g(x'_1, x'_2) = \frac{2}{a_s(x'_1)} \sqrt{\frac{\ln 2}{\pi}} e^{-4 \ln 2 \frac{x'^2_2}{a_s^2(x'_1)}}, \quad (\text{A.50})$$

with  $a_s(x'_1)$  the source width at half maximum (FWHM) of the tilted Gaussian beam. The source width  $a_s(x'_1)$  depends on  $x'_1$  and is equal to  $2w(x'_1)$  with  $w(x'_1)$  the radius of the Gaussian beam which is equal to

$$w(x'_1) = w_0 \left[ 1 + \left( \frac{\lambda_{\text{opt}} x'_1}{\pi w_0^2} \right)^2 \right]. \quad (\text{A.51})$$

In Eq. (A.51),  $w_0$  is the radius of the beam waist at  $x'_1 = 0$ ,  $\lambda_{\text{opt}}$  is the wavelength of the monochromatic incident laser beam. Under the assumption that  $\frac{\pi w_0^2}{\lambda_{\text{opt}}} \gg x'_1$ , which is a valid hypothesis in our experimental cases because  $\frac{\pi w_0^2}{\lambda_{\text{opt}}} \approx \frac{\pi (0.1 \text{ mm})^2}{532 \cdot 10^{-6} \text{ mm}} \approx 60 \text{ mm}$  and the optical penetration depth in aluminum is equal to a few nanometers, the radius of the

Gaussian beam  $w(x'_1)$  is independent of  $x'_1$ . Thus  $g(x'_1, x'_2)$  is only a function of  $x'_2$  and is equal to

$$g(x'_2) = \frac{2}{a_s} \sqrt{\frac{\ln 2}{\pi}} e^{-4 \ln 2 \frac{x'^2_2}{a_s^2}}. \quad (\text{A.52})$$

The Fourier transform of  $g(x'_2)$  is given by

$$\frac{1}{\sqrt{2\pi}} \int_{-\infty}^{+\infty} g(x'_2) e^{jk'_2 x'_2} dx'_2 = \frac{1}{\sqrt{2\pi}} e^{-a_s^2 k'^2_2 / (16 \ln 2)}. \quad (\text{A.53})$$

To obtain the Gaussian function in the Cartesian coordinate system ( $O$ ,  $\mathbf{x}_1$ ,  $\mathbf{x}_2$ ), an inverse Fourier transform of Eq. (A.53) is performed:

$$g(x_1, x_2) = \frac{1}{\sqrt{2\pi}} \int_{-\infty}^{+\infty} \frac{1}{\sqrt{2\pi}} e^{-a_s^2 k'^2_2 / (16 \ln 2)} e^{-jk'_2 x'_2} dk'_2, \quad (\text{A.54})$$

and a variable change is realized with

$$x'_2 = (x_2 - x_{2O'}) \cos \theta - (x_1 - x_{1O'}) \sin \theta, \quad (\text{A.55})$$

$$k'_2 = \frac{k_2}{\cos \theta}. \quad (\text{A.56})$$

Hence, the Gaussian function  $g(x_1, x_2)$  is given by

$$g(x_1, x_2) = \frac{1}{\sqrt{2\pi}} \int_{-\infty}^{+\infty} \underbrace{\frac{1}{\sqrt{2\pi} \cos \theta} e^{-a_s^2 k_2^2 / (16 \ln 2 \cos^2 \theta)} e^{jk_2 [(x_1 - x_{1O'}) \tan \theta + x_{2O'}]} e^{-jk_2 x_2}}_{G(x_1, k_2)} dk_2, \quad (\text{A.57})$$

with  $G(x_1, k_2)$  the Fourier transform of the tilted laser line source distribution in space which is used in Eq. (2.23b) with  $x_{1O'} = x_{2O'} = 0$ .

## A.2.2 Coefficients $A_{ij}^T$ and $B_i^T$

In Sec. 2.4.3, the linear system to solve in order to determine the temperature fields in media I and II [see Eq. (2.36)] is

$$\begin{bmatrix} A_{11}^T & A_{12}^T & 0 & 0 \\ A_{21}^T & A_{22}^T & A_{23}^T & A_{24}^T \\ A_{31}^T & A_{32}^T & A_{33}^T & A_{34}^T \\ 0 & 0 & A_{43}^T & A_{44}^T \end{bmatrix} \begin{bmatrix} \hat{T}_h^{I+} \\ \star \hat{T}_h^{I-} \\ \star \hat{T}_h^{II+} \\ \star \hat{T}_h^{II-} \end{bmatrix} = \begin{bmatrix} B_1^T \\ B_2^T \\ B_3^T \\ B_4^T \end{bmatrix}. \quad (\text{A.58})$$

To obtain a well-conditioned matrix, the unknowns of Eq. (A.58), with the symbol “ $\star$ ”, are written as

$$\star \hat{T}_h^{I-} = \hat{T}_h^{I-} e^{\Gamma_1^I h_1}, \quad \star \hat{T}_{h_+}^{II+} = \hat{T}_h^{II+} e^{-\Gamma_1^{II}(h_1 + \Delta h)}, \quad \star \hat{T}_h^{II-} = \hat{T}_h^{II-} e^{\Gamma_1^{II} H}. \quad (\text{A.59})$$

This technique to obtain a well-conditioned matrix is used in Ref. 150 (p. 152). The expressions of the coefficients  $A_{ij}^T$  and  $B_{ij}^T$ , of the linear system in Eq. (A.58), are

$$\begin{aligned} A_{11}^T &= -\Gamma_1^I \lambda_{11}^I - h_c, & A_{12}^T &= (\Gamma_1^I \lambda_{11}^I - h_c) e^{-\Gamma_1^I h_1}, \\ A_{21}^T &= -\Gamma_1^I \lambda_{11}^I e^{-\Gamma_1^I h_1}, & A_{22}^T &= \Gamma_1^I \lambda_{11}^I, \\ A_{23}^T &= \Gamma_1^{II} \lambda_{11}^{II}, & A_{24}^T &= -\Gamma_1^{II} \lambda_{11}^{II} e^{-\Gamma_1^{II} h_2}, \\ A_{31}^T &= (-R_c \Gamma_1^I \lambda_{11}^I + 1) e^{-\Gamma_1^I h_1}, & A_{32}^T &= R_c \Gamma_1^I \lambda_{11}^I + 1, \\ A_{33}^T &= -1, & A_{34}^T &= -e^{-\Gamma_1^{II} h_2}, \\ A_{43}^T &= (-\Gamma_1^{II} \lambda_{11}^{II} + h_c) e^{-\Gamma_1^{II} h_2}, & A_{44}^T &= \Gamma_1^{II} \lambda_{11}^{II} + h_c, \end{aligned}$$

and

$$\begin{aligned} B_1^T &= \hat{T}_p^{I-} [-\lambda_{11}^I [\beta_I(\theta_1) - jk_2 \tan \theta_1] + h_c] e^{-\beta_I(\theta_1) h_1} + \hat{T}_p^{I+} [\lambda_{11}^I [\beta_I(\theta_1) - jk_2 \tan \theta_1] + h_c] \\ &\quad - \hat{T}_\infty h_c, \\ B_2^T &= \lambda_{11}^I [\beta_I(\theta_1) - jk_2 \tan \theta_1] \left( -\hat{T}_p^{I-} e^{-jk_2 \tan \theta_1 h_1} + \hat{T}_p^{I+} e^{-\beta_I(\theta_1) h_1} e^{jk_2 \tan \theta_1 h_1} \right) \\ &\quad - \lambda_{11}^{II} [\beta_{II}(\theta_2) - jk_2 \tan \theta_2] \left( -\hat{T}_p^{II-} e^{-\beta_{II}(\theta_2) h_2} e^{-jk_2 \tan \theta_2 (h_1 + \Delta h)} + \hat{T}_p^{II+} e^{jk_2 \tan \theta_2 (h_1 + \Delta h)} \right), \\ B_3^T &= \hat{T}_p^{I-} [-\lambda_{11}^I R_c [\beta_I(\theta_1) - jk_2 \tan \theta_1] - 1] e^{-jk_2 \tan \theta_1 h_1} + \hat{T}_p^{II-} e^{-\beta_{II}(\theta_2) h_2} e^{-jk_2 \tan \theta_2 (h_1 + \Delta h)} \\ &\quad + \hat{T}_p^{I+} [\lambda_{11}^I R_c [\beta_I(\theta_1) - jk_2 \tan \theta_1] - 1] e^{-\beta_I(\theta_1) h_1} e^{jk_2 \tan \theta_1 h_1} + \hat{T}_p^{II+} e^{jk_2 \tan \theta_2 (h_1 + \Delta h)}, \\ B_4^T &= \hat{T}_p^{II-} [-\lambda_{11}^{II} [\beta_{II}(\theta_2) - jk_2 \tan \theta_2] - h_c] e^{-jk_2 \tan \theta_2 H} \\ &\quad + \hat{T}_p^{II+} [\lambda_{11}^{II} [\beta_{II}(\theta_2) - jk_2 \tan \theta_2] - h_c] e^{-\beta_{II}(\theta_2) h_2} e^{jk_2 \tan \theta_2 H} + \hat{T}_\infty h_c. \end{aligned}$$

## A.3 Elastodynamic problem

In Sec. 2.5, the solution of Eqs. (2.43a, 2.43b) is the sum of the homogeneous solution  $\hat{\mathbf{u}}_h(x_1, k_2, \omega)$  and the particular solution  $\hat{\mathbf{u}}_p(x_1, k_2, \omega)$ . Detailed calculations of these solutions in media I and II are given in the following.

### A.3.1 Homogeneous solutions of the elastodynamic equations

The homogeneous solution is the linear combination of two longitudinal (L) and two transverse (T) polarized waves, which are travelling along the positive and negative directions of the  $\mathbf{x}_1$ -axis as illustrated in Fig. 2.3 and defined by the equation

$$\hat{\mathbf{u}}_h(x_1, k_2, \omega) = \sum_{n=\{L,T\}} A^{n+} \hat{\mathbf{U}}_h^{n+}(k_2, \omega) e^{-jk_1^n x_1} + A^{n-} \hat{\mathbf{U}}_h^{n-}(k_2, \omega) e^{jk_1^n x_1}, \quad (\text{A.60})$$

with  $k_1^L$  and  $k_1^T$  the projections of the longitudinal and transverse wave vectors along the  $\mathbf{x}_1$ -axis:

$$k_1^L = \sqrt{X_-} \text{ and } k_1^T = \sqrt{X_+}, \quad (\text{A.61a})$$

and  $X_{\pm}$  defined in Eq. (2.47a). In Eq. (A.60),  $A^{n\pm}$  refer to the wave amplitudes that are subsequently determined by applying the boundary conditions and  $\hat{\mathbf{U}}_h^{n\pm}$  are the eigenvectors that are equal to

$$\hat{\mathbf{U}}_h^{n+}(k_2, \omega) = \begin{bmatrix} \hat{U}_{1h}^{n+} \\ \hat{U}_{2h}^{n+} \end{bmatrix} = \begin{bmatrix} a_{22} - (k_1^n)^2 C_{66} \\ k_1^n a_{12} \end{bmatrix}, \quad (\text{A.62a})$$

$$\hat{\mathbf{U}}_h^{n-}(k_2, \omega) = \begin{bmatrix} \hat{U}_{1h}^{n-} \\ \hat{U}_{2h}^{n-} \end{bmatrix} = \begin{bmatrix} a_{22} - (k_1^n)^2 C_{66} \\ -k_1^n a_{12} \end{bmatrix}. \quad (\text{A.62b})$$

According to Eqs. (A.62a) and (A.62b), we obtain the following equality:

$$\begin{bmatrix} \hat{U}_{1h}^{n+} \\ \hat{U}_{2h}^{n+} \end{bmatrix} = \begin{bmatrix} \hat{U}_{1h}^{n-} \\ -\hat{U}_{2h}^{n-} \end{bmatrix}. \quad (\text{A.63a})$$

### A.3. Elastodynamic problem

---

In medium I, the homogeneous solution  $\hat{\mathbf{u}}_h^I$  is written in terms of symmetric and anti-symmetric modes as introduced in Ref. 150 (p. 155) and Ref. 151 (p. 207). Thus, the eigenvectors for symmetric (*S*) and antisymmetric (*A*) modes are given by

$$\hat{\mathbf{U}}_h^{I,nS} = \frac{1}{2} \left[ \hat{\mathbf{U}}_h^{I,n-} e^{jk_1^{I,n}(x_1 - \frac{h_1}{2})} + \hat{\mathbf{U}}_h^{I,n+} e^{-jk_1^{I,n}(x_1 - \frac{h_1}{2})} \right], \quad (\text{A.64a})$$

$$\hat{\mathbf{U}}_h^{I,nA} = \frac{1}{2j} \left[ \hat{\mathbf{U}}_h^{I,n-} e^{jk_1^{I,n}(x_1 - \frac{h_1}{2})} - \hat{\mathbf{U}}_h^{I,n+} e^{-jk_1^{I,n}(x_1 - \frac{h_1}{2})} \right]. \quad (\text{A.64b})$$

Using Euler's formula

$$\cos \left[ k_1^{I,n} \left( x_1 - \frac{h_1}{2} \right) \right] = \frac{e^{jk_1^{I,n}(x_1 - \frac{h_1}{2})} + e^{-jk_1^{I,n}(x_1 - \frac{h_1}{2})}}{2}, \quad (\text{A.65a})$$

$$\sin \left[ k_1^{I,n} \left( x_1 - \frac{h_1}{2} \right) \right] = \frac{e^{jk_1^{I,n}(x_1 - \frac{h_1}{2})} - e^{-jk_1^{I,n}(x_1 - \frac{h_1}{2})}}{2j}, \quad (\text{A.65b})$$

and Eq. (A.63a), the symmetric and antisymmetric eigenvectors, given in Eqs. (A.64a) and (A.64b), are equal to

$$\hat{\mathbf{U}}_h^{I,nS} = \begin{bmatrix} \hat{U}_{1h}^{I,n-} \cos \left[ k_1^{I,n} \left( x_1 - \frac{h_1}{2} \right) \right] \\ j \hat{U}_{2h}^{I,n-} \sin \left[ k_1^{I,n} \left( x_1 - \frac{h_1}{2} \right) \right] \end{bmatrix}, \quad (\text{A.66a})$$

$$\hat{\mathbf{U}}_h^{I,nA} = \begin{bmatrix} \hat{U}_{1h}^{I,n-} \sin \left[ k_1^{I,n} \left( x_1 - \frac{h_1}{2} \right) \right] \\ -j \hat{U}_{2h}^{I,n-} \cos \left[ k_1^{I,n} \left( x_1 - \frac{h_1}{2} \right) \right] \end{bmatrix}. \quad (\text{A.66b})$$

The homogeneous solution in medium I is written as the sum of symmetric and antisymmetric modes:

$$\hat{\mathbf{u}}_h^I = \sum_{n=\{L,T\}} \xi_I^{nS} \hat{\mathbf{U}}_h^{I,nS} + \xi_I^{nA} \hat{\mathbf{U}}_h^{I,nA}. \quad (\text{A.67})$$

with  $\xi_I^{nS}$  and  $\xi_I^{nA}$  the amplitudes of the symmetric and antisymmetric modes in medium I, respectively. These amplitudes are then determined by applying the boundary conditions.

The projections of  $\hat{\mathbf{u}}_h^I$  onto  $\mathbf{x}_1$ -axis and  $\mathbf{x}_2$ -axis are equal to

$$\hat{u}_{1h}^I = \sum_{n=\{L,T\}} \hat{U}_{1h}^{I,n-} \left[ \xi_I^{nS} \cos \left[ k_1^{I,n} \left( x_1 - \frac{h_1}{2} \right) \right] + \xi_I^{nA} \sin \left[ k_1^{I,n} \left( x_1 - \frac{h_1}{2} \right) \right] \right], \quad (\text{A.68a})$$

$$\hat{u}_{2h}^I = \sum_{n=\{L,T\}} j\hat{U}_{2h}^{I,n-} \left[ \xi_I^{nS} \sin \left[ k_1^{I,n} \left( x_1 - \frac{h_1}{2} \right) \right] - \xi_I^{nA} \cos \left[ k_1^{I,n} \left( x_1 - \frac{h_1}{2} \right) \right] \right], \quad (\text{A.68b})$$

with  $\hat{U}_{1h}^{I,n-}$  and  $\hat{U}_{2h}^{I,n-}$  that are determined in Eq. (A.62b). In medium II, the homogeneous solution  $\hat{\mathbf{u}}_h^{\text{II}}$  is written as in Eq. (A.60):

$$\hat{\mathbf{u}}_h^{\text{II}} = \sum_{n=\{L,T\}} A_{\text{II}}^{n+} \hat{\mathbf{U}}_h^{\text{II},n+} e^{-jk_1^{\text{II},n} x_1} + A_{\text{II}}^{n-} \hat{\mathbf{U}}_h^{\text{II},n-} e^{jk_1^{\text{II},n} x_1}. \quad (\text{A.69})$$

Using Eq. (A.63a), the projection of  $\hat{\mathbf{u}}_h^{\text{II}}$  onto  $\mathbf{x}_1$ -axis and  $\mathbf{x}_2$ -axis gives

$$\hat{u}_{1h}^{\text{II}} = \sum_{n=\{L,T\}} \hat{U}_{1h}^{\text{II},n-} \left( A_{\text{II}}^{n+} e^{-jk_1^{\text{II},n} x_1} + A_{\text{II}}^{n-} e^{jk_1^{\text{II},n} x_1} \right), \quad (\text{A.70a})$$

$$\hat{u}_{2h}^{\text{II}} = \sum_{n=\{L,T\}} \hat{U}_{2h}^{\text{II},n-} \left( -A_{\text{II}}^{n+} e^{-jk_1^{\text{II},n} x_1} + A_{\text{II}}^{n-} e^{jk_1^{\text{II},n} x_1} \right), \quad (\text{A.70b})$$

with  $A_{\text{II}}^{n+}$  and  $A_{\text{II}}^{n-}$  the amplitudes of the wave that are propagating along the positive and negative direction of the  $\mathbf{x}_1$ -axis, respectively. They are determined afterwards by applying the boundary conditions.

### A.3.2 Particular solutions of the elastodynamic equations

The particular solutions are searched following the form of the source term  $C_{\alpha_1} \frac{\partial \hat{T}}{\partial x_1}$  and  $-jk_2 C_{\alpha_2} \hat{T}$  of Eqs. (2.43a, 2.43b). Therefore, using the analytic expression of the temperature fields  $\hat{T}$  in media I and II, given in Eqs. (2.38a, 2.38b), the particular solutions are

$$\begin{aligned} \hat{\mathbf{u}}_p^I(x_1, k_2, \omega) = & \hat{\mathbf{U}}_{p\Gamma}^{I+} e^{-\Gamma_1^I x_1} + \hat{\mathbf{U}}_{p\Gamma}^{I-} e^{\Gamma_1^I (x_1 - h_1)} \\ & + \hat{\mathbf{U}}_{p\beta}^{I+} e^{-\beta_1(\theta_1) x_1} e^{jk_2 \tan \theta_1 x_1} + \hat{\mathbf{U}}_{p\beta}^{I-} e^{\beta_1(\theta_1) (x_1 - h_1)} e^{-jk_2 \tan \theta_1 x_1}, \end{aligned} \quad (\text{A.71a})$$

$$\begin{aligned} \hat{\mathbf{u}}_p^{\text{II}}(x_1, k_2, \omega) = & \hat{\mathbf{U}}_{p\Gamma}^{\text{II}+} e^{-\Gamma_1^{\text{II}} [x_1 - (h_1 + \Delta h)]} + \hat{\mathbf{U}}_{p\Gamma}^{\text{II}-} e^{\Gamma_1^{\text{II}} (x_1 - H)} \\ & + \hat{\mathbf{U}}_{p\beta}^{\text{II}+} e^{-\beta_{\text{II}}(\theta_2) [x_1 - (h_1 + \Delta h)]} e^{jk_2 \tan \theta_2 x_1} + \hat{\mathbf{U}}_{p\beta}^{\text{II}-} e^{\beta_{\text{II}}(\theta_2) (x_1 - H)} e^{-jk_2 \tan \theta_2 x_1}. \end{aligned} \quad (\text{A.71b})$$

Each term of Eqs. (A.71a) and (A.71b) are injected into the elastodynamic equations (2.43a) and (2.43b) to obtain  $\hat{\mathbf{U}}_{p\Gamma}^{i+}$ ,  $\hat{\mathbf{U}}_{p\Gamma}^{i-}$ ,  $\hat{\mathbf{U}}_{p\beta}^{i+}$  and  $\hat{\mathbf{U}}_{p\beta}^{i-}$ , with  $i = \{I, \text{II}\}$ . To obtain  $\hat{\mathbf{U}}_{p\Gamma}^{I+}$ ,  $\hat{\mathbf{U}}_{p\Gamma}^{I-}$ ,  $\hat{\mathbf{U}}_{p\Gamma}^{\text{II}+}$  and  $\hat{\mathbf{U}}_{p\Gamma}^{\text{II}-}$ , which are linked to the thermal diffusion in medium I and II, we have to solve these four linear systems

$$\begin{bmatrix} a_{11}^I + C_{11}^I \Gamma_1^{I^2} & ja_{12}^I \Gamma_1^I \\ ja_{12}^I \Gamma_1^I & a_{22}^I + C_{66}^I \Gamma_1^{I^2} \end{bmatrix} \begin{bmatrix} \hat{U}_{1p\Gamma}^{I+} \\ \hat{U}_{2p\Gamma}^{I+} \end{bmatrix} = \begin{bmatrix} -C_{\alpha_1}^I \Gamma_1^I \hat{T}_h^{I+} \\ -jk_2 C_{\alpha_2}^I \hat{T}_h^{I+} \end{bmatrix}, \quad (\text{A.72})$$

$$\begin{bmatrix} a_{11}^I + C_{11}^I \Gamma_1^{I^2} & -ja_{12}^I \Gamma_1^I \\ -ja_{12}^I \Gamma_1^I & a_{22}^I + C_{66}^I \Gamma_1^{I^2} \end{bmatrix} \begin{bmatrix} \hat{U}_{1p\Gamma}^{I-} \\ \hat{U}_{2p\Gamma}^{I-} \end{bmatrix} = \begin{bmatrix} C_{\alpha_1}^I \Gamma_1^I \hat{T}_h^{I-} \\ -jk_2 C_{\alpha_2}^I \hat{T}_h^{I-} \end{bmatrix}, \quad (\text{A.73})$$

$$\begin{bmatrix} a_{11}^{II} + C_{11}^{II} \Gamma_1^{II^2} & ja_{12}^{II} \Gamma_1^{II} \\ ja_{12}^{II} \Gamma_1^{II} & a_{22}^{II} + C_{66}^{II} \Gamma_1^{II^2} \end{bmatrix} \begin{bmatrix} \hat{U}_{1p\Gamma}^{II+} \\ \hat{U}_{2p\Gamma}^{II+} \end{bmatrix} = \begin{bmatrix} -C_{\alpha_1}^{II} \Gamma_1^{II} \hat{T}_h^{II+} \\ -jk_2 C_{\alpha_2}^{II} \hat{T}_h^{II+} \end{bmatrix}, \quad (\text{A.74})$$

$$\begin{bmatrix} a_{11}^{II} + C_{11}^{II} \Gamma_1^{II^2} & -ja_{12}^{II} \Gamma_1^{II} \\ -ja_{12}^{II} \Gamma_1^{II} & a_{22}^{II} + C_{66}^{II} \Gamma_1^{II^2} \end{bmatrix} \begin{bmatrix} \hat{U}_{1p\Gamma}^{II-} \\ \hat{U}_{2p\Gamma}^{II-} \end{bmatrix} = \begin{bmatrix} C_{\alpha_1}^{II} \Gamma_1^{II} \hat{T}_h^{II-} \\ -jk_2 C_{\alpha_2}^{II} \hat{T}_h^{II-} \end{bmatrix}, \quad (\text{A.75})$$

with

$$a_{11}^i = \rho^i \omega^2 - k_2^2 C_{66}^i, \quad (\text{A.76a})$$

$$a_{22}^i = \rho^i \omega^2 - k_2^2 C_{22}^i, \quad (\text{A.76b})$$

$$a_{12}^i = k_2 (C_{12}^i + C_{66}^i). \quad (\text{A.76c})$$

It is the same procedure to obtain  $\hat{\mathbf{U}}_{p\beta}^{I+}$ ,  $\hat{\mathbf{U}}_{p\beta}^{I-}$ ,  $\hat{\mathbf{U}}_{p\beta}^{II+}$  and  $\hat{\mathbf{U}}_{p\beta}^{II-}$ , which are linked to the optical penetration of the laser beam in medium I and II. We have to solve four other linear systems that have the form

$$\begin{bmatrix} a_{11}^i + C_{11}^i (\beta_i - jk_2 \tan \theta_i)^2 & \pm ja_{12}^i (\beta_i - jk_2 \tan \theta_i) \\ \pm ja_{12}^i (\beta_i - jk_2 \tan \theta_i) & a_{22}^i + C_{66}^i (\beta_i - jk_2 \tan \theta_i)^2 \end{bmatrix} \begin{bmatrix} \hat{U}_{1p\beta}^{i\pm} \\ \hat{U}_{2p\beta}^{i\pm} \end{bmatrix} = \begin{bmatrix} -C_{\alpha_1}^i (\beta_i - jk_2 \tan \theta_i) (\pm \hat{T}_p^{i\pm}) \\ -jk_2 C_{\alpha_2}^i \hat{T}_p^{i\pm} \end{bmatrix}. \quad (\text{A.77})$$

### A.3.3 Application of the boundary conditions

The complete solution in media I and II is equal to the linear combination of the homogeneous and particular solutions

$$\hat{\mathbf{u}}^i(x_1, k_2, \omega) = \hat{\mathbf{u}}_h^i(x_1, k_2, \omega) + \hat{\mathbf{u}}_p^i(x_1, k_2, \omega). \quad (\text{A.78})$$

Therefore, in the medium I, the complete solution is equal to

$$\hat{\mathbf{u}}^I = \sum_{n=\{L,T\}} \left( \xi_I^{nS} \hat{\mathbf{U}}_h^{I,nS} + \xi_I^{nA} \hat{\mathbf{U}}_h^{I,nA} \right) + \hat{\mathbf{u}}_p^I, \quad (\text{A.79})$$

with  $\hat{\mathbf{U}}_h^{I,nS}$ ,  $\hat{\mathbf{U}}_h^{I,nA}$  and  $\hat{\mathbf{u}}_p^I$  given in Eqs. (A.66a), (A.66b) and (A.71a), respectively. In the medium II, the complete solution is equal to

$$\hat{\mathbf{u}}^{II} = \sum_{n=\{L,T\}} \left( A_{II}^{n+} \hat{\mathbf{U}}_h^{II,n+} e^{-jk_1^{II,n} x_1} + A_{II}^{n-} \hat{\mathbf{U}}_h^{II,n-} e^{jk_1^{II,n} x_1} \right) + \hat{\mathbf{u}}_p^{II}, \quad (\text{A.80})$$

with  $\hat{\mathbf{U}}_h^{II,n+}$ ,  $\hat{\mathbf{U}}_h^{II,n-}$  and  $\hat{\mathbf{u}}_p^{II}$  given in Eqs. (A.62a), (A.62b) and (A.71b), respectively. Therefore, eight amplitudes ( $\xi_I^{nS}$ ,  $\xi_I^{nA}$ ,  $A_{II}^{n+}$  and  $A_{II}^{n-}$  with  $n = \{L, T\}$ ) remain to be determined by applying the eight boundary conditions introduced in Eqs. (2.52, 2.53 and 2.54) and reminded below:

$$\hat{\sigma}_{11}^I|_{x_1=0} = \hat{\sigma}_{12}^I|_{x_1=0} = 0, \quad (\text{A.81})$$

$$\hat{\sigma}_{11}^{II}|_{x_1=H} = \hat{\sigma}_{12}^{II}|_{x_1=H} = 0, \quad (\text{A.82})$$

$$\begin{bmatrix} \hat{u}_1^I \\ \hat{u}_2^I \\ \hat{\sigma}_{11}^I \\ \hat{\sigma}_{12}^I \end{bmatrix}_{x_1=h_1} = \left[ L^M \right]_{4 \times 4} \begin{bmatrix} \hat{u}_1^{II} \\ \hat{u}_2^{II} \\ \hat{\sigma}_{11}^{II} \\ \hat{\sigma}_{12}^{II} \end{bmatrix}_{x_1=h_1+\Delta h}, \quad (\text{A.83})$$

with  $[L^M]$  the transfer matrix (pp. 53–60 in Ref. 157) used to couple the displacements ( $\hat{u}_1$ ,  $\hat{u}_2$ ) and the stresses ( $\hat{\sigma}_{11}$ ,  $\hat{\sigma}_{12}$ ) from medium I at  $x_1 = h_1$ , to medium II at  $x_1 = h_1 + \Delta h$  (see Sec. A.3.4). First, we need to determine the stress expressions  $\hat{\sigma}_{11}^i$  and  $\hat{\sigma}_{12}^i$  in media I and II using the Hooke's Law. Secondly, two  $4 \times 4$  linear systems are solved to find the eight amplitudes. Finally, the displacement fields ( $\hat{u}_1$  and  $\hat{u}_2$ ) are obtained in media I and II.

### Determination of $\hat{\sigma}_{11}^i$ and $\hat{\sigma}_{12}^i$ in media I and II

In medium  $i = \{I, II\}$ , the stress expressions  $\hat{\sigma}_{11}^i$  and  $\hat{\sigma}_{12}^i$  are divided into three parts, those associated with: homogeneous solutions (denoted  $h$ ), particular solutions ( $p$ ) and the source term ( $s$ ). Hence, the expressions are

$$\hat{\sigma}_{11}^i = \hat{\sigma}_{11h}^i + \hat{\sigma}_{11p}^i - \hat{\sigma}_{11s}^i, \quad (\text{A.84a})$$

### A.3. Elastodynamic problem

---

$$\hat{\sigma}_{12}^i = \hat{\sigma}_{12h}^i + \hat{\sigma}_{12p}^i, \quad (\text{A.84b})$$

with  $\hat{\sigma}_{11s}^i = C_{\alpha_1}^i \hat{T}^i$ . Each of these terms are detailed in the following.

#### Homogeneous solutions $\hat{\sigma}_{11h}^i$ and $\hat{\sigma}_{12h}^i$

In medium I, according to Hooke's law [Eq. (2.40)], the stress expressions  $\hat{\sigma}_{11h}^I$  and  $\hat{\sigma}_{12h}^I$  are equal to

$$\hat{\sigma}_{11h}^I = C_{11}^I \frac{\partial \hat{u}_{1h}^I}{\partial x_1} - jk_2 C_{12}^I \hat{u}_{2h}^I, \quad (\text{A.85a})$$

$$\hat{\sigma}_{12h}^I = C_{66}^I \left( -jk_2 \hat{u}_{1h}^I + \frac{\partial \hat{u}_{2h}^I}{\partial x_1} \right). \quad (\text{A.85b})$$

Using Eqs. (A.68a) and (A.68b), the expressions of  $\hat{u}_{1h}^I$ ,  $\frac{\partial \hat{u}_{1h}^I}{\partial x_1}$ ,  $\hat{u}_{2h}^I$  and  $\frac{\partial \hat{u}_{2h}^I}{\partial x_1}$  of Eqs. (A.85a) and (A.85b) are given by

$$\hat{u}_{1h}^I = \sum_{n=\{L,T\}} \hat{U}_{1h}^{I,n-} \zeta_{12}^{I,n}(x_1), \quad (\text{A.86a})$$

$$\frac{\partial \hat{u}_{1h}^I}{\partial x_1} = \sum_{n=\{L,T\}} k_1^{I,n} \hat{U}_{1h}^{I,n-} \zeta_{11}^{I,n}(x_1), \quad (\text{A.86b})$$

$$\hat{u}_{2h}^I = \sum_{n=\{L,T\}} -j \hat{U}_{2h}^{I,n-} \zeta_{11}^{I,n}(x_1), \quad (\text{A.86c})$$

$$\frac{\partial \hat{u}_{2h}^I}{\partial x_1} = \sum_{n=\{L,T\}} j k_1^{I,n} \hat{U}_{2h}^{I,n-} \zeta_{12}^{I,n}(x_1), \quad (\text{A.86d})$$

with

$$\zeta_{11}^{I,n}(x_1) = -\xi_I^{nS} \sin \left[ k_1^{I,n} \left( x_1 - \frac{h_1}{2} \right) \right] + \xi_I^{nA} \cos \left[ k_1^{I,n} \left( x_1 - \frac{h_1}{2} \right) \right], \quad (\text{A.87a})$$

$$\zeta_{12}^{I,n}(x_1) = \xi_I^{nS} \cos \left[ k_1^{I,n} \left( x_1 - \frac{h_1}{2} \right) \right] + \xi_I^{nA} \sin \left[ k_1^{I,n} \left( x_1 - \frac{h_1}{2} \right) \right]. \quad (\text{A.87b})$$

Therefore, the expressions of  $\hat{\sigma}_{11h}^I$  and  $\hat{\sigma}_{12h}^I$  are

$$\hat{\sigma}_{11h}^I = \sum_{n=\{L,T\}} \underbrace{\left( C_{11}^I k_1^{I,n} \hat{U}_{1h}^{I,n-} - C_{12}^I k_2 \hat{U}_{2h}^{I,n-} \right)}_{R_I^n} \zeta_{11}^{I,n}(x_1), \quad (\text{A.88a})$$

$$\hat{\sigma}_{12h}^I = \sum_{n=\{L,T\}} C_{66}^I \underbrace{\left( jk_1^{I,n} \hat{U}_{2h}^{I,n-} - jk_2 \hat{U}_{1h}^{I,n-} \right)}_{M_I^n} \zeta_{12}^{I,n}(x_1). \quad (\text{A.88b})$$

These expressions are now evaluated at  $x_1 = 0$ :

$$\hat{\sigma}_{11h}^I \Big|_{x_1=0} = \sum_{n=\{L,T\}} R_I^n \left[ \xi_I^{nS} \sin \left( k_1^{I,n} \frac{h_1}{2} \right) + \xi_I^{nA} \cos \left( k_1^{I,n} \frac{h_1}{2} \right) \right], \quad (\text{A.89a})$$

$$\hat{\sigma}_{12h}^I \Big|_{x_1=0} = \sum_{n=\{L,T\}} M_I^n \left[ \xi_I^{nS} \cos \left( k_1^{I,n} \frac{h_1}{2} \right) - \xi_I^{nA} \sin \left( k_1^{I,n} \frac{h_1}{2} \right) \right], \quad (\text{A.89b})$$

and at  $x_1 = h_1$ :

$$\hat{\sigma}_{11h}^I \Big|_{x_1=h_1} = \sum_{n=\{L,T\}} R_I^n \left[ -\xi_I^{nS} \sin \left( k_1^{I,n} \frac{h_1}{2} \right) + \xi_I^{nA} \cos \left( k_1^{I,n} \frac{h_1}{2} \right) \right], \quad (\text{A.90a})$$

$$\hat{\sigma}_{12h}^I \Big|_{x_1=h_1} = \sum_{n=\{L,T\}} M_I^n \left[ \xi_I^{nS} \cos \left( k_1^{I,n} \frac{h_1}{2} \right) + \xi_I^{nA} \sin \left( k_1^{I,n} \frac{h_1}{2} \right) \right]. \quad (\text{A.90b})$$

Following the same approach for medium II, the stresses  $\hat{\sigma}_{11h}^{\text{II}}$  and  $\hat{\sigma}_{12h}^{\text{II}}$  are equal to

$$\hat{\sigma}_{11h}^{\text{II}} = C_{11}^{\text{II}} \frac{\partial \hat{u}_{1h}^{\text{II}}}{\partial x_1} - jk_2 C_{12}^{\text{II}} \hat{u}_{2h}^{\text{II}}, \quad (\text{A.91a})$$

$$\hat{\sigma}_{12h}^{\text{II}} = C_{66}^{\text{II}} \left( -jk_2 \hat{u}_{1h}^{\text{II}} + \frac{\partial \hat{u}_{2h}^{\text{II}}}{\partial x_1} \right). \quad (\text{A.91b})$$

Using Eqs. (A.70a) and (A.70b), the expressions of  $\hat{u}_{1h}^{\text{II}}$ ,  $\frac{\partial \hat{u}_{1h}^{\text{II}}}{\partial x_1}$ ,  $\hat{u}_{2h}^{\text{II}}$  and  $\frac{\partial \hat{u}_{2h}^{\text{II}}}{\partial x_1}$  of Eqs. (A.91a) and (A.91b) are given by

$$\hat{u}_{1h}^{\text{II}} = \sum_{n=\{L,T\}} \hat{U}_{1h}^{\text{II},n-} \zeta_{12}^{\text{II},n}(x_1), \quad (\text{A.92a})$$

$$\frac{\partial \hat{u}_{1h}^{\text{II}}}{\partial x_1} = \sum_{n=\{L,T\}} jk_1^{\text{II},n} \hat{U}_{1h}^{\text{II},n-} \zeta_{11}^{\text{II},n}(x_1), \quad (\text{A.92b})$$

$$\hat{u}_{2h}^{\text{II}} = \sum_{n=\{L,T\}} \hat{U}_{2h}^{\text{II},n-} \zeta_{11}^{\text{II},n}(x_1), \quad (\text{A.92c})$$

$$\frac{\partial \hat{u}_{2h}^{\text{II}}}{\partial x_1} = \sum_{n=\{L,T\}} jk_1^{\text{II},n} \hat{U}_{2h}^{\text{II},n-} \zeta_{12}^{\text{II},n}(x_1), \quad (\text{A.92d})$$

### A.3. Elastodynamic problem

---

with

$$\zeta_{11}^{\text{II},n}(x_1) = -A_{\text{II}}^{\text{n}+} e^{-jk_1^{\text{II},n}x_1} + A_{\text{II}}^{\text{n}-} e^{jk_1^{\text{II},n}x_1}, \quad (\text{A.93a})$$

$$\zeta_{12}^{\text{II},n}(x_1) = A_{\text{II}}^{\text{n}+} e^{-jk_1^{\text{II},n}x_1} + A_{\text{II}}^{\text{n}-} e^{jk_1^{\text{II},n}x_1}. \quad (\text{A.93b})$$

Therefore, the expressions of  $\hat{\sigma}_{11h}^{\text{II}}$  and  $\hat{\sigma}_{12h}^{\text{II}}$  are

$$\hat{\sigma}_{11h}^{\text{II}} = \sum_{n=\{\text{L},\text{T}\}} j \underbrace{\left( C_{11}^{\text{II}} k_1^{\text{II},n} \hat{U}_{1h}^{\text{II},n-} - C_{12}^{\text{II}} k_2 \hat{U}_{2h}^{\text{II},n-} \right)}_{R_{\text{II}}^{\text{n}}} \zeta_{11}^{\text{II}}(x_1), \quad (\text{A.94a})$$

$$\hat{\sigma}_{12h}^{\text{II}} = \sum_{n=\{\text{L},\text{T}\}} C_{66}^{\text{II}} \underbrace{\left( j k_1^{\text{II},n} \hat{U}_{2h}^{\text{II},n-} - j k_2 \hat{U}_{1h}^{\text{II},n-} \right)}_{M_{\text{II}}^{\text{n}}} \zeta_{12}^{\text{II}}(x_1). \quad (\text{A.94b})$$

These expressions are now evaluated at  $x_1 = h_1 + \Delta h$ :

$$\hat{\sigma}_{11h}^{\text{II}} \Big|_{x_1=h_1+\Delta h} = \sum_{n=\{\text{L},\text{T}\}} R_{\text{II}}^{\text{n}} \left( -A_{\text{II}}^{\text{n}+} e^{-jk_1^{\text{II},n}(h_1+\Delta h)} + A_{\text{II}}^{\text{n}-} e^{jk_1^{\text{II},n}(h_1+\Delta h)} \right), \quad (\text{A.95a})$$

$$\hat{\sigma}_{12h}^{\text{II}} \Big|_{x_1=h_1+\Delta h} = \sum_{n=\{\text{L},\text{T}\}} M_{\text{II}}^{\text{n}} \left( A_{\text{II}}^{\text{n}+} e^{-jk_1^{\text{II},n}(h_1+\Delta h)} + A_{\text{II}}^{\text{n}-} e^{jk_1^{\text{II},n}(h_1+\Delta h)} \right), \quad (\text{A.95b})$$

and at  $x_1 = H$ :

$$\hat{\sigma}_{11h}^{\text{II}} \Big|_{x_1=H} = \sum_{n=\{\text{L},\text{T}\}} R_{\text{II}}^{\text{n}} \left( -A_{\text{II}}^{\text{n}+} e^{-jk_1^{\text{II},n}H} + A_{\text{II}}^{\text{n}-} e^{jk_1^{\text{II},n}H} \right), \quad (\text{A.96a})$$

$$\hat{\sigma}_{12h}^{\text{II}} \Big|_{x_1=H} = \sum_{n=\{\text{L},\text{T}\}} M_{\text{II}}^{\text{n}} \left( A_{\text{II}}^{\text{n}+} e^{-jk_1^{\text{II},n}H} + A_{\text{II}}^{\text{n}-} e^{jk_1^{\text{II},n}H} \right). \quad (\text{A.96b})$$

#### Particular solutions $\hat{\sigma}_{11p}^i$ and $\hat{\sigma}_{12p}^i$

In medium I, the stress expressions  $\hat{\sigma}_{11p}^{\text{I}}$  and  $\hat{\sigma}_{12p}^{\text{I}}$  are calculated with Hooke's law [Eq. (2.40)] and with the particular solutions of the elastodynamic equations which are obtained in Sec. A.3.2. In medium I, the evaluations of  $\hat{\sigma}_{11p}^{\text{I}}$  and  $\hat{\sigma}_{12p}^{\text{I}}$  at  $x_1 = 0$  are equal to

$$\hat{\sigma}_{11p}^{\text{I}} \Big|_{x_1=0} = C_{11}^{\text{I}} \frac{\partial \hat{u}_{1p}^{\text{I}}}{\partial x_1} \Big|_{x_1=0} - j k_2 C_{12}^{\text{I}} \hat{u}_{2p}^{\text{I}} \Big|_{x_1=0}, \quad (\text{A.97a})$$

$$\hat{\sigma}_{12p}^{\text{I}} \Big|_{x_1=0} = C_{66}^{\text{I}} \left( -j k_2 \hat{u}_{1p}^{\text{I}} \Big|_{x_1=0} + \frac{\partial \hat{u}_{2p}^{\text{I}}}{\partial x_1} \Big|_{x_1=0} \right), \quad (\text{A.97b})$$

with

$$\hat{u}_{1p}^I \Big|_{x_1=0} = \hat{U}_{1p\beta}^{I-} e^{-\beta_I(\theta_1)h_1} + \hat{U}_{1p\Gamma}^{I-} e^{-\Gamma_1^I h_1} + \hat{U}_{1p\beta}^{I+} + \hat{U}_{1p\Gamma}^{I+}, \quad (\text{A.98a})$$

$$\frac{\partial \hat{u}_{1p}^I}{\partial x_1} \Big|_{x_1=0} = [\beta_I(\theta_1) - jk_2 \tan \theta_1] \hat{U}_{1p\beta}^{I-} e^{-\beta_I(\theta_1)h_1} - [\beta_I(\theta_1) - jk_2 \tan \theta_1] \hat{U}_{1p\beta}^{I+} \quad (\text{A.98b})$$

$$+ \Gamma_1^I \hat{U}_{1p\Gamma}^{I-} e^{-\Gamma_1^I h_1} - \Gamma_1^I \hat{U}_{1p\Gamma}^{I+},$$

$$\hat{u}_{2p}^I \Big|_{x_1=0} = \hat{U}_{2p\beta}^{I-} e^{-\beta_I(\theta_1)h_1} + \hat{U}_{2p\Gamma}^{I-} e^{-\Gamma_1^I h_1} + \hat{U}_{2p\beta}^{I+} + \hat{U}_{2p\Gamma}^{I+}, \quad (\text{A.98c})$$

$$\frac{\partial \hat{u}_{2p}^I}{\partial x_1} \Big|_{x_1=0} = [\beta_I(\theta_1) - jk_2 \tan \theta_1] \hat{U}_{2p\beta}^{I-} e^{-\beta_I(\theta_1)h_1} - [\beta_I(\theta_1) - jk_2 \tan \theta_1] \hat{U}_{2p\beta}^{I+} \quad (\text{A.98d})$$

$$+ \Gamma_1^I \hat{U}_{2p\Gamma}^{I-} e^{-\Gamma_1^I h_1} - \Gamma_1^I \hat{U}_{2p\Gamma}^{I+}.$$

Then, the evaluations of  $\hat{\sigma}_{11p}^I$  and  $\hat{\sigma}_{12p}^I$  at  $x_1 = h_1$  are equal to

$$\hat{\sigma}_{11p}^I \Big|_{x_1=h_1} = C_{11}^I \frac{\partial \hat{u}_{1p}^I}{\partial x_1} \Big|_{x_1=h_1} - jk_2 C_{12}^I \hat{u}_{2p}^I \Big|_{x_1=h_1}, \quad (\text{A.99a})$$

$$\hat{\sigma}_{12p}^I \Big|_{x_1=h_1} = C_{66}^I \left( -jk_2 \hat{u}_{1p}^I \Big|_{x_1=h_1} + \frac{\partial \hat{u}_{2p}^I}{\partial x_1} \Big|_{x_1=h_1} \right), \quad (\text{A.99b})$$

with

$$\hat{u}_{1p}^I \Big|_{x_1=h_1} = \hat{U}_{1p\beta}^{I-} e^{-jk_2 \tan \theta_1 h_1} + \hat{U}_{1p\Gamma}^{I-} + \hat{U}_{1p\beta}^{I+} e^{-\beta_I(\theta_1)h_1} e^{jk_2 \tan \theta_1 h_1} + \hat{U}_{1p\Gamma}^{I+} e^{-\Gamma_1^I h_1}, \quad (\text{A.100a})$$

$$\frac{\partial \hat{u}_{1p}^I}{\partial x_1} \Big|_{x_1=h_1} = [\beta_I(\theta_1) - jk_2 \tan \theta_1] \hat{U}_{1p\beta}^{I-} e^{-jk_2 \tan \theta_1 h_1} \quad (\text{A.100b})$$

$$- [\beta_I(\theta_1) - jk_2 \tan \theta_1] \hat{U}_{1p\beta}^{I+} e^{-\beta_I(\theta_1)h_1} e^{jk_2 \tan \theta_1 h_1} + \Gamma_1^I \hat{U}_{1p\Gamma}^{I-} - \Gamma_1^I \hat{U}_{1p\Gamma}^{I+} e^{-\Gamma_1^I h_1},$$

$$\hat{u}_{2p}^I \Big|_{x_1=h_1} = \hat{U}_{2p\beta}^{I-} e^{-jk_2 \tan \theta_1 h_1} + \hat{U}_{2p\Gamma}^{I-} + \hat{U}_{2p\beta}^{I+} e^{-\beta_I(\theta_1)h_1} e^{jk_2 \tan \theta_1 h_1} + \hat{U}_{2p\Gamma}^{I+} e^{-\Gamma_1^I h_1}, \quad (\text{A.100c})$$

$$\frac{\partial \hat{u}_{2p}^I}{\partial x_1} \Big|_{x_1=h_1} = [\beta_I(\theta_1) - jk_2 \tan \theta_1] \hat{U}_{2p\beta}^{I-} e^{-jk_2 \tan \theta_1 h_1} \quad (\text{A.100d})$$

$$- [\beta_I(\theta_1) - jk_2 \tan \theta_1] \hat{U}_{2p\beta}^{I+} e^{-\beta_I(\theta_1)h_1} e^{jk_2 \tan \theta_1 h_1} + \Gamma_1^I \hat{U}_{2p\Gamma}^{I-} - \Gamma_1^I \hat{U}_{2p\Gamma}^{I+} e^{-\Gamma_1^I h_1}.$$

### A.3. Elastodynamic problem

In medium II, the evaluations of  $\hat{\sigma}_{11p}^{\text{II}}$  and  $\hat{\sigma}_{12p}^{\text{II}}$  at  $x_1 = h_1 + \Delta h$  are equal to

$$\hat{\sigma}_{11p}^{\text{II}} \Big|_{x_1=h_1+\Delta h} = C_{11}^{\text{II}} \frac{\partial \hat{u}_{1p}^{\text{II}}}{\partial x_1} \Big|_{x_1=h_1+\Delta h} - jk_2 C_{12}^{\text{II}} \hat{u}_{2p}^{\text{II}} \Big|_{x_1=h_1+\Delta h}, \quad (\text{A.101a})$$

$$\hat{\sigma}_{12p}^{\text{II}} \Big|_{x_1=h_1+\Delta h} = C_{66}^{\text{II}} \left( -jk_2 \hat{u}_{1p}^{\text{II}} \Big|_{x_1=h_1+\Delta h} + \frac{\partial \hat{u}_{2p}^{\text{II}}}{\partial x_1} \Big|_{x_1=h_1+\Delta h} \right), \quad (\text{A.101b})$$

with

$$\begin{aligned} \hat{u}_{1p}^{\text{II}} \Big|_{h_1+\Delta h} &= \hat{U}_{1p\beta}^{\text{II}-} e^{-\beta_{\text{II}}(\theta_2)h_2} e^{-jk_2 \tan \theta_2 (h_1+\Delta h)} + \hat{U}_{1p\Gamma}^{\text{II}-} e^{-\Gamma_1^{\text{II}}h_2} \\ &\quad + \hat{U}_{1p\beta}^{\text{II}+} e^{jk_2 \tan \theta_2 (h_1+\Delta h)} + \hat{U}_{1p\Gamma}^{\text{II}+}, \end{aligned} \quad (\text{A.102a})$$

$$\frac{\partial \hat{u}_{1p}^{\text{II}}}{\partial x_1} \Big|_{h_1+\Delta h} = [\beta_{\text{II}}(\theta_2) - jk_2 \tan \theta_2] \hat{U}_{1p\beta}^{\text{II}-} e^{-\beta_{\text{II}}(\theta_2)h_2} e^{-jk_2 \tan \theta_2 (h_1+\Delta h)} \quad (\text{A.102b})$$

$$- [\beta_{\text{II}}(\theta_2) - jk_2 \tan \theta_2] \hat{U}_{1p\beta}^{\text{II}+} e^{jk_2 \tan \theta_2 (h_1+\Delta h)} + \Gamma_1^{\text{II}} \hat{U}_{1p\Gamma}^{\text{II}-} e^{-\Gamma_1^{\text{II}}h_2} - \Gamma_1^{\text{II}} \hat{U}_{1p\Gamma}^{\text{II}+},$$

$$\begin{aligned} \hat{u}_{2p}^{\text{II}} \Big|_{h_1+\Delta h} &= \hat{U}_{2p\beta}^{\text{II}-} e^{-\beta_{\text{II}}(\theta_2)h_2} e^{-jk_2 \tan \theta_2 (h_1+\Delta h)} + \hat{U}_{2p\Gamma}^{\text{II}-} e^{-\Gamma_1^{\text{II}}h_2} \\ &\quad + \hat{U}_{2p\beta}^{\text{II}+} e^{jk_2 \tan \theta_2 (h_1+\Delta h)} + \hat{U}_{2p\Gamma}^{\text{II}+}, \end{aligned} \quad (\text{A.102c})$$

$$\frac{\partial \hat{u}_{2p}^{\text{II}}}{\partial x_1} \Big|_{h_1+\Delta h} = [\beta_{\text{II}}(\theta_2) - jk_2 \tan \theta_2] \hat{U}_{2p\beta}^{\text{II}-} e^{-\beta_{\text{II}}(\theta_2)h_2} e^{-jk_2 \tan \theta_2 (h_1+\Delta h)} \quad (\text{A.102d})$$

$$- [\beta_{\text{II}}(\theta_2) - jk_2 \tan \theta_2] \hat{U}_{2p\beta}^{\text{II}+} e^{jk_2 \tan \theta_2 (h_1+\Delta h)} + \Gamma_1^{\text{II}} \hat{U}_{2p\Gamma}^{\text{II}-} e^{-\Gamma_1^{\text{II}}h_2} - \Gamma_1^{\text{II}} \hat{U}_{2p\Gamma}^{\text{II}+}.$$

Finally, the evaluations of  $\hat{\sigma}_{11p}^{\text{II}}$  and  $\hat{\sigma}_{12p}^{\text{II}}$  at  $x_1 = H$  are equal to

$$\hat{\sigma}_{11p}^{\text{II}} \Big|_{x_1=H} = C_{11}^{\text{II}} \frac{\partial \hat{u}_{1p}^{\text{II}}}{\partial x_1} \Big|_{x_1=H} - jk_2 C_{12}^{\text{II}} \hat{u}_{2p}^{\text{II}} \Big|_{x_1=H}, \quad (\text{A.103a})$$

$$\hat{\sigma}_{12p}^{\text{II}} \Big|_{x_1=H} = C_{66}^{\text{II}} \left( -jk_2 \hat{u}_{1p}^{\text{II}} \Big|_{x_1=H} + \frac{\partial \hat{u}_{2p}^{\text{II}}}{\partial x_1} \Big|_{x_1=H} \right), \quad (\text{A.103b})$$

with

$$\hat{u}_{1p}^{\text{II}} \Big|_{x_1=H} = \hat{U}_{1p\beta}^{\text{II}-} e^{-jk_2 \tan \theta_2 H} + \hat{U}_{1p\Gamma}^{\text{II}-} + \hat{U}_{1p\beta}^{\text{II}+} e^{-\beta_{\text{II}}(\theta_2)h_2} e^{jk_2 \tan \theta_2 H} + \hat{U}_{1p\Gamma}^{\text{II}+} e^{-\Gamma_1^{\text{II}}h_2}, \quad (\text{A.104a})$$

$$\frac{\partial \hat{u}_{1p}^{\text{II}}}{\partial x_1} \Big|_{x_1=H} = [\beta_{\text{II}}(\theta_2) - jk_2 \tan \theta_2] \hat{U}_{1p\beta}^{\text{II}-} e^{-jk_2 \tan \theta_2 H} \quad (\text{A.104b})$$

$$- [\beta_{\text{II}}(\theta_2) - jk_2 \tan \theta_2] \hat{U}_{1p\beta}^{\text{II}+} e^{-\beta_{\text{II}}(\theta_2)h_2} e^{jk_2 \tan \theta_2 H} + \Gamma_1^{\text{II}} \hat{U}_{1p\Gamma}^{\text{II}-} - \Gamma_1^{\text{II}} \hat{U}_{1p\Gamma}^{\text{II}+} e^{-\Gamma_1^{\text{II}}h_2},$$

$$\hat{u}_{2p}^{\text{II}} \Big|_{x_1=H} = \hat{U}_{2p\beta}^{\text{II-}} e^{-jk_2 \tan \theta_2 H} + \hat{U}_{2p\Gamma}^{\text{II-}} + \hat{U}_{2p\beta}^{\text{II+}} e^{-\beta_{\text{II}}(\theta_2)h_2} e^{jk_2 \tan \theta_2 H} + \hat{U}_{2p\Gamma}^{\text{II+}} e^{-\Gamma_1^{\text{II}}h_2}, \quad (\text{A.104c})$$

$$\begin{aligned} \frac{\partial \hat{u}_{2p}^{\text{II}}}{\partial x_1} \Big|_{x_1=H} &= [\beta_{\text{II}}(\theta_2) - jk_2 \tan \theta_2] \hat{U}_{2p\beta}^{\text{II-}} e^{-jk_2 \tan \theta_2 H} \\ &\quad - [\beta_{\text{II}}(\theta_2) - jk_2 \tan \theta_2] \hat{U}_{2p\beta}^{\text{II+}} e^{-\beta_{\text{II}}(\theta_2)h_2} e^{jk_2 \tan \theta_2 H} + \Gamma_1^{\text{II}} \hat{U}_{2p\Gamma}^{\text{II-}} - \Gamma_1^{\text{II}} \hat{U}_{2p\Gamma}^{\text{II+}} e^{-\Gamma_1^{\text{II}}h_2}. \end{aligned} \quad (\text{A.104d})$$

### Source term $\hat{\sigma}_{11s}^i$

The stress expression associated with the source term  $\hat{\sigma}_{11s}^i = C_{\alpha_1}^i \hat{T}^i$  is obtained in media I and II with the expressions of the temperature field  $\hat{T}^i$  determined in Eqs. (2.38a) and (2.38b). This stress  $\hat{\sigma}_{11s}^i$  is evaluated below at  $x_1 = 0$ ,  $x_1 = h_1$ ,  $x_1 = h_1 + \Delta_h$  and  $x_1 = H$ :

$$\hat{\sigma}_{11s}^{\text{I}} \Big|_{x_1=0} = C_{\alpha_1}^{\text{I}} \left( \star \hat{T}_h^{\text{I-}} e^{-\Gamma_1^{\text{I}}h_1} + \hat{T}_h^{\text{I+}} + \hat{T}_p^{\text{I-}} e^{-\beta_1(\theta_1)h_1} + \hat{T}_p^{\text{I+}} \right), \quad (\text{A.105a})$$

$$\hat{\sigma}_{11s}^{\text{I}} \Big|_{x_1=h_1} = C_{\alpha_1}^{\text{I}} \left( \star \hat{T}_h^{\text{I-}} + \hat{T}_h^{\text{I+}} e^{-\Gamma_1^{\text{I}}h_1} + \hat{T}_p^{\text{I-}} e^{-jk_2 \tan \theta_1 h_1} + \hat{T}_p^{\text{I+}} e^{-\beta_1(\theta_1)h_1} e^{jk_2 \tan \theta_1 h_1} \right), \quad (\text{A.105b})$$

$$\begin{aligned} \hat{\sigma}_{11s}^{\text{II}} \Big|_{x_1=h_1+\Delta_h} &= C_{\alpha_1}^{\text{II}} \left( \star \hat{T}_h^{\text{II-}} e^{-\Gamma_1^{\text{II}}h_2} + \star \hat{T}_h^{\text{II+}} \right. \\ &\quad \left. + \hat{T}_p^{\text{II-}} e^{-\beta_{\text{II}}(\theta_2)h_2} e^{-jk_2 \tan \theta_2 (h_1+\Delta_h)} + \hat{T}_p^{\text{II+}} e^{jk_2 \tan \theta_2 (h_1+\Delta_h)} \right), \end{aligned} \quad (\text{A.105c})$$

$$\hat{\sigma}_{11s}^{\text{II}} \Big|_{x_1=H} = C_{\alpha_1}^{\text{II}} \left( \star \hat{T}_h^{\text{II-}} + \star \hat{T}_h^{\text{II+}} e^{-\Gamma_1^{\text{II}}h_2} + \hat{T}_p^{\text{II-}} e^{-jk_2 \tan \theta_2 H} + \hat{T}_p^{\text{II+}} e^{-\beta_{\text{II}}(\theta_2)h_2} e^{jk_2 \tan \theta_2 H} \right). \quad (\text{A.105d})$$

All the terms necessary to solve the elastodynamic problem have been introduced. The resolution of two  $4 \times 4$  linear systems to find the amplitudes of the eight elastic waves propagating in media I and II (four in medium I and four in medium II) is presented in the following.

## Resolution of the linear systems

In this section, the determination and the resolution of two  $4 \times 4$  linear systems to determine the amplitudes of the eight elastic waves propagating in media I and II are detailed. This approach is based on the one presented in Ref. 150 (pp. 159–162). First, the boundary condition introduced in Eqs. (A.81), (A.82) and (A.83) are written in matrix form. Then, two  $4 \times 4$  linear systems are determined to calculate the amplitudes of the eight elastic waves propagating in media I and II.

### Boundary conditions in matrix form

In medium I, the boundary conditions at  $x_1 = 0$  are given in Eq. (A.81). These

### A.3. Elastodynamic problem

two boundary conditions are written in matrix form using the stress expressions  $\hat{\sigma}_{11}^I$  and  $\hat{\sigma}_{12}^I$  evaluated at  $x_1 = 0$  and associated with the homogeneous solutions [Eqs. (A.89a) and (A.89b)], the particular solutions [Eqs. (A.97a) and (A.97b)] and the source term [Eq. (A.105a)]. We obtain

$$\underbrace{\begin{bmatrix} R_1^L s_1^L & R_1^T s_1^T & c_1^L R_1^L & c_1^T R_1^T \\ c_1^L M_1^L & c_1^T M_1^T & -M_1^L s_1^L & -M_1^T s_1^T \end{bmatrix}}_{\begin{bmatrix} * \psi_0^I \end{bmatrix}_{2 \times 4}} \underbrace{\begin{bmatrix} * \zeta_1^{LS} \\ * \zeta_1^{TS} \\ * \zeta_1^{LA} \\ * \zeta_1^{TA} \end{bmatrix}}_{\begin{bmatrix} * \zeta_1^{nS,A} \end{bmatrix}_{4 \times 1}} + \hat{\sigma}_{p,s}^I|_{x_1=0} = \begin{bmatrix} 0 \\ 0 \end{bmatrix}, \quad (\text{A.106})$$

with

$$s_1^n = \frac{1}{2j} \left( 1 - e^{-jh_1 k_1^{I,n}} \right), \quad c_1^n = \frac{1}{2} \left( 1 + e^{-jh_1 k_1^{I,n}} \right), \quad (\text{A.107a})$$

$$* \zeta_1^{nS} = \zeta_1^{nS} e^{jk_1^{I,n} h_1/2}, \quad * \zeta_1^{nA} = \zeta_1^{nA} e^{jk_1^{I,n} h_1/2}, \quad (\text{A.107b})$$

$$\hat{\sigma}_{p,s}^I|_{x_1=0} = \begin{bmatrix} \hat{\sigma}_{11p}^I|_{x_1=0} - \hat{\sigma}_{11s}^I|_{x_1=0} \\ \hat{\sigma}_{12p}^I|_{x_1=0} \end{bmatrix}. \quad (\text{A.107c})$$

To avoid diverging exponentials and to obtain a well-conditioned matrix  $[* \psi_0^I]_{2 \times 4}$ , the amplitudes  $\zeta_1^{nS}$  and  $\zeta_1^{nA}$  are multiplied by the diverging exponential in Eq. (A.107b) and are written with the symbol “\*”. This technique to obtain well-conditioned matrices has already been used in Eq. (A.59) to solve the heat diffusion problem and is also used in the following.

In medium II, the boundary conditions at  $x_1 = H$  are given in Eq. (A.82). These two boundary conditions are written in matrix form using the stress expressions  $\hat{\sigma}_{11}^I$  and  $\hat{\sigma}_{12}^I$  evaluated at  $x_1 = H$  and associated with the homogeneous solutions [Eqs. (A.96a) and (A.96b)], the particular solutions [Eqs. (A.103a) and (A.103b)] and the source term [Eq. (A.105d)]. We get

$$\underbrace{\begin{bmatrix} R_{II}^L & -R_{II}^L e^{-jh_2 k_1^{II,L}} & R_{II}^T & -R_{II}^T e^{-jh_2 k_1^{II,T}} \\ M_{II}^L & M_{II}^L e^{-jh_2 k_1^{II,L}} & M_{II}^T & M_{II}^T e^{-jh_2 k_1^{II,T}} \end{bmatrix}}_{\begin{bmatrix} * \psi_H^{II} \end{bmatrix}_{2 \times 4}} \underbrace{\begin{bmatrix} * A_{II}^{L-} \\ * A_{II}^{L+} \\ * A_{II}^{T-} \\ * A_{II}^{T+} \end{bmatrix}}_{\begin{bmatrix} * A_{II}^{n\pm} \end{bmatrix}_{4 \times 1}} + \hat{\sigma}_{p,s}^{II}|_{x_1=H} = \begin{bmatrix} 0 \\ 0 \end{bmatrix}, \quad (\text{A.108})$$

with

$${}^*A_{\text{II}}^{\text{n-}} = A_{\text{II}}^{\text{n-}} e^{jk_1^{\text{II},\text{n}}H} \quad \text{and} \quad {}^*A_{\text{II}}^{\text{n+}} = A_{\text{II}}^{\text{n+}} e^{-jk_1^{\text{II},\text{n}}(h_1+\Delta h)}, \quad (\text{A.109})$$

$$\hat{\boldsymbol{\sigma}}_{p,s}^{\text{II}}|_{x_1=H} = \begin{bmatrix} \hat{\sigma}_{11p}^{\text{II}}|_{x_1=H} & -\hat{\sigma}_{11s}^{\text{II}}|_{x_1=H} \\ \hat{\sigma}_{12p}^{\text{II}}|_{x_1=H} & \end{bmatrix}. \quad (\text{A.110})$$

Between media I and II, the boundary conditions are given in Eq. (A.83). These four boundary conditions are written in matrix form using the stress expressions  $\hat{\sigma}_{11}^{\text{I}}$  and  $\hat{\sigma}_{12}^{\text{I}}$  evaluated at  $x_1 = h_1$  and  $x_1 = h_1 + \Delta h$ . These expressions are associated with the homogeneous solutions [Eqs. (A.90a), (A.90b), (A.95a) and (A.95b)], the particular solutions [Eqs. (A.99a), (A.99b), (A.101a) and (A.101b)] and the source terms [Eqs. (A.105b) and (A.105c)]. We obtain

$$\begin{bmatrix} {}^*\psi_{h_1}^{\text{I}} \end{bmatrix}_{4 \times 4} \begin{bmatrix} {}^*\xi_{\text{I}}^{\text{nS,A}} \end{bmatrix}_{4 \times 1} + \begin{bmatrix} \hat{\boldsymbol{u}}_p^{\text{I}}|_{h_1} \\ \hat{\boldsymbol{\sigma}}_{p,s}^{\text{I}}|_{h_1} \end{bmatrix} = \begin{bmatrix} L^M \end{bmatrix}_{4 \times 4} \left( \begin{bmatrix} {}^*\psi_{h_1+\Delta h}^{\text{II}} \end{bmatrix}_{4 \times 4} \begin{bmatrix} {}^*A_{\text{II}}^{\text{n}\pm} \end{bmatrix}_{4 \times 1} + \begin{bmatrix} \hat{\boldsymbol{u}}_p^{\text{II}}|_{h_1+\Delta h} \\ \hat{\boldsymbol{\sigma}}_{p,s}^{\text{II}}|_{h_1+\Delta h} \end{bmatrix} \right), \quad (\text{A.111})$$

with

$$\begin{bmatrix} {}^*\psi_{h_1}^{\text{I}} \end{bmatrix}_{4 \times 4} = \left. \begin{array}{c} \left[ \begin{array}{cccc} c_{\text{I}}^{\text{L}} \hat{U}_{1h}^{\text{I,L-}} & c_{\text{I}}^{\text{T}} \hat{U}_{1h}^{\text{I,T-}} & s_{\text{I}}^{\text{L}} \hat{U}_{1h}^{\text{I,L-}} & s_{\text{I}}^{\text{T}} \hat{U}_{1h}^{\text{I,T-}} \\ j s_{\text{I}}^{\text{L}} \hat{U}_{2h}^{\text{I,L-}} & j s_{\text{I}}^{\text{T}} \hat{U}_{2h}^{\text{I,T-}} & -j c_{\text{I}}^{\text{L}} \hat{U}_{2h}^{\text{I,L-}} & -j c_{\text{I}}^{\text{T}} \hat{U}_{2h}^{\text{I,T-}} \\ -R_{\text{I}}^{\text{L}} s_{\text{I}}^{\text{L}} & -R_{\text{I}}^{\text{T}} s_{\text{I}}^{\text{T}} & c_{\text{I}}^{\text{L}} R_{\text{I}}^{\text{L}} & c_{\text{I}}^{\text{T}} R_{\text{I}}^{\text{T}} \\ c_{\text{I}}^{\text{L}} M_{\text{I}}^{\text{L}} & c_{\text{I}}^{\text{T}} M_{\text{I}}^{\text{T}} & M_{\text{I}}^{\text{L}} s_{\text{I}}^{\text{L}} & M_{\text{I}}^{\text{T}} s_{\text{I}}^{\text{T}} \end{array} \right] \\ \left. \begin{array}{l} \left[ {}^*\psi_{h_1,u}^{\text{I}} \right]_{2 \times 4} \\ \left[ {}^*\psi_{h_1,\sigma}^{\text{I}} \right]_{2 \times 4} \end{array} \right\} \end{array} \right\}, \quad (\text{A.112a})$$

$$\hat{\boldsymbol{u}}_p^{\text{I}}|_{h_1} = \begin{bmatrix} \hat{u}_{1p}^{\text{I}}|_{h_1} \\ \hat{u}_{2p}^{\text{I}}|_{h_1} \end{bmatrix}, \quad \hat{\boldsymbol{\sigma}}_{p,s}^{\text{I}}|_{h_1} = \begin{bmatrix} \hat{\sigma}_{11p}^{\text{I}}|_{h_1} & -\hat{\sigma}_{11s}^{\text{I}}|_{h_1} \\ \hat{\sigma}_{12p}^{\text{I}}|_{h_1} & \end{bmatrix}, \quad (\text{A.112b})$$

$$\begin{bmatrix} L^M \end{bmatrix}_{4 \times 4} = \left. \begin{array}{c} \left[ \begin{array}{cccc} L_{11}^M & L_{12}^M & L_{13}^M & L_{14}^M \\ L_{21}^M & L_{22}^M & L_{23}^M & L_{24}^M \\ L_{31}^M & L_{32}^M & L_{33}^M & L_{34}^M \\ L_{41}^M & L_{42}^M & L_{43}^M & L_{44}^M \end{array} \right] \\ \left. \begin{array}{l} \left[ L_u^M \right]_{2 \times 4} \\ \left[ L_\sigma^M \right]_{2 \times 4} \end{array} \right\} \end{array} \right\}, \quad (\text{A.112c})$$

### A.3. Elastodynamic problem

$$\left[ {}^*\psi_{h_1+\Delta h}^{\text{II}} \right]_{4 \times 4} = \begin{bmatrix} \hat{U}_{1h}^{\text{II,L-}} e^{-j h_2 k_1^{\text{II,L}}} & \hat{U}_{1h}^{\text{II,L-}} & \hat{U}_{1h}^{\text{II,T-}} e^{-j h_2 k_1^{\text{II,T}}} & \hat{U}_{1h}^{\text{II,T-}} \\ \hat{U}_{2h}^{\text{II,L-}} e^{-j h_2 k_1^{\text{II,L}}} & -\hat{U}_{2h}^{\text{II,L-}} & \hat{U}_{2h}^{\text{II,T-}} e^{-j h_2 k_1^{\text{II,T}}} & -\hat{U}_{2h}^{\text{II,T-}} \\ R_{\text{II}}^{\text{L}} e^{-j h_2 k_1^{\text{II,L}}} & -R_{\text{II}}^{\text{L}} & R_{\text{II}}^{\text{T}} e^{-j h_2 k_1^{\text{II,T}}} & -R_{\text{II}}^{\text{T}} \\ M_{\text{II}}^{\text{L}} e^{-j h_2 k_1^{\text{II,L}}} & M_{\text{II}}^{\text{L}} & M_{\text{II}}^{\text{T}} e^{-j h_2 k_1^{\text{II,T}}} & M_{\text{II}}^{\text{T}} \end{bmatrix}, \quad (\text{A.112d})$$

$$\hat{\mathbf{u}}_p^{\text{II}}|_{h_1+\Delta h} = \begin{bmatrix} \hat{u}_{1p}^{\text{II}}|_{h_1+\Delta h} \\ \hat{u}_{2p}^{\text{II}}|_{h_1+\Delta h} \end{bmatrix}, \quad \hat{\boldsymbol{\sigma}}_{p,s}^{\text{II}}|_{h_1+\Delta h} = \begin{bmatrix} \hat{\sigma}_{11p}^{\text{II}}|_{h_1+\Delta h} - \hat{\sigma}_{11s}^{\text{II}}|_{h_1+\Delta h} \\ \hat{\sigma}_{12p}^{\text{II}}|_{h_1+\Delta h} \end{bmatrix}. \quad (\text{A.112e})$$

The eight boundary conditions have been written in matrix form. The two  $4 \times 4$  linear systems to be solved in order to find the amplitudes of the eight elastic waves propagating in media I and II are presented below.

#### Determination of the linear systems to find the eight amplitudes

To find the eight amplitudes of the eight elastic waves propagating in media I and II, the first step consists in writing in a matrix form the two boundary conditions between media I and II (concerning the stresses) at  $x_1 = h_1$  and  $x_1 = h_1 + \Delta h$  [Eq. (A.111)] and the two boundary conditions in medium I at  $x_1 = 0$  [Eq. (A.106)], which gives

$$\boxed{\left[ {}^*\Gamma_{\xi h} \right]_{4 \times 4} \left[ {}^*\zeta_{\text{I}}^{\text{nS,A}} \right]_{4 \times 1} = \left[ {}^*\Gamma_{Ah} \right]_{4 \times 4} \left[ {}^*A_{\text{II}}^{\text{n}\pm} \right]_{4 \times 1} + \left[ {}^*\Gamma_{Ap} \right]_{4 \times 1}}, \quad (\text{A.113})$$

with

$$\left[ {}^*\Gamma_{\xi h} \right]_{4 \times 4} = \begin{bmatrix} \left[ {}^*\psi_{h_1,\sigma}^{\text{I}} \right]_{2 \times 4} \\ \left[ {}^*\psi_0^{\text{I}} \right]_{2 \times 4} \end{bmatrix}, \quad (\text{A.114a})$$

$$\left[ {}^*\Gamma_{Ah} \right]_{4 \times 4} = \begin{bmatrix} \left[ L_{\sigma}^{\text{M}} \right]_{2 \times 4} \left[ {}^*\psi_{h_1+\Delta h}^{\text{II}} \right]_{4 \times 4} \\ \left[ 0 \right]_{2 \times 4} \end{bmatrix}, \quad (\text{A.114b})$$

$$\left[ {}^*\Gamma_{Ap} \right]_{4 \times 1} = \begin{bmatrix} \left[ L_{\sigma}^{\text{M}} \right]_{2 \times 4} \left[ \hat{\mathbf{u}}_p^{\text{II}}|_{h_1+\Delta h} \right]_{4 \times 1} - \hat{\boldsymbol{\sigma}}_{p,s}^{\text{I}}|_{h_1} \\ - \hat{\boldsymbol{\sigma}}_{p,s}^{\text{I}}|_0 \end{bmatrix}. \quad (\text{A.114c})$$

Then, the two boundary conditions between media I and II (concerning the displacements) at  $x_1 = h_1$  and  $x_1 = h_1 + \Delta h$  [Eq. (A.111)] are also written in matrix form:

$$\left[ {}^*\psi_{h_1,u}^{\text{I}} \right]_{2 \times 4} \left[ {}^*\zeta_{\text{I}}^{\text{nS,A}} \right]_{4 \times 1} = \left[ L_u^{\text{M}} \right]_{2 \times 4} \left( \left[ {}^*\psi_{h_1+\Delta h}^{\text{II}} \right]_{4 \times 4} \left[ {}^*A_{\text{II}}^{\text{n}\pm} \right]_{4 \times 1} + \left[ \hat{\mathbf{u}}_p^{\text{II}}|_{h_1+\Delta h} \right]_{4 \times 1} \right) - \hat{\mathbf{u}}_p^{\text{I}}|_{h_1}. \quad (\text{A.115})$$

The second step consists in replacing the vector of amplitudes  $[\star\zeta_I^{nS,A}]_{4 \times 1}$  in Eq. (A.115) by the one obtained in Eq. (A.113) and to use the boundary condition in medium II at  $x_1 = H$  [Eq. (A.108)] to obtain the  $4 \times 4$  linear system:

$$\boxed{[\star\Phi_{Ah}]_{4 \times 4} [\star A_{II}^{n\pm}]_{4 \times 1} = [\star\Phi_{Ap}]_{4 \times 1}}, \quad (\text{A.116})$$

with

$$[\star\Phi_{Ah}]_{4 \times 4} = \begin{bmatrix} [\star\psi_{h_1,u}^I]_{2 \times 4} [\star\Gamma_{\xi h}]_{4 \times 4}^{-1} [\star\Gamma_{Ah}]_{4 \times 4} - [L_u^M]_{2 \times 4} [\star\psi_{h_1+\Delta h}^{II}]_{4 \times 4} \\ [\star\psi_H^{II}]_{2 \times 4} \end{bmatrix}, \quad (\text{A.117a})$$

$$[\star\Phi_{Ap}]_{4 \times 1} = \begin{bmatrix} -[\star\psi_{h_1,u}^I]_{2 \times 4} [\star\Gamma_{\xi h}]_{4 \times 4}^{-1} [\star\Gamma_{Ap}]_{4 \times 1} + [L_u^M]_{2 \times 4} \begin{bmatrix} \hat{\mathbf{u}}_p^{II}|_{h_1+\Delta h} \\ \hat{\boldsymbol{\sigma}}_{p,s}^{II}|_{h_1+\Delta h} \end{bmatrix}_{4 \times 1} - \hat{\mathbf{u}}_p^I|_{h_1} \\ -\hat{\boldsymbol{\sigma}}_{p,s}^{II}|_H \end{bmatrix}. \quad (\text{A.117b})$$

This  $4 \times 4$  linear system in Eq. (A.116) is solved numerically to obtain the four amplitudes  $\star A_{II}^{n\pm}$ , with  $n = \{L, T\}$ . Finally, Eq. (A.113) is solved numerically using the four amplitudes  $\star A_{II}^{n\pm}$  calculated in the previous step. Thus, the amplitudes of the four elastic waves that are propagating in medium I ( $\star\zeta_I^{nS,A}$ ) and the four elastic waves that are propagating in medium II ( $\star A_{II}^{n\pm}$ ) are fully determined.

### Complete solutions of the elastodynamic equations

In medium  $i = \{I, II\}$ , the complete solution is equal to the linear combination of the homogeneous and particular solutions

$$\boxed{\hat{\mathbf{u}}^i(x_1, k_2, \omega) = \hat{\mathbf{u}}_h^i(x_1, k_2, \omega) + \hat{\mathbf{u}}_p^i(x_1, k_2, \omega)}. \quad (\text{A.118})$$

Hence, in medium I, the linear combination of the homogeneous and particular solutions is equal to

$$\hat{\mathbf{u}}^I(x_1, k_2, \omega) = \hat{\mathbf{u}}_h^I(x_1, k_2, \omega) + \hat{\mathbf{u}}_p^I(x_1, k_2, \omega), \quad (\text{A.119})$$

### A.3. Elastodynamic problem

---

with  $\hat{\mathbf{u}}_p^I(x_1, k_2, \omega)$  the particular solution given in Eq. (A.71a). The homogeneous solution  $\hat{\mathbf{u}}_h^I$ , projected onto the  $\mathbf{x}_1$ - and  $\mathbf{x}_2$ -axes, is provided by

$$\hat{u}_{1h}^I = \sum_{n=\{L,T\}} \hat{U}_{1h}^{I,n-} \left[ {}^* \zeta_I^{nS} c_I^n(x_1) + {}^* \zeta_I^{nA} s_I^n(x_1) \right], \quad (\text{A.120a})$$

$$\hat{u}_{2h}^I = \sum_{n=\{L,T\}} j \hat{U}_{2h}^{I,n-} \left[ {}^* \zeta_I^{nS} s_I^n(x_1) - {}^* \zeta_I^{nA} c_I^n(x_1) \right], \quad (\text{A.120b})$$

with  $\hat{U}_{1h}^{I,n-}$  and  $\hat{U}_{2h}^{I,n-}$  given in Eq. (A.62b),  ${}^* \zeta_I^{nS}$  and  ${}^* \zeta_I^{nA}$  the four amplitudes obtained in the previous part and

$$c_I^n(x_1) = \frac{1}{2} \left( e^{jk_1^{I,n}(x_1-h_1)} + e^{-jk_1^{I,n}x_1} \right), \quad (\text{A.121a})$$

$$s_I^n(x_1) = \frac{1}{2j} \left( e^{jk_1^{I,n}(x_1-h_1)} - e^{-jk_1^{I,n}x_1} \right). \quad (\text{A.121b})$$

In medium II, the complete solution is equal to

$$\hat{\mathbf{u}}^{\text{II}}(x_1, k_2, \omega) = \hat{\mathbf{u}}_h^{\text{II}}(x_1, k_2, \omega) + \hat{\mathbf{u}}_p^{\text{II}}(x_1, k_2, \omega), \quad (\text{A.122})$$

with  $\hat{\mathbf{u}}_p^{\text{II}}(x_1, k_2, \omega)$  the particular solution given in Eq. (A.71b). The homogeneous solution  $\hat{\mathbf{u}}_h^{\text{II}}$ , projected onto the  $\mathbf{x}_1$ - and  $\mathbf{x}_2$ -axes, is given by

$$\hat{u}_{1h}^{\text{II}} = \sum_{n=\{L,T\}} \hat{U}_{1h}^{\text{II},n-} \left( {}^* A_{\text{II}}^{n+} e^{-jk_1^{\text{II},n}[x_1-(h_1+\Delta h)]} + {}^* A_{\text{II}}^{n-} e^{jk_1^{\text{II},n}(x_1-H)} \right), \quad (\text{A.123a})$$

$$\hat{u}_{2h}^{\text{II}} = \sum_{n=\{L,T\}} \hat{U}_{2h}^{\text{II},n-} \left( - {}^* A_{\text{II}}^{n+} e^{-jk_1^{\text{II},n}[x_1-(h_1+\Delta h)]} + {}^* A_{\text{II}}^{n-} e^{jk_1^{\text{II},n}(x_1-H)} \right), \quad (\text{A.123b})$$

with  $\hat{U}_{1h}^{\text{II},n-}$  and  $\hat{U}_{2h}^{\text{II},n-}$  given in Eq. (A.62b) and  ${}^* A_{\text{II}}^{n\pm}$  the four amplitudes obtained by solving Eq. (A.116).

#### A.3.4 Coupling matrix $[L_i^M]_{4 \times 4}$

In Sec. 2.5.3, the transfer matrix  $[L^M]$  (pp. 53–60 in Ref. 157) associated to the elastic boundary conditions between media I and II, introduced in Eq. (2.54), is given by

$$[L^M]_{4 \times 4} = \prod_{i=1}^{N_{\text{sublayers}}} [L_i^M]_{4 \times 4}, \quad (\text{A.124})$$

with  $[L_i^M]$  the transfer matrix of the  $i$ -th sublayer and  $N_{\text{sublayers}}$  the total number of sublayers which are between media I and II.

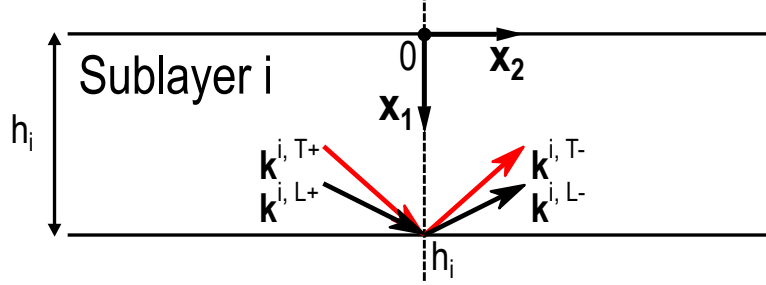


Figure A.3 – Representation of the  $i$ -th sublayer of thickness  $h_i$ . The wave vectors of the longitudinal (transverse) elastic waves are represented with black (red) arrows.

For a given sublayer of thickness  $h_i$  (see Fig. A.3), the displacement and stress vectors are linked between the upper and lower surfaces (of local coordinates  $x_1 = 0$  and  $x_1 = h_i$ , respectively) by the relation

$$\begin{bmatrix} \hat{u}_1^i \\ \hat{u}_2^i \\ \hat{\sigma}_{11}^i \\ \hat{\sigma}_{12}^i \end{bmatrix}_{x_1=0} = \underbrace{\begin{bmatrix} \psi_0^i \\ \psi_{h_i}^i \end{bmatrix}^{-1}}_{[L_i^M]_{4 \times 4}} \begin{bmatrix} \hat{u}_1^i \\ \hat{u}_2^i \\ \hat{\sigma}_{11}^i \\ \hat{\sigma}_{12}^i \end{bmatrix}_{x_1=h_i}. \quad (\text{A.125})$$

Assuming that there is no source term in the sublayers, which means that the generation of elastic waves in the sublayers is neglected, the transfer matrix  $[L_i^M]$  is equal to the product of  $[\psi_0^i]$  and the inverse of  $[\psi_{h_i}^i]$ . The former matrix is

$$\begin{bmatrix} \hat{u}_1^i \\ \hat{u}_2^i \\ \hat{\sigma}_{11}^i \\ \hat{\sigma}_{12}^i \end{bmatrix}_0 = \underbrace{\begin{bmatrix} \hat{U}_{1h}^{i,L-} \alpha_L^M & \hat{U}_{1h}^{i,L-} & \hat{U}_{1h}^{i,T-} \alpha_T^M & \hat{U}_{1h}^{i,T-} \\ \hat{U}_{2h}^{i,L-} \alpha_L^M & -\hat{U}_{2h}^{i,L-} & \hat{U}_{2h}^{i,T-} \alpha_T^M & -\hat{U}_{2h}^{i,T-} \\ R_i^L \alpha_L^M & -R_i^L & R_i^T \alpha_T^M & -R_i^T \\ M_i^L \alpha_L^M & M_i^L & M_i^T \alpha_T^M & M_i^T \end{bmatrix}}_{[\psi_0^i]_{4 \times 4}} \begin{bmatrix} A_i^{L-} \\ A_i^{L+} \\ A_i^{T-} \\ A_i^{T+} \end{bmatrix}, \quad (\text{A.126})$$

and relates the amplitudes of the backward and forward longitudinal and shear elastic waves in the sublayer to the displacement and stress components at its upper surface. The latter matrix of the product is given by

$$\begin{bmatrix} \hat{u}_1^i \\ \hat{u}_2^i \\ \hat{\sigma}_{11}^i \\ \hat{\sigma}_{12}^i \end{bmatrix}_{h_i} = \underbrace{\begin{bmatrix} \hat{U}_{1h}^{i,L-} & \hat{U}_{1h}^{i,L-} \alpha_L^M & \hat{U}_{1h}^{i,T-} & \hat{U}_{1h}^{i,T-} \alpha_T^M \\ \hat{U}_{2h}^{i,L-} & -\hat{U}_{2h}^{i,L-} \alpha_L^M & \hat{U}_{2h}^{i,T-} & -\hat{U}_{2h}^{i,T-} \alpha_T^M \\ R_i^L & -R_i^L \alpha_L^M & R_i^T & -R_i^T \alpha_T^M \\ M_i^L & M_i^L \alpha_L^M & M_i^T & M_i^T \alpha_T^M \end{bmatrix}}_{\left[ \psi_{h_i}^i \right]_{4 \times 4}} \begin{bmatrix} A_i^{L-} \\ A_i^{L+} \\ A_i^{T-} \\ A_i^{T+} \end{bmatrix}, \quad (\text{A.127})$$

with  $\hat{U}_h^{i,n-}$  given in Eq. (2.49a) and

$$\alpha_n^M = e^{-jk_1^{i,n} h_i}, \quad \text{with } n = \{L, T\}, \quad (\text{A.128a})$$

$$R_i^n = j \left( C_{11}^i k_1^{i,n} \hat{U}_{1h}^{i,n-} - C_{12}^i k_2 \hat{U}_{2h}^{i,n-} \right), \quad (\text{A.128b})$$

$$M_i^n = C_{66}^i \left( j k_1^{i,n} \hat{U}_{2h}^{i,n-} - j k_2 \hat{U}_{1h}^{i,n-} \right). \quad (\text{A.128c})$$

These two matrices,  $[\psi_0^i]$  and  $[\psi_{h_i}^i]$ , are obtained by writing the four waves (of longitudinal and transverse polarizations) propagating in the  $i$ -th sublayer as a function of the amplitudes  $A_i^{\pm}$  and evaluating these expressions at  $x_1 = 0$  and  $x_1 = h_i$ . Then, by replacing the amplitudes  $A_i^{\pm}$  of Eq. (A.126) with those obtained by inverting the linear system in Eq. (A.127), the transfer matrix of Eq. (A.125) is determined. Note that in the case where the elastic wavelength can be considered large relative to the thickness of the  $i$ -th sublayer, the transfer matrix simplifies to<sup>178,202</sup>

$$\left[ L_i^M \right]_{4 \times 4} \approx \begin{bmatrix} 1 & 0 & -\frac{1}{K_N} & 0 \\ 0 & 1 & 0 & -\frac{1}{K_T} \\ 0 & 0 & 1 & 0 \\ 0 & 0 & 0 & 1 \end{bmatrix}, \quad (\text{A.129})$$

with the normal and transverse interfacial stiffnesses ( $K_N$  and  $K_T$ ) equal to

$$K_N = \frac{C_{11}^i}{h_i}, \quad K_T = \frac{C_{66}^i}{h_i}. \quad (\text{A.130})$$

The latter approximation could be of interest, when adapted, to lower the number of parameters to retrieve in an inverse problem, e.g., for the nondestructive evaluation of adhesive bonding.



## Appendix B

# Coupling matrix $[L_i^M]$ expressed with the angles

The transfer matrix<sup>147,157,179</sup> is used to model the adhesive sublayer, which is assumed homogeneous and linear. Following the approach of Brekhovskikh,<sup>157</sup> the transfer matrix  $[L_i^M]$ , detailed below, couples the displacements  $(u_1^i, u_2^i)$  and stresses  $(\sigma_{11}^i, \sigma_{12}^i)$  of the upper and lower surfaces of the  $i$ -th sublayer:

$$\begin{bmatrix} u_1^i \\ u_2^i \\ \sigma_{11}^i \\ \sigma_{12}^i \end{bmatrix}_{x_1=h_1} = \begin{bmatrix} L_{i,11}^M & L_{i,12}^M & L_{i,13}^M & L_{i,14}^M \\ L_{i,21}^M & L_{i,22}^M & L_{i,23}^M & L_{i,24}^M \\ L_{i,31}^M & L_{i,32}^M & L_{i,33}^M & L_{i,34}^M \\ L_{i,41}^M & L_{i,42}^M & L_{i,43}^M & L_{i,44}^M \end{bmatrix} \begin{bmatrix} u_1^i \\ u_2^i \\ \sigma_{11}^i \\ \sigma_{12}^i \end{bmatrix}_{x_1=h_1+h_i}. \quad (\text{B.1})$$

When isotropic mechanical properties are assumed, the expressions of each terms of  $[L_i^M]$  are equal to

$$\begin{aligned} L_{i,11}^M &= [1 - \cos(2\theta_i^T)] \cos(\alpha_i^T h_i) + \cos(2\theta_i^T) \cos(\alpha_i^L h_i), \\ L_{i,12}^M &= -j(1 - a_i) \sin(\alpha_i^T h_i) \tan \theta_i^T + j \frac{C_{66}^i}{C_{11}^i} \sin(2\theta_i^L) \sin(\alpha_i^L h_i), \\ L_{i,13}^M &= \frac{-\sin \theta_i^L \sin(\alpha_i^T h_i) \tan \theta_i^T - \sin(\alpha_i^L h_i) \cos \theta_i^L}{C_{11}^i k_i^L}, \\ L_{i,14}^M &= L_{i,23}^M = \frac{j \sin \theta_i^T}{C_{66}^i k_i^T} [\cos(\alpha_i^L h_i) - \cos(\alpha_i^T h_i)], \\ L_{i,21}^M &= j [-\sin(2\theta_i^T) \sin(\alpha_i^T h_i) + \sin(\alpha_i^L h_i) \cos(2\theta_i^T) \tan \theta_i^L], \\ L_{i,22}^M &= a_i \cos(\alpha_i^L h_i) + (1 - a_i) \cos(\alpha_i^T h_i), \\ L_{i,24}^M &= \frac{-\sin \theta_i^T \sin(\alpha_i^L h_i) \tan \theta_i^L - \sin(\alpha_i^T h_i) \cos \theta_i^T}{C_{66}^i k_i^T}, \end{aligned}$$

$$\begin{aligned}
 L_{i,31}^M &= \frac{C_{11}^i k_i^L (1 - a_i) \sin(\alpha_i^L h_i) \cos(2\theta_i^T)}{\cos \theta_i^L} + k_i^T (C_{11}^i - C_{12}^i) \sin \theta_i^T \sin(2\theta_i^T) \sin(\alpha_i^T h_i), \\
 L_{i,32}^M &= j k_i^T (1 - a_i) (C_{11}^i - C_{12}^i) \sin \theta_i^T [\cos(\alpha_i^T h_i) - \cos(\alpha_i^L h_i)], \\
 L_{i,42}^M &= 2a_i C_{66}^i k_i^L \sin(\alpha_i^L h_i) \cos \theta_i^L + C_{66}^i k_i^T (1 - a_i) \frac{\cos(2\theta_i^T)}{\cos \theta_i^T} \sin(\alpha_i^T h_i), \tag{B.2}
 \end{aligned}$$

with  $j$  the imaginary number,  $h_i$  the thickness of the  $i$ -th sublayer,  $a_i = 1 - \cos(2\theta_i^T)$  a parameter defined with  $\theta_i^T$  the angle of T-polarized waves with respect to  $\mathbf{x}_1$ . The parameter  $\alpha_i^n = k_i^n \cos \theta_i^n$  is determined with the wavenumber  $k_i^n$  and the angle  $\theta_i^n$  ( $n = \{L, T\}$  for longitudinal and transverse polarizations, respectively). Due to the isotropic mechanical properties, the following equalities stand: for the elastic coefficient  $C_{66}^i = \frac{C_{11}^i - C_{12}^i}{2}$  and for the  $L_i^M$  coefficients  $L_{i,11}^M = L_{i,33}^M$ ,  $L_{i,12}^M = L_{i,43}^M$ ,  $L_{i,21}^M = L_{i,34}^M$ ,  $L_{i,22}^M = L_{i,44}^M$  and  $L_{i,32}^M = L_{i,41}^M$ .

Furthermore, if the thickness of the  $i$ -th sublayer is assumed small compared to the wavelength, the coupling matrix can be simplified as follows

$$[L_i^M]_{4 \times 4} \approx \begin{bmatrix} 1 & 0 & -\frac{1}{K_N} & 0 \\ 0 & 1 & 0 & -\frac{1}{K_T} \\ 0 & 0 & 1 & 0 \\ 0 & 0 & 0 & 1 \end{bmatrix}, \tag{B.3}$$

with  $K_N = \frac{C_{11}^i}{h_i}$  and  $K_T = \frac{C_{66}^i}{h_i}$  the normal and transverse interfacial stiffnesses, respectively.

To obtain the transfer matrix introduced in Eq. (B.1), the method presented in Ref. 157 (pp. 53–60) is used and detailed in the following. The  $i$ -th sublayer of thickness  $h_i$  is shown in Fig. B.1.

This sublayer is assumed linear, homogeneous and isotropic. The origin of the local coordinates is placed at the upper surface of this sublayer. The displacement vector  $\mathbf{u}^i(x_1, x_2, t)$  is written in this medium and is equal to

$$\begin{aligned}
 \mathbf{u}^i(x_1, x_2, t) &= \left( A_i^{L+} e^{-jk_i^L \cos \theta_i^L (x_1 - h_i)} \mathbf{n}_i^{L+} + A_i^{T+} e^{-jk_i^T \cos \theta_i^T (x_1 - h_i)} \mathbf{n}_i^{T+} \right. \\
 &\quad \left. + A_i^{L-} e^{jk_i^L \cos \theta_i^L (x_1 - h_i)} \mathbf{n}_i^{L-} + A_i^{T-} e^{jk_i^T \cos \theta_i^T (x_1 - h_i)} \mathbf{n}_i^{T-} \right) e^{j(\omega t - k_2 x_2)}, \tag{B.4}
 \end{aligned}$$

with  $A_i^{L\pm}$  ( $A_i^{T\pm}$ ) the amplitudes of the longitudinal (transverse) elastic waves that are travelling along the positive and negative directions of the  $\mathbf{x}_1$ -axis, as illustrated in Fig. B.1.

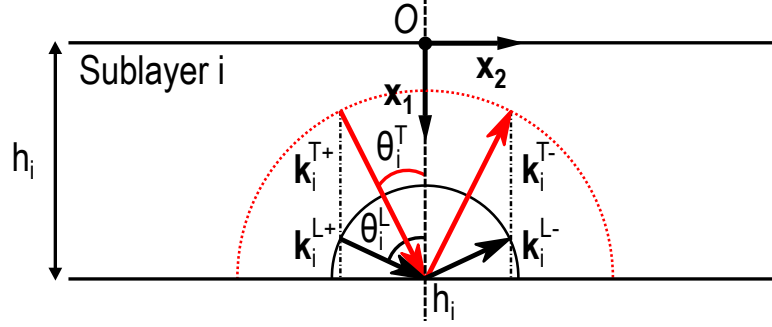


Figure B.1 – Illustration of the  $i$ -th sublayer of thickness  $h_i$ . The wave vectors of the longitudinal (transverse) elastic waves are represented with black (red) arrows.

The angles  $\theta_i^L$  and  $\theta_i^T$  are also represented in Fig. B.1 and are the angles between the wave vectors of longitudinal and transverse elastic waves, respectively, and the  $\mathbf{x}_1$ -direction. Due to Snell's laws, the projections of these wave vectors along the  $\mathbf{x}_2$ -axis are equal to

$$k_2 = k_i^L \sin \theta_i^L = k_i^T \sin \theta_i^T. \quad (\text{B.5})$$

Furthermore, in Eq. (B.4), the polarization vectors of longitudinal (L) and transverse (T) waves are given by

$$\mathbf{n}_i^{L+} = \begin{bmatrix} \cos \theta_i^L \\ \sin \theta_i^L \end{bmatrix}, \mathbf{n}_i^{T+} = \begin{bmatrix} \sin \theta_i^T \\ -\cos \theta_i^T \end{bmatrix}, \mathbf{n}_i^{L-} = \begin{bmatrix} -\cos \theta_i^L \\ \sin \theta_i^L \end{bmatrix} \text{ and } \mathbf{n}_i^{T-} = \begin{bmatrix} \sin \theta_i^T \\ \cos \theta_i^T \end{bmatrix}. \quad (\text{B.6})$$

The first step is to evaluate the displacements  $(u_1^i, u_2^i)$  and the stresses  $(\sigma_{11}^i, \sigma_{12}^i)$  at  $x_1 = h_i$ . To obtain the stresses  $\sigma_{11}^i$  and  $\sigma_{12}^i$ , Hooke's law is applied and leads to

$$\sigma_{11}^i \Big|_{x_1=h_i} = C_{11}^i \frac{\partial u_1^i}{\partial x_1} \Big|_{x_1=h_i} + C_{12}^i \frac{\partial u_2^i}{\partial x_2} \Big|_{x_1=h_i}, \quad (\text{B.7a})$$

$$\sigma_{12}^i \Big|_{x_1=h_i} = C_{66}^i \left( \frac{\partial u_1^i}{\partial x_2} \Big|_{x_1=h_i} + \frac{\partial u_2^i}{\partial x_1} \Big|_{x_1=h_i} \right), \quad (\text{B.7b})$$

with the partial derivative terms written below without the  $e^{j(\omega t - k_2 x_2)}$  dependency to lighten the equations:

$$\frac{\partial u_1^i}{\partial x_1} \Big|_{x_1=h_i} = j \left[ -k_i^L \cos^2 \theta_i^L (A_i^{L+} + A_i^{L-}) - k_i^T \cos \theta_i^T \sin \theta_i^T (A_i^{T+} - A_i^{T-}) \right], \quad (\text{B.8a})$$

$$\left. \frac{\partial u_1^i}{\partial x_2} \right|_{x_1=h_i} = j \left[ -k_i^L \cos \theta_i^L \sin \theta_i^L (A_i^{L+} - A_i^{L-}) - k_i^T \sin^2 \theta_i^T (A_i^{T+} + A_i^{T-}) \right], \quad (\text{B.8b})$$

$$\left. \frac{\partial u_2^i}{\partial x_1} \right|_{x_1=h_i} = j \left[ -k_i^L \cos \theta_i^L \sin \theta_i^L (A_i^{L+} - A_i^{L-}) + k_i^T \cos^2 \theta_i^T (A_i^{T+} + A_i^{T-}) \right], \quad (\text{B.8c})$$

$$\left. \frac{\partial u_2^i}{\partial x_2} \right|_{x_1=h_i} = j \left[ -k_i^L \sin^2 \theta_i^L (A_i^{L+} + A_i^{L-}) + k_i^T \cos \theta_i^T \sin \theta_i^T (A_i^{T+} - A_i^{T-}) \right]. \quad (\text{B.8d})$$

Thus, the first linear system at  $x_1 = h_i$  is equal to

$$\begin{bmatrix} u_1^i \\ u_2^i \\ \sigma_{11}^i \\ \sigma_{12}^i \end{bmatrix}_{x_1=h_i} = \begin{bmatrix} 0 & L_{12}^{h_i} & L_{13}^{h_i} & 0 \\ L_{21}^{h_i} & 0 & 0 & L_{24}^{h_i} \\ L_{31}^{h_i} & 0 & 0 & L_{34}^{h_i} \\ 0 & L_{42}^{h_i} & L_{43}^{h_i} & 0 \end{bmatrix} \begin{bmatrix} A_i^{L+} + A_i^{L-} \\ A_i^{L+} - A_i^{L-} \\ A_i^{T+} + A_i^{T-} \\ A_i^{T+} - A_i^{T-} \end{bmatrix}, \quad (\text{B.9})$$

with

$$\begin{aligned} L_{12}^{h_i} &= \cos \theta_i^L, & L_{13}^{h_i} &= \sin \theta_i^T, \\ L_{21}^{h_i} &= \sin \theta_i^L, & L_{24}^{h_i} &= -\cos \theta_i^T, \\ L_{31}^{h_i} &= -j k_i^L (C_{11}^i \cos^2 \theta_i^L + C_{12}^i \sin^2 \theta_i^L), & L_{34}^{h_i} &= -j k_i^T \sin(2\theta_i^T) \frac{C_{11}^i - C_{12}^i}{2}, \\ L_{42}^{h_i} &= -j C_{66}^i k_i^L \sin(2\theta_i^L), & L_{43}^{h_i} &= j C_{66}^i k_i^T \cos(2\theta_i^T). \end{aligned} \quad (\text{B.10})$$

Then, the linear system in Eq. (B.9) is inverted to obtain the amplitudes as a function of displacements and stresses evaluated at  $x_1 = h_i$ :

$$\begin{bmatrix} A_i^{L+} + A_i^{L-} \\ A_i^{L+} - A_i^{L-} \\ A_i^{T+} + A_i^{T-} \\ A_i^{T+} - A_i^{T-} \end{bmatrix} = \begin{bmatrix} 0 & L_{12}^{-1,h_i} & L_{13}^{-1,h_i} & 0 \\ L_{21}^{-1,h_i} & 0 & 0 & L_{24}^{-1,h_i} \\ L_{31}^{-1,h_i} & 0 & 0 & L_{34}^{-1,h_i} \\ 0 & L_{42}^{-1,h_i} & L_{43}^{-1,h_i} & 0 \end{bmatrix} \begin{bmatrix} u_1^i \\ u_2^i \\ \sigma_{11}^i \\ \sigma_{12}^i \end{bmatrix}_{x_1=h_i}, \quad (\text{B.11})$$

with

$$\begin{aligned} L_{12}^{-1,h_i} &= \frac{(C_{11}^i - C_{12}^i) \sin \theta_i^L}{C_{11}^i}, & L_{13}^{-1,h_i} &= \frac{j}{C_{11}^i k_i^L}, \\ L_{21}^{-1,h_i} &= \frac{\cos(2\theta_i^T)}{\cos \theta_i^L}, & L_{24}^{-1,h_i} &= \frac{j \sin \theta_i^T}{C_{66}^i k_i^T \cos \theta_i^L}, \end{aligned}$$

Appendix B. Coupling matrix  $[L_i^M]$  expressed with the angles

---

$$\begin{aligned} L_{31}^{-1,hi} &= 2 \sin \theta_i^T, & L_{34}^{-1,hi} &= -\frac{J}{C_{66}^i k_i^T}, \\ L_{42}^{-1,hi} &= \frac{\sin^2 \theta_i^L (C_{11}^i - C_{12}^i) - C_{11}^i}{C_{11}^i \cos \theta_i^T}, & L_{43}^{-1,hi} &= \frac{J \sin \theta_i^L}{C_{11}^i k_i^L \cos \theta_i^T}. \end{aligned} \quad (\text{B.12})$$

The second step is to evaluate the displacements ( $u_1^i, u_2^i$ ) and the stresses ( $\sigma_{11}^i, \sigma_{12}^i$ ) at  $x_1 = 0$ . Hooke's law is applied to obtain the stresses  $\sigma_{11}^i$  and  $\sigma_{12}^i$  evaluated at  $x_1 = 0$ , which gives

$$\sigma_{11}^i \Big|_{x_1=0} = C_{11}^i \frac{\partial u_1^i}{\partial x_1} \Big|_{x_1=0} + C_{12}^i \frac{\partial u_2^i}{\partial x_2} \Big|_{x_1=0}, \quad (\text{B.13a})$$

$$\sigma_{12}^i \Big|_{x_1=0} = C_{66}^i \left( \frac{\partial u_1^i}{\partial x_2} \Big|_{x_1=0} + \frac{\partial u_2^i}{\partial x_1} \Big|_{x_1=0} \right). \quad (\text{B.13b})$$

with the partial derivative terms written below without the  $e^{j(\omega t - k_2 x_2)}$  dependency to lighten the equations:

$$\frac{\partial u_1^i}{\partial x_1} \Big|_{x_1=0} = j \left[ -k_i^L \cos^2 \theta_i^L ({}^*A_i^{L+} + {}^*A_i^{L-}) - k_i^T \cos \theta_i^T \sin \theta_i^T ({}^*A_i^{T+} - {}^*A_i^{T-}) \right], \quad (\text{B.14a})$$

$$\frac{\partial u_1^i}{\partial x_2} \Big|_{x_1=0} = j \left[ -k_i^L \cos \theta_i^L \sin \theta_i^L ({}^*A_i^{L+} - {}^*A_i^{L-}) - k_i^T \sin^2 \theta_i^T ({}^*A_i^{T+} + {}^*A_i^{T-}) \right], \quad (\text{B.14b})$$

$$\frac{\partial u_2^i}{\partial x_1} \Big|_{x_1=0} = j \left[ -k_i^L \cos \theta_i^L \sin \theta_i^L ({}^*A_i^{L+} - {}^*A_i^{L-}) + k_i^T \cos^2 \theta_i^T ({}^*A_i^{T+} + {}^*A_i^{T-}) \right], \quad (\text{B.14c})$$

$$\frac{\partial u_2^i}{\partial x_2} \Big|_{x_1=0} = j \left[ -k_i^L \sin^2 \theta_i^L ({}^*A_i^{L+} + {}^*A_i^{L-}) + k_i^T \cos \theta_i^T \sin \theta_i^T ({}^*A_i^{T+} - {}^*A_i^{T-}) \right], \quad (\text{B.14d})$$

and

$${}^*A_i^{L+} = A_i^{L+} e^{jk_i^L \cos \theta_i^L h_i}, \quad {}^*A_i^{L-} = A_i^{L-} e^{-jk_i^L \cos \theta_i^L h_i}, \quad (\text{B.15a})$$

$${}^*A_i^{T+} = A_i^{T+} e^{jk_i^T \cos \theta_i^T h_i}, \quad {}^*A_i^{T-} = A_i^{T-} e^{-jk_i^T \cos \theta_i^T h_i}. \quad (\text{B.15b})$$

Using Euler's formula, sums and differences of the terms  ${}^*A_i^{n\pm}$  (with  $n = \{L, T\}$ ) which are obtained in Eqs. (B.14a–B.14d), are equal to

$${}^*A_i^{n+} + {}^*A_i^{n-} = (A_i^{n+} + A_i^{n-}) \cos(\alpha_i^n h_i) + j (A_i^{n+} - A_i^{n-}) \sin(\alpha_i^n h_i), \quad (\text{B.16a})$$

$${}^*A_i^{n+} - {}^*A_i^{n-} = j (A_i^{n+} + A_i^{n-}) \sin(\alpha_i^n h_i) + (A_i^{n+} - A_i^{n-}) \cos(\alpha_i^n h_i), \quad (\text{B.16b})$$

with  $\alpha_i^n = k_i^n \cos \theta_i^n$ . Then, we end up with the linear system:

$$\begin{bmatrix} u_1^i \\ u_2^i \\ \sigma_{11}^i \\ \sigma_{12}^i \end{bmatrix}_{x_1=0} = \begin{bmatrix} L_{11}^0 & L_{12}^0 & L_{13}^0 & L_{14}^0 \\ L_{21}^0 & L_{22}^0 & L_{23}^0 & L_{24}^0 \\ L_{31}^0 & L_{32}^0 & L_{33}^0 & L_{34}^0 \\ L_{41}^0 & L_{42}^0 & L_{43}^0 & L_{44}^0 \end{bmatrix} \begin{bmatrix} A_i^{L+} + A_i^{L-} \\ A_i^{L+} - A_i^{L-} \\ A_i^{T+} + A_i^{T-} \\ A_i^{T+} - A_i^{T-} \end{bmatrix}, \quad (\text{B.17})$$

with

$$\begin{aligned} L_{11}^0 &= j \cos \theta_i^L \sin(\alpha_i^L h_i), & L_{12}^0 &= \cos \theta_i^L \cos(\alpha_i^L h_i), \\ L_{13}^0 &= \sin \theta_i^T \cos(\alpha_i^T h_i), & L_{14}^0 &= j \sin \theta_i^T \sin(\alpha_i^T h_i), \\ L_{21}^0 &= \sin \theta_i^L \cos(\alpha_i^L h_i), & L_{22}^0 &= j \sin \theta_i^L \sin(\alpha_i^L h_i), \\ L_{23}^0 &= -j \cos \theta_i^T \sin(\alpha_i^T h_i), & L_{24}^0 &= -\cos \theta_i^T \cos(\alpha_i^T h_i), \\ L_{31}^0 &= -j k_i^L (C_{11}^i \cos^2 \theta_i^L + C_{12}^i \sin^2 \theta_i^L) \cos(\alpha_i^L h_i), & L_{32}^0 &= k_i^L (C_{11}^i \cos^2 \theta_i^L + C_{12}^i \sin^2 \theta_i^L) \sin(\alpha_i^L h_i), \\ L_{33}^0 &= k_i^T \frac{(C_{11}^i - C_{12}^i)}{2} \sin(2\theta_i^T) \sin(\alpha_i^T h_i), & L_{34}^0 &= -j k_i^T \frac{(C_{11}^i - C_{12}^i)}{2} \sin(2\theta_i^T) \cos(\alpha_i^T h_i), \\ L_{41}^0 &= C_{66}^i k_i^L \sin(2\theta_i^L) \sin(\alpha_i^L h_i), & L_{42}^0 &= -j C_{66}^i k_i^L \sin(2\theta_i^L) \cos(\alpha_i^L h_i), \\ L_{43}^0 &= j C_{66}^i k_i^T \cos(2\theta_i^T) \cos(\alpha_i^T h_i), & L_{44}^0 &= -C_{66}^i k_i^T \cos(2\theta_i^T) \sin(\alpha_i^T h_i). \end{aligned} \quad (\text{B.18})$$

Finally, replacing sums and differences of the terms  $*A_i^{n\pm}$  in Eq. (B.17) by the ones obtained in Eq. (B.11), leads to the expression of the transfer matrix  $\left[ L_i^M \right]_{4 \times 4}$ :

$$\begin{bmatrix} u_1^i \\ u_2^i \\ \sigma_{11}^i \\ \sigma_{12}^i \end{bmatrix}_{x_1=0} = \underbrace{\begin{bmatrix} L_{i,11}^M & L_{i,12}^M & L_{i,13}^M & L_{i,14}^M \\ L_{i,21}^M & L_{i,22}^M & L_{i,23}^M & L_{i,24}^M \\ L_{i,31}^M & L_{i,32}^M & L_{i,33}^M & L_{i,34}^M \\ L_{i,41}^M & L_{i,42}^M & L_{i,43}^M & L_{i,44}^M \end{bmatrix}}_{\left[ L_i^M \right]_{4 \times 4}} \begin{bmatrix} u_1^i \\ u_2^i \\ \sigma_{11}^i \\ \sigma_{12}^i \end{bmatrix}_{x_1=h_i} \quad (\text{B.19})$$

with

$$\begin{aligned} L_{i,11}^M &= [1 - \cos(2\theta_i^T)] \cos(\alpha_i^T h_i) + \cos(2\theta_i^T) \cos(\alpha_i^L h_i), \\ L_{i,12}^M &= -j(1 - a_i) \sin(\alpha_i^T h_i) \tan \theta_i^T + j \frac{(C_{11}^i - C_{12}^i)}{2C_{11}^i} \sin(2\theta_i^L) \sin(\alpha_i^L h_i), \end{aligned}$$

Appendix B. Coupling matrix  $[L_i^M]$  expressed with the angles

---

$$\begin{aligned}
L_{i,13}^M &= \frac{-\sin \theta_i^L \sin(\alpha_i^T h_i) \tan \theta_i^T - \sin(\alpha_i^L h_i) \cos \theta_i^L}{C_{11}^i k_i^L}, \\
L_{i,14}^M &= L_{i,23}^M = \frac{j \sin \theta_i^T}{C_{66}^i k_i^T} [\cos(\alpha_i^L h_i) - \cos(\alpha_i^T h_i)], \\
L_{i,21}^M &= j [-\sin(2\theta_i^T) \sin(\alpha_i^T h_i) + \sin(\alpha_i^L h_i) \cos(2\theta_i^T) \tan \theta_i^L], \\
L_{i,22}^M &= a_i \cos(\alpha_i^L h_i) + (1 - a_i) \cos(\alpha_i^T h_i), \\
L_{i,24}^M &= \frac{-\sin \theta_i^T \sin(\alpha_i^L h_i) \tan \theta_i^L - \sin(\alpha_i^T h_i) \cos \theta_i^T}{C_{66}^i k_i^T}, \\
L_{i,31}^M &= \frac{C_{11}^i k_i^L (1 - a_i) \sin(\alpha_i^L h_i) \cos(2\theta_i^T)}{\cos \theta_i^L} + k_i^T (C_{11}^i - C_{12}^i) \sin \theta_i^T \sin(2\theta_i^T) \sin(\alpha_i^T h_i), \\
L_{i,32}^M &= j k_i^T (1 - a_i) (C_{11}^i - C_{12}^i) \sin \theta_i^T [\cos(\alpha_i^T h_i) - \cos(\alpha_i^L h_i)], \\
L_{i,33}^M &= a_i \cos(\alpha_i^T h_i) + (1 - a_i) \cos(\alpha_i^L h_i), \\
L_{i,34}^M &= j (1 - a_i) \sin(\alpha_i^L h_i) \tan \theta_i^L - j \frac{(C_{11}^i - C_{12}^i)}{2C_{66}^i} \sin(2\theta_i^T) \sin(\alpha_i^T h_i), \\
L_{i,41}^M &= 2j C_{66}^i k_i^T \sin \theta_i^T \cos(2\theta_i^T) [\cos(\alpha_i^T h_i) - \cos(\alpha_i^L h_i)], \\
L_{i,42}^M &= 2a_i C_{66}^i k_i^L \sin(\alpha_i^L h_i) \cos \theta_i^L + C_{66}^i k_i^T (1 - a_i) \frac{\cos(2\theta_i^T)}{\cos \theta_i^T} \sin(\alpha_i^T h_i), \\
L_{i,43}^M &= -j \sin(\alpha_i^T h_i) \cos(2\theta_i^T) \tan \theta_i^T + j \frac{C_{66}^i}{C_{11}^i} \sin(2\theta_i^L) \sin(\alpha_i^L h_i), \\
L_{i,44}^M &= [1 - \cos(2\theta_i^T)] \cos(\alpha_i^L h_i) + \cos(2\theta_i^T) \cos(\alpha_i^T h_i), \tag{B.20}
\end{aligned}$$

and  $a_i = \frac{(C_{11}^i - C_{12}^i)}{C_{11}^i} \sin^2 \theta_i^L$ . Due to the isotropic mechanical properties, the following equalities stand: for the elastic coefficient  $C_{66}^i = \frac{C_{11}^i - C_{12}^i}{2}$  and for the parameter  $a_i = 1 - \cos(2\theta_i^T)$ . Thus, the  $L_i^M$  coefficients given in Eq. (B.20) can be simplified and are equal to

$$\begin{aligned}
L_{i,11}^M &= L_{i,33}^M = [1 - \cos(2\theta_i^T)] \cos(\alpha_i^T h_i) + \cos(2\theta_i^T) \cos(\alpha_i^L h_i), \\
L_{i,12}^M &= L_{i,43}^M = -j \cos(2\theta_i^T) \sin(\alpha_i^T h_i) \tan \theta_i^T + j \frac{C_{66}^i}{C_{11}^i} \sin(2\theta_i^L) \sin(\alpha_i^L h_i), \\
L_{i,13}^M &= \frac{-\sin \theta_i^L \sin(\alpha_i^T h_i) \tan \theta_i^T - \sin(\alpha_i^L h_i) \cos \theta_i^L}{C_{11}^i k_i^L}, \\
L_{i,14}^M &= L_{i,23}^M = \frac{j \sin \theta_i^T}{C_{66}^i k_i^T} [\cos(\alpha_i^L h_i) - \cos(\alpha_i^T h_i)], \\
L_{i,21}^M &= L_{i,34}^M = j [-\sin(2\theta_i^T) \sin(\alpha_i^T h_i) + \sin(\alpha_i^L h_i) \cos(2\theta_i^T) \tan \theta_i^L], \\
L_{i,22}^M &= L_{i,44}^M = [1 - \cos(2\theta_i^T)] \cos(\alpha_i^L h_i) + \cos(2\theta_i^T) \cos(\alpha_i^T h_i),
\end{aligned}$$

$$\begin{aligned}
 L_{i,24}^M &= \frac{-\sin \theta_i^T \sin(\alpha_i^L h_i) \tan \theta_i^L - \sin(\alpha_i^T h_i) \cos \theta_i^T}{C_{66}^i k_i^T}, \\
 L_{i,31}^M &= \frac{C_{11}^i k_i^L \sin(\alpha_i^L h_i) \cos^2(2\theta_i^T)}{\cos \theta_i^L} + k_i^T 2C_{66}^i \sin \theta_i^T \sin(2\theta_i^T) \sin(\alpha_i^T h_i), \\
 L_{i,32}^M &= L_{i,41}^M = 2j k_i^T \cos(2\theta_i^T) C_{66}^i \sin \theta_i^T [\cos(\alpha_i^T h_i) - \cos(\alpha_i^L h_i)], \\
 L_{i,42}^M &= 2 [1 - \cos(2\theta_i^T)] C_{66}^i k_i^L \sin(\alpha_i^L h_i) \cos \theta_i^L + C_{66}^i k_i^T \frac{\cos^2(2\theta_i^T)}{\cos \theta_i^T} \sin(\alpha_i^T h_i). \quad (\text{B.21})
 \end{aligned}$$

## Appendix C

# Reflection/transmission coefficients

In this Appendix, the reflection/transmission coefficients are calculated when a plane wave of longitudinal or transverse polarization is incident on one or more sublayers of total thickness  $\Delta h$ . These sublayers are located between two semi-infinite media (media I and II), as shown in Fig. C.1. They are modeled with the transfer matrix method,<sup>147,157</sup> as described in Appendix B. Hence, the transfer matrix  $[L^M]$  is equal to

$$[L^M]_{4 \times 4} = \prod_{i=1}^{N_{\text{sublayers}}} [L_i^M]_{4 \times 4}, \quad (\text{C.1})$$

with  $[L_i^M]$  the transfer matrix of the  $i$ -th sublayer and  $N_{\text{sublayers}}$  the total number of sublayers which are located between media I and II. In the following, media I and II and all sublayers are assumed linear, homogeneous and isotropic. Furthermore, the total thickness  $\Delta h$ , in Fig. C.1, is equal to

$$\Delta h = \sum_{i=1}^{N_{\text{sublayers}}} h_i, \quad (\text{C.2})$$

with  $h_i$  the thickness of the  $i$ -th sublayer.

In Sec. C.1, the reflection/transmission coefficients are calculated for an incident plane wave of longitudinal polarization. The reflection coefficients ( $R_{\text{LL}}, R_{\text{LT}}$ ) and the transmission coefficients ( $T_{\text{LL}}, T_{\text{LT}}$ ) are obtained.

In Sec. C.2, the reflection/transmission coefficients are calculated for an incident plane wave of transverse polarization. The reflection coefficients ( $R_{\text{TT}}, R_{\text{TL}}$ ) and the transmission coefficients ( $T_{\text{TT}}, T_{\text{TL}}$ ) are determined.

## C.1 Incident plane wave: longitudinal polarization

To calculate the reflection/transmission coefficients for an incident plane wave of longitudinal polarization, the method is divided into three steps. First, the displacement vector  $\mathbf{u}^I(x_1, x_2, t) = [u_1^I, u_2^I]$  and the stress vector  $\boldsymbol{\sigma}^I(x_1, x_2, t) = [\sigma_{11}^I, \sigma_{12}^I]$  are determined in medium I and evaluated at  $x_1 = 0$  (see Sec. C.1.1). Secondly, the displacement vector  $\mathbf{u}^{II}(x_1, x_2, t)$  and the stress vector  $\boldsymbol{\sigma}^{II}(x_1, x_2, t)$  are determined in medium II and evaluated at  $x_1 = \Delta h$  (see Sec. C.1.2). Thirdly, the boundary conditions are applied with the transfer matrix  $[L^M]$  to find the reflection/transmission coefficients by solving a  $4 \times 4$  linear system (see Sec. C.1.3).

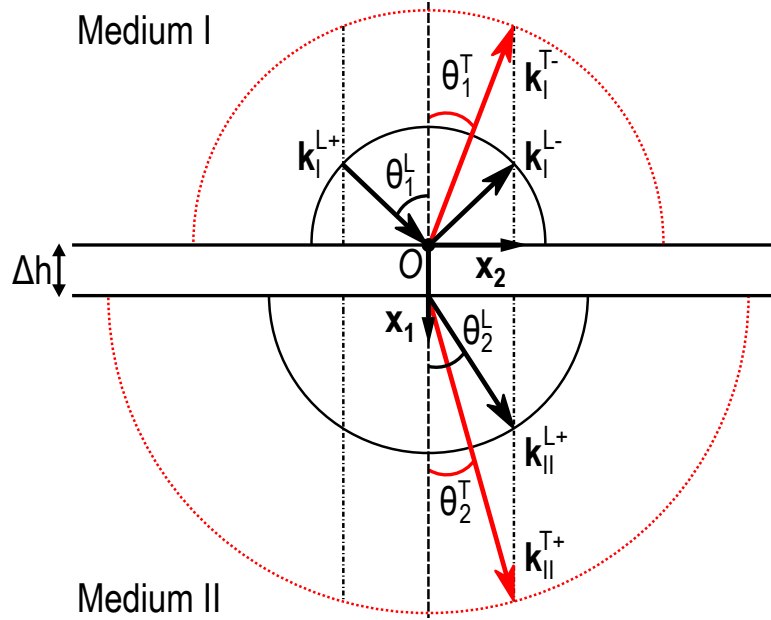


Figure C.1 – Schematic diagram of a longitudinal plane wave incident on one or more sublayers of total thickness  $\Delta h$  which are located between two semi-infinite media I and II. The wave vectors of the longitudinal (transverse) plane waves are represented with black (red) arrows.

### C.1.1 Displacement/stress vectors in medium I

In medium I, the displacement vector  $\mathbf{u}^I(x_1, x_2, t)$  is equal to

$$\mathbf{u}^I(x_1, x_2, t) = \left( A_1^{L+} e^{-j\mathbf{k}_1^{L+} \cdot \mathbf{x}} \mathbf{n}_1^{L+} + A_1^{L-} e^{-j\mathbf{k}_1^{L-} \cdot \mathbf{x}} \mathbf{n}_1^{L-} + A_1^{T-} e^{-j\mathbf{k}_1^{T-} \cdot \mathbf{x}} \mathbf{n}_1^{T-} \right) e^{j\omega t}, \quad (\text{C.3})$$

C.1. Incident plane wave: longitudinal polarization

---

with  $A_1^{L+}$  the amplitude of the incident longitudinal plane wave,  $A_1^{L-}$  the amplitude of the reflected longitudinal plane wave and  $A_1^{T-}$  the amplitude of the reflected transverse plane wave. The associated wave vectors (represented in Fig. C.1) are:

$$\mathbf{k}_1^{L+} = k_1^L \mathbf{n}_1^{L+} = k_1^L \begin{bmatrix} \cos \theta_1^L \\ \sin \theta_1^L \end{bmatrix}, \quad (\text{C.4a})$$

$$\mathbf{k}_1^{L-} = k_1^L \mathbf{n}_1^{L-} = k_1^L \begin{bmatrix} -\cos \theta_1^L \\ \sin \theta_1^L \end{bmatrix}, \quad (\text{C.4b})$$

$$\mathbf{k}_1^{T-} = k_1^T \begin{bmatrix} -\cos \theta_1^T \\ \sin \theta_1^T \end{bmatrix} \quad \text{and} \quad \mathbf{n}_1^{T-} = \begin{bmatrix} \sin \theta_1^T \\ \cos \theta_1^T \end{bmatrix}, \quad (\text{C.4c})$$

with  $\mathbf{n}_1^{L+}$ ,  $\mathbf{n}_1^{L-}$  and  $\mathbf{n}_1^{T-}$  the polarization vectors of the incident and reflected planes waves. Then, Eq. (C.3) is written as a function of the reflection coefficients  $R_{LL} = \frac{A_1^{L-}}{A_1^{L+}}$  and  $R_{LT} = \frac{A_1^{T-}}{A_1^{L+}}$ :

$$\mathbf{u}^I = A_1^{L+} \left( e^{-jk_1^L \cos \theta_1^L x_1} \mathbf{n}_1^{L+} + R_{LL} e^{jk_1^L \cos \theta_1^L x_1} \mathbf{n}_1^{L-} + R_{LT} e^{jk_1^T \cos \theta_1^T x_1} \mathbf{n}_1^{T-} \right) e^{j(\omega t - k_2 x_2)}. \quad (\text{C.5})$$

According to Snell's laws, the projections of the wave vectors  $\mathbf{k}_1^{L+}$ ,  $\mathbf{k}_1^{L-}$  and  $\mathbf{k}_1^{T-}$  along the  $x_2$ -axis are equal to

$$k_2 = k_1^L \sin \theta_1^L = k_1^T \sin \theta_1^T. \quad (\text{C.6})$$

Hence, the angle  $\theta_1^T$ , shown in Fig. C.1, is equal to

$$\begin{cases} \theta_1^T = \arcsin \left( \frac{k_1^L}{k_1^T} \sin \theta_1^L \right), & \text{if } \left| \frac{k_1^L}{k_1^T} \sin \theta_1^L \right| \leq 1, \\ \cos \theta_1^T = j \sqrt{-1 + \left( \frac{k_1^L}{k_1^T} \sin \theta_1^L \right)^2}, & \text{if } \left| \frac{k_1^L}{k_1^T} \sin \theta_1^L \right| \geq 1. \end{cases} \quad (\text{C.7a})$$

$$\left. \begin{cases} \cos \theta_1^T = j \sqrt{-1 + \left( \frac{k_1^L}{k_1^T} \sin \theta_1^L \right)^2}, & \text{if } \left| \frac{k_1^L}{k_1^T} \sin \theta_1^L \right| \geq 1. \end{cases} \right. \quad (\text{C.7b})$$

Next, the stresses  $\sigma_{11}^I$  and  $\sigma_{12}^I$  are obtained with Hooke's law and are evaluated at  $x_1 = 0$ , which gives

$$\sigma_{11}^I \Big|_{x_1=0} = C_{11}^I \frac{\partial u_1^I}{\partial x_1} \Big|_{x_1=0} + C_{12}^I \frac{\partial u_2^I}{\partial x_2} \Big|_{x_1=0}, \quad (\text{C.8a})$$

$$\sigma_{12}^I|_{x_1=0} = C_{66}^I \left( \frac{\partial u_1^I}{\partial x_2} \Big|_{x_1=0} + \frac{\partial u_2^I}{\partial x_1} \Big|_{x_1=0} \right), \quad (\text{C.8b})$$

with the partial derivative terms written below without the  $e^{j(\omega t - k_2 x_2)}$  dependency to lighten the equations

$$\frac{\partial u_1^I}{\partial x_1} \Big|_{x_1=0} = jA_I^{L+} \left( -k_1^L \cos^2 \theta_1^L - k_1^L \cos^2 \theta_1^L R_{LL} + k_1^T \cos \theta_1^T \sin \theta_1^T R_{LT} \right), \quad (\text{C.9a})$$

$$\frac{\partial u_1^I}{\partial x_2} \Big|_{x_1=0} = jA_I^{L+} \left( -k_1^L \cos \theta_1^L \sin \theta_1^L + k_1^L \cos \theta_1^L \sin \theta_1^L R_{LL} - k_1^T \sin^2 \theta_1^T R_{LT} \right), \quad (\text{C.9b})$$

$$\frac{\partial u_2^I}{\partial x_1} \Big|_{x_1=0} = jA_I^{L+} \left( -k_1^L \cos \theta_1^L \sin \theta_1^L + k_1^L \cos \theta_1^L \sin \theta_1^L R_{LL} + k_1^T \cos^2 \theta_1^T R_{LT} \right), \quad (\text{C.9c})$$

$$\frac{\partial u_2^I}{\partial x_2} \Big|_{x_1=0} = jA_I^{L+} \left( -k_1^L \sin^2 \theta_1^L - k_1^L \sin^2 \theta_1^L R_{LL} - k_1^T \cos \theta_1^T \sin \theta_1^T R_{LT} \right). \quad (\text{C.9d})$$

### C.1.2 Displacement/stress vectors in medium II

In medium II, the displacement vector  $\mathbf{u}^{\text{II}}(x_1, x_2, t)$  is equal to

$$\mathbf{u}^{\text{II}}(x_1, x_2, t) = \left( A_{\text{II}}^{L+} e^{-j\mathbf{k}_{\text{II}}^{L+} \cdot \mathbf{x}} \mathbf{n}_{\text{II}}^{L+} + A_{\text{II}}^{T+} e^{-j\mathbf{k}_{\text{II}}^{T+} \cdot \mathbf{x}} \mathbf{n}_{\text{II}}^{T+} \right) e^{j\omega t}, \quad (\text{C.10})$$

with  $A_{\text{II}}^{L+}$  the amplitude of the transmitted longitudinal plane wave and  $A_{\text{II}}^{T+}$  the amplitude of the transmitted transverse plane wave. The associated wave vectors (represented in Fig. C.1) are:

$$\mathbf{k}_{\text{II}}^{L+} = k_{\text{II}}^L \mathbf{n}_{\text{II}}^{L+} = k_{\text{II}}^L \begin{bmatrix} \cos \theta_2^L \\ \sin \theta_2^L \end{bmatrix}, \quad (\text{C.11a})$$

$$\mathbf{k}_{\text{II}}^{T+} = k_{\text{II}}^T \begin{bmatrix} \cos \theta_2^T \\ \sin \theta_2^T \end{bmatrix} \quad \text{and} \quad \mathbf{n}_{\text{II}}^{T+} = \begin{bmatrix} \sin \theta_2^T \\ -\cos \theta_2^T \end{bmatrix}. \quad (\text{C.11b})$$

with  $\mathbf{n}_{\text{II}}^{L+}$  and  $\mathbf{n}_{\text{II}}^{T+}$  the polarization vectors of the transmitted longitudinal and transverse planes waves, respectively. Then, Eq. (C.10) is written as a function of the transmission coefficients  $T_{LL} = \frac{A_{\text{II}}^{L+}}{A_I^{L+}}$  and  $T_{LT} = \frac{A_{\text{II}}^{T+}}{A_I^{L+}}$ :

$$\mathbf{u}^{\text{II}} = A_I^{L+} \left( T_{LL} e^{-jk_{\text{II}}^L \cos \theta_2^L x_1} \mathbf{n}_{\text{II}}^{L+} + T_{LT} e^{-jk_{\text{II}}^T \cos \theta_2^T x_1} \mathbf{n}_{\text{II}}^{T+} \right) e^{j(\omega t - k_2 x_2)}. \quad (\text{C.12})$$

C.1. Incident plane wave: longitudinal polarization

---

According to Snell's laws, the projections of the wave vectors  $\mathbf{k}_{\text{II}}^{\text{L}+}$  and  $\mathbf{k}_{\text{II}}^{\text{T}+}$  along the  $\mathbf{x}_2$ -axis are equal to

$$k_2 = k_{\text{II}}^{\text{L}} \sin \theta_2^{\text{L}} = k_{\text{II}}^{\text{T}} \sin \theta_2^{\text{T}} = k_{\text{I}}^{\text{L}} \sin \theta_1^{\text{L}}. \quad (\text{C.13})$$

Hence, the angles  $\theta_2^{\text{L}}$  and  $\theta_2^{\text{T}}$ , shown in Fig. C.1, are equal to

$$\left\{ \begin{array}{l} \theta_2^{\text{L}} = \arcsin \left( \frac{k_{\text{I}}^{\text{L}}}{k_{\text{II}}^{\text{L}}} \sin \theta_1^{\text{L}} \right), \text{ if } \left| \frac{k_{\text{I}}^{\text{L}}}{k_{\text{II}}^{\text{L}}} \sin \theta_1^{\text{L}} \right| \leq 1, \\ \cos \theta_2^{\text{L}} = j \sqrt{-1 + \left( \frac{k_{\text{I}}^{\text{L}}}{k_{\text{II}}^{\text{L}}} \sin \theta_1^{\text{L}} \right)^2}, \text{ if } \left| \frac{k_{\text{I}}^{\text{L}}}{k_{\text{II}}^{\text{L}}} \sin \theta_1^{\text{L}} \right| \geq 1, \end{array} \right. \quad (\text{C.14a})$$

$$\left\{ \begin{array}{l} \cos \theta_2^{\text{L}} = j \sqrt{-1 + \left( \frac{k_{\text{I}}^{\text{L}}}{k_{\text{II}}^{\text{L}}} \sin \theta_1^{\text{L}} \right)^2}, \text{ if } \left| \frac{k_{\text{I}}^{\text{L}}}{k_{\text{II}}^{\text{L}}} \sin \theta_1^{\text{L}} \right| \geq 1, \\ \theta_2^{\text{L}} = \arcsin \left( \frac{k_{\text{I}}^{\text{L}}}{k_{\text{II}}^{\text{L}}} \sin \theta_1^{\text{L}} \right), \text{ if } \left| \frac{k_{\text{I}}^{\text{L}}}{k_{\text{II}}^{\text{L}}} \sin \theta_1^{\text{L}} \right| \leq 1, \end{array} \right. \quad (\text{C.14b})$$

$$\left\{ \begin{array}{l} \theta_2^{\text{T}} = \arcsin \left( \frac{k_{\text{I}}^{\text{L}}}{k_{\text{II}}^{\text{T}}} \sin \theta_1^{\text{L}} \right), \text{ if } \left| \frac{k_{\text{I}}^{\text{L}}}{k_{\text{II}}^{\text{T}}} \sin \theta_1^{\text{L}} \right| \leq 1, \\ \cos \theta_2^{\text{T}} = j \sqrt{-1 + \left( \frac{k_{\text{I}}^{\text{L}}}{k_{\text{II}}^{\text{T}}} \sin \theta_1^{\text{L}} \right)^2}, \text{ if } \left| \frac{k_{\text{I}}^{\text{L}}}{k_{\text{II}}^{\text{T}}} \sin \theta_1^{\text{L}} \right| \geq 1. \end{array} \right. \quad (\text{C.15a})$$

$$\left\{ \begin{array}{l} \cos \theta_2^{\text{T}} = j \sqrt{-1 + \left( \frac{k_{\text{I}}^{\text{L}}}{k_{\text{II}}^{\text{T}}} \sin \theta_1^{\text{L}} \right)^2}, \text{ if } \left| \frac{k_{\text{I}}^{\text{L}}}{k_{\text{II}}^{\text{T}}} \sin \theta_1^{\text{L}} \right| \geq 1. \\ \theta_2^{\text{T}} = \arcsin \left( \frac{k_{\text{I}}^{\text{L}}}{k_{\text{II}}^{\text{T}}} \sin \theta_1^{\text{L}} \right), \text{ if } \left| \frac{k_{\text{I}}^{\text{L}}}{k_{\text{II}}^{\text{T}}} \sin \theta_1^{\text{L}} \right| \leq 1. \end{array} \right. \quad (\text{C.15b})$$

Next, the stresses  $\sigma_{11}^{\text{II}}$  and  $\sigma_{12}^{\text{II}}$  are obtained with Hooke's law and are evaluated at  $x_1 = \Delta h$ , which gives

$$\sigma_{11}^{\text{II}}|_{x_1=\Delta h} = C_{11}^{\text{II}} \left. \frac{\partial u_1^{\text{II}}}{\partial x_1} \right|_{x_1=\Delta h} + C_{12}^{\text{II}} \left. \frac{\partial u_2^{\text{II}}}{\partial x_2} \right|_{x_1=\Delta h}, \quad (\text{C.16a})$$

$$\sigma_{12}^{\text{II}}|_{x_1=\Delta h} = C_{66}^{\text{II}} \left( \left. \frac{\partial u_1^{\text{II}}}{\partial x_2} \right|_{x_1=\Delta h} + \left. \frac{\partial u_2^{\text{II}}}{\partial x_1} \right|_{x_1=\Delta h} \right), \quad (\text{C.16b})$$

with the partial derivative terms written below without the  $e^{j(\omega t - k_2 x_2)}$  dependency to lighten the equations

$$\left. \frac{\partial u_1^{\text{II}}}{\partial x_1} \right|_{x_1=\Delta h} = j A_{\text{I}}^{\text{L}+} \left( -k_{\text{II}}^{\text{L}} \cos^2 \theta_2^{\text{L}} e^{-j k_{\text{II}}^{\text{L}} \cos \theta_2^{\text{L}} \Delta h} T_{\text{LL}} - k_{\text{II}}^{\text{T}} \cos \theta_2^{\text{T}} \sin \theta_2^{\text{T}} e^{-j k_{\text{II}}^{\text{T}} \cos \theta_2^{\text{T}} \Delta h} T_{\text{LT}} \right), \quad (\text{C.17a})$$

$$\left. \frac{\partial u_1^{\text{II}}}{\partial x_2} \right|_{x_1=\Delta h} = j A_{\text{I}}^{\text{L}+} \left( -k_{\text{II}}^{\text{L}} \cos \theta_2^{\text{L}} \sin \theta_2^{\text{L}} e^{-j k_{\text{II}}^{\text{L}} \cos \theta_2^{\text{L}} \Delta h} T_{\text{LL}} - k_{\text{II}}^{\text{T}} \sin^2 \theta_2^{\text{T}} e^{-j k_{\text{II}}^{\text{T}} \cos \theta_2^{\text{T}} \Delta h} T_{\text{LT}} \right), \quad (\text{C.17b})$$

$$\left. \frac{\partial u_2^{\text{II}}}{\partial x_1} \right|_{x_1=\Delta h} = j A_{\text{I}}^{\text{L}+} \left( -k_{\text{II}}^{\text{L}} \cos \theta_2^{\text{L}} \sin \theta_2^{\text{L}} e^{-j k_{\text{II}}^{\text{L}} \cos \theta_2^{\text{L}} \Delta h} T_{\text{LL}} + k_{\text{II}}^{\text{T}} \cos^2 \theta_2^{\text{T}} e^{-j k_{\text{II}}^{\text{T}} \cos \theta_2^{\text{T}} \Delta h} T_{\text{LT}} \right), \quad (\text{C.17c})$$

$$\left. \frac{\partial u_2^{\text{II}}}{\partial x_2} \right|_{x_1=\Delta h} = jA_{\text{I}}^{\text{L}+} \left( -k_{\text{II}}^{\text{L}} \sin^2 \theta_2^{\text{L}} e^{-jk_{\text{II}}^{\text{L}} \cos \theta_2^{\text{L}} \Delta h} T_{\text{LL}} + k_{\text{II}}^{\text{T}} \cos \theta_2^{\text{T}} \sin \theta_2^{\text{T}} e^{-jk_{\text{II}}^{\text{T}} \cos \theta_2^{\text{T}} \Delta h} T_{\text{LT}} \right). \quad (\text{C.17d})$$

### C.1.3 Application of the boundary conditions

Finally, the boundary conditions between media I and II are applied to obtain the reflection/transmission coefficients  $R_{\text{LL}}$ ,  $R_{\text{LT}}$ ,  $T_{\text{LL}}$  and  $T_{\text{LT}}$ . The transfer matrix  $[L^M]$  introduced in Eq. (C.1) is used to couple the displacements and stresses in medium I (see Sec. C.1.1) evaluated at  $x_1 = 0$  to the displacements and stresses in medium II (see Sec. C.1.2) evaluated at  $x_1 = \Delta h$ , as shown below

$$\begin{bmatrix} u_1^{\text{I}} \\ u_2^{\text{I}} \\ \sigma_{11}^{\text{I}} \\ \sigma_{12}^{\text{I}} \end{bmatrix}_{x_1=0} = \begin{bmatrix} L_{11}^M & L_{12}^M & L_{13}^M & L_{14}^M \\ L_{21}^M & L_{22}^M & L_{23}^M & L_{24}^M \\ L_{31}^M & L_{32}^M & L_{33}^M & L_{34}^M \\ L_{41}^M & L_{42}^M & L_{43}^M & L_{44}^M \end{bmatrix} \begin{bmatrix} u_1^{\text{II}} \\ u_2^{\text{II}} \\ \sigma_{11}^{\text{II}} \\ \sigma_{12}^{\text{II}} \end{bmatrix}_{x_1=\Delta h}. \quad (\text{C.18})$$

The linear system for calculating the reflection/transmission coefficients is determined by replacing the displacements and stresses in Eq. (C.18) by those obtained in Sec. C.1.1 and C.1.2. Then, by rewriting the four equations as a function of  $R_{\text{LL}}$ ,  $R_{\text{LT}}$ ,  $T_{\text{LL}}$  and  $T_{\text{LT}}$ , the linear system to be solved is

$$\begin{bmatrix} V_{11} & V_{12} & V_{13} & V_{14} \\ V_{21} & V_{22} & V_{23} & V_{24} \\ V_{31} & V_{32} & V_{33} & V_{34} \\ V_{41} & V_{42} & V_{43} & V_{44} \end{bmatrix} \begin{bmatrix} R_{\text{LL}} \\ R_{\text{LT}} \\ T_{\text{LL}} \\ T_{\text{LT}} \end{bmatrix} = \begin{bmatrix} \cos \theta_1^{\text{L}} \\ \sin \theta_1^{\text{L}} \\ -jk_{\text{I}}^{\text{L}} (C_{11}^{\text{I}} \cos^2 \theta_1^{\text{L}} + C_{12}^{\text{I}} \sin^2 \theta_1^{\text{L}}) \\ -jC_{66}^{\text{I}} k_{\text{I}}^{\text{L}} \sin (2\theta_1^{\text{L}}) \end{bmatrix}, \quad (\text{C.19})$$

with

$$\begin{aligned} V_{11} &= \cos \theta_1^{\text{L}}, & V_{12} &= -\sin \theta_1^{\text{T}}, \\ V_{21} &= -\sin \theta_1^{\text{L}}, & V_{22} &= -\cos \theta_1^{\text{T}}, \\ V_{31} &= jk_{\text{I}}^{\text{L}} (C_{11}^{\text{I}} \cos^2 \theta_1^{\text{L}} + C_{12}^{\text{I}} \sin^2 \theta_1^{\text{L}}), & V_{32} &= -jk_{\text{I}}^{\text{T}} \sin (2\theta_1^{\text{T}}) \frac{(C_{11}^{\text{I}} - C_{12}^{\text{I}})}{2}, \\ V_{41} &= -jC_{66}^{\text{I}} k_{\text{I}}^{\text{L}} \sin (2\theta_1^{\text{L}}), & V_{42} &= -jC_{66}^{\text{I}} k_{\text{I}}^{\text{T}} \cos (2\theta_1^{\text{T}}), \end{aligned} \quad (\text{C.20})$$

and for  $i = \{1, 2, 3, 4\}$

$$\begin{aligned}
 V_{i3} &= \left[ L_{i1}^M \cos \theta_2^L + L_{i2}^M \sin \theta_2^L - jL_{i3}^M k_{II}^L (C_{11}^{II} \cos^2 \theta_2^L + C_{12}^{II} \sin^2 \theta_2^L) \right. \\
 &\quad \left. - jL_{i4}^M C_{66}^{II} k_{II}^L \sin (2\theta_2^L) \right] e^{-jk_{II}^L \cos \theta_2^L \Delta h}, \\
 V_{i4} &= \left[ L_{i1}^M \sin \theta_2^T - L_{i2}^M \cos \theta_2^T - jL_{i3}^M k_{II}^T \frac{(C_{11}^{II} - C_{12}^{II})}{2} \sin (2\theta_2^T) \right. \\
 &\quad \left. + jL_{i4}^M C_{66}^{II} k_{II}^T \cos (2\theta_2^T) \right] e^{-jk_{II}^T \cos \theta_2^T \Delta h}. \tag{C.21}
 \end{aligned}$$

## C.2 Incident plane wave: transverse polarization

To calculate the reflection/transmission coefficients for an incident plane wave of transverse polarization, the method is similar to the previous one. First, the displacement vector  $\mathbf{u}^I(x_1, x_2, t) = [u_1^I, u_2^I]$  and the stress vector  $\boldsymbol{\sigma}^I(x_1, x_2, t) = [\sigma_{11}^I, \sigma_{12}^I]$  are determined in medium I and evaluated at  $x_1 = 0$  (see Sec. C.2.1). Secondly, the displacement vector  $\mathbf{u}^{II}(x_1, x_2, t)$  and the stress vector  $\boldsymbol{\sigma}^{II}(x_1, x_2, t)$  are determined in medium II and evaluated at  $x_1 = \Delta h$  (see Sec. C.2.2). Thirdly, the boundary conditions are applied with the transfer matrix  $[L^M]$  to find the reflection/transmission coefficients by solving a  $4 \times 4$  linear system (see Sec. C.2.3).

### C.2.1 Displacement/stress vectors in medium I

In medium I, the displacement vector  $\mathbf{u}^I(x_1, x_2, t)$  is equal to

$$\mathbf{u}^I(x_1, x_2, t) = \left( A_I^{T+} e^{-jk_I^{T+} \cdot \mathbf{x}} \mathbf{n}_I^{T+} + A_I^{L-} e^{-jk_I^{L-} \cdot \mathbf{x}} \mathbf{n}_I^{L-} + A_I^{T-} e^{-jk_I^{T-} \cdot \mathbf{x}} \mathbf{n}_I^{T-} \right) e^{j\omega t}, \tag{C.22}$$

with  $A_I^{T+}$  the amplitude of the incident transverse plane wave,  $A_I^{T-}$  the amplitude of the reflected transverse plane wave and  $A_I^{L-}$  the amplitude of the reflected longitudinal plane wave. The associated wave vectors (represented in Fig. C.2) are:

$$\mathbf{k}_I^{T+} = k_I^T \begin{bmatrix} \cos \theta_1^T \\ \sin \theta_1^T \end{bmatrix} \text{ and } \mathbf{n}_I^{T+} = \begin{bmatrix} \sin \theta_1^T \\ -\cos \theta_1^T \end{bmatrix}, \tag{C.23a}$$

$$\mathbf{k}_I^{L-} = k_I^L \mathbf{n}_I^{L-} = k_I^L \begin{bmatrix} -\cos \theta_1^L \\ \sin \theta_1^L \end{bmatrix}, \tag{C.23b}$$

$$\mathbf{k}_I^{T-} = k_I^T \begin{bmatrix} -\cos \theta_1^T \\ \sin \theta_1^T \end{bmatrix} \text{ and } \mathbf{n}_I^{T-} = \begin{bmatrix} \sin \theta_1^T \\ \cos \theta_1^T \end{bmatrix}, \tag{C.23c}$$

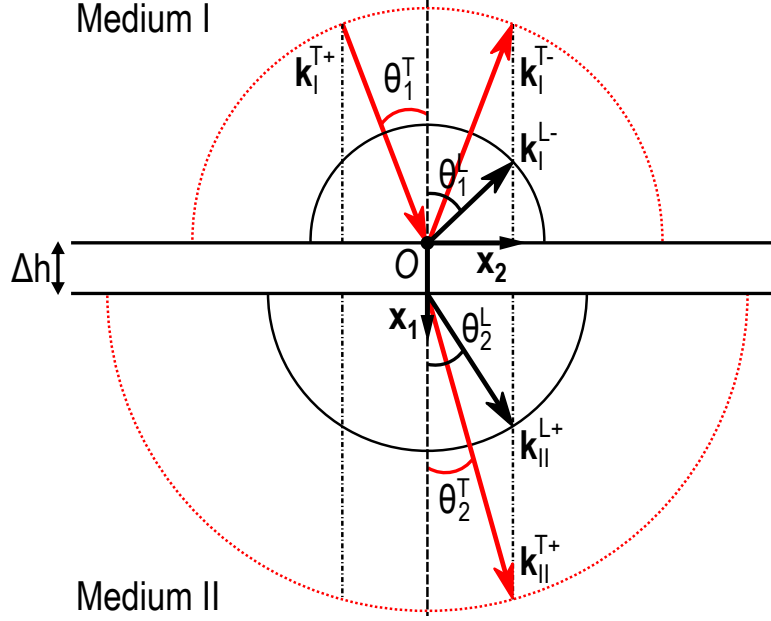


Figure C.2 – Schematic diagram of a transverse plane wave incident on one or more sublayers of total thickness  $\Delta h$  which are located between two semi-infinite media I and II. The wave vectors of the longitudinal (transverse) plane waves are represented with black (red) arrows.

with  $\mathbf{n}_I^{T+}$ ,  $\mathbf{n}_I^{T-}$  and  $\mathbf{n}_I^{L-}$  the polarization vectors of the incident and reflected planes waves. Then, Eq. (C.22) is written as a function of the reflection coefficients  $R_{TT} = \frac{A_I^{T-}}{A_I^{T+}}$  and  $R_{TL} = \frac{A_I^{L-}}{A_I^{T+}}$ :

$$\mathbf{u}^I = A_I^{T+} \left( e^{-jk_I^T \cos \theta_1^T x_1} \mathbf{n}_I^{T+} + R_{TL} e^{jk_I^L \cos \theta_1^L x_1} \mathbf{n}_I^{L-} + R_{TT} e^{jk_I^T \cos \theta_1^T x_1} \mathbf{n}_I^{T-} \right) e^{j(\omega t - k_2 x_2)}. \quad (\text{C.24})$$

According to Snell's laws, the projections of the wave vectors  $\mathbf{k}_I^{T+}$ ,  $\mathbf{k}_I^{T-}$  and  $\mathbf{k}_I^{L-}$  along the  $\mathbf{x}_2$ -axis are equal to

$$k_2 = k_I^L \sin \theta_1^L = k_I^T \sin \theta_1^T. \quad (\text{C.25})$$

## C.2. Incident plane wave: transverse polarization

---

Hence, the angle  $\theta_1^L$ , shown in Fig. C.2, is equal to

$$\begin{cases} \theta_1^L = \arcsin\left(\frac{k_1^T}{k_1^L} \sin \theta_1^T\right), & \text{if } \left|\frac{k_1^T}{k_1^L} \sin \theta_1^T\right| \leq 1, \\ \cos \theta_1^L = j\sqrt{-1 + \left(\frac{k_1^T}{k_1^L} \sin \theta_1^T\right)^2}, & \text{if } \left|\frac{k_1^T}{k_1^L} \sin \theta_1^T\right| \geq 1. \end{cases} \quad (\text{C.26a})$$

$$\quad \quad \quad (\text{C.26b})$$

Next, the stresses  $\sigma_{11}^I$  and  $\sigma_{12}^I$  are obtained with Hooke's law and are evaluated at  $x_1 = 0$ , which gives

$$\sigma_{11}^I|_{x_1=0} = C_{11}^I \frac{\partial u_1^I}{\partial x_1}\Big|_{x_1=0} + C_{12}^I \frac{\partial u_2^I}{\partial x_2}\Big|_{x_1=0}, \quad (\text{C.27a})$$

$$\sigma_{12}^I|_{x_1=0} = C_{66}^I \left( \frac{\partial u_1^I}{\partial x_2}\Big|_{x_1=0} + \frac{\partial u_2^I}{\partial x_1}\Big|_{x_1=0} \right), \quad (\text{C.27b})$$

with the partial derivative terms written below without the  $e^{j(\omega t - k_2 x_2)}$  dependency to lighten the equations

$$\frac{\partial u_1^I}{\partial x_1}\Big|_{x_1=0} = jA_I^{\text{T}+} (-k_1^T \cos \theta_1^T \sin \theta_1^T - k_1^L \cos^2 \theta_1^L R_{\text{TL}} + k_1^T \cos \theta_1^T \sin \theta_1^T R_{\text{TT}}), \quad (\text{C.28a})$$

$$\frac{\partial u_1^I}{\partial x_2}\Big|_{x_1=0} = jA_I^{\text{T}+} (-k_1^T \sin^2 \theta_1^T + k_1^L \cos \theta_1^L \sin \theta_1^L R_{\text{TL}} - k_1^T \sin^2 \theta_1^T R_{\text{TT}}), \quad (\text{C.28b})$$

$$\frac{\partial u_2^I}{\partial x_1}\Big|_{x_1=0} = jA_I^{\text{T}+} (k_1^T \cos^2 \theta_1^T + k_1^L \cos \theta_1^L \sin \theta_1^L R_{\text{TL}} + k_1^T \cos^2 \theta_1^T R_{\text{TT}}), \quad (\text{C.28c})$$

$$\frac{\partial u_2^I}{\partial x_2}\Big|_{x_1=0} = jA_I^{\text{T}+} (k_1^T \cos \theta_1^T \sin \theta_1^T - k_1^L \sin^2 \theta_1^L R_{\text{TL}} - k_1^T \cos \theta_1^T \sin \theta_1^T R_{\text{TT}}). \quad (\text{C.28d})$$

### C.2.2 Displacement/stress vectors in medium II

In medium II, the displacement vector  $\mathbf{u}^{\text{II}}(x_1, x_2, t)$  is equal to

$$\mathbf{u}^{\text{II}}(x_1, x_2, t) = \left( A_{\text{II}}^{\text{L}+} e^{-j\mathbf{k}_{\text{II}}^{\text{L}+} \cdot \mathbf{x}} \mathbf{n}_{\text{II}}^{\text{L}+} + A_{\text{II}}^{\text{T}+} e^{-j\mathbf{k}_{\text{II}}^{\text{T}+} \cdot \mathbf{x}} \mathbf{n}_{\text{II}}^{\text{T}+} \right) e^{j\omega t}, \quad (\text{C.29})$$

with  $A_{\text{II}}^{\text{L}+}$  the amplitude of the transmitted longitudinal plane wave and  $A_{\text{II}}^{\text{T}+}$  the amplitude of the transmitted transverse plane wave. The associated wave vectors (represented in Fig. C.2) are:

$$\mathbf{k}_{\text{II}}^{\text{L}+} = k_{\text{II}}^{\text{L}} \mathbf{n}_{\text{II}}^{\text{L}+} = k_{\text{II}}^{\text{L}} \begin{bmatrix} \cos \theta_2^{\text{L}} \\ \sin \theta_2^{\text{L}} \end{bmatrix}, \quad (\text{C.30a})$$

$$\mathbf{k}_{\text{II}}^{\text{T}+} = k_{\text{II}}^{\text{T}} \begin{bmatrix} \cos \theta_2^{\text{T}} \\ \sin \theta_2^{\text{T}} \end{bmatrix} \quad \text{and} \quad \mathbf{n}_{\text{II}}^{\text{T}+} = \begin{bmatrix} \sin \theta_2^{\text{T}} \\ -\cos \theta_2^{\text{T}} \end{bmatrix}, \quad (\text{C.30b})$$

with  $\mathbf{n}_{\text{II}}^{\text{L}+}$  and  $\mathbf{n}_{\text{II}}^{\text{T}+}$  the polarization vectors of the transmitted longitudinal and transverse planes waves, respectively. Then, Eq. (C.29) is written as a function of the transmission coefficients  $T_{\text{TT}} = \frac{A_{\text{II}}^{\text{T}+}}{A_{\text{I}}^{\text{T}+}}$  and  $T_{\text{TL}} = \frac{A_{\text{II}}^{\text{L}+}}{A_{\text{I}}^{\text{T}+}}$ :

$$\mathbf{u}^{\text{II}} = A_{\text{I}}^{\text{T}+} \left( T_{\text{TL}} e^{-jk_{\text{II}}^{\text{L}} \cos \theta_2^{\text{L}} x_1} \mathbf{n}_{\text{II}}^{\text{L}+} + T_{\text{TT}} e^{-jk_{\text{II}}^{\text{T}} \cos \theta_2^{\text{T}} x_1} \mathbf{n}_{\text{II}}^{\text{T}+} \right) e^{j(\omega t - k_2 x_2)}. \quad (\text{C.31})$$

According to Snell's laws, the projections of the wave vectors  $\mathbf{k}_{\text{II}}^{\text{L}+}$  and  $\mathbf{k}_{\text{II}}^{\text{T}+}$  along the  $\mathbf{x}_2$ -axis are equal to

$$k_2 = k_{\text{II}}^{\text{L}} \sin \theta_2^{\text{L}} = k_{\text{II}}^{\text{T}} \sin \theta_2^{\text{T}} = k_{\text{I}}^{\text{T}} \sin \theta_1^{\text{T}}. \quad (\text{C.32})$$

Hence, the angles  $\theta_2^{\text{L}}$  and  $\theta_2^{\text{T}}$ , shown in Fig. C.2, are equal to

$$\left\{ \begin{array}{l} \theta_2^{\text{L}} = \arcsin \left( \frac{k_{\text{I}}^{\text{T}}}{k_{\text{II}}^{\text{L}}} \sin \theta_1^{\text{T}} \right), \text{ if } \left| \frac{k_{\text{I}}^{\text{T}}}{k_{\text{II}}^{\text{L}}} \sin \theta_1^{\text{T}} \right| \leq 1, \\ \cos \theta_2^{\text{L}} = j \sqrt{-1 + \left( \frac{k_{\text{I}}^{\text{T}}}{k_{\text{II}}^{\text{L}}} \sin \theta_1^{\text{T}} \right)^2}, \text{ if } \left| \frac{k_{\text{I}}^{\text{T}}}{k_{\text{II}}^{\text{L}}} \sin \theta_1^{\text{T}} \right| \geq 1. \end{array} \right. \quad (\text{C.33a})$$

$$\left\{ \begin{array}{l} \theta_2^{\text{T}} = \arcsin \left( \frac{k_{\text{I}}^{\text{T}}}{k_{\text{II}}^{\text{T}}} \sin \theta_1^{\text{T}} \right), \text{ if } \left| \frac{k_{\text{I}}^{\text{T}}}{k_{\text{II}}^{\text{T}}} \sin \theta_1^{\text{T}} \right| \leq 1, \\ \cos \theta_2^{\text{T}} = j \sqrt{-1 + \left( \frac{k_{\text{I}}^{\text{T}}}{k_{\text{II}}^{\text{T}}} \sin \theta_1^{\text{T}} \right)^2}, \text{ if } \left| \frac{k_{\text{I}}^{\text{T}}}{k_{\text{II}}^{\text{T}}} \sin \theta_1^{\text{T}} \right| \geq 1. \end{array} \right. \quad (\text{C.33b})$$

$$\left\{ \begin{array}{l} \theta_2^{\text{L}} = \arcsin \left( \frac{k_{\text{I}}^{\text{T}}}{k_{\text{II}}^{\text{L}}} \sin \theta_1^{\text{T}} \right), \text{ if } \left| \frac{k_{\text{I}}^{\text{T}}}{k_{\text{II}}^{\text{L}}} \sin \theta_1^{\text{T}} \right| \leq 1, \\ \cos \theta_2^{\text{L}} = j \sqrt{-1 + \left( \frac{k_{\text{I}}^{\text{T}}}{k_{\text{II}}^{\text{L}}} \sin \theta_1^{\text{T}} \right)^2}, \text{ if } \left| \frac{k_{\text{I}}^{\text{T}}}{k_{\text{II}}^{\text{L}}} \sin \theta_1^{\text{T}} \right| \geq 1. \end{array} \right. \quad (\text{C.34a})$$

$$\left\{ \begin{array}{l} \theta_2^{\text{T}} = \arcsin \left( \frac{k_{\text{I}}^{\text{T}}}{k_{\text{II}}^{\text{T}}} \sin \theta_1^{\text{T}} \right), \text{ if } \left| \frac{k_{\text{I}}^{\text{T}}}{k_{\text{II}}^{\text{T}}} \sin \theta_1^{\text{T}} \right| \leq 1, \\ \cos \theta_2^{\text{T}} = j \sqrt{-1 + \left( \frac{k_{\text{I}}^{\text{T}}}{k_{\text{II}}^{\text{T}}} \sin \theta_1^{\text{T}} \right)^2}, \text{ if } \left| \frac{k_{\text{I}}^{\text{T}}}{k_{\text{II}}^{\text{T}}} \sin \theta_1^{\text{T}} \right| \geq 1. \end{array} \right. \quad (\text{C.34b})$$

Next, the stresses  $\sigma_{11}^{\text{II}}$  and  $\sigma_{12}^{\text{II}}$  are obtained with Hooke's law and are evaluated at  $x_1 = \Delta h$ , which gives

$$\sigma_{11}^{\text{II}} \Big|_{x_1=\Delta h} = C_{11}^{\text{II}} \frac{\partial u_1^{\text{II}}}{\partial x_1} \Big|_{x_1=\Delta h} + C_{12}^{\text{II}} \frac{\partial u_2^{\text{II}}}{\partial x_2} \Big|_{x_1=\Delta h}, \quad (\text{C.35a})$$

## C.2. Incident plane wave: transverse polarization

---

$$\sigma_{12}^{\text{II}}|_{x_1=\Delta h} = C_{66}^{\text{II}} \left( \frac{\partial u_1^{\text{II}}}{\partial x_2} \Big|_{x_1=\Delta h} + \frac{\partial u_2^{\text{II}}}{\partial x_1} \Big|_{x_1=\Delta h} \right), \quad (\text{C.35b})$$

with the partial derivative terms written below without the  $e^{j(\omega t - k_2 x_2)}$  dependency to lighten the equations

$$\frac{\partial u_1^{\text{II}}}{\partial x_1} \Big|_{x_1=\Delta h} = jA_{\text{I}}^{\text{T}+} \left( -k_{\text{II}}^{\text{L}} \cos^2 \theta_2^{\text{L}} e^{-jk_{\text{II}}^{\text{L}} \cos \theta_2^{\text{L}} \Delta h} T_{\text{TL}} - k_{\text{II}}^{\text{T}} \cos \theta_2^{\text{T}} \sin \theta_2^{\text{T}} e^{-jk_{\text{II}}^{\text{T}} \cos \theta_2^{\text{T}} \Delta h} T_{\text{TT}} \right), \quad (\text{C.36a})$$

$$\frac{\partial u_1^{\text{II}}}{\partial x_2} \Big|_{x_1=\Delta h} = jA_{\text{I}}^{\text{T}+} \left( -k_{\text{II}}^{\text{L}} \cos \theta_2^{\text{L}} \sin \theta_2^{\text{L}} e^{-jk_{\text{II}}^{\text{L}} \cos \theta_2^{\text{L}} \Delta h} T_{\text{TL}} - k_{\text{II}}^{\text{T}} \sin^2 \theta_2^{\text{T}} e^{-jk_{\text{II}}^{\text{T}} \cos \theta_2^{\text{T}} \Delta h} T_{\text{TT}} \right), \quad (\text{C.36b})$$

$$\frac{\partial u_2^{\text{II}}}{\partial x_1} \Big|_{x_1=\Delta h} = jA_{\text{I}}^{\text{T}+} \left( -k_{\text{II}}^{\text{L}} \cos \theta_2^{\text{L}} \sin \theta_2^{\text{L}} e^{-jk_{\text{II}}^{\text{L}} \cos \theta_2^{\text{L}} \Delta h} T_{\text{TL}} + k_{\text{II}}^{\text{T}} \cos^2 \theta_2^{\text{T}} e^{-jk_{\text{II}}^{\text{T}} \cos \theta_2^{\text{T}} \Delta h} T_{\text{TT}} \right), \quad (\text{C.36c})$$

$$\frac{\partial u_2^{\text{II}}}{\partial x_2} \Big|_{x_1=\Delta h} = jA_{\text{I}}^{\text{T}+} \left( -k_{\text{II}}^{\text{L}} \sin^2 \theta_2^{\text{L}} e^{-jk_{\text{II}}^{\text{L}} \cos \theta_2^{\text{L}} \Delta h} T_{\text{TL}} + k_{\text{II}}^{\text{T}} \cos \theta_2^{\text{T}} \sin \theta_2^{\text{T}} e^{-jk_{\text{II}}^{\text{T}} \cos \theta_2^{\text{T}} \Delta h} T_{\text{TT}} \right). \quad (\text{C.36d})$$

### C.2.3 Application of the boundary conditions

Finally, the boundary conditions between media I and II are applied to obtain the reflection/transmission coefficients  $R_{\text{TL}}$ ,  $R_{\text{TT}}$ ,  $T_{\text{TL}}$  and  $T_{\text{TT}}$ . The transfer matrix  $[L^M]$  introduced in Eq. (C.1) is used to couple the displacements and stresses in medium I (see Sec. C.2.1) evaluated at  $x_1 = 0$  to the displacements and stresses in medium II (see Sec. C.2.2) evaluated at  $x_1 = \Delta h$ , as shown below

$$\begin{bmatrix} u_1^{\text{I}} \\ u_2^{\text{I}} \\ \sigma_{11}^{\text{I}} \\ \sigma_{12}^{\text{I}} \end{bmatrix}_{x_1=0} = \begin{bmatrix} L_{11}^M & L_{12}^M & L_{13}^M & L_{14}^M \\ L_{21}^M & L_{22}^M & L_{23}^M & L_{24}^M \\ L_{31}^M & L_{32}^M & L_{33}^M & L_{34}^M \\ L_{41}^M & L_{42}^M & L_{43}^M & L_{44}^M \end{bmatrix} \begin{bmatrix} u_1^{\text{II}} \\ u_2^{\text{II}} \\ \sigma_{11}^{\text{II}} \\ \sigma_{12}^{\text{II}} \end{bmatrix}_{x_1=\Delta h}. \quad (\text{C.37})$$

The linear system for calculating the reflection/transmission coefficients is determined by replacing the displacements and stresses in Eq. (C.37) by those obtained in Sec. C.22 and C.29. Then, by rewriting the four equations as a function of  $R_{\text{TL}}$ ,  $R_{\text{TT}}$ ,  $T_{\text{TL}}$  and  $T_{\text{TT}}$ , the linear system to be solved is

$$\begin{bmatrix} W_{11} & W_{12} & W_{13} & W_{14} \\ W_{21} & W_{22} & W_{23} & W_{24} \\ W_{31} & W_{32} & W_{33} & W_{34} \\ W_{41} & W_{42} & W_{43} & W_{44} \end{bmatrix} \begin{bmatrix} R_{\text{TL}} \\ R_{\text{TT}} \\ T_{\text{TL}} \\ T_{\text{TT}} \end{bmatrix} = \begin{bmatrix} \sin \theta_1^{\text{T}} \\ -\cos \theta_1^{\text{T}} \\ -jk_1^{\text{T}} \frac{(C_{11}^{\text{I}} - C_{12}^{\text{I}})}{2} \sin(2\theta_1^{\text{T}}) \\ jC_{66}^{\text{I}} k_1^{\text{T}} \cos(2\theta_1^{\text{T}}) \end{bmatrix}, \quad (\text{C.38})$$

with

$$\begin{aligned} W_{11} &= \cos \theta_1^{\text{L}}, & W_{12} &= -\sin \theta_1^{\text{T}}, \\ W_{21} &= -\sin \theta_1^{\text{L}}, & W_{22} &= -\cos \theta_1^{\text{T}}, \\ W_{31} &= jk_1^{\text{L}} (C_{11}^{\text{I}} \cos^2 \theta_1^{\text{L}} + C_{12}^{\text{I}} \sin^2 \theta_1^{\text{L}}), & W_{32} &= -jk_1^{\text{T}} \sin(2\theta_1^{\text{T}}) \frac{(C_{11}^{\text{I}} - C_{12}^{\text{I}})}{2}, \\ W_{41} &= -jC_{66}^{\text{I}} k_1^{\text{L}} \sin(2\theta_1^{\text{L}}), & W_{42} &= -jC_{66}^{\text{I}} k_1^{\text{T}} \cos(2\theta_1^{\text{T}}), \end{aligned} \quad (\text{C.39})$$

and for  $i = \{1, 2, 3, 4\}$

$$\begin{aligned} W_{i3} &= \left[ L_{i1}^{\text{M}} \cos \theta_2^{\text{L}} + L_{i2}^{\text{M}} \sin \theta_2^{\text{L}} - jL_{i3}^{\text{M}} k_{\text{II}}^{\text{L}} (C_{11}^{\text{II}} \cos^2 \theta_2^{\text{L}} + C_{12}^{\text{II}} \sin^2 \theta_2^{\text{L}}) \right. \\ &\quad \left. - jL_{i4}^{\text{M}} C_{66}^{\text{II}} k_{\text{II}}^{\text{L}} \sin(2\theta_2^{\text{L}}) \right] e^{-jk_{\text{II}}^{\text{L}} \cos \theta_2^{\text{L}} \Delta h}, \\ W_{i4} &= \left[ L_{i1}^{\text{M}} \sin \theta_2^{\text{T}} - L_{i2}^{\text{M}} \cos \theta_2^{\text{T}} - jL_{i3}^{\text{M}} k_{\text{II}}^{\text{T}} \frac{(C_{11}^{\text{II}} - C_{12}^{\text{II}})}{2} \sin(2\theta_2^{\text{T}}) \right. \\ &\quad \left. + jL_{i4}^{\text{M}} C_{66}^{\text{II}} k_{\text{II}}^{\text{T}} \cos(2\theta_2^{\text{T}}) \right] e^{-jk_{\text{II}}^{\text{T}} \cos \theta_2^{\text{T}} \Delta h}. \end{aligned} \quad (\text{C.40})$$

# Bibliography

- [1] P. Cognard, “Collage des matériaux caractéristiques, mise en œuvre des colles,” *Techniques de l’ingénieur* (2002) [URL link](#), (in French), [Accessed on 10/18/2017]. Cited on p. 7.
- [2] S. Chataigner, “Structural adhesive bonding and composite materials in civil engineering: theoretical contributions and applications,” *Habilitation à diriger des recherches*, Université de Paris-Est, 2016, [URL link](#), (in French), [Accessed on 02/28/2018]. Cited on p. 7.
- [3] L. Dufour, “Characterisation and modelling of multi-materials bonded structures under dynamic loading,” Ph.D. thesis, Université de Valenciennes et du Hainaut-Cambresis, 2017, [URL link](#), (in French), [Accessed on 10/18/2017]. Cited on pp. ix, 8, 12, 13, and 14.
- [4] M.-A. Bruneaux, “Durability of adhesively bonded structures: development of a predictive mechanical modelling taking into account physico-chemical characteristics of the adhesive,” Ph.D. thesis, Ecole des Ponts ParisTech, 2004, [URL link](#), (in French), [Accessed on 10/26/2017]. Cited on p. 8.
- [5] S. Chauffaille, “Durabilité des assemblages collés : aspect mécaniques et physico-chimiques,” Ph.D. thesis, Université de Bordeaux, 2011, [URL link](#), (in French), [Accessed on 10/18/2017]. Cited on pp. 8 and 12.
- [6] D. Maugis and M. Barquins, *Adhésion, Collage et mécanique de la Rupture*, 40–42 (Sasse H.R. (eds) *Adhesion between polymers and concrete*. Springer), doi: 10.1007/978-1-4899-3454-3\_5, (in French). Cited on p. 8.
- [7] J. Cognard, *Science et technologie du collage* (Presses polytechniques et universitaires romandes, 2003), [URL link](#), (in French), [Accessed on 10/18/2017]. Cited on pp. ix, 8, 9, 12, and 13.
- [8] M. Coulaud, “Rôle des interfaces et interphases dans les assemblages collés,” Ph.D. thesis, INSA de Lyon, 2007, [URL link](#), (in French), [Accessed on 10/18/2017]. Cited on p. 8.
- [9] B. Parbhoo, L.-A. O'hare, and S. Leadley, “Fundamental aspects of adhesion technology in silicones,” in *Adhesion Science and Engineering* (Elsevier, 2002), pp. 677–709, doi: 10.1016/b978-044451140-9/50014-7. Cited on p. 8.

- [10] E. Siryabe, “Ultrasonic non-destructive evaluation of the adhesion at the interfaces of bonded joints,” Ph.D. thesis, Université de Bordeaux, 2016, [URL link](#), (in French), [Accessed on 10/17/2017]. Cited on pp. ix, 9, 11, 16, 21, and 22.
- [11] C. C. H. Guyott, P. Cawley, and R. D. Adams, “The non-destructive testing of adhesively bonded structure: a review,” *J. Adhesion* **20**(2), 129–159 (1986) doi: [10.1080/00218468608074943](#). Cited on pp. 9 and 16.
- [12] R. D. Adams and P. Cawley, “A review of defect types and nondestructive testing techniques for composites and bonded joints,” *NDT Int.* **21**(4), 208–222 (1988) doi: [10.1016/0308-9126\(88\)90333-1](#). Cited on pp. 9 and 16.
- [13] R. D. Adams and B. W. Drinkwater, “Non-destructive testing of adhesively-bonded joints,” *Int. J. Mater. Prod. Technol.* **14**(5/6), 385–398 (1999) doi: [10.1504/ijmpt.1999.036279](#). Cited on pp. 9 and 16.
- [14] B. Ehrhart, B. Valeske, and C. Bockenheimer, *Non-destructive evaluation (NDE) of aerospace composites: methods for testing adhesively bonded composites*, 220–237 (Elsevier), doi: [10.1533/9780857093554.2.220](#). Cited on pp. ix, 9, 10, 16, and 18.
- [15] R. L. V. Kumar, M. R. Bhat, and C. R. L. Murthy, “Evaluation of kissing bond in composite adhesive lap joints using digital image correlation: Preliminary studies,” *Int. J. Adhes. Adhes.* **42**, 60–68 (2013) doi: [10.1016/j.ijadhadh.2013.01.004](#). Cited on p. 9.
- [16] D. Jiao and J. L. Rose, “An ultrasonic interface layer model for bond evaluation,” *J. Adhes. Sci. Technol.* **5**(8), 631–646 (1991) doi: [10.1163/156856191X00530](#). Cited on pp. 9, 10, 22, and 100.
- [17] C. Jeenjitkaew, Z. Luklinska, and F. Guild, “Morphology and surface chemistry of kissing bonds in adhesive joints produced by surface contamination,” *Int. J. Adhes. Adhes.* **30**(7), 643–653 (2010) doi: [10.1016/j.ijadhadh.2010.06.005](#). Cited on p. 9.
- [18] P. B. Nagy, “Ultrasonic detection of kissing bonds at adhesive interfaces,” *J. Adhes. Sci. Technol.* **5**(8), 619–630 (1991) doi: [10.1163/156856191X00521](#). Cited on pp. 9 and 22.
- [19] P. B. Nagy, “Ultrasonic classification of imperfect interfaces,” *J. Nondestruct. Eval.* **11**(3-4), 127–139 (1992) doi: [10.1007/BF00566404](#). Cited on pp. 9 and 22.
- [20] M. Wood, P. Charlton, and D. Yan, “Ultrasonic evaluation of artificial kissing bonds in CFRP composites,” *e-J. Non-Destr. Test.* **19**(12), 1–10 (2014) [URL link](#), [Accessed on 11/02/2017]. Cited on p. 9.

- [21] C. J. Brotherhood, B. W. Drinkwater, and F. J. Guild, “The effect of compressive loading on the ultrasonic detectability of kissing bonds in adhesive joints,” *J. Nondestruct. Eval.* **21**(3), 95–104 (2002) doi: [10.1023/A:1022584822730](https://doi.org/10.1023/A:1022584822730). Cited on p. 10.
- [22] N. P. Marty, N. Desai, and J. Andersson, “NDT of kissing bonds in aeronautical structures,” in *16<sup>th</sup> World Conference on NDT* (2004), [URL link](#), [Accessed on 07/30/2020]. Cited on p. 10.
- [23] S. De Barros, “An interface model for the simulation of the behaviour of adhesively bonded joints,” Ph.D. thesis, Université de Versailles-Saint Quentin en Yvelines, 2005, [URL link](#), (in French), [Accessed on 10/18/2017]. Cited on p. 12.
- [24] S. Joannès, “Mechanical characterisation and numerical tool for the design of structural adhesive joints,” Ph.D. thesis, École Nationale Supérieure des Mines de Paris, 2007, [URL link](#), (in French), [Accessed on 03/05/2018]. Cited on p. 12.
- [25] O. Mario, “Etude du vieillissement des assemblages structuraux acier/aluminium : influence de l’environnement sur le dimensionnement,” Ph.D. thesis, École Nationale Supérieure des Mines de Paris, 2007, [URL link](#), (in French), [Accessed on 03/05/2018]. Cited on p. 12.
- [26] E. Gay, “Composite behaviour under laser driven shock : Development of an adhesion test using shock for composite bonded assemblies,” Ph.D. thesis, Ecole Nationale Supérieure d’Arts et Métiers, 2011, [URL link](#), (in French), [Accessed on 03/05/2018]. Cited on p. 12.
- [27] D. M. Gleich, *Stress analysis of structural bonded joints*, 11–47 (Delft University Press), [URL link](#), [Accessed on 03/02/2018]. Cited on p. 12.
- [28] G. C. Mays and A. R. Hutchinson, *Adhesives in Civil Engineering* (Cambridge University Press, 2005), [URL link](#), [Accessed on 03/06/2018]. Cited on pp. 12 and 13.
- [29] J.-A. Petit, Y. Baziard, V. Nassiet, and B. Hassoune-Rhabbour, “Durabilité des assemblages collés - approche prédictive,” *Techniques de l’ingénieur* (2006) [URL link](#), (in French), [Accessed on 10/18/2017]. Cited on pp. ix, 12, and 14.
- [30] M. Arcan, Z. Hashin, and A. Voloshin, “A method to produce uniform plane-stress states with applications to fiber-reinforced materials,” *Exp. Mech.* **18**(4), 141–146 (1978) doi: [10.1007/bf02324146](https://doi.org/10.1007/bf02324146). Cited on pp. 12 and 13.
- [31] F. Fortier and S. Clouet, “Rubans adhésifs,” *Techniques de l’ingénieur* (2011) [URL link](#), (in French), [Accessed on 03/05/2018]. Cited on p. 12.
- [32] D. R. Moore, “An introduction to the special issue on peel testing,” *Int. J. Adhes. Adhes.* **28**(4-5), 153–157 (2008) doi: [10.1016/j.ijadhadh.2007.01.001](https://doi.org/10.1016/j.ijadhadh.2007.01.001). Cited on p. 12.

- [33] K. Kendall, “The adhesion and surface energy of elastic solids,” *J. Phys. D: Appl. Phys.* **4**(8), 1186–1195 (1971) doi: [10.1088/0022-3727/4/8/320](https://doi.org/10.1088/0022-3727/4/8/320). Cited on p. 12.
- [34] J. Destouesse Villa, “Caractérisation et modélisation des joints de colles sous sollicitations bi-axiales statiques,” Ph.D. thesis, ENSTA Bretagne, 2018, [URL link](#), (in French), [Accessed on 10/02/2020]. Cited on p. 13.
- [35] L. Alfonso, C. Badulescu, and N. Carrere, “Use of the modified arcan fixture to study the strength of bonded assemblies for automotive applications,” *Int. J. Adhes. Adhes.* **80**, 104–114 (2018) doi: [10.1016/j.ijadhadh.2017.09.014](https://doi.org/10.1016/j.ijadhadh.2017.09.014). Cited on pp. ix, 13, and 15.
- [36] J. Y. Cognard, P. Davies, B. Gineste, and L. Sohier, “Development of an improved adhesive test method for composite assembly design,” *Compos. Sci. Technol.* **65**(3-4), 359–368 (2005) doi: [10.1016/j.compscitech.2004.09.008](https://doi.org/10.1016/j.compscitech.2004.09.008). Cited on p. 13.
- [37] S. Sassi, M. Tarfaoui, and H. B. Yahia, “An investigation of in-plane dynamic behavior of adhesively-bonded composite joints under dynamic compression at high strain rate,” *Compos. Struct.* **191**, 168–179 (2018) doi: [10.1016/j.compstruct.2018.02.057](https://doi.org/10.1016/j.compstruct.2018.02.057). Cited on p. 14.
- [38] B. Bourel, G. Haugou, F. Lauro, R. Deltombe, D. Lesueur, and B. Bennani, “Modélisation et caractérisation des joints collés à hautes vitesses de déformation,” *MATEC Web Conf.* **7**, 02014 (2013) doi: [10.1051/matecconf/20130702014](https://doi.org/10.1051/matecconf/20130702014), (in French). Cited on p. 14.
- [39] G. Challita and R. Othman, “Finite-element analysis of SHPB tests on double-lap adhesive joints,” *Int. J. Adhes. Adhes.* **30**(4), 236–244 (2010) doi: [10.1016/j.ijadhadh.2010.02.004](https://doi.org/10.1016/j.ijadhadh.2010.02.004). Cited on p. 14.
- [40] A. Janin, “Methodology for characterization and modelling of an adhesive joint under dynamic multiaxial loadings,” Ph.D. thesis, Université Paris-Saclay, 2018, [URL link](#), (in French), [Accessed on 10/02/2020]. Cited on p. 14.
- [41] G. M. Light and H. Kwun, “Nondestructive evaluation of adhesive bond quality: state of the art review,” , Nondestructive Testing Information Analysis Center (NTIAC) (1989), [URL link](#), [Accessed on 03/08/2018]. Cited on p. 16.
- [42] R. D. Adams and B. W. Drinkwater, “Nondestructive testing of adhesively-bonded joints,” *NDT&E Int.* **30**(2), 93–98 (1997) doi: [10.1016/s0963-8695\(96\)00050-3](https://doi.org/10.1016/s0963-8695(96)00050-3). Cited on p. 16.
- [43] M. D. Bode, M. J. Holle, and D. Westlund, “Literature review of weak adhesive bond fabrication and nondestructive inspection for strength measurement,” , U.S. Department of Transportation, Federal Aviation Administration (2015), [URL link](#), [Accessed on 03/08/2018]. Cited on p. 16.

- [44] T. P. Pialucha, “The reflection coefficient from interface layers in NDT of adhesive joints,” Ph.D. thesis, University of London, 1992, [URL link](#), [Accessed on 12/01/2017]. Cited on pp. 16 and 22.
- [45] R. Ecault, “Experimental and numerical investigations on the dynamic behaviour of aeronautic composites under laser shock - Optimization of a shock wave adhesion test for bonded composites,” Ph.D. thesis, ISAE-ENSMA Ecole Nationale Supérieure de Mécanique et d’Aérotechnique - Poitiers, 2013, [URL link](#), [Accessed on 03/08/2018]. Cited on pp. 16 and 18.
- [46] M. Michaloudaki, “An approach to quality assurance of structural adhesive joints,” Ph.D. thesis, Technische Universität München, 2005, [URL link](#), [Accessed on 02/21/2018]. Cited on p. 16.
- [47] H. Lourme, “Etude des assemblages collés par ondes guidées ultrasonores : étude expérimentale et modélisation par éléments finis,” Ph.D. thesis, Université de Bordeaux, 2009, [URL link](#), (in French), [Accessed on 10/25/2017]. Cited on pp. 16 and 25.
- [48] B. Le Crom - Levasseur, “Ultrasonic evaluation of composite patch repair on metallic structures,” Ph.D. thesis, Université de Bordeaux, 2010, [URL link](#), (in French), [Accessed on 10/26/2017]. Cited on pp. 16 and 25.
- [49] A. Baudot, “Etude et mise au point de méthodes de mesures non destructives permettant de caractériser les paramètres critiques de l’adhésion sur structures collées,” Ph.D. thesis, Université Aix-Marseille, 2015, [URL link](#), (in French), [Accessed on 10/04/2017]. Cited on p. 16.
- [50] B. Ehrhart, “Quality assessment of bonded primary CFRP structures by means of laser proof testing,” Ph.D. thesis, Universität Bremen, 2016, [URL link](#), [Accessed on 03/09/2018]. Cited on p. 16.
- [51] P. Zabbal, “Development of a non-destructive ultrasonic inspection device of a bonded structure using a reverberant cavity with time reversal process,” Ph.D. thesis, Université de Bordeaux, 2018, [URL link](#), (in French), [Accessed on 10/02/2020]. Cited on p. 16.
- [52] P. Cawley and R. D. Adams, “The mechanics of the coin-tap method of non-destructive testing,” *J. Sound Vib.* **122**(2), 299–316 (1988) doi: [10.1016/S0022-460X\(88\)80356-0](#). Cited on p. 16.
- [53] R. Schliekelmann, “Non-destructive testing of adhesive bonded metal-to-metal joints 2,” *Non-Destruct. Test.* **5**(3), 144–153 (1972) doi: [10.1016/0029-1021\(72\)90032-1](#). Cited on p. 16.

- [54] C. C. H. Guyott, P. Cawley, and R. D. Adams, “Use of the fokker bond tester on joints with varying adhesive thickness,” *P. I. Mech. Eng. B.-J. Eng.* **201**(1), 41–49 (1987) doi: [10.1243/PIME\\_PROC\\_1987\\_201\\_043\\_02](https://doi.org/10.1243/PIME_PROC_1987_201_043_02). Cited on p. 16.
- [55] A. A. Khalil and A. N. Kagho, “Non-destructive testing of adhesively bonded joints using vibrational analysis,” *Int. J. Adhes. Adhes.* **11**(2), 121–127 (1991) doi: [10.1016/0143-7496\(91\)90038-J](https://doi.org/10.1016/0143-7496(91)90038-J). Cited on p. 16.
- [56] F. Ciampa, P. Mahmoodi, F. P., and M. Meo, “Recent advances in active infrared thermography for non-destructive testing of aerospace components,” *Sensors* **18**(2), 609 (2018) doi: [10.3390/s18020609](https://doi.org/10.3390/s18020609). Cited on p. 17.
- [57] J. Renshaw, J. C. Chen, S. D. Holland, and R. B. Thompson, “The sources of heat generation in vibrothermography,” *NDT&E Int.* **44**(8), 736–739 (2011) doi: [10.1016/j.ndteint.2011.07.012](https://doi.org/10.1016/j.ndteint.2011.07.012). Cited on p. 17.
- [58] B. Hosten, C. Biateau, C. Bacon, C. Pradère, J.-C. Batsale, and A. Meziane, “Sonothermography in composite materials: Finite element modeling and experimental validation,” *NDT&E Int.* **51**, 120–126 (2012) doi: [10.1016/j.ndteint.2012.04.009](https://doi.org/10.1016/j.ndteint.2012.04.009). Cited on p. 17.
- [59] C. Gao, W. Q. Meeker, and D. Mayton, “Detecting cracks in aircraft engine fan blades using vibrothermography nondestructive evaluation,” *Reliab. Eng. Syst. Safe.* **131**, 229–235 (2014) doi: [10.1016/j.ress.2014.05.009](https://doi.org/10.1016/j.ress.2014.05.009). Cited on p. 17.
- [60] L. Zhu and X. Guo, “Vibro-thermography of debonding defects in composite plates,” in *Proceedings of the International Conference on QIRT Asia* (2017), doi: [10.21611/qirt.2017.026](https://doi.org/10.21611/qirt.2017.026). Cited on p. 17.
- [61] J. Rantala, D. Wu, and G. Busse, “Amplitude-modulated lock-in vibrothermography for NDE of polymers and composites,” *Res. Nondestr. Eval.* **7**(4), 215–228 (1996) doi: [10.1080/09349849609409580](https://doi.org/10.1080/09349849609409580). Cited on p. 17.
- [62] V. P. Vavilov and D. D. Burleigh, “Review of pulsed thermal NDT: Physical principles, theory and data processing,” *NDT&E Int.* **73**, 28–52 (2015) doi: [10.1016/j.ndteint.2015.03.003](https://doi.org/10.1016/j.ndteint.2015.03.003). Cited on p. 17.
- [63] J. A. Schroeder, T. Ahmed, B. Chaudhry, and S. Shepard, “Non-destructive testing of structural composites and adhesively bonded composite joints: pulsed thermography,” *Compos. Part A.-Appl. S.* **33**(11), 1511–1517 (2002) doi: [10.1016/S1359-835X\(02\)00139-2](https://doi.org/10.1016/S1359-835X(02)00139-2). Cited on p. 17.
- [64] M. Genest, M. Martinez, N. Mrad, G. Renaud, and A. Fahr, “Pulsed thermography for non-destructive evaluation and damage growth monitoring of bonded repairs,” *Compos. Struct.* **88**(1), 112–120 (2009) doi: [10.1016/j.compstruct.2008.02.010](https://doi.org/10.1016/j.compstruct.2008.02.010). Cited on p. 17.

- [65] P. H. Shin, S. C. Webb, and K. J. Peters, “Pulsed phase thermography imaging of fatigue-loaded composite adhesively bonded joints,” *NDT&E Int.* **79**, 7–16 (2016) doi: [10.1016/j.ndteint.2015.11.008](https://doi.org/10.1016/j.ndteint.2015.11.008). Cited on p. 17.
- [66] C. Meola, G. M. Carlomagno, and G. Giorleo, “Using infrared thermography to analyze substrate and adhesive effects in bonded structures,” *J. Adhes. Sci. Technol.* **18**(6), 617–634 (2004) doi: [10.1163/156856104839301](https://doi.org/10.1163/156856104839301). Cited on p. 17.
- [67] M. Ducouso, S. Bardy, Y. Rouchausse, T. Bergara, F. Jenson, L. Berthe, L. Videau, and N. Cuvillier, “Quantitative evaluation of the mechanical strength of titanium/composite bonding using laser-generated shock waves,” *Appl. Phys. Lett.* **112**(11), 111904 (2018) doi: [10.1063/1.5020352](https://doi.org/10.1063/1.5020352). Cited on pp. 18, 39, 85, 97, and 100.
- [68] L. Berthe, M. Arrigoni, M. Boustie, J. P. Cuq-Lelandais, C. Broussillou, G. Fabre, M. Jeandin, V. Guipont, and M. Nivard, “State-of-the-art laser adhesion test (LASAT),” *Nondestruct. Test. Eva.* **26**(3-4), 303–317 (2011) doi: [10.1080/10589759.2011.573550](https://doi.org/10.1080/10589759.2011.573550). Cited on pp. ix, 18, 19, and 97.
- [69] G. Fabre, “Influence of optical properties and of the damaging of EB-PVD thermal barrier coatings for the measurement of adhesion by laser shock LASAT-2D,” Ph.D. thesis, Ecole Nationale Supérieure des Mines de Paris, 2013, [URL link](#), (in French), [Accessed on 10/02/2020]. Cited on p. 18.
- [70] S. Bardy, “Control and optimization of laser shock adhesion test on bonded assemblies,” Ph.D. thesis, Ecole Nationale Supérieure des Arts de Métiers, 2017, [URL link](#), (in French), [Accessed on 07/30/2020]. Cited on p. 18.
- [71] M. V. Rao, R. Samuel, and K. Ramesh, “Dual vacuum stressing technique for holographic nondestructive testing of honeycomb sandwich panels,” *NDT Int.* **23**(5), 267–270 (1990) doi: [10.1016/0308-9126\(90\)92153-r](https://doi.org/10.1016/0308-9126(90)92153-r). Cited on p. 18.
- [72] B. Liu, X. Guo, G. Qi, and D. Zhang, “Quality evaluation of rubber-to-metal bonded structures based on shearography,” *Sci. China Phys. Mech.* **58**(7), 1–8 (2015) doi: [10.1007/s11433-015-5658-7](https://doi.org/10.1007/s11433-015-5658-7). Cited on p. 18.
- [73] M. G. Droubi, N. H. Faisal, A. Stuart, J. Mowat, C. Nobel, and M. N. El-Shaib, “Acoustic emission testing of composite-to-metal and metal-to-metal adhesive bond strengths,” in *Proceedings of the 32<sup>nd</sup> European conference on acoustic emission testing*, Prague, Czech Republic. (2016), pp. 95–104, [URL link](#), [Accessed on 03/08/2018]. Cited on p. 18.
- [74] H. A. Jama, E. M. A. Hussein, and P. Lee-Sullivan, “Detection of debonding in composite-aluminum joints using gamma-ray compton scattering,” *NDT&E Int.* **31**(2), 99–103 (1998) doi: [10.1016/s0963-8695\(97\)00029-7](https://doi.org/10.1016/s0963-8695(97)00029-7). Cited on p. 19.

- [75] D. Vavrik, I. Jeon, E. Lehmann, A. Kaestner, and J. Vacik, “Inspection of the metal composite materials using a combination of X-ray radiography and Neutron imaging,” *J. Instrum.* **6**(03), C03001 (2011) doi: [10.1088/1748-0221/6/03/C03001](https://doi.org/10.1088/1748-0221/6/03/C03001). Cited on p. 19.
- [76] H. G. Tattersall, “The ultrasonic pulse-echo technique as applied to adhesion testing,” *J. Phys. D: Appl. Phys.* **6**(7), 819–832 (1973) doi: [10.1088/0022-3727/6/7/305](https://doi.org/10.1088/0022-3727/6/7/305). Cited on pp. 20 and 97.
- [77] F. H. Chang, P. L. Flynn, D. E. Gordon, and J. R. Bell, “Principles and application of ultrasonic spectroscopy in NDE of adhesive bonds,” *IEEE T. Son. Ultrason.* **23**(5), 334–338 (1976) doi: [10.1109/t-su.1976.30887](https://doi.org/10.1109/t-su.1976.30887). Cited on pp. 20, 21, and 97.
- [78] R. E. Challis, R. J. Freemantle, G. P. Wilkinson, and J. D. H. White, “Compression wave NDE of adhered metal lap joints: uncertainties and echo feature extraction,” *Ultrasonics* **34**(2-5), 315–319 (1996) doi: [10.1016/0041-624x\(95\)00116-k](https://doi.org/10.1016/0041-624x(95)00116-k). Cited on p. 20.
- [79] S. A. Titov, R. G. Maev, and A. N. Bogachenkov, “Pulse-echo NDT of adhesively bonded joints in automotive assemblies,” *Ultrasonics* **48**(6-7), 537–546 (2008) doi: [10.1016/j.ultras.2008.07.001](https://doi.org/10.1016/j.ultras.2008.07.001). Cited on p. 20.
- [80] B. Mojškerč, T. Kek, and J. Grum, “Pulse-echo ultrasonic testing of adhesively bonded joints in glass façades,” *Stroj. Vestn.-J. Mech. E.* **62**(3), 147–153 (2016) doi: [10.5545/sv-jme.2015.2988](https://doi.org/10.5545/sv-jme.2015.2988). Cited on pp. 20 and 21.
- [81] E. Siryabe, M. Rénier, A. Meziane, J. Galy, and M. Castaings, “Apparent anisotropy of adhesive bonds with weak adhesion and non-destructive evaluation of interfacial properties,” *Ultrasonics* **79**, 34–51 (2017) doi: [10.1016/j.ultras.2017.02.020](https://doi.org/10.1016/j.ultras.2017.02.020). Cited on pp. ix, 21, 22, 40, and 97.
- [82] W.-L. Wu, X.-G. Wang, Z.-C. Huang, and N.-X. Wu, “Measurements of the weak bonding interfacial stiffness by using air-coupled ultrasound,” *AIP Adv.* **7**(12), 125316 (2017) doi: [10.1063/1.5001248](https://doi.org/10.1063/1.5001248). Cited on pp. 21 and 97.
- [83] S. I. Rokhlin and D. Marom, “Study of adhesive bonds using low-frequency obliquely incident ultrasonic waves,” *J. Acoust. Soc. Am.* **80**(2), 585–590 (1986) doi: [10.1121/1.394053](https://doi.org/10.1121/1.394053). Cited on p. 22.
- [84] A. Pilarski and J. L. Rose, “Ultrasonic oblique incidence for improved sensitivity in interface weakness determination,” *NDT Int.* **21**(4), 241–246 (1988) doi: [10.1016/0308-9126\(88\)90337-9](https://doi.org/10.1016/0308-9126(88)90337-9). Cited on p. 22.
- [85] A. Pilarski and J. L. Rose, “A transverse-wave ultrasonic oblique-incidence technique for interfacial weakness detection in adhesive bonds,” *J. Appl. Phys.* **63**(2), 300–307 (1988) doi: [10.1063/1.340294](https://doi.org/10.1063/1.340294). Cited on pp. 22 and 97.

- [86] W. Wang and S. I. Rokhlin, “Evaluation of interfacial properties in adhesive joints of aluminum alloys using angle-beam ultrasonic spectroscopy,” *J. Adhes. Sci. Technol.* **5**(8), 647–666 (1991) doi: [10.1163/156856191x00549](https://doi.org/10.1163/156856191x00549). Cited on p. 22.
- [87] D. Lévesque, A. Legros, A. Michel, and L. Piché, “High resolution ultrasonic interferometry for quantitative nondestructive characterization of interfacial adhesion in multilayer (metal/polymer/metal) composites,” *J. Adhes. Sci. Technol.* **7**(7), 719–741 (1993) doi: [10.1163/156856193x00385](https://doi.org/10.1163/156856193x00385). Cited on p. 22.
- [88] S. I. Rokhlin, A. I. Lavrentyev, and B. Li, “Ultrasonic evaluation of environmental durability of adhesive joints,” *Res. Nondestr. Eval.* **5**(2), 95–109 (1993) doi: [10.1080/09349849309409545](https://doi.org/10.1080/09349849309409545). Cited on p. 22.
- [89] A. K. Moidu, A. N. Sinclair, and J. K. Spelt, “A new ultrasonic technique for the interfacial characterization of adhesive joints,” in *IEEE Ultrasonics Symposium*, IEEE (1996), pp. 757–760, doi: [10.1109/ultsym.1996.584083](https://doi.org/10.1109/ultsym.1996.584083). Cited on p. 22.
- [90] A. I. Lavrentyev and S. I. Rokhlin, “Determination of elastic moduli, density, attenuation, and thickness of a layer using ultrasonic spectroscopy at two angles,” *J. Acoust. Soc. Am.* **102**(6), 3467–3477 (1997) doi: [10.1121/1.420394](https://doi.org/10.1121/1.420394). Cited on p. 22.
- [91] A. I. Lavrentyev and S. I. Rokhlin, “Ultrasonic spectroscopy of imperfect contact interfaces between a layer and two solids,” *J. Acoust. Soc. Am.* **103**(2), 657–664 (1998) doi: [10.1121/1.423235](https://doi.org/10.1121/1.423235). Cited on p. 22.
- [92] A. K. Moidu, A. N. Sinclair, and J. K. Spelt, “Nondestructive characterization of adhesive joint durability using ultrasonic reflection measurements,” *Res. Nondestr. Eval.* **11**(2), 81–95 (1999) doi: [10.1080/09349849909409638](https://doi.org/10.1080/09349849909409638). Cited on p. 22.
- [93] L. Wang, B. Xie, and S. I. Rokhlin, “Determination of embedded layer properties using adaptive time-frequency domain analysis,” *J. Acoust. Soc. Am.* **111**(6), 2644–2653 (2002) doi: [10.1121/1.1473634](https://doi.org/10.1121/1.1473634). Cited on p. 22.
- [94] A. Baltazar, L. Wang, B. Xie, and S. I. Rokhlin, “Inverse ultrasonic determination of imperfect interfaces and bulk properties of a layer between two solids,” *J. Acoust. Soc. Am.* **114**(3), 1424–1434 (2003) doi: [10.1121/1.1600723](https://doi.org/10.1121/1.1600723). Cited on pp. 22 and 97.
- [95] S. I. Rokhlin, M. Hefets, and M. Rosen, “An ultrasonic interface-wave method for predicting the strength of adhesive bonds,” *J. Appl. Phys.* **52**(4), 2847–2851 (1981) doi: [10.1063/1.329016](https://doi.org/10.1063/1.329016). Cited on p. 24.
- [96] L. Singher, “Bond strength measurement by ultrasonic guided waves,” *Ultrasonics* **35**(4), 305–315 (1997) doi: [10.1016/s0041-624x\(96\)00109-6](https://doi.org/10.1016/s0041-624x(96)00109-6). Cited on pp. ix and 24.

- [97] B. Le Crom and M. Castaings, “Inferring shear stiffness of adhesive bonds using SH guided ultrasonic waves,” in *10ème Congrès Français d’Acoustique*, Lyon, France (2010), [URL link](#), [Accessed on 10/18/2017]. Cited on p. 25.
- [98] B. Le Crom and M. Castaings, “Shear horizontal guided wave modes to infer the shear stiffness of adhesive bond layers,” *J. Acoust. Soc. Am.* **127**(4), 2220–2230 (2010) doi: [10.1121/1.3309441](#). Cited on pp. ix, 25, 26, and 97.
- [99] M. Castaings, “SH ultrasonic guided waves for the evaluation of interfacial adhesion,” *Ultrasonics* **54**(7), 1760–1775 (2014) doi: [10.1016/j.ultras.2014.03.002](#). Cited on pp. 25 and 97.
- [100] T. Kundu, A. Maji, T. Ghosh, and K. Maslov, “Detection of kissing bonds by Lamb waves,” *Ultrasonics* **35**(8), 573–580 (1998) doi: [10.1016/s0041-624x\(97\)00095-4](#). Cited on p. 26.
- [101] N. Mori, S. Biwa, and T. Hayashi, “Reflection and transmission of Lamb waves at an imperfect joint of plates,” *J. Appl. Phys.* **113**(7), 074901 (2013) doi: [10.1063/1.4791711](#). Cited on p. 26.
- [102] N. Mori and S. Biwa, “Transmission of Lamb waves and resonance at an adhesive butt joint of plates,” *Ultrasonics* **72**, 80–88 (2016) doi: [10.1016/j.ultras.2016.07.013](#). Cited on p. 26.
- [103] E. Siryabe, M. Renier, A. Meziane, and M. Castaings, “The transmission of Lamb waves across adhesively bonded lap joints to evaluate interfacial adhesive properties,” *Physcs. Proc.* **70**, 541–544 (2015) doi: [10.1016/j.phpro.2015.08.012](#). Cited on p. 26.
- [104] C. Gauthier, M. E.-C. El-Kettani, J. Galy, M. Predoi, D. Leduc, and J.-L. Izbicki, “Lamb waves characterization of adhesion levels in aluminum/epoxy bi-layers with different cohesive and adhesive properties,” *Int. J. Adhes. Adhes.* **74**, 15–20 (2017) doi: [10.1016/j.ijadhadh.2016.12.002](#). Cited on p. 27.
- [105] R. Seifried, L. J. Jacobs, and J. Qu, “Propagation of guided waves in adhesive bonded components,” *NDT&E Int.* **35**(5), 317–328 (2002) doi: [10.1016/s0963-8695\(01\)00056-1](#). Cited on pp. 27 and 97.
- [106] M. J. S. Lowe and P. Cawley, “The applicability of plate wave techniques for the inspection of adhesive and diffusion bonded joints,” *J. Nondestr. Eval.* **13**(4), 185–200 (1994) doi: [10.1007/BF00742584](#). Cited on p. 27.
- [107] P. B. Nagy and L. Adler, “Nondestructive evaluation of adhesive joints by guided waves,” *J. Appl. Phys.* **66**(10), 4658–4663 (1989) doi: [10.1063/1.343822](#). Cited on p. 27.

- [108] J. M. Allin, “Disbond detection in adhesive joints using low-frequency ultrasound,” Ph.D. thesis, University of London, 2002, [URL link](#), [Accessed on 12/01/2017]. Cited on p. 27.
- [109] P. N. Dewen, “The non-destructive evaluation of the cohesive properties of adhesively bonded joints,” Ph.D. thesis, Imperial College London, 1991, [URL link](#), [Accessed on 03/20/2018]. Cited on p. 27.
- [110] H. Cho, Y. Yaguchi, and H. Ito, “Characterization of the bond quality of adhesive plates utilizing zero-group-velocity Lamb waves measured by a laser ultrasonics technique,” *Mech. Eng. J.* **2**(1), 14–00335–14–00335 (2015) doi: [10.1299/mej.14-00335](#). Cited on p. 27.
- [111] S. Mezil, J. Laurent, D. Royer, and C. Prada, “Non contact probing of interfacial stiffnesses between two plates by zero-group velocity Lamb modes,” *Appl. Phys. Lett.* **105**(2), 021605 (2014) doi: [10.1063/1.4890110](#). Cited on pp. 28 and 97.
- [112] S. Mezil, F. Bruno, S. Raetz, J. Laurent, D. Royer, and C. Prada, “Investigation of interfacial stiffnesses of a tri-layer using zero-group velocity Lamb modes,” *J. Acoust. Soc. Am.* **138**(5), 3202–3209 (2015) doi: [10.1121/1.4934958](#). Cited on pp. ix, 28, 29, 40, 92, 97, and 99.
- [113] F. Bruno, “Optimisation des modes de Lamb à vitesse de groupe nulle engendrés par laser et évaluation locale de structures collées,” Ph.D. thesis, Université Paris Diderot, 2016, [URL link](#), (in French), [Accessed on 03/12/2018]. Cited on p. 28.
- [114] V. Vlasie and M. Rousseau, “Acoustical validation of the rheological models for a structural bond,” *Wave Motion* **37**(4), 333–349 (2003) doi: [10.1016/s0165-2125\(02\)00092-6](#). Cited on pp. ix, 29, 92, and 98.
- [115] A. Saidoun, “Numerical and experimental analysis of the nonlinear interaction acoustic wave/fatigue crack by using the higher harmonics method,” Ph.D. thesis, Université de Bordeaux, 2017, [URL link](#), (in French), [Accessed on 10/20/2017]. Cited on p. 29.
- [116] I. Y. Solodov, N. Krohn, and G. Busse, “CAN: an example of nonclassical acoustic nonlinearity in solids,” *Ultrasonics* **40**(1-8), 621–625 (2002) doi: [10.1016/s0041-624x\(02\)00186-5](#). Cited on p. 29.
- [117] T. P. Berndt and R. E. Green, “A nonlinear ultrasonic approach to evaluate adhesive bond cure conditions,” *AIP Conf. Proc.* **497**(1), 394–399 (1999) doi: [10.1063/1.1302033](#). Cited on p. 30.
- [118] C. J. Brotherhood, B. W. Drinkwater, and S. Dixon, “The detectability of kissing bonds in adhesive joints using ultrasonic techniques,” *Ultrasonics* **41**(7), 521–529 (2003) doi: [10.1016/s0041-624x\(03\)00156-2](#). Cited on pp. 30 and 31.

- [119] D. Yan, B. W. Drinkwater, and S. A. Neild, “Measurement of the ultrasonic nonlinearity of kissing bonds in adhesive joints,” *NDT&E Int.* **42**(5), 459–466 (2009) doi: [10.1016/j.ndteint.2009.02.002](https://doi.org/10.1016/j.ndteint.2009.02.002). Cited on pp. x, 30, and 31.
- [120] S. Liu, A. J. Croxford, S. A. Neild, and Z. Zhou, “Effects of experimental variables on the nonlinear harmonic generation technique,” *IEEE T. Ultrason. Ferr.* **58**(7), 1442–1451 (2011) doi: [10.1109/tuffc.2011.1963](https://doi.org/10.1109/tuffc.2011.1963). Cited on p. 30.
- [121] G. Shui, Y.-S. Wang, P. Huang, and J. Qu, “Nonlinear ultrasonic evaluation of the fatigue damage of adhesive joints,” *NDT&E Int.* **70**, 9–15 (2015) doi: [10.1016/j.ndteint.2014.11.002](https://doi.org/10.1016/j.ndteint.2014.11.002). Cited on pp. x, 31, and 32.
- [122] S. Biwa and Y. Ishii, “Second-harmonic generation in an infinite layered structure with nonlinear spring-type interfaces,” *Wave Motion* **63**, 55–67 (2016) doi: [10.1016/j.wavemoti.2016.01.004](https://doi.org/10.1016/j.wavemoti.2016.01.004). Cited on p. 32.
- [123] Y. Ishii, S. Biwa, and T. Adachi, “Second-harmonic generation in a multilayered structure with nonlinear spring-type interfaces embedded between two semi-infinite media,” *Wave Motion* **76**, 28–41 (2018) doi: [10.1016/j.wavemoti.2017.07.009](https://doi.org/10.1016/j.wavemoti.2017.07.009). Cited on p. 32.
- [124] D. Yun, J. Kim, and K.-Y. Jhang, “Imaging of contact acoustic nonlinearity using synthetic aperture technique,” *Ultrasonics* **53**(7), 1349–1354 (2013) doi: [10.1016/j.ultras.2013.04.002](https://doi.org/10.1016/j.ultras.2013.04.002). Cited on p. 33.
- [125] J. N. Potter, A. J. Croxford, and P. D. Wilcox, “Nonlinear ultrasonic phased array imaging,” *Phys. Rev. Lett.* **113**(14), 144301 (2014) doi: [10.1103/physrevlett.113.144301](https://doi.org/10.1103/physrevlett.113.144301). Cited on pp. x and 33.
- [126] P. Zabbal, G. Ribay, and J. Jumel, “Nonlinear ultrasound for nondestructive evaluation of adhesive joints,” *AIP Conf. Proc.* **2102**(1), 020030 (2019) doi: [10.1063/1.5099734](https://doi.org/10.1063/1.5099734). Cited on pp. x, 34, 97, and 120.
- [127] Z. Zhang, P. B. Nagy, and W. Hassan, “Analytical and numerical modeling of non-collinear shear wave mixing at an imperfect interface,” *Ultrasonics* **65**, 165–176 (2016) doi: [10.1016/j.ultras.2015.09.021](https://doi.org/10.1016/j.ultras.2015.09.021). Cited on pp. x, 35, and 36.
- [128] E. Escobar-Ruiz, A. Ruiz, W. Hassan, D. C. Wright, I. J. Collison, P. Cawley, and P. B. Nagy, “Non-linear ultrasonic NDE of titanium diffusion bonds,” *J. Nondestr. Eval.* **33**(2), 187–195 (2014) doi: [10.1007/s10921-013-0217-5](https://doi.org/10.1007/s10921-013-0217-5). Cited on p. 35.
- [129] A. J. Croxford, P. D. Wilcox, B. W. Drinkwater, and P. B. Nagy, “The use of non-collinear mixing for nonlinear ultrasonic detection of plasticity and fatigue,” *J. Acoust. Soc. Am.* **126**(5), EL117–EL122 (2009) doi: [10.1121/1.3231451](https://doi.org/10.1121/1.3231451). Cited on p. 35.

- [130] P. Blanloeuil, “Analysis of the contact acoustic nonlinearity for nondestructive evaluation,” Ph.D. thesis, Université de Bordeaux, 2013, [URL link](#), (in French), [Accessed on 03/21/2018]. Cited on p. 35.
- [131] A. Demčenko, L. Mainini, and V. A. Korneev, “A study of the noncollinear ultrasonic-wave-mixing technique under imperfect resonance conditions,” *Ultrasonics* **57**, 179–189 (2015) doi: [10.1016/j.ultras.2014.11.009](#). Cited on p. 35.
- [132] T. Ju, J. D. Achenbach, L. J. Jacobs, and J. Qu, “A non-collinear mixing technique to measure the acoustic nonlinearity parameter of an adhesive bond from one side of the sample,” *AIP Conf. Proc.* **1806**(1), 020011 (2017) doi: [10.1063/1.4974552](#). Cited on p. 35.
- [133] S. Mezil, “Nonlinear optoacoustics method for crack detection and characterization,” Ph.D. thesis, Université du Maine, 2012, [URL link](#), [Accessed on 10/13/2017]. Cited on pp. x, 36, and 37.
- [134] S. Mezil, N. Chigarev, V. Tournat, and V. Gusev, “Evaluation of crack parameters by a nonlinear frequency-mixing laser ultrasonics method,” *Ultrasonics* **69**, 225–235 (2016) doi: [10.1016/j.ultras.2016.04.005](#). Cited on pp. 36 and 109.
- [135] D. M. Donskoy and A. M. Sutin, “Detection and characterization of defects with vibro-acoustic modulation technique,” *J. Intell. Mater. Syst. Struct.* **9**(9), 765–771 (1999) doi: [10.1177/1045389x9800900909](#). Cited on p. 37.
- [136] T. Goursolle, “Propriétés acoustiques non linéaires classiques et non classiques : Applications au contrôle de santé des matériaux de l’industrie aéronautique,” Ph.D. thesis, Université François Rabelais - Tours, 2007, [URL link](#), (in French), [Accessed on 03/21/2018]. Cited on pp. x, 37, and 38.
- [137] S. I. Rokhlin, L. Wang, B. Xie, V. A. Yakovlev, and L. Adler, “Frequency modulated dual angle ultrasonic spectroscopy of adhesive bonds,” *AIP Conf. Proc.* **760**(1), 393 – 400 (2005) doi: [10.1063/1.1916703](#). Cited on pp. x, 38, and 39.
- [138] V. Gusev and A. Karabutov, *Laser Optoacoustics* (American Inst. of Physics, 1993). Cited on p. 43.
- [139] D. Royer and E. Dieulesaint, *Elastic Waves in Solids II: Generation, Acousto-optic Interaction, Applications*, Advanced Texts in Physics, 1 ed. (Springer, 2000). Cited on p. 43.
- [140] R. M. White, “Generation of elastic waves by transient surface heating,” *J. Appl. Phys.* **34**(12), 3559–3567 (1963) doi: [10.1063/1.1729258](#). Cited on p. 43.
- [141] C. B. Scruby, R. J. Dewhurst, D. A. Hutchins, and S. B. Palmer, “Quantitative studies of thermally generated elastic waves in laser-irradiated metals,” *J. Appl. Phys.* **51**(12), 6210–6216 (1980) doi: [10.1063/1.327601](#). Cited on pp. 43 and 80.

- [142] L. R. F. Rose, “Point-source representation for laser-generated ultrasound,” *J. Acoust. Soc. Am.* **75**(3), 723–732 (1984) doi: [10.1121/1.390583](https://doi.org/10.1121/1.390583). Cited on p. 43.
- [143] M. Dubois, F. Enguehard, and L. Bertrand, “Analytical one-dimensional model to study the ultrasonic precursor generated by a laser,” *Phys. Rev. E* **50**(2), 1548–1551 (1994) doi: [10.1103/PhysRevE.50.1548](https://doi.org/10.1103/PhysRevE.50.1548). Cited on p. 43.
- [144] R. Coulette, E. Lafond, M.-H. Nadal, C. Gondard, F. Lepoutre, and O. Pétillon, “Laser-generated ultrasound applied to two layered materials characterization: semi-analytical model and experimental validation,” *Ultrasonics* **36**(1-5), 239–243 (1998) doi: [10.1016/S0041-624X\(97\)00060-7](https://doi.org/10.1016/S0041-624X(97)00060-7). Cited on p. 43.
- [145] T. W. Murray, S. Krishnaswamy, and J. D. Achenbach, “Laser generation of ultrasound in films and coatings,” *Appl. Phys. Lett.* **74**(23), 3561–3563 (1999) doi: [10.1063/1.124161](https://doi.org/10.1063/1.124161). Cited on p. 43.
- [146] A. Cheng, T. W. Murray, and J. D. Achenbach, “Simulation of laser-generated ultrasonic waves in layered plates,” *J. Acoust. Soc. Am.* **110**(2), 848–855 (2001) doi: [10.1121/1.1381536](https://doi.org/10.1121/1.1381536). Cited on p. 43.
- [147] W. T. Thomson, “Transmission of elastic waves through a stratified solid medium,” *J. Appl. Phys.* **21**(2), 89–93 (1950) doi: [10.1063/1.1699629](https://doi.org/10.1063/1.1699629). Cited on pp. 43, 73, 76, 165, and 173.
- [148] B. Audoin and S. Guilbaud, “Acoustic waves generated by a line source in a viscoelastic anisotropic medium,” *Appl. Phys. Lett.* **72**(7), 774–776 (1998) doi: [10.1063/1.120889](https://doi.org/10.1063/1.120889). Cited on pp. 43 and 75.
- [149] H. Meri, “Rayonnement d’ultrasons générés par laser dans les matériaux anisotropes : effets de la pénétration optique, de la diffusion de la chaleur et de la diffusion de la densité électronique,” Ph.D. thesis, Université Bordeaux I, 2004, [URL link](#), (in French), [Accessed on 03/21/2018]. Cited on p. 43.
- [150] M. Perton, “Ultrasounds radiated by a laser point source in transverse isotropic media. Applications to the stiffness tensor measurement of cylinders and thin layers,” Ph.D. thesis, Université Bordeaux I, 2006, [URL link](#), (in French), [Accessed on 03/21/2018]. Cited on pp. 43, 55, 60, 145, 147, and 156.
- [151] S. Raetz, “Development of numerical methods for the imaging of optoacoustic sources in solid media,” Ph.D. thesis, Université Bordeaux I, 2012, [URL link](#), (in French), [Accessed on 03/21/2018]. Cited on pp. xiv, xvi, 43, 120, 131, and 147.
- [152] Z. Shen, B. Xu, X. Ni, and J. Lu, “Numerical simulation of laser-generated ultrasonic waves in layered plates,” *J. Phys. D: Appl. Phys.* **37**(17), 2364–2370 (2004) doi: [10.1088/0022-3727/37/17/004](https://doi.org/10.1088/0022-3727/37/17/004). Cited on pp. 43 and 75.

- [153] G. Yan, S. Raetz, N. Chigarev, J. Blondeau, V. E. Gusev, and V. Tournat, “Cumulative fatigue damage in thin aluminum films evaluated non-destructively with lasers via zero-group-velocity Lamb modes,” *NDT&E Int.* **116**, 102323 (2020) doi: [10.1016/j.ndteint.2020.102323](https://doi.org/10.1016/j.ndteint.2020.102323). Cited on pp. 43 and 75.
- [154] I. A. Veres, T. Berer, and P. Burgholzer, “Numerical modeling of thermoelastic generation of ultrasound by laser irradiation in the coupled thermoelasticity,” *Ultrasonics* **53**(1), 141–149 (2013) doi: [10.1016/j.ultras.2012.05.001](https://doi.org/10.1016/j.ultras.2012.05.001). Cited on pp. 43 and 75.
- [155] M. Born and E. Wolf, *Principles of Optics : Electromagnetic Theory of Propagation, Interference and Diffraction of Light [7th (expanded) edition]* (Cambridge University Press, 1999). Cited on pp. 46, 47, 136, 137, 139, and 140.
- [156] J. Singh, ed., *Optical Properties of Materials and Their Applications* (Wiley, 2019). Cited on pp. 47 and 137.
- [157] L. M. Brekhovskikh, *Waves in Layered Media (Second Edition)*, Applied mathematics and mechanics 16 (Academic Press, Elsevier, 1980). Cited on pp. 48, 60, 73, 76, 140, 150, 161, 165, 166, and 173.
- [158] S. Raetz, T. Dehoux, and B. Audoin, “Effect of laser beam incidence angle on the thermoelastic generation in semi-transparent materials,” *J. Acoust. Soc. Am.* **130**(6), 3691–3697 (2011) doi: [10.1121/1.3658384](https://doi.org/10.1121/1.3658384). Cited on pp. 49, 50, 52, and 138.
- [159] D. W. Hahn and M. N. Özışik, *Heat Conduction (Third Edition)* (John Wiley & Sons, Inc., 2012). Cited on p. 54.
- [160] M. Bouchon and K. Aid, “Near-field of a seismic source in a layered medium with irregular interfaces,” *Geophys. J. Int.* **50**, 669–684 (1977) doi: [10.1111/j.1365-246x.1977.tb01340.x](https://doi.org/10.1111/j.1365-246x.1977.tb01340.x). Cited on p. 60.
- [161] R. L. Weaver, W. Sachse, and L. Niu, “Transient ultrasonic waves in a viscoelastic plate: Applications to materials characterization,” *J. Acoust. Soc. Am.* **85**(6), 2262–2267 (1989) doi: [10.1121/1.397771](https://doi.org/10.1121/1.397771). Cited on p. 60.
- [162] R. L. Weaver, W. Sachse, and K. Y. Kim, “Transient elastic waves in a transversely isotropic plate,” *J. Appl. Mech.* **63**(2), 337 (1996) doi: [10.1115/1.2788870](https://doi.org/10.1115/1.2788870). Cited on p. 60.
- [163] M. N. Polyanskiy, “Refractive index database,” <https://refractiveindex.info>, [Accessed on 06/19/2020]. Cited on p. 61.
- [164] F. Reverdy and B. Audoin, “Elastic constants determination of anisotropic materials from phase velocities of acoustic waves generated and detected by lasers,” *J. Acoust. Soc. Am.* **109**(5), 1965–1972 (2001) doi: [10.1121/1.1358298](https://doi.org/10.1121/1.1358298). Cited on pp. 69, 71, and 73.

- [165] F. Reverdy and B. Audoin, “Ultrasonic measurement of elastic constants of anisotropic materials with laser source and laser receiver focused on the same interface,” *J. Appl. Phys.* **90**(9), 4829–4835 (2001) doi: [10.1063/1.1405828](https://doi.org/10.1063/1.1405828). Cited on pp. 69, 71, and 73.
- [166] Y. H. Berthelot and I. J. Busch-Vishniac, “Thermoacoustic radiation of sound by a moving laser source,” *J. Acoust. Soc. Am.* **81**(2), 317–327 (1987) doi: [10.1121/1.394952](https://doi.org/10.1121/1.394952). Cited on p. 70.
- [167] R. Ing, M. Fink, and F. Gires, “Directivity patterns of a moving thermoelastic source in solid media,” *IEEE T. Ultrason. Ferr.* **39**(2), 285–292 (1992) doi: [10.1109/58.139127](https://doi.org/10.1109/58.139127). Cited on p. 70.
- [168] B. W. Drinkwater and P. D. Wilcox, “Ultrasonic arrays for non-destructive evaluation: A review,” *NDT&E Int.* **39**(7), 525–541 (2006) doi: [10.1016/j.ndteint.2006.03.006](https://doi.org/10.1016/j.ndteint.2006.03.006). Cited on p. 70.
- [169] J. S. Steckenrider, T. W. Murray, J. W. Wagner, and J. B. Deaton, “Sensitivity enhancement in laser ultrasonics using a versatile laser array system,” *J. Acoust. Soc. Am.* **97**(1), 273–279 (1995) doi: [10.1121/1.412311](https://doi.org/10.1121/1.412311). Cited on p. 70.
- [170] J. U. White, “Long optical paths of large aperture,” *J. Opt. Soc. Am.* **32** (1942) doi: [10.1364/JOSA.32.000285](https://doi.org/10.1364/JOSA.32.000285). Cited on p. 70.
- [171] J. Vogel, A. Bruinsma, and A. Berkhout, *Beamsteering of laser-generated ultrasound*, 141–152 (Elsevier), doi: [10.1016/B978-0-408-02348-1.50027-5](https://doi.org/10.1016/B978-0-408-02348-1.50027-5). Cited on p. 70.
- [172] J. Jarzynski and Y. H. Berthelot, “The use of optical fibers to enhance the laser generation of ultrasonic waves,” *J. Acoust. Soc. Am.* **85**(1), 158–162 (1989) doi: [10.1121/1.397725](https://doi.org/10.1121/1.397725). Cited on p. 70.
- [173] C. Pei, D. Yi, T. Liu, X. Kou, and Z. Chen, “Fully noncontact measurement of inner cracks in thick specimen with fiber-phased-array laser ultrasonic technique,” *NDT&E Int.* **113**, 102273 (2020) doi: [10.1016/j.ndteint.2020.102273](https://doi.org/10.1016/j.ndteint.2020.102273). Cited on p. 70.
- [174] M.-H. Noroy, D. Royer, and M. Fink, “The laser-generated ultrasonic phased array: Analysis and experiments,” *J. Acoust. Soc. Am.* **94**(4), 1934–1943 (1993) doi: [10.1121/1.407516](https://doi.org/10.1121/1.407516). Cited on p. 70.
- [175] M.-H. Noroy, D. Royer, and M. Fink, “Transient elastic wave generation by an array of thermoelastic sources,” *Appl. Phys. Lett.* **63**(24), 3276–3278 (1993) doi: [10.1063/1.110173](https://doi.org/10.1063/1.110173). Cited on p. 70.
- [176] M.-H. Noroy, D. Royer, and M. Fink, “Shear-wave focusing with a laser-ultrasound phased-array,” *IEEE T. Ultrason. Ferr.* **42**(6), 981–988 (1995) doi: [10.1109/58.476540](https://doi.org/10.1109/58.476540). Cited on pp. 70 and 74.

- [177] T. Murray, J. Deaton, and J. Wagner, “Experimental evaluation of enhanced generation of ultrasonic waves using an array of laser sources,” *Ultrasonics* **34**(1), 69–77 (1996) doi: [10.1016/0041-624x\(95\)00090-p](https://doi.org/10.1016/0041-624x(95)00090-p). Cited on p. 70.
- [178] J. P. Jones and J. S. Whittier, “Waves at a flexibly bonded interface,” *J. Appl. Mech.* **34**(4), 905–909 (1967) doi: [10.1115/1.3607854](https://doi.org/10.1115/1.3607854). Cited on pp. 73, 76, 98, and 163.
- [179] S. I. Rokhlin and Y. J. Wang, “Analysis of boundary conditions for elastic wave interaction with an interface between two solids,” *J. Acoust. Soc. Am.* **89**(2), 503–515 (1991) doi: [10.1121/1.400374](https://doi.org/10.1121/1.400374). Cited on pp. 73 and 165.
- [180] V. Vlasie and M. Rousseau, “Acoustical validation of the rheological models for a structural bond,” *Wave Motion* **37**(4), 333–349 (2003) doi: [10.1016/s0165-2125\(02\)00092-6](https://doi.org/10.1016/s0165-2125(02)00092-6). Cited on p. 73.
- [181] T. Stratoudaki, M. Clark, and P. D. Wilcox, “Laser induced ultrasonic phased array using full matrix capture data acquisition and total focusing method,” *Opt. Express* **24**(19), 21921–21938 (2016) doi: [10.1364/OE.24.021921](https://doi.org/10.1364/OE.24.021921). Cited on p. 74.
- [182] A. Viel and B. Audoin, “Directivity of GHz shear acoustic waves launched by the absorption of short laser pulses at the interface between a transparent and an absorbing material,” *J. Appl. Phys.* **123**(4), 043102 (2018) doi: [10.1063/1.5003999](https://doi.org/10.1063/1.5003999). Cited on p. 74.
- [183] S. Raetz, T. Dehoux, M. Pertou, and B. Audoin, “Acoustic beam steering by light refraction: Illustration with directivity patterns of a tilted volume photoacoustic source,” *J. Acoust. Soc. Am.* **134**(6), 4381–4392 (2013) doi: [10.1121/1.4828825](https://doi.org/10.1121/1.4828825). Cited on p. 74.
- [184] B. Audoin, H. Meri, and C. Rossignol, “Two-dimensional diffraction of plasma, thermal, and elastic waves generated by an infrared laser pulse in semiconductors,” *Phys. Rev. B* **74**(21) (2006) doi: [10.1103/physrevb.74.214304](https://doi.org/10.1103/physrevb.74.214304). Cited on p. 75.
- [185] R. Hodé, S. Raetz, J. Blondeau, N. Chigarev, N. Cuvillier, V. Tournat, and M. Ducouso, “Nondestructive evaluation of structural adhesive bonding using the attenuation of zero-group-velocity Lamb modes,” *Appl. Phys. Lett.* **116**(10), 104101 (2020) doi: [10.1063/1.5143215](https://doi.org/10.1063/1.5143215). Cited on pp. 85 and 96.
- [186] Z. Wang, A. Bovik, H. Sheikh, and E. Simoncelli, “Image quality assessment: From error visibility to structural similarity,” *IEEE T. Image Process.* **13**(4), 600–612 (2004) doi: [10.1109/tip.2003.819861](https://doi.org/10.1109/tip.2003.819861). Cited on p. 93.
- [187] M. Ducouso, A. Dalodière, and A. Baillard, “Evaluation of the thermal aging of aeronautical composite materials using Lamb waves,” *Ultrasonics* **94**, 174–182 (2019) doi: [10.1016/j.ultras.2018.09.014](https://doi.org/10.1016/j.ultras.2018.09.014). Cited on p. 93.

- [188] B. Ehrhart, R. Ecault, F. Touchard, M. Boustie, L. Berthe, C. Bockenheimer, and B. Valeske, “Development of a laser shock adhesion test for the assessment of weak adhesive bonded CFRP structures,” *Int. J. Adhes. Adhes.* **52**, 57–65 (2014) doi: [10.1016/j.ijadhadh.2014.04.002](https://doi.org/10.1016/j.ijadhadh.2014.04.002). Cited on p. 97.
- [189] P. B. Nagy and L. Adler, “Nondestructive evaluation of adhesive joints by guided waves,” *J. Appl. Phys.* **66**(10), 4658–4663 (1989) doi: [10.1063/1.343822](https://doi.org/10.1063/1.343822). Cited on p. 97.
- [190] C. Gauthier, M. Ech-Cherif El-Kettani, J. Galy, M. Predoi, and D. Leduc, “Structural adhesive bonding characterization using guided Lamb waves and the vertical modes,” *Int. J. Adhes. Adhes.* **98**, 102467– (2020) doi: [10.1016/j.ijadhadh.2019.102467](https://doi.org/10.1016/j.ijadhadh.2019.102467). Cited on p. 97.
- [191] C. Prada, O. Balogun, and T. Murray, “Laser-based ultrasonic generation and detection of zero-group velocity Lamb waves in thin plates,” *Appl. Phys. Lett.* **87**, 194109 (2005) doi: [10.1063/1.2128063](https://doi.org/10.1063/1.2128063). Cited on p. 97.
- [192] D. Clorennec, C. Prada, and D. Royer, “Laser ultrasonic inspection of plates using zero-group velocity Lamb modes,” *IEEE Trans. Ultrason. Ferroelectr. Freq. Control* **57**(5), 1125–1132 (2010) doi: [10.1109/TUFFC.2010.1523](https://doi.org/10.1109/TUFFC.2010.1523). Cited on p. 97.
- [193] H. Cho, Y. Hara, and T. Matsuo, “Evaluation of the thickness and bond quality of three-layered media using zero-group-velocity Lamb waves,” *J. Phys. Conf. Ser.* **520**, 012023 (2014) doi: [10.1088/1742-6596/520/1/012023](https://doi.org/10.1088/1742-6596/520/1/012023). Cited on p. 97.
- [194] H. Cho, Y. Yaguchi, and H. Ito, “Characterization of the bond quality of adhesive plates utilizing zero-group-velocity Lamb waves measured by a laser ultrasonics technique,” *Mech. Eng. J.* **2**(1), 14–00335 (2015) doi: [10.1299/mej.14-00335](https://doi.org/10.1299/mej.14-00335). Cited on p. 97.
- [195] S. Dahmen, “Influence of volumic fraction of adhesive in elastic and viscous thin bonded aluminum/adhesive/aluminum plate on Lamb modes that have ZGV modes,” *Ultrasonics* **94**, 37–49 (2019) doi: [10.1016/j.ultras.2018.12.005](https://doi.org/10.1016/j.ultras.2018.12.005). Cited on p. 97.
- [196] O. Balogun, T. W. Murray, and C. Prada, “Simulation and measurement of the optical excitation of the S1 zero group velocity Lamb wave resonance in plates,” *J. Appl. Phys.* **102**(6), 064914 (2007) doi: [10.1063/1.2784031](https://doi.org/10.1063/1.2784031). Cited on pp. 97 and 101.
- [197] C. Grünsteidl, T. W. Murray, T. Berer, and I. A. Veres, “Inverse characterization of plates using zero group velocity Lamb modes,” *Ultrasonics* **65**, 1–4 (2016) doi: [10.1016/j.ultras.2015.10.015](https://doi.org/10.1016/j.ultras.2015.10.015). Cited on p. 97.

- [198] F. Faëse, S. Raetz, N. Chigarev, C. Mechri, J. Blondeau, B. Campagne, V. E. Gusev, and V. Tournat, “Beam shaping to enhance zero group velocity Lamb mode generation in a composite plate and nondestructive testing application,” *NDT&E Int.* **85**, 13–19 (2017) doi: [10.1016/j.ndteint.2016.09.003](https://doi.org/10.1016/j.ndteint.2016.09.003). Cited on p. 97.
- [199] C. Grünsteidl, T. Berer, M. Hettich, and I. Veres, “Determination of thickness and bulk sound velocities of isotropic plates using zero-group-velocity Lamb waves,” *Appl. Phys. Lett.* **112**(25), 251905 (2018) doi: [10.1063/1.5034313](https://doi.org/10.1063/1.5034313). Cited on p. 97.
- [200] G. Yan, S. Raetz, N. Chigarev, V. E. Gusev, and V. Tournat, “Characterization of progressive fatigue damage in solid plates by laser ultrasonic monitoring of zero-group-velocity Lamb modes,” *Phys. Rev. Appl.* **9**, 061001 (2018) doi: [10.1103/PhysRevApplied.9.061001](https://doi.org/10.1103/PhysRevApplied.9.061001). Cited on p. 97.
- [201] D. Royer and E. Dieulesaint, *Elastic Waves in Solids I: Free and Guided Propagation* (Springer Berlin Heidelberg, 1999). Cited on p. 98.
- [202] S. I. Rokhlin and Y. J. Wang, “Analysis of boundary conditions for elastic wave interaction with an interface between two solids,” *J. Acoust. Soc. Am.* **89**(2), 503–515 (1991) doi: [10.1121/1.400374](https://doi.org/10.1121/1.400374). Cited on pp. 98 and 163.
- [203] C. Prada, D. Clorennec, and D. Royer, “Power law decay of zero group velocity Lamb modes,” *Wave Motion* **45**(6), 723 – 728 (2008) doi: [10.1016/j.wavemoti.2007.11.005](https://doi.org/10.1016/j.wavemoti.2007.11.005). Cited on p. 104.
- [204] C.-Y. Ni, N. Chigarev, V. Tournat, N. Delorme, Z.-H. Shen, and V. E. Gusev, “Probing of laser-induced crack modulation by laser-monitored surface waves and surface skimming bulk waves,” *J. Acoust. Soc. Am.* **131**(3), EL250–EL255 (2012) doi: [10.1121/1.3684737](https://doi.org/10.1121/1.3684737). Cited on p. 109.
- [205] K. A. Milton and J. Schwinger, *Electromagnetic Radiation: Variational Methods, Waveguides and Accelerators* (Springer Berlin Heidelberg, 2006). Cited on p. 136.
- [206] K. Zhang and D. Li, *Electromagnetic Theory for Microwaves and Optoelectronics* (Springer Berlin Heidelberg, 2008). Cited on p. 136.





**Titre :** Développement de méthodes ultrasons-laser pour l'évaluation non destructive des assemblages aéronautiques collés

**Mots clés :** Ultrasons laser ; Assemblages collés ; END ; Modélisation semi-analytique ; ZGV

**Résumé :** Actuellement, l'allègement des structures aéronautiques est un enjeu industriel majeur afin de réduire la consommation en carburant des moteurs et diminuer les émissions polluantes. L'assemblage par collage répond à ce besoin d'allègement et possède de nombreux avantages comparé aux techniques plus conventionnelles comme le soudage ou le rivetage. En effet, cette méthode ne nécessite pas l'ajout de rivets et permet d'assembler des matériaux composites ayant un rapport résistance/masse élevé. Néanmoins, aucune méthode d'évaluation non destructive (END) ne permet à ce jour de certifier la tenue mécanique des assemblages collés. Lever ce dernier verrou technologique permettrait un déploiement important du collage dans l'industrie.

L'objectif de cette thèse est de développer des méthodes ultrasons-laser pour l'END des

assemblages collés. Cette technique optique pour générer et détecter des ultrasons dans un matériau offre l'avantage d'être totalement sans contact. Un modèle semi-analytique permettant de simuler la propagation d'ondes générées par laser dans un multicouche est tout d'abord présenté. Puis, deux méthodes de contrôle capables de distinguer expérimentalement des collages industriels avec et sans défauts sont introduites. La première porte sur la résolution d'un problème inverse à partir d'ondes planes synthétisées et réfléchies par le collage. La seconde est basée sur l'atténuation de résonances locales des modes de Lamb à vitesse de groupe nulle (ZGV). Ces deux méthodes permettent d'identifier des paramètres quantitatifs pour distinguer des collages structuraux ayant des tenues mécaniques différentes.

**Title:** Development of laser ultrasonic methods for the nondestructive evaluation of bonded aeronautical assemblies

**Keywords:** Laser ultrasonics; Bonded assemblies; NDE; Semi-analytic modeling; ZGV

**Abstract:** Currently, the weight lightening of aircraft structures is a major industrial issue in order to reduce engine fuel consumption and greenhouse gas emissions. Adhesive bonding addresses this need for lighter structures and has many advantages compared to more conventional techniques such as welding or riveting. Indeed, this method does not require the addition of rivets and allows to assemble composite materials with a high strength-to-weight ratio. However, to date there is no nondestructive evaluation (NDE) method to certify the mechanical strength of bonded assemblies. Overcoming this last technological limitation would enable a significant deployment of adhesive bonding in the industry.

The objective of this thesis is to develop laser

ultrasonic methods for the NDE of bonded assemblies. This optical technique to generate and detect ultrasound in a material has the advantage of being fully contactless. A semi-analytic model to simulate the propagation of laser generated waves in a multilayer structure is first presented. Then, two control methods which can experimentally discriminate between industrial bonds with and without defects are introduced. The first one concerns the resolution of an inverse problem using synthesized plane waves reflected from the bonding. The second one is based on the attenuation of local resonances of zero-group-velocity (ZGV) Lamb modes. These two methods allow the identification of quantitative parameters to distinguish structural bonds of different mechanical strengths.